AN INVESTIGATION INTO INVAGINATED MEMBRANE SYSTEM DEVELOPMENT, DYNAMICS, AND ACTIN REGULATION THROUGHOUT MEGAKARYOPOIESIS

by

THOMAS JAMES O'SULLIVAN

A thesis submitted to the University of Birmingham for the degree of DOCTOR OF PHILOSOPHY

Institute of Cardiovascular Sciences
College of Medical and Dental Sciences
University of Birmingham
March 2022

UNIVERSITY OF
BIRMINGHAM

University of Birmingham Research Archive

e-theses repository

This unpublished thesis/dissertation is copyright of the author and/or third parties. The intellectual property rights of the author or third parties in respect of this work are as defined by The Copyright Designs and Patents Act 1988 or as modified by any successor legislation.

Any use made of information contained in this thesis/dissertation must be in accordance with that legislation and must be properly acknowledged. Further distribution or reproduction in any format is prohibited without the permission of the copyright holder.

ABSTRACT

Thrombocytopenia is a condition defined by low blood platelet count, often linked to defects in platelet synthesis. Megakaryocytes are the precursors to platelets that undergo endomitosis and grow to up to 64n ploidy in the bone marrow. In the later stages of megakaryocyte development, a reservoir of membrane mass known as the invaginated membrane system (IMS) accumulates within megakaryocyte cytoplasm. Importantly, structural defects in the IMS can be seen in a range of conditions characterised by thrombocytopenia (*Wiskott Aldrich syndrome*, *Bernard-Soulier syndrome* and *filaminopathies*), linking defects in IMS maturation to a low platelet count. Furthermore, many thrombocytopenic conditions are caused by mutations in proteins linked to F-actin regulation (*FLNA, ACTB, MYH9, WAS*), whilst chemical inhibition of actin cytoskeleton during megakaryopoiesis leads to aberrated or halted IMS development, highlighting actin cytoskeleton as an essential component for functional IMS maturation.

During development, the IMS transverses through several distinctive morphological stages. Whilst IMS development has been broadly categorised: *accumulation, expansion, and polarisation*, there is a lack of definition surrounding IMS morphologies, or how IMS transitions through those morphologies during development. This study uses a range of microscopy techniques and bespoke image analysis pipelines to measure 4D IMS morphology in large populations of megakaryocytes. Here, we categorise megakaryocytes into 7 different stages of development: *vacant, accumulation, compression, expansion, polarisation, destabilisation, and proplatelet formation* using qualitative morphometric data, and probe F-actin regulation of IMS maturation. Our data shows that:

- Megakaryocytes transition through polarisation of the IMS prior to proplatelet formation.
- A network of underlying invaginated tubules which prelude IMS compression and expansion.
- K-means cluster analysis can be used to perform unlabelled classification of morphometric datasets, and define rates of IMS maturation.

Furthermore, we provide evidence for:

- An Arp2/3 regulated actin cytoskeleton during IMS maturation
- An F-actin regulated polarisation and expulsion of the IMS.

CONTENTS

1 INTRODUCTION 10

1.1 Structure and dynamics of actin cytoskeleton 10
1.1.1 Actin treadmilling 10
1.1.4 The Membrane to F-actin Interface 17
1.2 Development of the invaginated membrane system within megakaryocytes 21
1.3 Morphometrics, multivariate analysis, and volumetric imaging 28
1.4 Thesis aims 32
2 METHODS 33

2.1 Ethics and origin of murine 33
2.2 Reagents list 33
2.3 Culture of murine bone marrow derived hematopoietic stem cell 34
2.4 Bovine serum albumin selection gradient 35
2.5 Immunostaining 35
2.6 Immunostaining of megakaryocytes on poly-L-lysine 36
2.7 Immunostaining of megakaryocytes on fibrinogen 37
2.8 Megakaryocyte mobility on different substrates 37
2.9 Megakaryocyte and IMS viability assay 38
2.10 Inhibiting IMS maturation 38
2.11 Wide-field imaging 38
2.12 IncuCyte imaging 39
2.13 Confocal imaging 39
2.14 iSPIM imaging 39
2.15 DiSPIM alignment 40
2.16 Expansion microscopy 42
2.17 Statistics and data analysis 43
3 MEASURING INVAGINATED MEMBRANE SYSTEM DEVELOPMENT WITH WIDE-FIELD FLUORESCENCE IMAGING 44

3.1 Aims 44
3.2 IMS is described by GP1b-α and CD41/61 in fixed megakaryocytes 44
3.3 Developing an image analysis pipeline for 2D wide-field fluorescence microscopy 47
3.4 Defining parameters to describe 2D IMS maturation 53
3.5 ANOVA of wide-field IMS analysis pipeline showed no significant difference between cultures derived from separate mice 55

3.6 The wide-field IMS analysis pipeline illustrates cytochalasin-D induced morphological change 63
3.7 Summary of Chapter 3 67
4 MEASURING INVAGINATED MEMBRANE SYSTEM DEVELOPMENT WITH PHASE CONTRAST INCUCYTE IMAGING 69
4.1 Aims 69
4.2 Developing an image analysis pipeline for IncuCyte megakaryocyte assay 69
4.3 IncuCyte IMS analysis pipeline shows no significant difference between cultures derived from separate mice 75
4.4 Summary of Chapter 4 78
5 A TEMPORAL ANALYSIS OF IMS DEVELOPMENT *IN VITRO* 79
5.1 Aims 79
5.2 Introduction 79
5.3 Mature megakaryocytes are most abundant between D2-3 of *in vitro* cultures 81
5.4 Megakaryocytes are immobilised by poly-L-lysine without perturbing IMS development 85
5.5 Time course of IMS morphological stage within *in vitro* cultures 87
5.6 Megakaryocytes develop normally in the presence of poly-L-lysine and CellMask 94
5.7 Summary of Chapter 5 96
6 LIVE, SINGLE CELL ANALYSIS OF IMS MATURATION WITH SINGLE PLANE ILLUMINATION MICROSCOPY. 97
6.1 Aims 97
6.2 Introduction 97
6.3 LifeAct and CellMask describe IMS in live-cell megakaryocytes 98
6.4 Developing an image analysis pipeline for 4D SPIM imaging 100
6.5 Defining parameters to describe 3D IMS maturation 103
6.6 Describing IMS parameter relationships throughout megakaryocyte maturation 106
6.7 Unsupervised K-means cluster analysis accurately segments developing megakaryocytes into four categories 115
6.8 Exploring the dynamics of IMS morphological transitions throughout megakaryocyte development 121
6.9 Investigating the ultrastructure of IMS morphological stages 131
6.10 Summary of Chapter 6 132
7 EXPLORING ACTIN DRIVEN BIOCHEMICAL MECHANISMS OF IMS DEVELOPMENT. 135

7.1 Aim....135
7.2 Introduction....135
7.3 Probing F-actin involvement in IMS development through inhibition with Cytochalasin-D and Jasplakinolide....137
7.4 Probing the role of formins and ARP2/3 complex in IMS development through inhibition with CK666 and SMIFH2....145
7.5 Probing the role of PLC in IMS development through inhibition with U73122....152
7.6 Summary of Chapter 7....157
8 DISCUSSION....159
8.1 An updated model of IMS maturation....159
8.2 Providing a toolkit for measuring megakaryocyte maturation....168
9 Conclusion....176
10 ACKNOWLEDGEMENTS....178
11 REFERENCES....179

List of tables and figures

Figure 1.1 F-actin treadmilling..... 12
Figure 1.2 Actin polymerisation and depolymerisation mechanisms *in vivo*..... 14
Figure 1.3 Mechanism of myosin movement..... 16
Figure 1.4 Three outcomes of cross-linked depolymerisation..... 17
Figure 1.5 Interaction between PI-4, 5-P and F-actin nucleation proteins..... 19
Figure 1.6 Fundamental F-actin macro-organisations..... 20
Figure 1.7 IMS developmental pathway..... 25
Figure 1.8 iSPIM schematic and beam..... 31
Figure 2.1 DiSPIM alignment..... 41
Figure 3.1 - Fixed cell dyes for measuring IMS morphology..... 46
Figure 3.2 Effect of different threshold functions..... 49
Figure 3.3 Effect of Rolling ball background subtraction and smoothing..... 50
Figure 3.4 Effect of smoothing on an Otsu threshold..... 51
Figure 3.5. Effect of Circularity and Size filter..... 52
Figure 3.6 Morphological parameters defining IMS ROIs..... 53
Figure 3.7 Univariate analysis of variance between sample populations..... 57

Figure 3.8 Mean of phalloidin ROI populations…… 62
Figure 3.9. Effect of Cytochalasin-D on IMS morphology…… 64
Figure 3.10. Effect of Cytochalasin-D on morphometrics…… 66
Figure 4.1. Thresholding and smoothing of IncuCyte images…… 71
Figure 4.2. Thresholding and smoothing w. fill holes and watershed of IncuCyte images……. 72
Figure 4.3. Thresholding and smoothing w. circularity and size filters of IncuCyte images…... 73
Figure 4.4. Concatenation and summation of both 20x and 40x smoothing workflows……... 74
Figure 4.5. Mean of IncuCyte ROI populations…… 77
Figure 5.1 Change in nucleus size and GP1b-α expression in maturing megakaryocytes…….. 82
Figure 5.2 Megakaryocyte size and abundance over time…… 84
Figure 5.3 Tracking of megakaryocytes…… 87
Figure 5.4 Temporal dynamics of IMS stages during megakaryopoiesis…… 89
Figure 5.5. Population means for basic IMS parameters over day 1-5…….. 91
Figure 5.6. Population means for IMS alternative parameters over day 1-5…… 92
Figure 5.7. IMS population change over time…… 93
Figure 5.8. Effect of reagents on IMS development…… 95
Figure 6.1 Live cell dyes for measuring IMS morphology…… 99
Figure 6.2. Overview of image analysis pipeline for SPIM imaging……... 102
Figure 6.3. Pair plot and coefficient of variance for parameters……... 104
Figure 6.4 Correlation heat map……..105
Figure 6.5 Manual categorisation of LifeAct SPIM at 30 minutes, pair plot…… 109
Figure 6.6 Manual categorisation of LifeAct SPIM at 30 minutes, bivariate relationships……. 110
Figure 6.7 Manual categorisation of LifeAct SPIM at 30 minutes, uMAP…… 111
Figure 6.8 Manual categorisation of CellMask SPIM at 30 minutes, pair plot…… 113
Figure 6.9 Manual categorisation of CellMask SPIM at 30 minutes, bivariate relationship…… 114
Figure 6.10 Invaginated membrane system differentiation…… 115
Figure 6.11 K-means categorisation of LifeAct SPIM at 30 minutes, bivariate relationships... 118
Figure 6.12 K-means categorisation of LifeAct SPIM at 30 minutes, pair plot…….. 119
Figure 6.13 IMS differentiation with k-means segmentation…….. 120
Figure 6.14 Quantification of LifeAct IMS differentiation over time…… 123
Figure 6.15 ARIVIS tracking efficiency over time lapse images…… 124
Figure 6.16 Transitions of morphology over time…… 129
Figure 6.17 Rates of morphological parameter change within k-means defined clusters……. 130

Figure 6.18 IMS thread work and compression…….. 131

Figure 6.19 Expansion microscopy of phalloidin at IMS during expansion……..……132

Figure 7.1 Effect of cytochalasin-D on IMS development…… 140

Figure 7.2 Effect of jasplakinolide on IMS development…….. 141

Figure 7.3 Effect of cytochalasin-D and jasplakinolide on IMS morphological stage……. 142

Figure 7.4 Effect of cytochalasin-D on IMS morphometrics……... 143

Figure 7.5 Effect of jasplakinolide on IMS morphometrics…….. 144

Figure 7.6 Effect of SMIFH2 on IMS development…….. 147

Figure 7.7 Effect of CK666 on IMS development…… 148

Figure 7.8 Effect of SMIFH2 and CK666 on IMS morphological stage…….. 149

Figure 7.9 Effect of SMIFH2 on IMS morphometrics…….. 150

Figure 7.10 Effect of CK666 on IMS morphometrics…….. 151

Figure 7.11 Effect of U73122 on IMS development…… 153

Figure 7.12 Effect of U73343 on IMS development …….. 154

Figure 7.13 Effect of U73122 and U73343 on IMS morphological stage…….. 155

Figure 7.14 Effect of U73122 and U73343 on IMS morphometrics…… 156

Figure 7.15 Effect of inhibitors on IMS maturation…… 157

Figure 8.1 Early maturation theory……..……..…….. 161

Figure 8.2 IMS maturation tool kit analysis……...…….. 169

Figure 8.3 Alternative phenotypic morphometrics……..……..…….. 174

Table 1.1 Genetic causes of thrombocytopenia related to IMS dysregulation……..…… 27

Table 3.1 Formula and descriptions of morphological parameters used to define the IMS…… 54

Table 3.2 Variance within cultures derived from a single mouse…… 60

Table 3.3. Variance within cultures derived from individual mice…….. 61

Table 3.4. Drug induced variance in wide-field analysis pipeline…… 65

Table 4.1. Variance within IncuCyte cultures derived from a single mouse…… 76

Table 4.2. Variance within IncuCyte cultures derived from individual mice…… 76

1 INTRODUCTION

Platelets are essential blood cells required for haemostasis (Holinstat, 2017). For correct function of haemostasis, platelet production and consumption must be carefully regulated, which allows a narrow range of blood platelet count. Both acquired and inherited conditions, known collectively as thrombocytopenia, can lead to a low blood platelet count (>150,000 platelets per μL) (Drachman, 2004; Johnson et al., 2016).Therefore, understanding how platelets are produced from their progenitor cells, megakaryocytes, is a critical step in treating thrombocytopenia. The invaginated membrane system (IMS), also known as the demarcation membrane system (DMS), is an internalised reservoir of lipid membrane within late-stage megakaryocytes that provides cell membrane for future platelets (Machlus & Italiano, 2013), yet little is known about how the IMS develops. Furthermore, IMS development and maturation is intimately linked to actin cytoskeleton function, with dysregulation of the actin cytoskeleton leading to defects in IMS maturation (Antkowiak et al., 2016).

1.1 Structure and dynamics of actin cytoskeleton

1.1.1 Actin treadmilling

Actin is a small globular protein (G-actin) which can polymerise to form long stable filaments (F-actin) capable of force production. G-actin monomers are polar, and consist of two major domains split into four subdomains surrounding a hinge region. The hinge region is accessible via two clefts between domain 2 and 4, and 1 and 3. The 2 to 4 cleft is associated with the binding of ATP and Mg^{2+}, whereas the 1 to 3 cleft is hydrophobic and functions as a point of interaction between actin binding proteins (ABPs). Therefore, actin can be thought of as two halves flexing on a hinge, the rotation of which is dependent on small molecules, ions, and ABPs (Oda et al., 2009). Under

physiological conditions, G-actin is loaded with both Mg^{2+}, and ATP (Pollard et al., 2000). There are three main stages to actin polymerization *in vivo,* (figure 1.1), *(Wear et al., 2000)*:

1) Nucleation

    An initial nucleus of 3 to 4 actin monomers is formed. This stage of polymerization is the rate limiting step.

2) Elongation

    After nucleation, filaments elongate rapidly.

3) Steady state

    *Eventually, the rate of polymerisation is equal to the rate of depolymerisation due to free G-actin monomer concentra*tions.

Actin is an ATPase, and so ATP coupled Actin can exist as either: Actin-ATP, Actin-ADP·Pi, or Actin-ADP. Simplistically, actin-ATP is polymerised at the barbed end (+ve) of F-actin, ATP hydrolyses throughout the filament, and actin-ADP depolymerises at the pointed end (-ve) of F-actin. This is known as actin treadmilling, and a single G-actin monomer can re-enter the pool of free G-actin by exchanging its ADP for ATP, (Fujiwara et al., 2007).

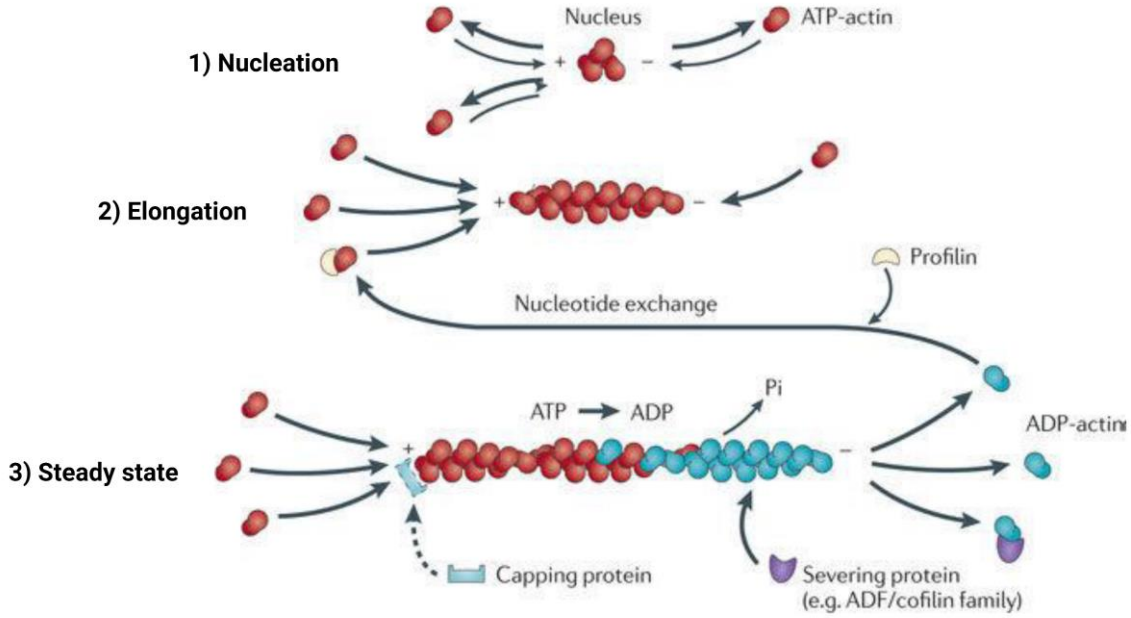


Figure 1.1 **F-actin treadmilling.** G-actin, and subsequently F-actin, are polar molecules. Actin is polymerised in its ATP bound form at the barbed end (+ve) and depolymerised in its ADP bound form at the pointed end (-ve). Hydrolysis occurs throughout filament. There are three main stages to actin filament formation: **Nucleation -** Small nucleuses of 3 - 4 actin monomers are formed. **Elongation -** Rapid addition to the barbed end of the filament. **Steady state -** As less free G-actin is available, the amount of depolymerisation is mediated by several key ABPs including profilin, severing proteins, and capping proteins. Adapted from (Nürnberg et al., 2011).

In vivo, there are two monomeric ABPs that can affect the pool of free G-actin. Thymosin β4 is an actin sequestering molecule, and therefore thymosin β4 bound actin cannot polymerise. Profilin, on the other hand, refuels the free pool of actin by facilitating the exchange of ADP for ATP, and increases the polymerisation rate at the barbed end of F-actin in the presence of formins (Carlier & Shekhar, 2017). Thymosin β4 is also exchanged for profilin readily and so acts to buffer the pool of free G-actin (Xue & Robinson, 2013).

1.1.2 Regulation of F-actin polymerisation and depolymerisation

GTPase proteins act as master regulators of actin polymerisation, and recruitment of ABPs. GTPase proteins are located within the membrane and respond to external

stimuli to recruit formins, Arp2/3, and myosin, as well as other ABPs, either directly or through kinase activation (Sit & Manser, 2011; vicente-manzanares, Ma, et al., 2009). The three best characterised Rho GTPase proteins within the megakaryocyte are RhoA, Cdc42, and Rac1 (Pleines et al., 2019).

Formins are dimer proteins which act to promote actin nucleation. Rho GTPases activate formins through direct binding and interference with the auto-inhibition mechanism (Schönichen & Geyer, 2010), although there are many different formins which are activated and recruited via different mechanisms (Zuidscherwoude et al., 2019). Monomers of formins contains two major conserved domains: FH1 and FH2, and a less conserved FH3 domain. Profilin, is a ligand for the FH1 domain, and the FH1 domain is essential for the use of profilin bound G-actin (Watanabe et al., 1997). The interaction between profilin and the FH1 domain causes an increased elongation rate at the barbed end of F-actin. The FH2 domains act as a dimer and are thought to directly interact with the actin filament to promote nucleation (Goode & Eck, 2007). Furthermore, formins act as mechanosensors, and a contraction of the attached actin filament inhibits formin dependent polymerisation (Zimmermann et al., 2017). Profilin also binds to microtubules, which links actin and microtubule organisation via formins, linking actin and microtubule dynamics (Nejedla et al., 2016). During human megakaryocyte maturation three formins are highly expressed: FHOD1, DAAM1, and DIAPH1, with FHOD1 showing the highest expression (THOMAS et al., 2011), however in addition to these formins, murine megakaryocytes also contain high expression levels of formins Fmnl3 and Inf2.

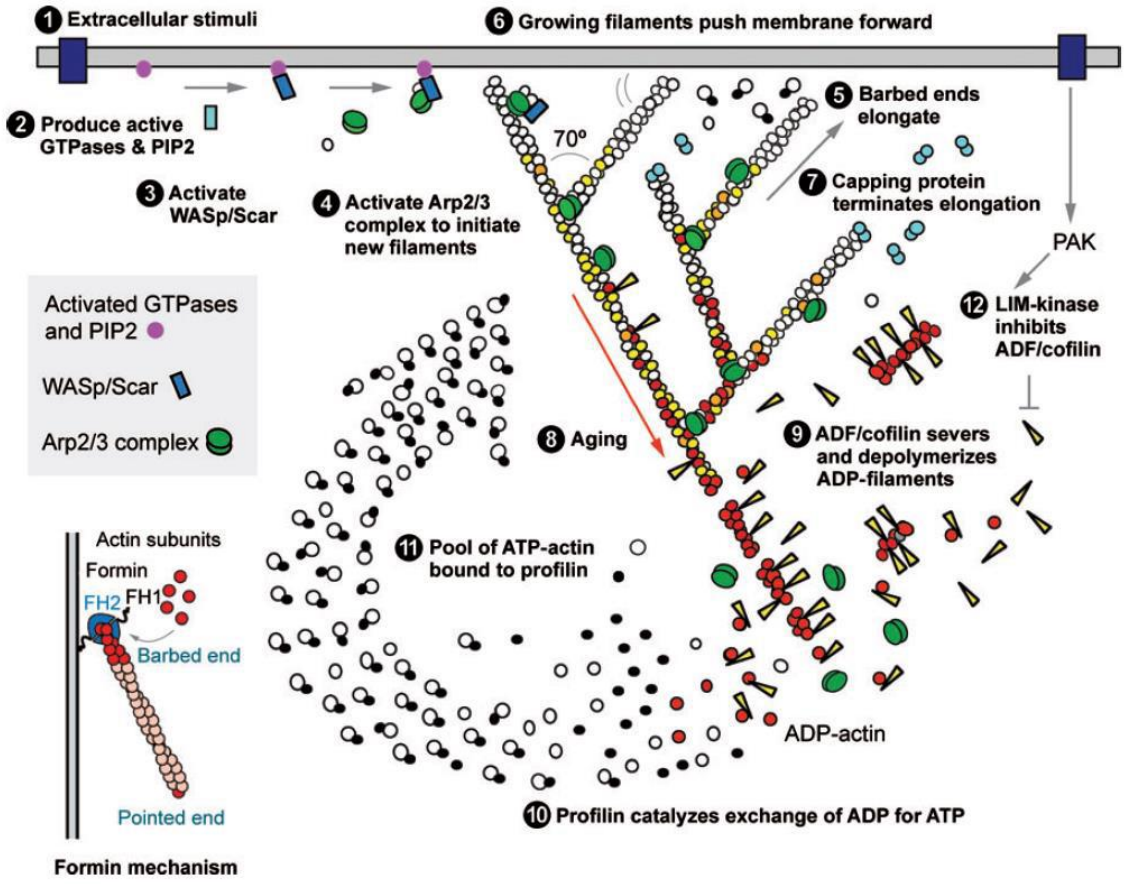


Figure 1.2 **Actin polymerisation and depolymerisation mechanisms *in vivo*. 1)** Initiation of polymerisation via external stimuli, **2)** Spatial activation of membrane bound GTPases and PIP2, **3)** Activation of WASp/Scar (Arp2/3) regulating complex, **4)** Activation of Arp2/3, mediated branching and nucleation, **5)** Polymerisation at barbed ends of actin filaments, **6)** Polymerisation force production on membrane, **7)** Capping proteins terminate polymerisation, **8)** Actin-ATP hydrolysis, **9)** Severing molecules act to both, increase actin depolymerisation and promote polymerisation rate due to formation of new actin nucleus, **10)** Profilin acts to re-stock free actin, **11)** Profilin-actin pool, **12)** Inhibition of severing factors (Pollard, 2007).

Arp2/3, a second F-actin nucleation factor, efficiently nucleates and branches actin filaments in the presence of nucleation promoting factors, such as WASP and SCAR/WAVE proteins (Lane et al., 2014). Arp2/3 binds to a primary filament and promotes the nucleation of a secondary filament and a 70˚ angle (Pizarro-Cerdá et al., 2017). Therefore, Arp2/3 increases the number of available barbed ends. Interestingly, profilin directly hinders Arp2/3 complex F-actin elongation through competitive

inhibition of G-actin with WASP, and therefore promotes formin mediated actin polymerisation (Suarez et al., 2015).

Capping proteins are a major regulator of actin dynamics that act to block polymerisation of barbed ends or reduce pointed end depolymerisation. Additionally, capping proteins are sterically inhibited by phosphatidylinotisol-4, 5-bisphosphate (PI-4,5-P_2) (Edwards et al., 2014). Some capping proteins such as gelsolin also act as severing proteins, however the major severing proteins reside in the cofilin/ADF family. Severing proteins act to cleave the F-actin, both depolymerising and creating additional barbed ends for an increased global polymerisation rate (Bernstein & Bamburg, 2010; Poukkula et al., 2011) (figure 1.2).

1.1.3 Actin Force Production

Myosin type II is an essential motor protein in most functions of the actin cytoskeleton (Heissler & Manstein, 2013). Myosin type II are able to produce contractile force, “walk” along actin filaments, and crosslink two actin filaments together. There are many classes of myosin, however class II is the major myosin component of the actin cytoskeleton. Myosin II is also the main instigator for mechano-transduction in cells. Myosin II is a hexamer consisting of two long heavy chains (MHCII), two regulatory light chains (RLC), and two essential light chains (ELC). The MHCII is split into globular head domain and a long-coiled tail domain, which are separated by a lever domain. ELC and RLC chains bind to this lever domain (Aguilar-Cuenca et al., 2014; Xiao et al., 2016). Myosin motor activity is an ATP dependent mechanism facilitated by the globular head domain of the protein (figure 1.3). Myosin type II is shown to be activated by RhoA and CDc42 downstream kinases, such as Rho kinase (ROCK), which phosphorylate the RLC (Wilkinson et al., 2005).

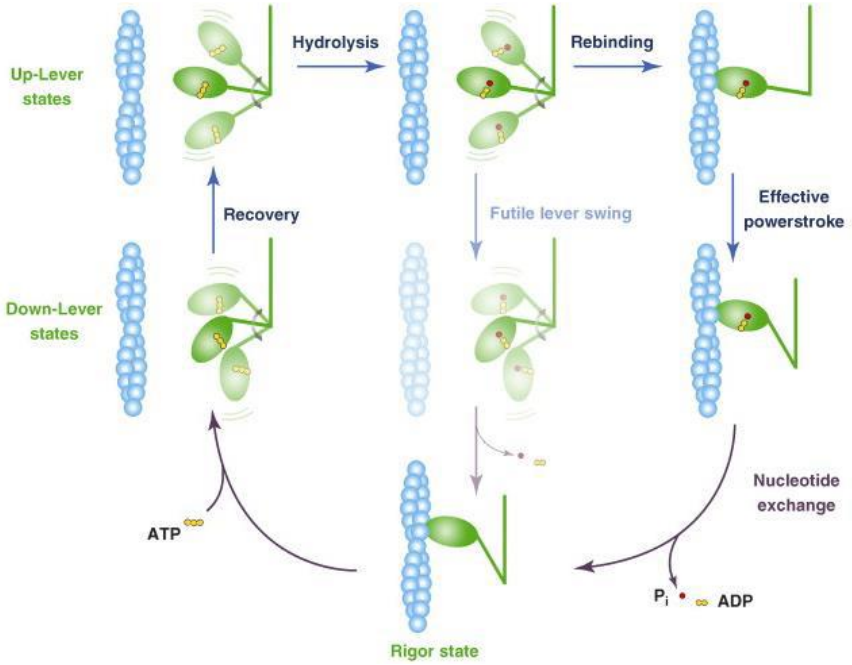


Figure 1.3 **Mechanism of myosin movement.** ATP bind to the head domain and causes the lever domain to pivot via allosteric hindrance. Hydrolysis of ATP is only possible in the up-lever state. Hydrolysis of ATP prevents the lever domain from pivoting, and allows for the head to rebind to F-actin. Rebinding to actin causes the level domain to pivot once more into the down lever position, and move the myosin along the filament. ADP and Pi than dissociate from the head domain, allowing the process to restart (Málnási-Csizmadia & Kovács, 2010).

Myosin II also functions in a second mechanism of F-actin contraction. Studies into the contraction mechanism of the actin-myosin ring (AMR), during cytokinesis, have shown that contraction still occurs with a deletion of the myosin II motor domain. However, contraction is slowed considerably with a deletion of myosin light chain. Contraction of the AMR also shows no density change in its structure, suggesting that the AMR contracts via a depolymerisation mechanism. In this model, myosin swings between depolymerising filaments to mediate contraction of membranes (figure 1.4) (Mendes Pinto et al., 2012).

Lastly, actin can produce force via polymerisation. Myosin is not required in this model, as the energy for force production comes from the exothermic polymerisation of F-

actin. Examples of this include endocytosis and exocytosis, formation of filopodia and lamellipodia, as well as “actin rockets” produced by some species of bacteria for locomotion (Carlsson, 2018).

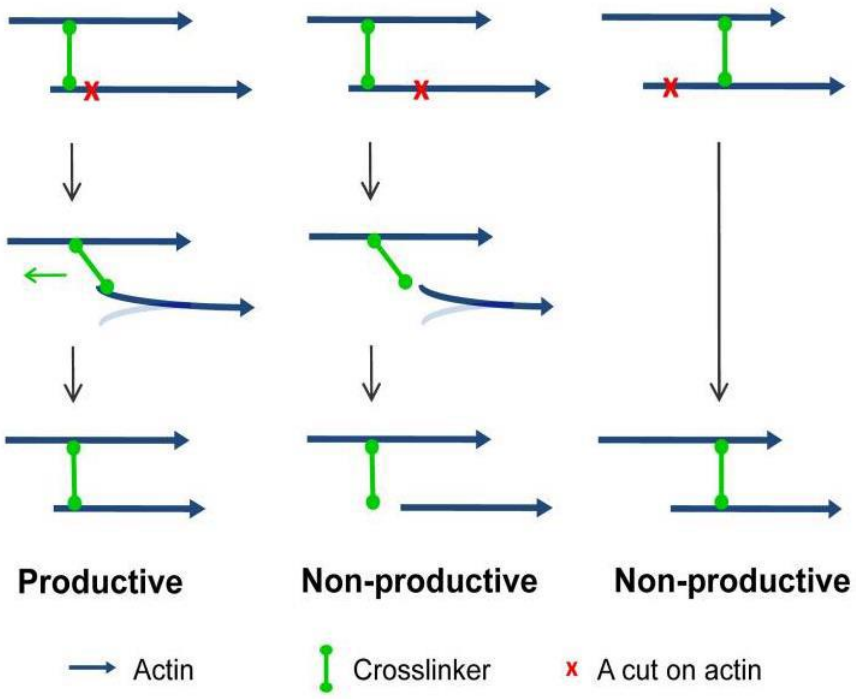


Figure 1.4 **Three outcomes of cross-linked depolymerisation.** From left to right, outcome 1 shows productive depolymerisation. Severing of the F-actin via cofilin causes a detachment of the cross linker. The cross linker releases the depolymerised fragment, and moves via Brownian motion, recapturing the depolymerised end of the F-actin. Elastic potential provides force necessary for contraction. Outcome 2 shows a variant of non-productive depolymerisation. Cofilin severs F-actin too far from the cross linker, stopping the recapture of the depolymerised end. Outcome 3 shows a second variant of non-productive depolymerisation. Cofilin severs F-actin where no cross linker is released (Mendes Pinto et al., 2012).

1.1.4 The Membrane to F-actin Interface

To produce force, the actin cytoskeleton has to be directly anchored to the membrane. Connections to the membrane can be either through transmembrane proteins, or membrane/protein binding domains. The adhesion receptors dystroglycans and integrins are transmembrane proteins which bind to the actin cytoskeleton through

recruitment of, dystrophin and utrophin, and talin and vinculin, respectively. Integrins and dystroglycans link to the extracellular matrix to actin, and act as mechanosensors for actin polymerisation (Spence et al., 2004; Vicente-Manzanares, Choi, et al., 2009)). Internal and external stimulus activate these extracellular sensors, which in turn coordinate the localisation and activation of Rho GTPases in the plasma membrane. Formins directly bind to GTPases and have been shown to interact with the lipid membrane through a PTEN domain which directly integrates into the membrane. Similarly, the Arp2/3 complex contains a PH motif, also allowing the protein to bind to the membrane (Bezanilla et al., 2015).

F-actin is able to alter membrane shape through propagation of force, however binding of ABPs to membranes or the integration of certain lipids and proteins into a membrane can also alter the membranes physical attributes, such as curvature (McMahon & Boucrot, 2015; Stahelin, 2009). The FBAR protein is a well recorded membrane binding protein capable of inducing curvature. The FBAR protein also acts as a recruitment protein for other ABPs such as Arp2/3 and formins, marking it as an important regulator of actin polymerisation (Bezanilla et al., 2015).

The composition of the peripheral membrane is predominantly phospholipid (Suetsugu et al., 2014). Phosphoinositides are a group of phospholipids that have been associated with regulating actin polymerisation via direct interaction with ABPs (Senju et al., 2017). RhoA and Rac1 upregulate the production of PI-4,5-P_2, the most abundant phosphoinositide in cells, through activation of phosphatidylinositol 4 phosphate 5 kinase (PIP5K). In turn, PI-4,5-P_2 binds and recruits PTEN domain containing formins, and WASP/ WAVE proteins, allowing for rapid actin elongation at PI-4,5-P_2 rich membranes. Furthermore, PI-4,5-P_2, along with PI-3,4,5-P_3, have the

additional function of binding to profilin, increasing the pool of unbound actin monomers (Goldschmidt-Clermont et al., 1990). As previously mentioned, profilin bound actin inhibits Arp2/3. Therefore, PI-4,5-P_2 is theorized to regulate the balance between formin, and Arp2/3 mediated nucleation and elongation of F-actin. Hydrolysis of PI-4,5-P_2 by phospholipase C releases profilin, possibly acting as a mechanism to increase formin mediated nucleation and elongation of F-actin (Saarikangas et al., 2010) (figure 1.5).

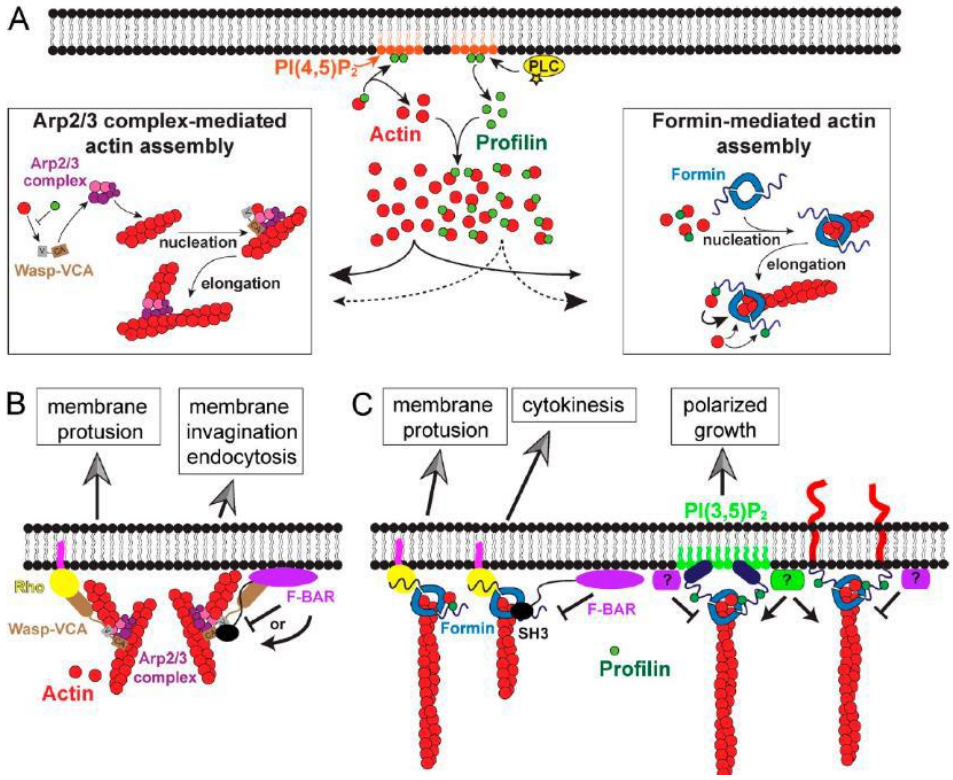


Figure 1.5 **Interaction between PI-4, 5-P_2 and F-actin nucleation proteins a)** PI-4,5-P_2 binds to profilin, removing it from the system. Profilin bound actin inhibits Arp2/3 activity, and promotes formin activity. Therefore, it is theorised that PI-4,5-P_2 regulates the balance between formin and Arp2/3 activity. Hydrolysis of PI-4,5-P_2 via phospholipase C causes a release of profilin back into the system. **b)** Rho and F-BAR regulation of Arp2/3 complex activity. Rho actively recruits WASP/WAVE nucleation promotor factors that modulates Arp2/3 activity. F-BAR domains interact with WASP to either enhance or inhibit Arp2/3 activity. Arp2/3 activity has been linked to membrane protrusion, and membrane invagination endocytosis. **c)** Rho and F-BAR regulation of formin activity. Rho directly binds formin to localize them to the cell membrane. F-BAR proteins can inhibit or enhance formin activity. Formins can directly bind to phosphatidylinositol 3,5 bisphosphate (PI-3,5-P_2) via the PTEN dominant, or transverse the membrane via an N-terminal transmembrane domain (Saarikangas et al., 2010). Formin activity has been linked to membrane protrusion, cytokinesis, and polarised F-actin growth (Bezanilla et al., 2015).

1.1.5 Actin macro-structures

Originally, the three major Rho GTPases (RhoA, Cdc42, and Rac1), were thought to produce stress fibres, filopodia, and lamellipodia, respectively. However, it is now clear that the mechanisms of how these regulators of F-actin structural architecture function undergo are more complex. Predominantly, an F-actin network can be arranged as either straight (recruitment of formins), branched (recruitment of Arp2/3), or anti-parallel. The composition will affect the stiffness, contractility, and rate of polymerisation of the actin system, adapting it to different functions (figure 1.6) (Letort et al., 2015).

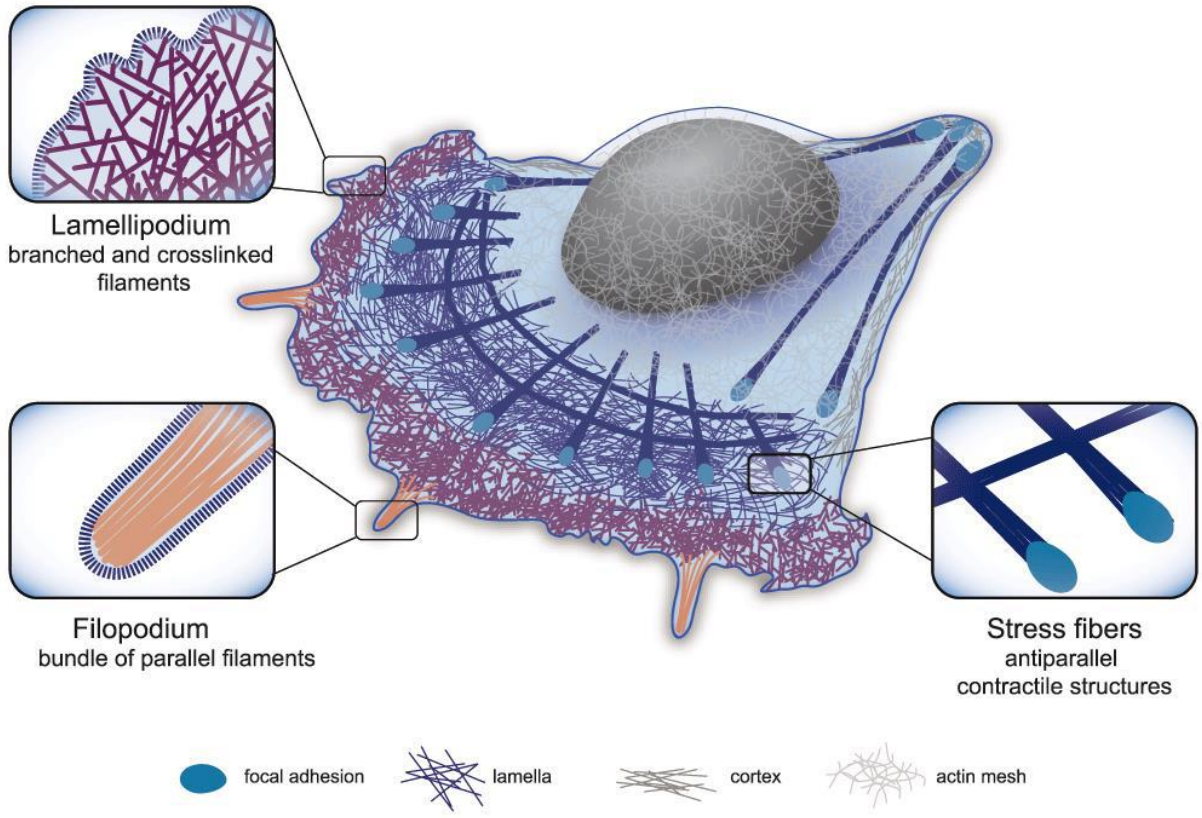


Figure 1.6 **Fundamental F-actin macro-organisations.** F-actin can be arranged as either a bundle of parallel filaments (Filopodia), a network of branched filaments (Lamellipodia), or anti-parallel bundles (Stress fibres), (Letort et al., 2015).

1.2 Development of the invaginated membrane system within megakaryocytes

The IMS is a large, internalised pool of membrane material that develops in late stages of megakaryocyte development. The IMS ultimately provides the membrane material required for the formation of platelets, however although some details of the process are known, the full mechanism behind the key stages of IMS development remain undiscovered (Nakao & Angrist, 1968). Maturation of the IMS is dependent of the activity of the mechano-sensory, GP1b-IX-V receptor complex (Dütting et al., 2017). This complex is highly associated with the development of the IMS as shown by electron microscopy (Eckly et al., 2014). Therefore, the GP1b-IX-V complex is regularly used as a biomarker for the IMS. GP1b-IX-V is also thought to be a regulator of Cdc42 activity, linking GP1b-IX-V activation to F-actin regulation (Pleines et al., 2010). Similarly, PI-4,5-P_2 is heavily associated with the IMS throughout maturation and presents a potential biomarker (Schulze et al., 2006) and is also a known regulator of actin polymerisation (Senju et al., 2017).

Megakaryocytes are large polyploid cells that develop from haematopoietic stem cells within the bone marrow, and eventually extend long membrane protrusions into the lumen of capillaries, which branch and bud to form platelets. Polyploidy is a product of the cells switching from mitotic to endomitotic division due to the incomplete furrowing of the AMR at the equatorial membrane during late cytokinesis. Endomitosis occurs immediately before or in conjunction with IMS formation and can be thought of as a prelude to IMS development. Incomplete furrowing of the AMR has been linked to an absence of activated RhoA in the ingression furrow and a subsequent loss of MYH10 and MYH9 from the mitotic furrow (Lordier et al., 2012). Interestingly, MYH9 is heavily

upregulated elsewhere in the megakaryocyte throughout maturation. Furthermore, Rho GEFs ECT2 and GEF are required for localisation and function of RhoA, also exhibit decreased expression during megakaryocyte maturation (Gao et al., 2012). There is a partial accumulation of these components during the early cycles of endomitosis, but as the ploidy increases the depth of ingression and the accumulation of these proteins decreases. Endomitosis corresponds with high numbers of platelets, but is not essential for platelet production, with 2N megakaryocytes producing one or two platelets, and 16N megakaryocytes giving rise to ~2000 platelets (Mattia et al., 2002). During this period of endomitosis, the two phases of IMS development occur: IMS formation via peripheral membrane invagination, and IMS reformation and polarisation (Machlus & Italiano, 2013). These events precede an extension of the megakaryocyte membrane into what is known as the proplatelet, a pre-platelet body. Importantly, an increase in ploidy reflects an increase in IMS mass, highlighting that the larger a megakaryocyte is, the more platelet mass it can produce (figure 1.7).

1.2.1 IMS invagination and formation

Original theories for platelet production suggested that the IMS demarcates the cytoplasm into platelet territories (Nakao & Angrist, 1968). Whilst the IMS does demarcate the membrane, the name suggests that the IMS demarcates pre-organised platelets. However, evidence now shows that this internal membrane system is continuous with the peripheral membrane (Mahaut-Smith et al., 2003), and pulse chase experiments staining peripheral GP1b-β show the inward movement and internalisation of the peripheral membrane over time (Eckly et al., 2014). These studies led to the theory that the IMS originates from a peripheral membrane invagination.

Pharmacological studies using Cytochalasin D or Latrunculin A to inhibit actin polymerisation in early stages of megakaryocyte maturation causes a regression of IMS invagination and a redistribution of GP1b-β throughout the peripheral membrane. This highlights that F-actin is essential for IMS invagination (Antkowiak et al., 2016). The biochemical mechanisms behind invagination remain a mystery, but actin is known to traffic vesicles of specific composition towards the site of membrane invagination in other systems such as the actin-myosin ring (VerPlank & Li, 2005). This is thought to allow an increase in surface area for invagination, and provide a membrane composition more suitable to manipulation and curvature, but it could also be a method of accumulating specific proteins such as cytoskeletal components and platelet specific proteins such as CD41/61, GP1b complex, or GPVI.

Images capturing the proximity of the endoplasmic reticulum (ER) with the IMS, and the exposed trans-Golgi facing the IMS suggested that expansion of the IMS may be aided by ER and Golgi systems (Eckly et al., 2014). This is backed up by experimental evidence that shows the trafficking pathway of Golgi derived glycosyltransferases into platelets (Wandall et al., 2012). This direct interaction between Golgi, ER and IMS would provide an ideal environment to change the composition of the IMS from predominantly peripheral membrane based, to a composition including more platelet specific proteins which may be expressed more heavily as ploidy increases. Lastly, invagination of the peripheral membrane can occur multiple times, and it has been suggested that the failure of the actin-myosin ring to ingress during endomitosis, and the invagination of the IMS is linked, as observations show that IMS invagination occurs as the actin-myosin ring assembly fails (Eckly et al., 2014).

1.2.2 IMS reformation and polarisation

Next the IMS condenses and polarises to form a hollow shell cupped by the peripheral membrane of the cell before the IMS condenses further into a sphere of membrane rather than a shell (Antkowiak et al., 2016).

The formation of this polarised structure is dependent on Cdc42 activity, which itself is downregulated in the presence of RhoA. Knockdown of Cdc42 leads to a loss of any IMS polarisation, whereas a knockdown of RhoA leads to macrothrombocytopenia, early development of polarisation, as well as a decreased membrane stiffness and contractility. Additionally, knockdown of PKCε, a regulator of RhoA function, also promotes proplatelet formation and platelet release (Gobbi et al., 2013). Knockdown of DIAPH1, a RhoA effector in megakaryocyte maturation, leads to increased proplatelet formation and the formation of stable microtubules, as well as a reduction in F-actin (Pan et al., 2014). Together, these findings suggesting a RhoA/ Cdc42 regulatory mechanism where RhoA is heavily down regulated during polarisation (Dütting et al., 2017).

Surprisingly, Rac1/RhoA and Rac1 knockouts showed no difference in platelet production, suggesting a redundancy between Cdc42 and Rac1. In contrast, a Rac1/Cdc42 double knockdown exhibits macrothrombocytopenia and abnormal platelet function (Pleines et al., 2010).

The reliance of the reformation and polarisation stage on the actin cytoskeleton is highlighted by pharmacological studies with cytochalasin-D, and latrunculin A, chemicals which cause actin depolymerisation and inhibit actin polymerisation. Megakaryocytes treated with these chemicals show a complete loss of internalized IMS structure, and an expansion of the nucleus. Furthermore, deletion of MYH9

similarly causes an expansion of IMS tubules, suggesting that myosin dependent force production plays a role in actin contraction and IMS stability during polarisation (Antkowiak et al., 2016).

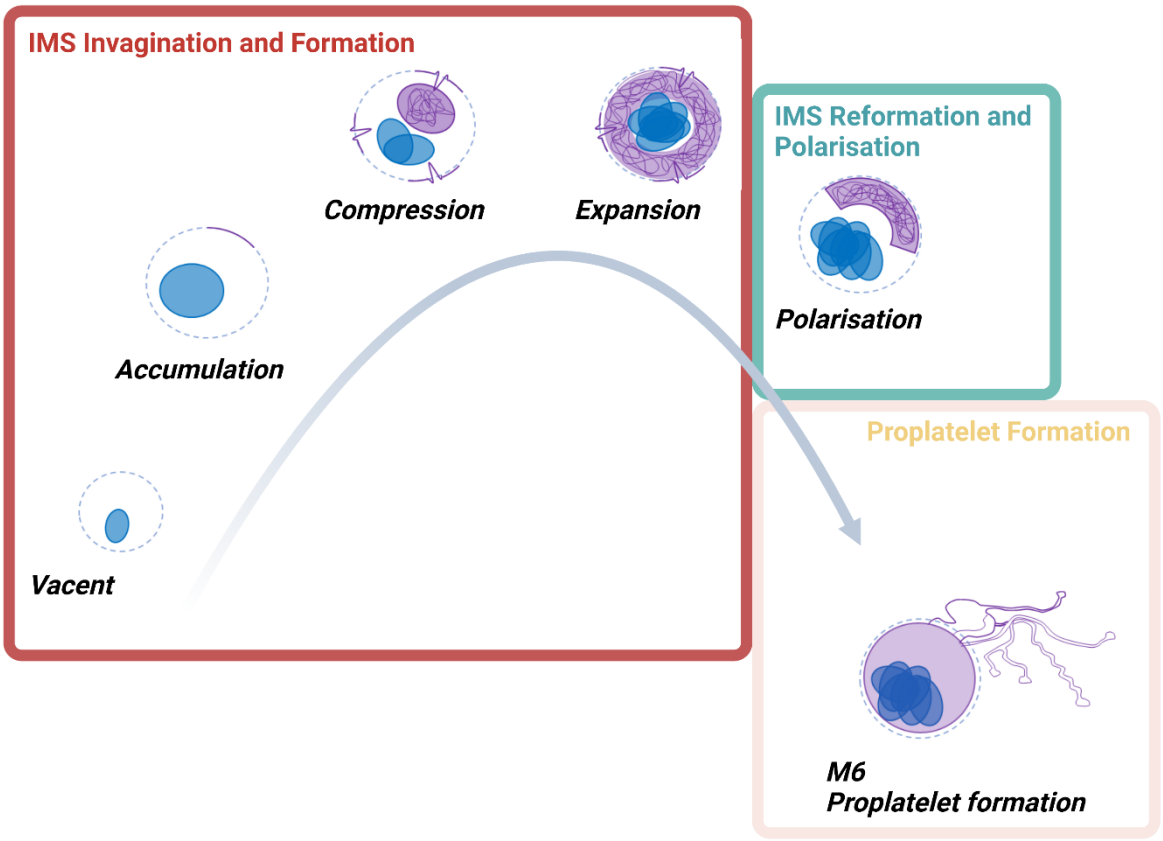


Figure 1.7 **IMS developmental pathway.** Initially, the IMS appears as an accumulation of GP1b complex and F-actin at the periphery of the cell. Later, the membrane ingresses via an unknown mechanism, and IMS expands within specific loci within the megakaryocyte until the megakaryocyte is full of IMS. Prior to proplatelet formation, the IMS has be observed to polarise towards one side of the megakaryocyte. During proplatelet formation, IMS is assumed to be consumed for proplatelet elongation.

1.2.3 IMS proplatelet formation

The extension of proplatelets occurs at the peripheral membrane proximal to the IMS. The extension mechanism depends on microtubule and dynein function, with ATP dependent motor movement causing a sliding of microtubules to form the proplatelet. Building on this, inhibition of the polymerisation of tubulin does not affect proplatelet

extension, and therefore is not involved in force production required form proplatelet extension (Bender et al., 2015). Inhibition of polymerisation and depolymerisation of actin by cytochalasin-D shows an increased proplatelet extension rate, suggesting that actin works against microtubule forces of extension (Richardson et al., 2005). Inhibition of actin also decreases platelet branching (Antkowiak et al., 2016).

Release of platelets into the blood is another mechanism that is not yet fully understood. Mature megakaryocytes degrade the basement membrane by forming actin structures known as podosomes (Schachtner et al., 2013). A down regulation of Cdc42, or deletion of its downstream nucleation activating factor WASP, both cause a loss of matrix degrading podosomes and ultimately lead to micro-thrombocytopenia (Pleines et al., 2010; Sabri et al., 2006). Microscopy has been used to visualise proplatelet extension across the lumen of capillaries *in vitro* and *in vivo*, suggesting that shear forces are in part responsible for ultimate cleavage of platelets from the tips of proplatelets (Dunois-Lardé et al., 2009). Actin inhibition via cytochalasin-D, latrunculin A, and jasplakinolide all showed an inhibition in platelet budding from proplatelet tip, an enlarged proplatelet tip, and a regression in the majority of proplatelets formed (Antkowiak et al., 2016). This would suggest that actin plays an integral role in the structure of the proplatelets and possibly in the abscission of platelets from the tip.

To allow podosomes to degrade, the megakaryocyte must contact the capillary. Originally, it was thought that the megakaryocyte may migrate towards the capillary through the development of lamellipodia (Dütting et al., 2017). However, recent studies have shown that the distance between capillaries is small enough for a megakaryocyte to come into contact just through expansion during maturation (Stegner et al., 2017).

Further studies on the environment of bone marrow illustrate that environmental stiffness effects IMS development (Aguilar et al., 2018; Aguilar et al., 2016). However, there are still many questions to answer about how the actin cytoskeleton effects IMS development and platelet formation (Poulter & Thomas, 2015).

1.2.4 Thrombocytopenia and IMS development

Thrombocytopenia describes a multitude of diseases which manifest in the production of low blood platelet counts, and can be caused by defects in either platelet production, or clearance from the blood stream. Therefore, IMS development likely plays an important role in many thrombocytopenias, and IMS dysregulation can be linked to genetic factors to establish which components drive IMS maturation (table 1.1). In particular, cytoskeletal proteins and anchors seem vital for IMS development, with some key proteins including: Wiskott-Aldrich syndrome protein (linked to Arp2/3 regulation), Myosin 9, filamin A, and the formin DIAPH1 (Bluteau et al., 2009; Johnson et al., 2016; Jurak Begonja et al., 2011; Poulter & Thomas, 2015; Strassel et al., 2009).

Table 1.1 **Genetic causes of thrombocytopenia related to IMS dysregulation.** Most genetic causes leading to both thrombocytopenia and IMS dysregulation are linked to cytoskeletal proteins or related receptor proteins. Importantly, Bernard-Soulier syndrome and Wiskott-Aldrich syndrome are two well characterised diseases in which the cause of thrombocytopenia and aid in cytoskeleton recruitment and function.

Genetic factor	Disease	Function
GP1b-α, β, or IX	Bernard-Soulier syndrome	- Receptor ligand - Cytoskeletal anchor
WAS	Wiskott-Aldrich syndrome	- Cytoskeletal protein - Actin nucleation
MYH9	~	- Actin force generation
FLNA	Filaminopathies	- Cytoskeletal stability

		- Cytoskeletal anchor
ACTN1	~	- Actin cytoskeleton
DIAPH1	~	- Actin nucleation

1.3 Morphometrics, multivariate analysis, and volumetric imaging

1.3.1 Morphometrics

Whilst cellular development is often categorized by multi-omic techniques (proteomics, transcriptomic, and genomics) which are able to detect cellular activity and content (Hasin et al., 2017; Lederer & La Manno, 2020; Miao et al., 2021), morphological analysis provides structural information, linking cellular mechanics to physical characteristics (Binder et al., 2021; Roy et al., 2017). Throughout megakaryocyte differentiation the IMS expands and develops, presenting a range of varying, but distinct morphologies. Yet, little is understood about the morphological relevance of IMS structures, or their temporal occurrence and relationship, leading to the need for a conclusive assessment of IMS morphology before in-depth biochemical studies can be conducted. Biological imaging is a fast and ever-growing field with a wide range of specialised techniques that provides a large breadth of information from a single sample. Fluorescence imaging in particular allows for specific proteins to be defined by a multitude of spatial and temporal parameters, providing the ideal tool to visualise specific 4D morphological structures (Chudakov et al., 2010; Combs, 2010; Duwé & Dedecker, 2019).

Whilst biological imaging is a powerful analytical tool, the extraction of quantitative data from these images often requires knowledge and experience in languages such a Python, Java, and MATLAB. This can deter detailed analysis of microscopy images by

those without the necessary computer science skills, meaning often only limited manual analysis is performed (Kuznetsova et al., 2019; Lürig et al., 2021; Voigt et al., 2021; Zeng et al., 2017). However, developments in computer aided image analysis over the last 20 years have created a foundation of plug-ins, open-source software, and functions creating massive potential for identification, segmentation, feature extraction, classification, and analysis of large volumes of quantitative information from microscopy images. This allows those with lesser 'coding' experience to define phenotypes in more detail with less bias and to streamline previous labour-intensive analysis.

Furthermore, a large number of morphological descriptors are measured when describing an objects morphology, leading to large datasets containing multiple variables. Multivariable analysis (MVA) incorporate are range of techniques which mine datasets to find patterns and relationships (Vargason et al., 2017), with K-means clustering being one of the most established and well used. K-means is an iterative process following three steps: 1) Centroids are placed within the dataset, 2) Observations are associated to the centroid closest to them, and 3) Centroids are moved to the mean value of those observations (Bock, 2007; Chetty & Shukla, 2014). This process repeats until the centroids accurately represent the distribution of the dataset, categorising observations into different clusters (Ref for cluster analysis). Typically, K-means is used to classify a subset of the dataset, or training dataset. With the clusters derived from the training dataset the wider dataset even similar datasets can be predicted and classified. As such K-means presents a valuable tool for automatic classification of morphological data.

1.3.2 Wide-field, and inverted single plane illumination microscopy

The visualisation and accurate measurement of morphology in cell populations requires imaging techniques which provide high spatial and temporal resolutions, without sacrificing field of view (FOV) (Tarazona et al., 2020). Furthermore, damage induced by illumination can lead to misinterpretation of morphological change and as such imaging techniques used for live-cell imaging need to be gentle, and illuminate the sample with a low photon dose to preserve healthy maturation throughout image acquisition (Hoebe et al., 2007; Icha et al., 2017; Kiepas et al., 2020; Laissue et al., 2017).

Light-sheet fluorescent microscopy (LSFM) describes a variety of microscope techniques which utilise planar illumination to form thin sheets of light on a sample. Whilst episcopic approaches such as wide-field and confocal illuminate the entire sample during image acquisition, only a small plane of the sample is illuminated during LSFM acquisition, meaning samples can be imaged for days with minimal photon damage (Gritti et al., 2016; Pampaloni et al., 2011; Stelzer, 2015; Wu et al., 2011).

Inverted single plane illumination microscopy (iSPIM) is a LSFM technique which allows for the imaging of conventionally grown samples. iSPIM is a reconstruction of an inverted microscope, altering the light path to travel through two separate objectives placed at 90° angles. Rather than shaping the laser into a hyperbolic sheet, in iSPIM imaging the laser beam is rapidly oscillated laterally in order to create a thin, curved light sheet. This light sheet can be moved across the sample either by changing the angel of the beam, or by moving a motorised stage, allowing rapid 3D volumes to be captured 30x faster than spinning-confocal disk (figure 1.8) (Kumar et al., 2014; Wu et al., 2011). Importantly, as the beam is osculated it dwells at the edges of the sheet

leading to an increased illumination intensity, and a trade-off between temporal resolution and FOV. The beam is Gaussian in its distribution, and can also be thinned to reduce refractive aberrations and increase spatial resolution. However, as the beam thins, the thinnest region of the beam also decreases, which again leads to a trade-off in spatial resolution and FOV (Levy et al., 2019).

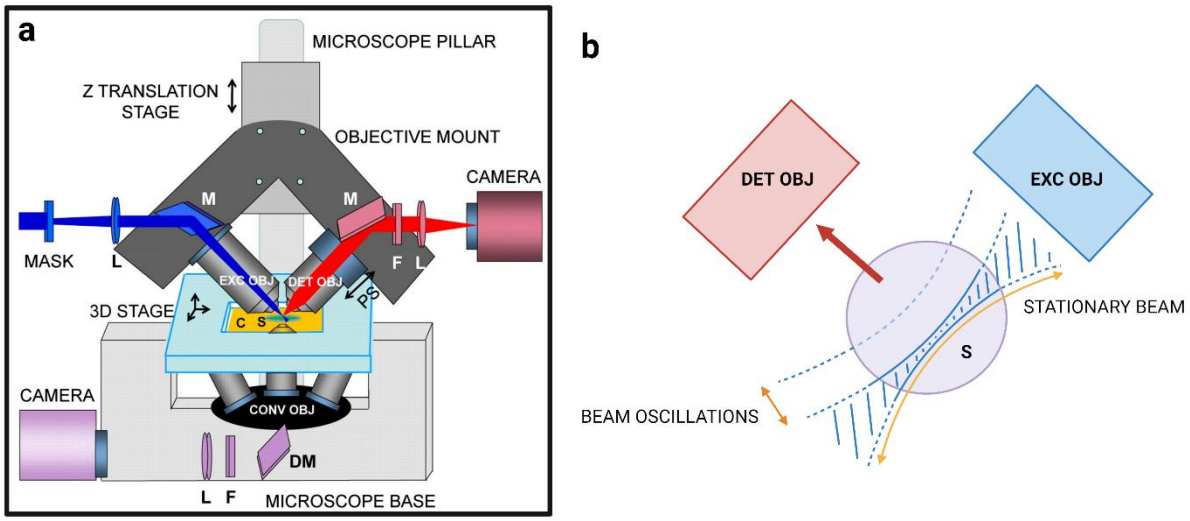


Figure 1.8 **iSPIM schematic and beam. a)** iSPIM contains two orthogonally placed objectives which allow excitation and detections beam paths to be separated. More importantly, this also allows for illumination and detection of a single focal plane, limiting of out-of-focus light acquired. The iSPIM has a motorised stage for spatial movement of the specimen during image acquisition, alongside a standard episcopic objective for sample location (Wu et al., 2011). **b)** The iSPIM illuminated the sample with a Gaussian beam (**gold arrow**), which is oscillated to create the light sheet (**orange arrow**).

Whilst iSPIM has many advantages, objectives used for iSPIM are limited to the physical constraints of the set up, and both objectives and sample are required to be in imaging media to minimise refraction. Furthermore, beam alignment and optics, alongside image processing and analysis of iSPIM samples present a large barrier for biologists. Lastly, iSPIM produces large datasets, which require dedicated servers to store and process. Whilst iSPIM still remains the best tool for live-cell volumetric imaging for developmental biology, other techniques can be used in tandem to combine the advantages of both.

Wide-field microscopy is a method of fluorescent light microscopy where the emitted fluorescence of the specimen is focused on a detector through the same objective used to focus excitation light, using a dichroic mirror to separate the two wavelengths. Wide-field fluorescence microscopy has a diffraction limited has resolution of 200 to 300 nm and a poor optical sectioning, but it can provide a vast amount of image data quickly in comparison to other diffraction limited fluorescence microscopy techniques. Furthermore, whilst wide-field imaging would be unsuitable for live-cell imaging, entire cultures of fixed megakaryocytes can be imaged to establish coarse relationships, and reinforce more detailed iSPIM imaging (Sasaki, 2022).

1.4 Thesis aims

- Develop methods for assessing large populations of megakaryocyte maturation at low resolution using wide-field imaging techniques.
- Develop a method for assessing megakaryocyte maturation in live cells using iSPIM.
- Use developed techniques to probe and categorise IMS morphological change over time.
- Use developed techniques to probe the role of actin cytoskeleton in IMS development.

2 METHODS

2.1 Ethics and origin of murine

Mice were housed and bred according to Home Office Regulations and in accordance with local and national regulations. Work was carried out under Home Office Licence P0E98D513 granted to the University of Birmingham. Lifeact-GFP mice were generated as previously described (Riedl et al) and wild type C57BlK6 mice were obtained from Harlan Laboratories (Oxford, UK) (Riedl et al., 2010).

2.2 Reagents list

Chemical	Company	Cat Number
SCF	Peprotech	250-03
Thrombopoietin	Peprotech	315-14
DMEM	ThermoFisher	11965092
Dynabeads™ Sheep Anti-Rat IgG	ThermoFisher	11035
Ly-6G/Ly-6C Monoclonal Antibody (RB6-8C5)	ThermoFisher	14-5931-82
Anti CD11b Monoclonal Antibody (M1/70)	ThermoFisher	14-0112-82
CD45R (B220) Monoclonal Antibody (RA3-6B2)	ThermoFisher	14-0452-82
Anti CD16/32 Monoclonal Antibody (93)	ThermoFisher	14-0161-82
Stempro-34	ThermoFisher	10639011
Bovine serum albumin	Sigma Aldrich	A7030-10G
Triton-x 100	Sigma Aldrich	9036-19-5
Formaldehyde	Sigma Aldrich	HT501128
Goat serum	ThermoFisher	16210064
Ibidi 96 well plates	Ibidi	89626
Fibrinogen	Enzyme Research Laboratories	FIB 1
Poly-L-lysine	ThermoFisher	25988-63-0
MethyloCult	StemCell Technologies	M3434
Agarose	ThermoFisher	A9539
CellMask	ThermoFisher	C10046
DAPI	Sigma Aldrich	10236276001
Phalloidin Alexa-488	ThermoFisher	A12379
GP1b-α Alexa-647	Emfret	M040-3

Heparin	Sigma Aldrich	9041-08-1
Tetraspec microspheres 0.1 µm	ThermoFisher	T7279
Slides (1.5#, 24 x 50 mm)	Cell Path	SAH-2450-03A
FM-1-64	ThermoFisher	T3163
FM-4-64	ThermoFisher	T3166
HPTS	Sigma Aldrich	H1529
Fluorescein	Sigma Aldrich	F7505
AcX	Sigma Aldrich	15661
DMSO	ThermoFisher	D2438-5X10ML
TEMED	Sigma Aldrich	T9281-25ML
APS	Sigma Aldrich	A3678
Acrylamide	Sigma Aldrich	A9099-25G
Sodium acrylate	Sigma Aldrich	408220-25G
N,*N*′Methylenebisacrylamide	Sigma Aldrich	M7279-25G
Proteinase K	ThermoFisher	EO0491

2.3 Culture of murine bone marrow derived hematopoietic stem cell

Bone marrow was flushed with Dulbecco's modified eagle medium (DMEM/strep/glutamine) from the femur and tibia of mice using a 25-gauge needle. This solution was centrifuged at 1200 rpm for 5 minutes and resuspended in 5 mL of Ammonium-Chloride-Potassium (ACK) lysis buffer (0.15 M NH_4Cl; 1 mM $KHCO_3$; 0.1 mM Na_2EDTA pH 7.3) for 5 minutes to remove red blood cells, before being filtered through a 70 µm nylon mesh filter to remove larger extracellular matrix and particle debris. Cells were centrifuged at 1200 rpm for 5 minutes and resuspended in 1ml of DMEM with 3 µL of Anti-Gr-1, Anti-cd11b, Anti B220, and Anti-CD16/32 antibodies. Cells were left to incubate in antibodies on ice for 30-45 minutes.

Cells were centrifuged at 1200 rpm for 5 minutes and resuspended in 1 mL of DMEM with 50 µL of washed magnetic dyna-beads. This suspension was again centrifuged at 1200 rpm for 5 minutes and resuspended to mix dyna-beads with antibody bound cells before magnetic isolation of dyna-beads. The remaining dyna-beads were washed in 500 µL DMEM, centrifuged at 1200 rpm for 5 minutes, and resuspended. A second round of magnetic pull down was applied to improve yield. The purified cell solution

was counted, centrifuged at 1200 rpm for 5 minutes, and resuspended in 1.5 mL Stempro-34 media (Stempro/nutrient solution/pen/strep/glutamine) with 20 ng/mL stem cell factor (SCF), and incubated at 37°C, 5% CO_2 for 2 days. After 2 days, cells were centrifuged at 1200 rpm for 5 minutes, and resuspended in Stempro-34 media with 50 ng/mL murine thrombopoietin (TPO), and 20 ng/mL SCF.

2.4 Bovine serum albumin selection gradient

Bovine serum albumin (BSA) was made to 3% and 1.5% w/v in phosphate buffer solution (PBS), and run through a 0.22 Millipore filter. Cells were centrifuged at 1200 rpm for 5 minutes and resuspended in 1 mL of DMEM, and 1 mL of PBS. This solution was gently placed on top of the BSA gradient and allowed to sit for 30 minutes. The top 6 mL of the gradient was centrifuged at 1200 rpm for 5 minutes and resuspended in 1.5 mL Stempro-34 media with 50 ng/mL murine TPO, and 20 ng/mL SCF for a second round of differentiation. The bottom 4 mL of the gradient was centrifuged at 1200 rpm for 5 minutes, resuspended in 1 mL DMEM, and allowed to rest at 37 °C, 5% CO_2 for 1 to 2 hours.

2.5 Immunostaining

Cells were seeded at an appropriate density and left to settle before a fixative, 4% formaldehyde (FA), was added for 10 minutes. Cells were then washed in PBS three times and place in a detergent, 0.1% Triton-x 100, for 5 minutes. This was followed by another three washes with PBS before blocking buffer (2% goat serum, 1% BSA) was added for 30 to 45 minutes. Cells were then incubated in a primary antibody and blocking buffer solution overnight at 4°C. Plates were placed on an orbital shaker and

kept wrapped in parafilm and aluminium foil to prevent dehydration and photo-degradation of any fluorophores.

The following day cells were washed in PBS to remove primary antibody and incubated in PBS solution containing secondary antibody(s) and any necessary small molecule dyes. This was wrapped in aluminium foil and left for an hour at room temperature. Cells were washed again in PBS before imaging.

2.6 Immunostaining of megakaryocytes on poly-L-lysine

Poly-L-lysine was applied for 5 minutes to an Ibidi 96 well, optical bottom plate. Excess was then removed with deionised water before allowing the well to dry for 2 hours at room temperature. Hematopoietic stem cells were seeded in the coated wells at $1x10^6$ per mL, with 200 µL deposited in each well and left to mature. Deionised water was added to outer wells of the plate to limit evaporation of sample.

A fixative and detergent solution of 7.2% FA and 0.2% Triton-x 100 was gently mixed at a ratio of 1:1 with the media, so as not to remove fluid or disturb cells prior to fixing. This was left for 10 minutes; in which time the plate was spun at 40 RCF (110 cm rotor diameter) for 2 minutes to allow megakaryocytes to separate from solution. The well was diluted down four times, each time removing 200 µL of fixative and detergent solution and replacing it with PBS and spinning cells from solution. After, 200 µL was removed from solution, replaced with 200 µL blocking buffer (4% goat serum, 2% BSA: PBS), and left to incubate at room temperature for 45 minutes. Primary antibody(s) in blocking buffer were added to samples by spinning the plate down, removing 300 µL, and adding 100 µL of antibody solution. Plates were left overnight at 4°C to incubate. After incubation, plates were spun and diluted in PBS to remove primary antibody. A

solution of secondary antibody and any necessary small molecule dyes in PBS was added to the sample and incubated for an hour at room temperature. Plates were spun down and diluted again in PBS before imaging. On the last dilution, cells were resuspended into solution and spun down to allow them to settle in an even distribution across the well bottom.

2.7 Immunostaining of megakaryocytes on fibrinogen

Coverslips were sterilised with 70 % ethanol and left to air dry in a 24 well plate within a cell culture hood. Once dry, the coverslips were incubated in fibrinogen for an hour before being incubated in heat denatured BSA for 1 hour. Maturing megakaryocytes were isolated via a BSA gradient and seeded onto fibrinogen coated coverslips for 3 hours at 37 °C and 5 % CO_2 before fixation.

2.8 Megakaryocyte mobility on different substrates

Wells of optical bottom ibidi 96-well plates were coated in either poly-L-lysine for 5 min, or vitronectin for 45 min at room temperature before being washed with deionised water. At day 3 after TPO addition, LifeAct megakaryocytes were isolated with a BSA gradient and resuspended in either DMEM-methylcellulose (0.1 %, 0.2 %, 0.4 % w/v in DMEM), DMEM-agarose (0.05 %, 0.1 %, 0.2 % w/v in DMEM), or DMEM solutions. DMEM megakaryocyte suspensions were added to uncoated, poly-L-lysine coated, and vitronectin coated wells, whilst methylcellulose and agarose suspensions were added to uncoated wells. Plates were spun at 30 x g for 5 min. A wide field microscope with a 10x objective was used to obtain images once every 10 min for 12 hours. Images were pre-processed in Zen and analysed in Fiji using the TrackMate plugin (Tinevez et al., 2017).

2.9 Megakaryocyte and IMS viability assay

Hematopoietic stem cells were grown at either $5x10^7$ ml^{-1}, $1x10^6$ ml^{-1}, or $2x10^6$ ml^{-1}, whilst a subset of cells at $1x10^6$ ml^{-1} were grown in the presence of reagents: CellMask, poly-L-lysine coated wells, Heparin, DMEM, or fluorescent beads. Grown megakaryocytes were isolated with a BSA gradient at day 3 of maturation and seeded in poly-L-lysine coated wells at $1x10^6$ ml^{-1} in a 24 well plate for fixation and immuno-labelling.

2.10 Inhibiting IMS maturation

Inhibitors were diluted with DMSO and added to cultures seeded at cells at $1x10^6$ ml^{-1} alongside TPO and SCF at day 0 of culture development. Inhibitor assays were isolated at day 3 of culture development, immune-stained on poly-L-lysine, and imaged with wide-field microscopy. Images were processed and measured using the wide-field analysis pipeline.

2.11 Wide-field imaging

Wide-field images were acquired using an Axio-Observer 7 inverted epifluorescence microscope (Carl Zeiss) with Definite Focus 2 autofocus, Colibri 7 LED illumination source, Hammamatsu Flash 4 V2 sCMOS camera (pixel number: 2048 x 2048, pixel size: 100 x 100 nm), filter sets 38 and 50 for Alexa488 and Alexa647 respectively and DIC optics. Images were taken with either a 63x 1.4 NA oil immersion objective lens, a 40x 1.2 NA, a 20x 0.8 NA, or 4x air objective lens. Acquisition was performed using Zen 2.3 Pro software.

2.12 IncuCyte imaging

IncuCyte images of live megakaryocyte were obtained using an IncuCyte ZOOM with a 20x objective. A 4x4 tile of phase contrast images (pixel number: 1392 x 1038, pixel size: 610 x 610 nm) was taken at each specified time point. Images acquired using the IncuCyte ZOOM software, and were segmented and measured in Fiji using the IncuCyte megakaryocyte assay pipeline described in chapter 3.

2.13 Confocal imaging

Confocal images were obtained with a Zeiss LSM 880 confocal microscope. Images were taken using Plan-ACHROMAT 40x and 63x, 1.2NA objectives, and an airyscan detection unit. Acquisition was performed using Zen 2.3 Pro software.

2.14 iSPIM imaging

Slides (1.5#, 24 x 50 mm) were sterilised with 70 % ethanol and left to air dry in a 24 well plate within a cell culture hood. Once dry, a wax pen was used to draw a small square (~ 2 cm^2) the slides to provide a hydrophobic barrier for cell medium. Poly-L-lysine was added and left for 5 minutes before washing with deionised water three times and leaving to dry once more. After drying the slide was placed within the Mariana's DiSPIM specimen holder and securely screwed, taking care not to over tighten and risk cracking the slide. Once in place, the specimen holder was incubated at 37 °C for 15 minutes to prevent temperature shock to cells.

Megakaryocyte cultures were taken 3 days after addition of TPO, and isolated via a BSA gradient. Mature megakaryocytes were suspended in 1 µL phenol red free DMEM supplemented with Stempro nutrients, and 0.5 µL was added to hydrophobic square on the glass slide. Since megakaryocytes were still in suspension, they aggregated in

the centre of the media. Therefore, density of megakaryocytes was visualised by eye, with a mass of white precipitate indicating a good number of megakaryocytes for imaging. The sample holder was then taken to the microscope and gently placed inside the incubated imaging chamber at 37 °C and 5 % CO_2.

At 30 minutes prior to imaging, cell mask dye was added to 5 mL of phenol red free DMEM supplemented with Stempro nutrients at a 1:10,000 dilution. The media was then gently pipetted into the sample, being careful not to remove megakaryocytes. This addition media was added carrier to allow the immersion objectives to fully submerge in the media for imaging. Lastly, water was pipetted into a reservoir surrounding the imaging chamber to prevent evaporation and refractive index change. Samples were left for 30 minutes to incubate in cell mask before imaging.

Light-sheet images were taken using a 3i Marianas light-sheet with a Nikon CFI NIR Apo 40X, 0.8NA, 3.5 mm water dipping objective and a Hamamatsu ORCA-Flash 4.0 V3 sCMOS camera (pixel number: 2048 x 2048, pixel size: 370 x 370 x 760 nm). Images were acquired and pre-processed using Slidebook 6.

2.15 DiSPIM alignment

Prior to imaging, 5 µL of imaging media with fluorescein was pipetted into the DiSPIM 1.5#, 24 x 50 mm slide sample holder for beam alignment. The DiSPIM was aligned as follows:

1) DiSPIM iris was closed fully to produce a thick pencil beam.
2) The beams were coarsely aligned by turning the thread on each objective and visualising beams by eye.

3) Mirror steering screws were adjusted to focus and move the beam positions (figure 2.1a).
4) Dichroic mirror tilt was adjusted to overlay both beams,
5) Camera mirror cubes were adjusted to overlay epi spots (figure 2.1c).
6) Pencil beams were focused by opening the iris.
7) Light sheets were focused by adjusting scanner tilt (figure 2.1d).
8) Width of the beam was adjusted to beyond the camera FOV.
9) Coverslip location was found by moving the objectives down until the coverslip aligned with the cross section of the beams (figure 2.1e).

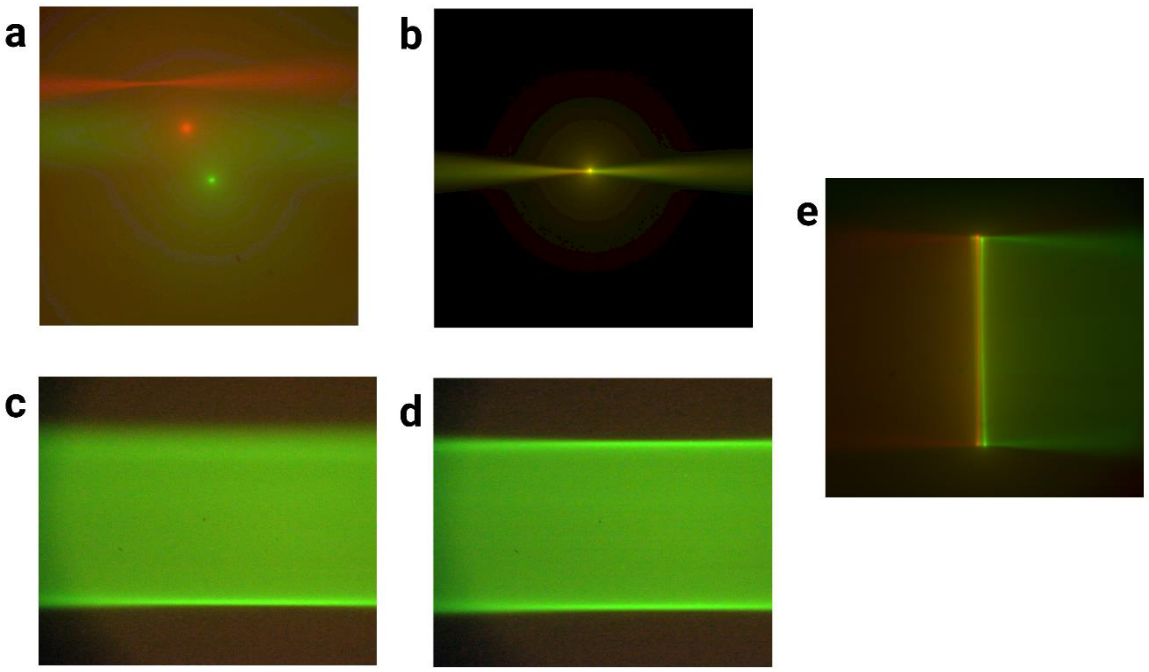


Figure 2.1 **DiSPIM alignment. a)** Unfocused epi spots and beams were aligned by adjusting mirror steering screws, dichroic mirror tilt screw, and camera mirror cubes screws. **b)** Aligned epi spots and beams. **c)** Beam oscillation was brought into focus by adjusting the scanner tilt. **d)** Focused beam oscillation. **e)** Sample z-height was found by lowing the objectives until the coverslip co-aligned with the cross section of the beams.

2.16 Expansion microscopy

Cells were treated and immuno-stained as required prior to subsequent steps Acryloyl-X (6-((acryloyl)amino)hexanoic acid, succinimidyl ester) (AcX) was re-suspended in anhydrous DMSO with a final concentration of 10 mg/mL. This was then aliquoted and stored in a frozen desiccated environment for up to 2 months. Following two washes with 1xPBS, cells were incubated with AcX (0.1 mg/ml) in PBS for >6 hours at room temperature. Specimens were washed with 1xPBS prior to gelation. All components of the gelation solution were purchased from Sigma Aldrich. Monomer solution (1xPBS, 2M NaCl, 8.625% (w/w) sodium acrylate, 2.5% (w/w) acrylamide, 0.15% (w/w) N,N'-methylenebisacrylamide) was mixed, frozen in aliquots of 940 µL and thawed prior to use. Concentrated stocks of ammonium persulfate (APS) and tetramethylethylenediamine (TEMED) at 10% (w/w) in water were diluted into the monomer solution to concentrations of 0.2% (w/w) on ice prior to gelation, with the initiator (APS) added last. The gelation solution (80 µl) was placed on a parafilm-covered slide in a humidified chamber. Coverslips were inverted onto the droplet with cells face down. Gelation was allowed to proceed at 37 ^{o}C for two hours. Gels were removed from the slide and immersed in digestion buffer (1xTAE, 0.5% Triton X-100, 0.8M guanidine HCl) containing 8 units/ml and Proteinase K (New England Biolabs Inc.) was added freshly to the digestion buffer. Gels were digested either at room temperature overnight or 37 ^{o}C for 4 hours. The gels (sometimes still attached to the cover glass) were removed from the digestion buffer and placed in 50 ml of water to expand. Water was exchanged every 30 minutes until expansion was complete (typically 3-4 exchanges) (Tillberg et al., 2016).

2.17 Statistics and data analysis

Graph pad was used to conduct statistical tests. Multi-comparison ANOVA tests were used to establish significance ($p = 0.05$) between samples.

3 MEASURING INVAGINATED MEMBRANE SYSTEM DEVELOPMENT WITH WIDE-FIELD FLUORESCENCE IMAGING

3.1 Aims

Whilst IMS morphological development is often categorised by manual observation, computational image analysis can provide a more robust and unbiased measure. Furthermore, wide-field imaging of megakaryocyte populations offers a coarse tool for understanding of IMS development at a low resolution, but with a large sample size. As such the aims of this section are as follows:

- Design a labelling method for fixed imaging of megakaryocytes
- Design an image analysis pipeline for 4D wide-field imaging.
- Identify suitable 2D morphological measurements of IMS.
- Assess variability in wide-field pipeline measures
- Assess sensitivity in wide-field pipeline measures

3.2 IMS is described by GP1b-α and CD41/61 in fixed megakaryocytes

GP1b-IX-V is a protein complex specific to megakaryocytes and platelets, and is essential for correct megakaryocyte maturation. A lack or dysfunction of GP1b-IX-V manifests as an under-development of the IMS, and macrothrombocytopaenia (Catherine et al., 2009; Dütting et al., 2017; Poujol et al., 2002). Previous studies have used GP1b-α, GP1b-β, or CD41 to stain IMS specific regions within megakaryocytes (Eckly et al., 2014; Schulze et al., 2006), whilst others have shown that F-actin is heavily upregulated at the IMS (Antkowiak et al., 2016). Here fixed megakaryocytes were stained with GP1b-α, CD41, CD41/61, GPVI, and the F-actin binding agent phalloidin.

Initial observations confirmed the GP1b-α labelled structured regions within megakaryocytes with a high contrast (figure 3.1). To allow maximum flexibility for future dual and multi-colour labelling experiments, the GP1b-α antibody conjugated to Alexa-647 was used for subsequent experiments.

Interestingly, the CD41/61 complex antibody highlighted structured regions within megakaryocytes similar to GP1b-α, however, the CD41/61 labelled structured regions had less contrast in comparison to the GP1b-α label (figure 3.1a). In comparison, CD41 and GPVI antibodies (data not shown) highlighted the entire megakaryocyte evenly, making them unsuitable labels for robust IMS (figure 3.1b).

Phalloidin 488 also labelled structured regions within megakaryocytes corresponding to GP1b-α staining alongside cell cortex (figure 3.1c). Phalloidin did not specifically label only GP1b-α structures, however there is a clear association between the two labels. Based on these observations, future studies in this chapter used GP1b-α-647 and phalloidin-488 to describe IMS structure and F-actin organisation respectively, due to their high signal to noise ratio compared to other labels.

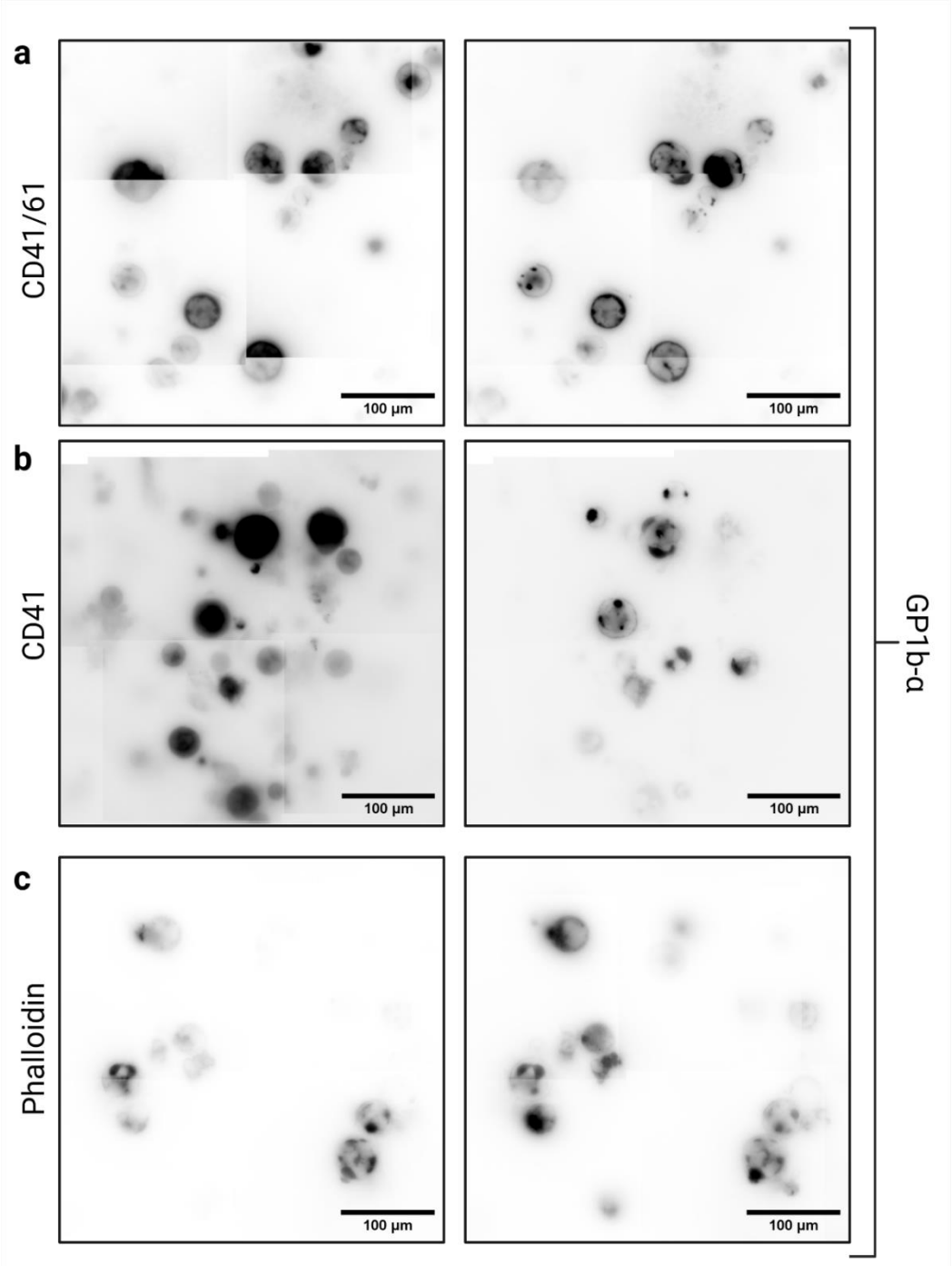


Figure 3.1 - **Fixed cell dyes for measuring IMS morphology. a)** Fixed murine megakaryocytes stained with CD41/61 and GP1b-α. CD41/61 corresponded with GP1b-α specific sites, but with less contrast and intensity. **b)** Fixed megakaryocytes stained with CD41 and GP1b-α. CD41 labelled evenly throughout megakaryocytes, with larger megakaryocytes expressing more. This was the case regardless of image exposure. **c)** Fixed megakaryocytes stained with phalloidin and GP1b-α. Phalloidin labels similar structures to GP1b-α alongside some different structures. Images representative of three murine megakaryocyte cultures.

3.3 Developing an image analysis pipeline for 2D wide-field fluorescence microscopy

After image acquisition using a widefield epifluorescence microscope, GP1b-α and phalloidin channels were segmented to generate binary masks of the IMS (foreground) and the background. Binarizing images based on pixel intensity with a range of thresholding algorithms available within Fiji (https://imagej.net/contribute/citing), produced a range of masks which predominantly either described IMS within megakaryocytes (RenyiEntropy, Yen, Intermodes & MaxEntropy), or the megakaryocytes as a whole (Otsu, Triangle, Huang, Li, IsoData, & Default) allowing segmentation of different components of the cell from the same images (figure 3.2). Several threshold algorithms failed to adequately segment the image giving either no segmentation (minimum, Shanbhag), or over segmentation of the whole cell (Mean, MinError & Percentile).

To improve the accuracy of the thresholding and segmentation, the effect of rolling ball background subtraction prior to Mean, Otsu, Triangle, and Intermodes thresholding was assessed. For all algorithms tested, a lower rolling ball radius (50 to 200 μm) brought out more detail in the IMS and cell cortex, but introduced high contrast noise otherwise known as speckling into the image, whilst a higher rolling ball radius (300 μm) caused more whole megakaryocytes to be identified by thresholding (figure 3.3). This suggests that a rolling ball radius around 200 μm is optimal for identifying individual IMS regions whilst still removing uneven image backgrounds. However, to reduce speckling in images processed with a lower rolling ball radii, the effect of pixel smoothing pre-thresholding on rolling ball processing was investigated. Pixel smoothing was applied for either 2, 4 or 6 iterations before rolling ball background

subtraction was applied with a radius of either 50, 100, or 300 prior to Otsu thresholding (figure 3.4). Higher iterations of smoothing (6) removed uneven noise and speckling, but sacrificed feature definition. Whilst lower iterations of smoothing (2 to 4) failed to adequately remove speckling. By combining a high number of smoothing iterations (6) before a rolling ball subtraction of 200 μm, IMS features were retained within the image with little speckling and an even background.

Finally, size and circularity filters were applied to processed images to remove immature cells or debris from processed images (figure 3.5). A low circularity filter (> 0.1 to 0.2) removed some artefacts, whilst a high circularity filter (> 0.4 to 0.8) removed IMS objects alongside remaining artefacts. A low size filter (> 20 to 50 μm^2) retained artefacts, whilst a high size filter (> 400 μm^2) removed IMS objects. This suggests that a circularity filter of > 0.2, and a size filter of > 100 μm^2 seemed optimal for selecting IMS objects from images. Size was also limited to < 1600 μm^2 as larger objects tended to be either more than a single IMS, or not IMS.

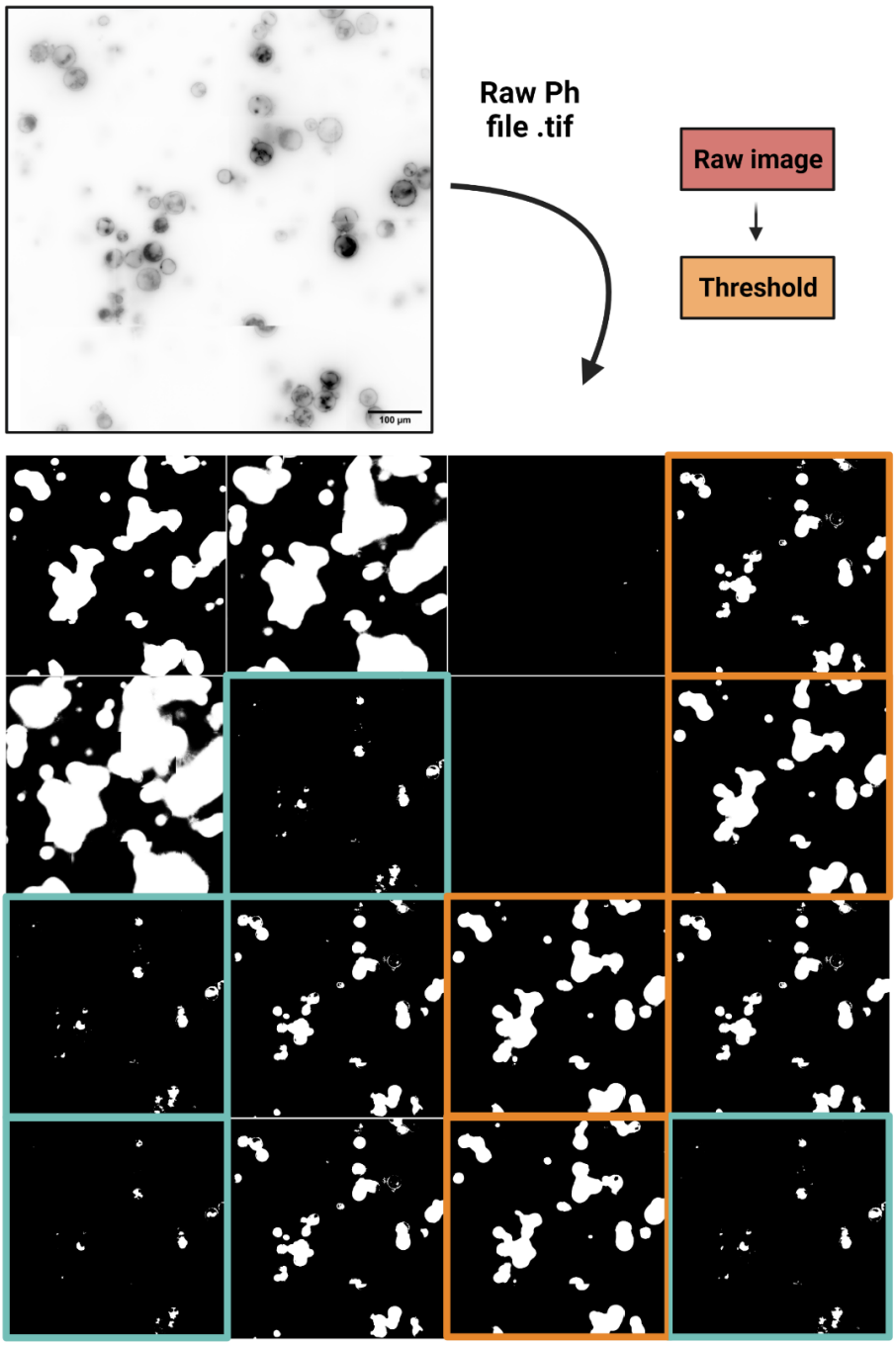


Figure 3.2 **Effect of different threshold functions.** Megakaryocytes were cultured for three days, fixed and stained with phalloidin, and imaged with a widefield fluorescence microscope. To segment IMS structures, threshold functions available through Fiji were applied to images (from *left to right, top to bottom*): Mean, MinError, Minimum, Otsu, Percentile, RenyiEntropy, Shanbhag, Triangle, Yen, Default, Huang, IJ_IsoData, Intermodes, IsoData, Li, MaxEntropy. Thresholds which segmented megakaryocytes as a whole *(Otsu, Triangle, Huang, Li, IsoData, & Default)* are highlighted in orange whilst thresholds which segmented IMS within megakaryocytes *(RenyiEntropy, Yen, Intermodes & MaxEntropy)* are highlighted in green**.**

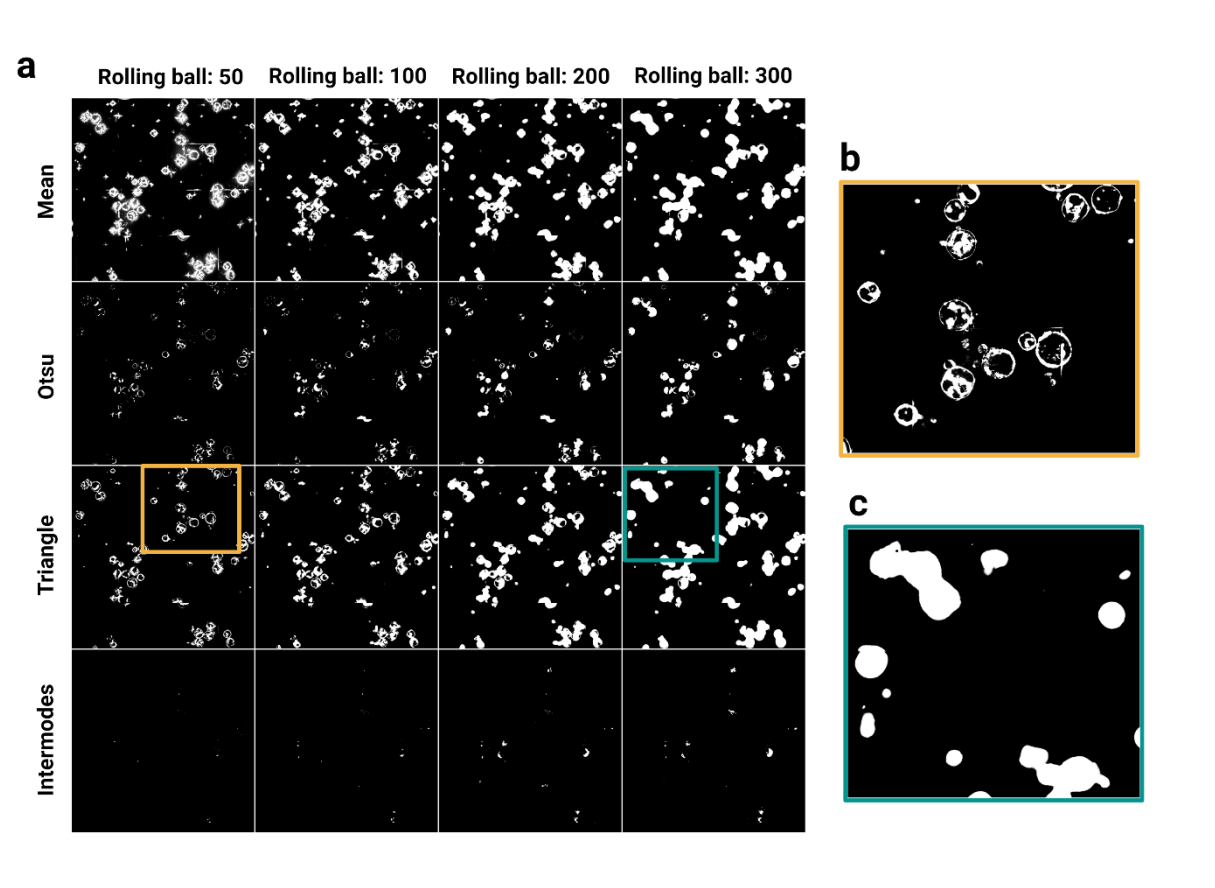


Figure 3.3 **Effect of Rolling ball background subtraction and smoothing.** Megakaryocytes were cultured for three days, fixed and stained with phalloidin, and imaged with a widefield fluorescence microscope. **a)** Prior to threshold segmentation (figure 3.2), a rolling ball background subtraction was applied to the image at: 50, 100, 200, or 300 (*left to right*) shown on: Mean, Otsu, Triangle, and Intermodes (*top to bottom*). **b)** With a lower radius, rolling ball background subtraction brings out more detail in IMS and cell cortex, but introduces speckling into the image. **c)** At higher radius, whole megakaryocytes are better defined, but a 'cross like' artefact is introduced, making spheres more diamond in shape.

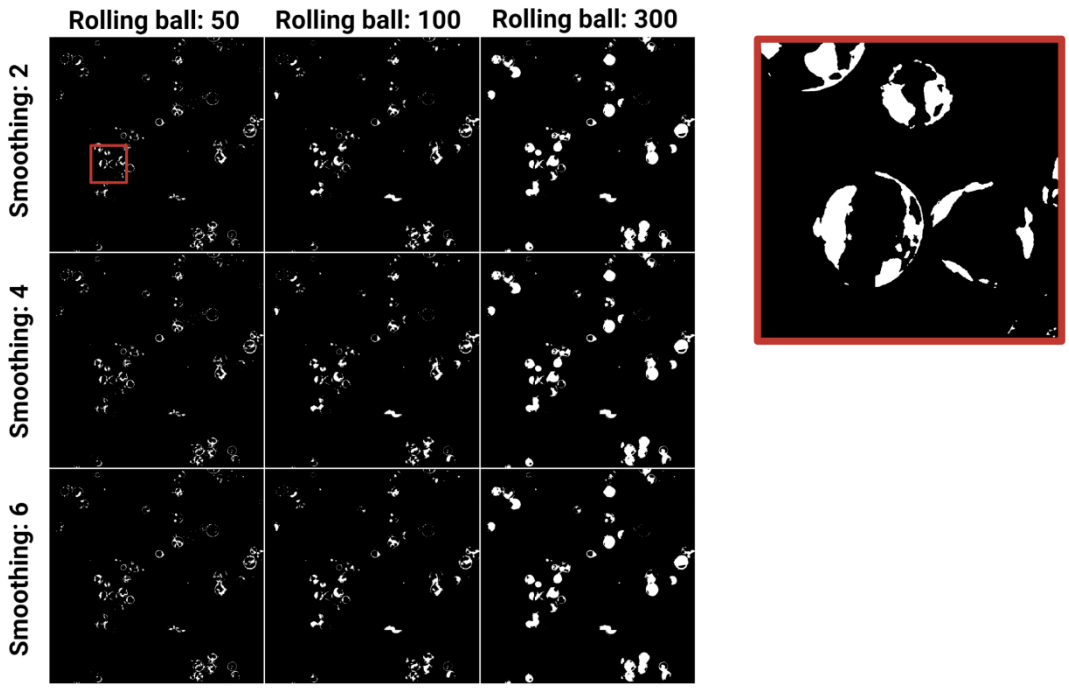


Figure 3.4 **Effect of smoothing.** Megakaryocytes were cultured for three days, fixed and stained with phalloidin, and imaged with a widefield fluorescence microscope. After applying a rolling ball background subtraction (figure 3.3) smoothing at 2, 4 and 6 iterations was applied to remove speckling artefacts introduced by the background subtraction. The rolling ball algorithm was tested with a radius of: 50, 100, and 300, prior to Triangle auto thresholding. Even low iterations of smoothing (2) removed the speckling artefact.

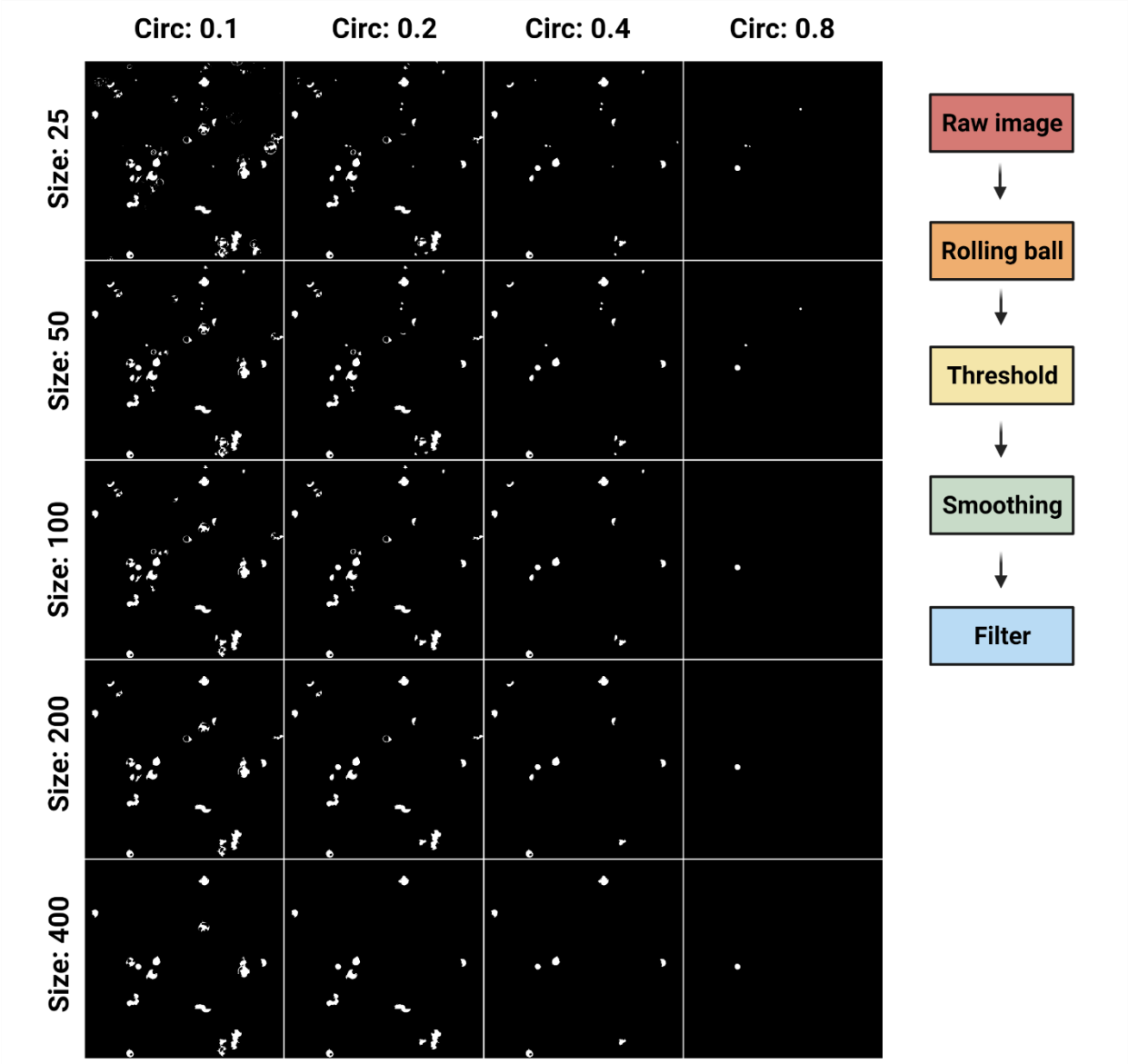


Figure 3.5. **Effect of Circularity and Size filter.** Megakaryocytes were cultured for three days, fixed and stained with phalloidin, and imaged with a widefield fluorescence microscope. After background subtraction, smoothing, and thresholding, a circularity and size filter were applied to the segmentation. Particles were filtered out at 0.1, 0.2, 0.4 and 0.8, and 25, 50, 100, 200, and 400 μm^2. Below 100 μm^2 small fragments and debris are retained, but above 200 μm^2 IMS structures are lost. A circularity filters appear less essential as small debris are retained at higher circularities where IMS objects are lost. Therefore, a low circularity threshold between 0.2 and 0.4, and a size threshold between 100 and 200 μm^2 seems optimal.

3.4 Defining parameters to describe 2D IMS maturation

Having created a pipeline that successfully produced binary masks of IMS regions, the next stage was to identify parameters that described IMS in megakaryocytes to allow quantitative description of IMS development.

The field of morphometrics provides a vast number of parameters to define object shape (Alizadeh et al., 2018; Lobo et al., 2016; Sánchez-Corrales et al., 2018). From this, a series of relevant morphological descriptors were chosen to define and quantify different stages of IMS development. These were IMS area, IMS perimeter, IMS integrated density, IMS mean grey value, IMS circularity, IMS maximum Feret's diameter, and IMS minimum Feret's diameter (figure 3.6 & table 3.1). Therefore, these parameters were taken forward to characterise and describe IMS objects.

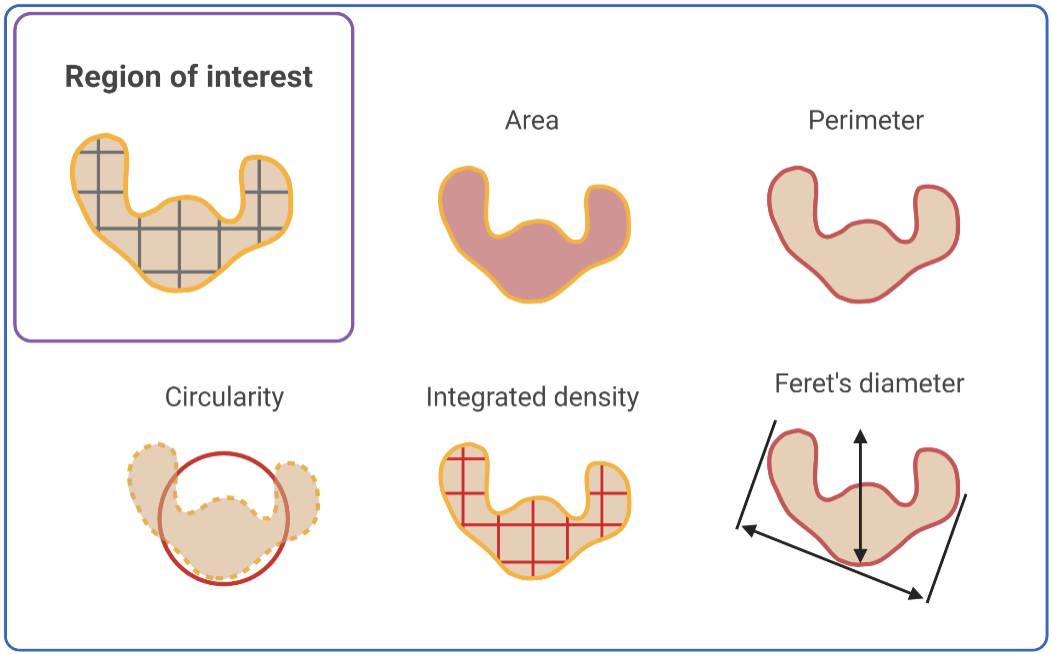


Figure 3.6 **Morphological parameters defining IMS ROIs**, showing visualisation of measurement in dark red for parameters: area, perimeter, circularity, integrated density, and Feret's diameter.

Table 3.1 **Formula and descriptions of morphological parameters used to define the IMS** (Recio-Tótoro et al., 2021).

Shape descriptor	*Formula*	*Notes*
Area	$n * s$	The number of pixels in a selection multiplied by the pixel size of the image.
Perimeter	$(2*(h + w)) * s$ Or $\sum_{i=1}^{n-1} d$	The selection width (w) added to the height (h), multiplied by two. Or Where d is a list of pixels in the selection boundary, with values either equal to 1 if connected by faces, or $\sqrt{2}$ if connected by vertices.
Circularity or Compactness	$\frac{4\pi * \mathrm{A}}{p^2}$	The ratio of the area of object to (A) to that of a circle with the same perimeter (p).
Raw Integrated Density	$\sum_{i=1}^{n} x_i$	The sum of pixel values, where x is a list of n pixel values.
Integrated Density	$\left(\sum_{i=1}^{n} x_i\right) * s$	The sum of pixel values, where x is a list of n pixel values, multiplied by the scaling factor of the image.
Mean grey value	$\frac{IntDens}{Area}$	The overall density of the pixel value in scaled units. Integrated density divided by the area of the object.
Min Feret's diameter		The minimum distance two parallel lines flanking the object.
Max Feret's diameter		The maximum distance two parallel lines flanking the object.

3.5 ANOVA of wide-field IMS analysis pipeline showed no significant difference between cultures derived from separate mice

Whilst the wide-field analysis pipeline works to provide morphological measurements, it is unclear how variable those measurements will be. To assess the variability of the wide-field analysis pipeline, cultures derived from four mice were split into three cultures each, resulting in twelve cultures grown in parallel and measured. Subsequently, the variation between cultures grown from an individual mouse, and between cultures grown from multiple mice could be analysed (figure 3.7a-c). To describe populations the following basic statistics were measured (figure 3.7c):

- Mean ($\bar{x}$)

  The mean value of a single population.

- Standard deviation (σ)

  The distribution of observations within a single population.

- Coefficient of variance (NSD)

  The normalised distribution of observations within a single population

From these values, the variance between populations were described by the following (figure 3.7d):

- Coefficient of variance of the Mean (NSDoM)

  The variance in the mean between populations.

- Coefficient of variance of the Coefficient of variance (NSDoNSD)

The variance in the distribution between populations.

- Kruskal-Wallis one-way ANOVA

A method of establishing if two or more non-parametric populations originate from the same distribution.

- one-way ANOVA

A method for establishing if two or more parametric populations originate from the same distribution.

To support these measures, histograms of populations were compared. Population values were divided between 100 bins, with each bin defined within a range of 0 to the maximum value within the compared conditions. Values were also normalised, where all values within each bin summated to 1. The similarity between these histograms was measured with the equation:

$$\sum_{i=1}^{n} \left(M_i - \sqrt{(A_i - B_i)^2} \right) * 100$$

Where n is the number of bins, A is the bin value of population A, B is the bin value for population B, and M is the max value of the bin between A and B. Similarity between histograms gives a separate measure of the variability between sample populations (figure 3.7e).

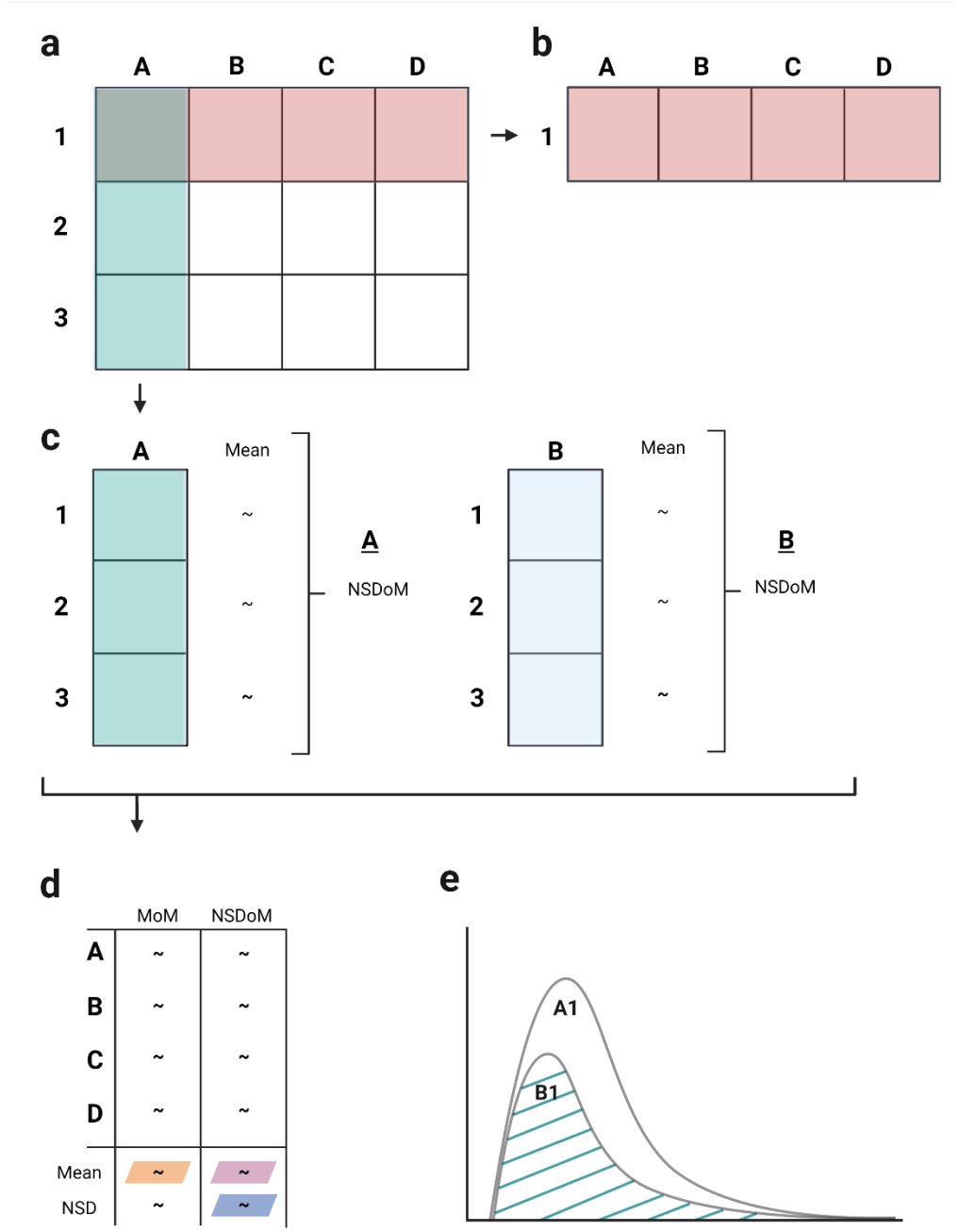


Figure 3.7 **Univariate analysis of variance between sample populations**. **a)** Cultures were derived from four mice, with each mouse being split into three cultures. **b)** Variance in cultures either grown from multiple mice or **c)** a individual mouse are accessed by measuring the mean and normalised standard deviation (NSD). For illustrative purposes only calculations derived from the means of cultures derived from individual mouse are shown here. The NSD of the mean (NSDoM) and mean of the mean (MoM) are calculated from the mean values of each of the three cultures derived from an individual mouse (1, 2, and 3 of mouse A). **d)** Taking these values for each mouse (A, B, C, and D), the NSD and mean is calculated. Importantly, these values are colour coded with orange, purple, and blue, to correlate with values presented (table 2 & 3). **e)** Lastly, the similarity between histograms was compared, with the green pattern illustrating the histogram similarity.

Firstly, variance in phalloidin and GP1b-α ROI populations was assessed (table 3.2 and table 3.3). Histogram similarity shows roughly a 5% difference between phalloidin and GP1b-α ROI populations, with between 70% and 80% similarity on the whole. Phalloidin and GP1b-α ROI populations have a small NSDoM, with phalloidin ROI populations having marginally smaller values. Interestingly, whilst IMS integrated density appears to be highly variable in phalloidin ROIs, IMS area appears to be most variable in GP1b-α ROIs. Counter to this, in general GP1b-α ROI populations have a smaller NSDoNSD in comparison to phalloidin ROI populations. However, IMS integrated density remained high in GP1b-α ROIs. A Kruskal-Wallis ANOVA found that both labels showed significant difference between ROI populations. This data suggests:

1) Whilst population means appear to be more consistent in phalloidin ROI populations, GP1b-α ROI populations are less variable.
2) Integrated density appears to have a higher variability then most other parameters.

Next, the variance in cultures derived from multiple, or an individual mouse were assessed. Histogram similarity shows that there is little variance in ROI populations derived from either multiple or the individual mouse, with both groups maintaining between 70% to 80% similarity. However, there is a slight increase in NSDoM and NSDoNSD within ROI populations derived from multiple mice. Conversely, a Kruskal-Wallis ANOVA found more significantly different populations in ROI populations derived from an individual mouse.

To assess the effect of sample number on ROI population variance, ROI populations from all cultures derived from individual mice were grouped into single populations and measured. With an increase in number of observations from 432 ± 27% to 1707 ± 17%, there is a marginal reduction in NSDoM (~ 8.7% to ~ 6.0%) and NSDoNSD (~ 8.1% to ~ 5.9%). Furthermore, a Kruskal-Wallis ANOVA showed significant difference between ROI populations, but a one-way ANOVA test found no significant difference between ROI population means (figure 3.8). This findings suggest:

1) Variance in ROI populations derived from multiple mice are more variable than cultures derived from an individual mouse.
2) Variance in ROI populations derived from an individual mouse accounts for much of the variability overall.
3) Both ROI populations derived from multiple mice and from an individual mice show significant difference when measured with a Kruskal-Wallis test.
4) Measuring variance ROI populations means with a one-way ANOVA test shows no significant difference between ROI populations. However, this compresses population data into a single value, and results in a loss of information.

Table 3.2 **Variance within cultures derived from an individual mouse**. Murine megakaryocyte cultures were fixed, labelled with phalloidin and GP1b-α at day three of differentiation, and processed with the wide-field analysis pipeline. Statistical values were measured to evaluate variance between morphological parameters for each dye within individual mice. The table shows the average histogram similarity (Histogram ~), normalised standard deviation of mean (NSDoM), normalised standard deviation of normalised standard deviation (NSDoNSD), and number of groups with a p-value < 0.05 as defined by a pairwise Kruskal-Wallis test. Ranges of values across cultures derived from an individual mouse are highlighted in blue. Values have been colour coded for convenience and refer to figure 3.7. Data was gathered from four murine megakaryocyte cultures.

	Phalloidin (individual mouse)			
	Histogram ~	**NSDoM**	**NSDoNSD**	**KW>0.05**
Area	81.0 ± 2.3	9.6 ± 40.2	7.0 ± 19.0	4/12
Perimeter	80.5 ± 3.5	4.9 ± 36.9	8.1 ± 31.3	3/12
IntDen	81.9 ± 2.4	14.8 ± 53.0	7.9 ± 38.4	9/12
Circularity	77.6 ± 2.3	4.7 ± 35.8	7.2 ± 28.6	7/12
Feret's Min	77.1 ± 4.0	6.2 ± 46.6	6.9 ± 27.2	5/12
Feret's Max	81.3 ± 2.5	3.4 ± 45.0	7.7 ± 14.8	3/12
	GP1b-α (individual mouse)			
	Histogram ~	**NSDoM**	**NSDoNSD**	**KW>0.05**
Area	77.6 ± 4.1	15.9 ± 73.2	5.8 ± 79.1	5/12
Perimeter	76.3 ± 3.3	9.6 ± 76.8	5.0 ± 55.7	4/12
IntDen	80.0 ± 4.5	8.9 ± 62.0	14.7 ± 90.1	3/12
Circularity	72.9 ± 5.7	2.5 ± 68.8	6.1 ± 33.8	2/12
Feret's min	73.5 ± 5.6	9.1 ± 83.3	4.9 ± 85.5	4/12
Feret's max	74.1 ± 4.5	8.1 ± 67.3	5.0 ± 36.6	5/12

Table 3.3. **Variance within cultures derived from multiple mice**. Murine megakaryocyte cultures were fixed, labelled with phalloidin and GP1b-α at day three of differentiation, and processed with the wide-field analysis pipeline. Statistical values were measured to evaluate variance between morphological parameters for each dye between multiple mice. The table shows the average histogram similarity (Histogram ~), normalised standard deviation of mean (NSDoM), normalised standard deviation of normalised standard deviation (NSDoNSD), and number of groups with a p-value < 0.05 as defined by a pairwise Kruskal-Wallis test. Ranges of values across cultures derived from a single mouse are highlighted in blue. Values have been colour coded for convenience and refer to figure 3.7. Data was gathered from four murine megakaryocyte cultures.

	Phalloidin (multiple mice)			
	Histogram ~	**NSDoM**	**NSDoNSD**	**KW>0.05**
Area	81.2 ± 1.4	5.9 ± 23.5	8.0 ± 40.9	0/9
Perimeter	80.7 ± 2.0	4.4 ± 18.3	8.0 ± 76.1	0/9
IntDen	81.4 ± 1.4	12.7 ± 69.5	7.7 ± 52.1	2/9
Circularity	78.4 ± 2.5	4.7 ± 32.7	5.5 ± 76.4	4/9
Feret's min	79.1 ± 2.1	3.4 ± 38.7	6.5 ± 79.1	0/9
Feret's max	80.4 ± 2.3	2.7 ± 25.1	6.6 ± 78.8	0/9
	GP1b-α (multiple mice)			
	Histogram ~	**NSDoM**	**NSDoNSD**	**KW>0.05**
Area	76.4 ± 1.2	18.2 ± 73.9	6.7 ± 15.0	3/9
Perimeter	76.6 ± 2.0	13.1 ± 61.9	8.8 ± 40.7	3/9
IntDen	80.0 ± 5.4	14.8 ± 25.6	16.8 ± 73.6	2/9
Circularity	73.2 ± 4.7	3.9 ± 33.1	10.4 ± 44.7	4/9
Feret's min	74.7 ± 2.9	10.8 ± 80.2	7.0 ± 74.7	0/9
Feret's max	73.6 ± 4.1	9.4 ± 81.4	5.3 ± 73.6	0/9

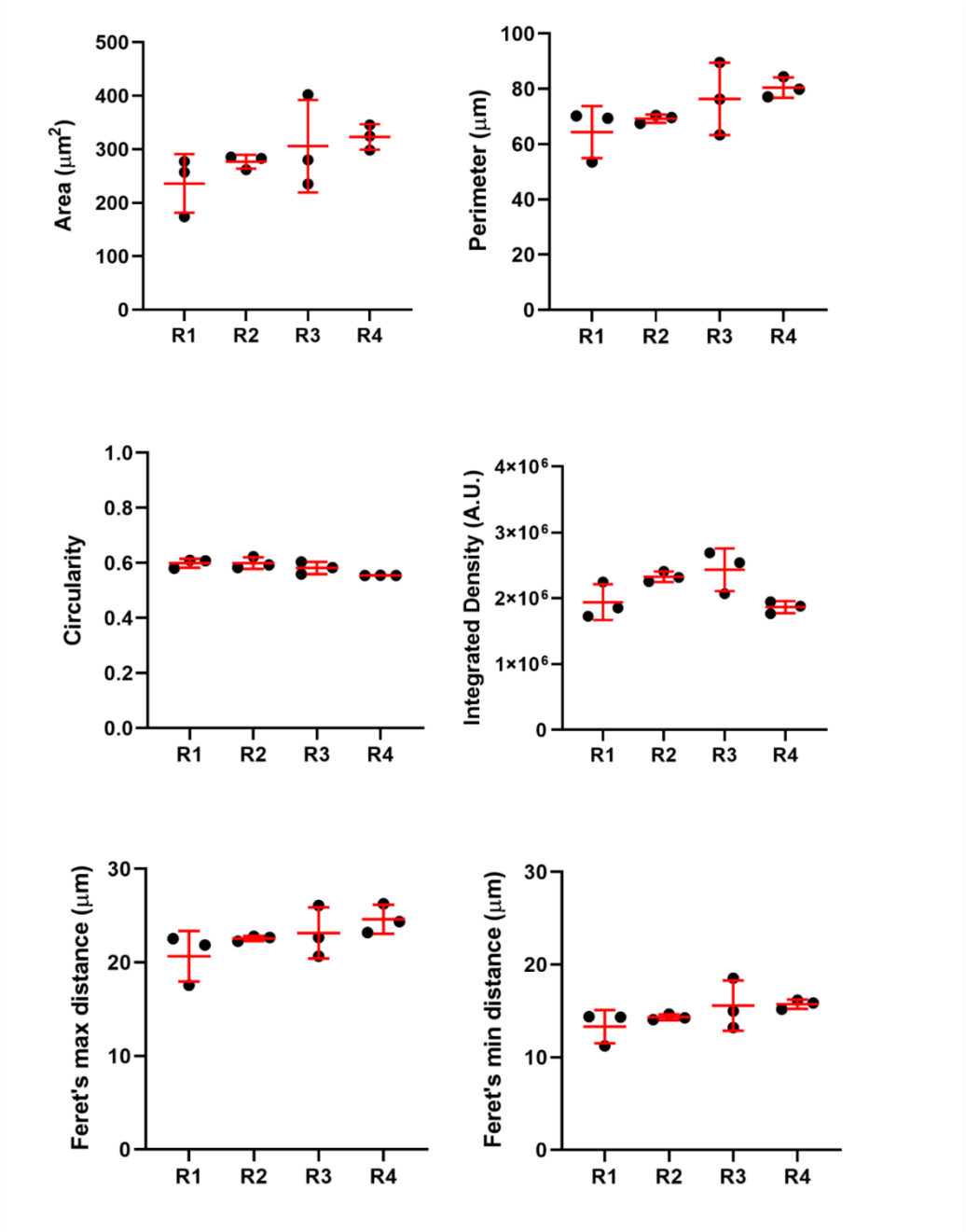


Figure 3.8 – **Variance of phalloidin ROI populations mean**. Morphological parameters were measured in cultures at day three of differentiation via the wide-field analysis pipeline. Three cultures were derived from each individual mouse to compare variability in the assay. The mean of each population was taken and compared. No IMS morphological parameters have significantly different populations between either cultures derived from a single mouse or culture derived from individual mice as determined by a one-way ANOVA test. In general, variance between cultures derived from a single mouse is similar to variance of cultures derived from individual mice. Data taken from four murine megakaryocyte cultures.

3.6 The wide-field IMS analysis pipeline illustrates cytochalasin-D induced morphological change

Next, the sensitivity of the pipeline was assessed by measuring a drug induced change in IMS morphology. To achieve this, the NSDoM between control ROI populations and drug treated ROI populations was compared. Cytochalasin-D, an inhibitor of F-actin polymerisation, was added to cultures alongside cytokines at day 0 of megakaryocyte differentiation to induce a measurable change in IMS morphology.

IMS morphological change is reflected in the wide-field analysis. Observing the culture manually, an increasing concentration of cytochalasin-D leads to both GP1b-α and phalloidin IMS regions becoming smaller, and denser within the megakaryocyte (figure 3.9). Furthermore, GP1b-α IMS regions are much sparser at higher concentrations of cytochalasin (5 µM). In comparison, phalloidin regions seem to be more resilient, becoming smaller but still present at high concentrations (5 µM). This is reflected by the NSDoM between control and drug dose (table 3.4). As cytochalasin-D concentration is increased, there is an increase in NSDoM within GP1b-α ROI populations. Whilst the NSDoM of phalloidin ROI populations changes less, there is still an increase in NSDoM. Looking at variance, morphological induced change induced by low doses of cytochalasin-D was often not found to be significantly different from the control ROI populations by a one-way ANOVA (figure 3.10). This data suggests:

1) Morphological change is reflected in wide-field analysis measurements.
2) Only see dramatic change in morphology with a high dose.

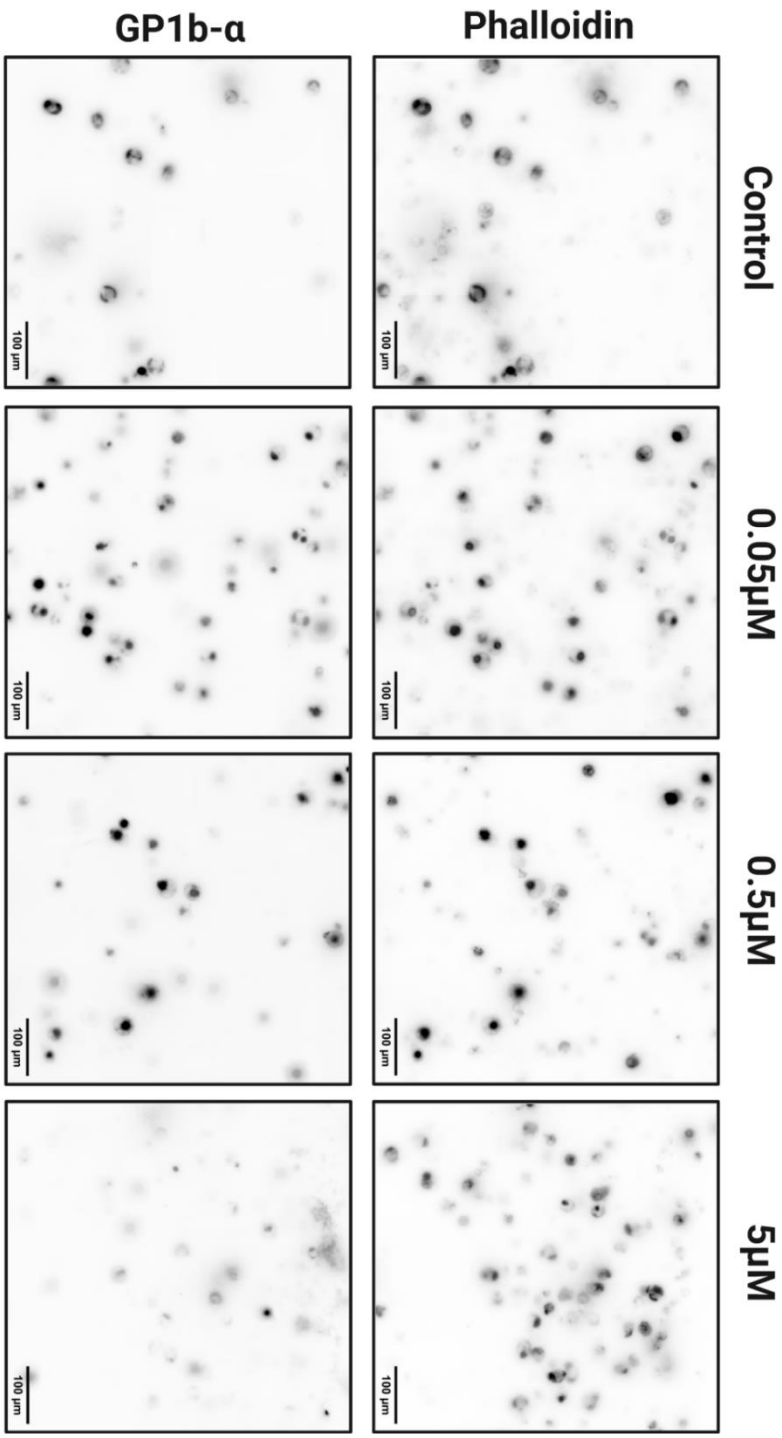


Figure 3.9. **Effect of Cytochalasin-D on IMS morphology.** Cytochalasin-D was added to murine HSCs alongside TPO and SCF at 0.05, 0.5, and 5 μM in DMSO. After three days of differentiation, cultures were fixed, labelled with phalloidin and GP1b-α, and imaged via wide-field fluorescence microscopy. Images were then processed via the wide-field analysis pipeline. The control shows healthy IMS, however an increase in cytochalasin-D concentration causes an increasingly dense and small IMS. At higher concentrations GP1b-α IMS disappears all together. Representative images of three murine megakaryocytes cultures.

Table 3.4. **Drug induced variance in wide-field analysis pipeline**. One-way ANOVA was conducted between control and dose populations of cytochalasin-D treated megakaryocyte populations. The p-values were recorded and categorised based on significance: **Green** - p-value below 0.05, **Orange** - p-value below 0.1, **Red** - p-value above 0.1.

NSDoM			
	Phalloidin		
	Control - 0.05µM	**Control - 0.5µM**	**Control - 5µM**
Area	0.1147	0.0180	0.1993
Perimeter	0.1163	0.0105	0.1896
Circularity	0.6209	0.6081	0.3304
IntDens	0.9864	0.1370	0.2476
Feret's Max	0.0891	0.0082	0.2511
Feret's Min	0.1610	0.0487	0.1293
Univariate	**GP1b-α**		
	Control - 0.05µM	**Control - 0.5µM**	**Control - 5µM**
Area	0.0701	0.0293	0.1367
Perimeter	0.0652	0.0228	0.0678
Circularity	0.8626	0.9475	0.0429
IntDens	0.8541	0.8434	0.0425
Feret's Max	0.0646	0.0196	0.0819
Feret's Min	0.0616	0.0406	0.1201

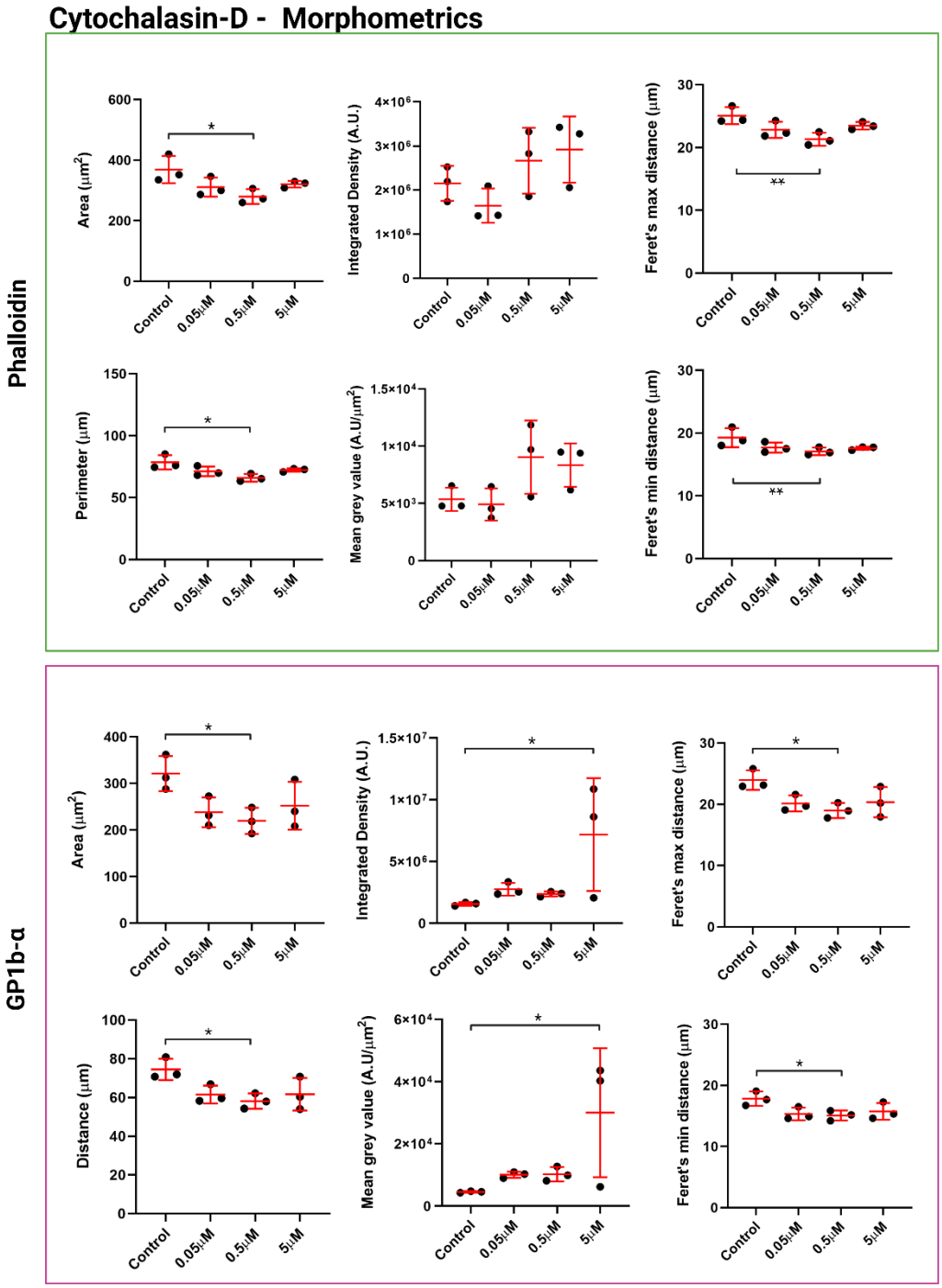


Figure 3.10. **Effect of Cytochalasin-D on morphometrics.** Cytochalasin was added to murine HSCs alongside TPO and SCF at 0.05, 0.5, and 5 μM in DMSO. After three days of differentiation, cultures were fixed, labelled with phalloidin and GP1b-α, and imaged via wide-field fluorescence microscopy. Images were then processed via the wide-field analysis pipeline. A clear change in morphology can be seen in the GP1b-α ROI populations. Phalloidin ROI populations also change drastically, becoming smaller and denser. This is reflected in an increase in IMS integrated density, with a decrease in IMS area. Each data point represents the mean of a ROI population. Bars indicate mean and standard deviation. Dataset was gathered from three murine megakaryocyte cultures.

3.7 Summary of Chapter 3

At the start of this chapter aims were outlined. For the ease of reading, these aims will be directly linked to the corresponding findings and solutions for a later more in-depth discussion.

- Design a labelling method for fixed imaging of megakaryocytes

CD41/61 and GP1b-α describe IMS maturation in fixed megakaryocytes, however GP1b-α provides a greater signal to noise ratio. Furthermore, phalloidin also describes IMS structures within fixed megakaryocytes.

- Design an image analysis pipeline for 3D wide-field imaging.

A pipeline was successfully designed to pre-process, segment, label, and measure 2D IMS morphology. However, this method assesses 2D IMS objects rather than single megakaryocytes. Further work will need to be conducted on accurate 3D, single cell segmentation.

- Identify suitable 2D morphological measurements of IMS.

The IMS area, IMS integrated density, IMS mean grey value, IMS circularity, Feret's minimum diameter, and Feret's maximum diameter were used to measure megakaryocyte maturation.

- Assess variability in wide-field pipeline measures

Wide-field pipeline measurements show false negative results for non-parametric statistical tests, a comparison of population means shows no significant difference between populations derived from separate mice.

- Assess sensitivity in wide-field pipeline measures

Wide-field pipeline measurements show significant difference in response to morphological change induced by cytochalasin-D treatment.

4 MEASURING INVAGINATED MEMBRANE SYSTEM DEVELOPMENT WITH PHASE CONTRAST INCUCYTE IMAGING

4.1 Aims

Although wide-field analysis of fixed megakaryocytes allows for a coarse assessment of IMS morphology, the process of fixation and immune-labelling removes fragile stages of IMS development from the cultures, obscuring the ground truth of megakaryocyte culture development. By using live-cell, non-invasive imaging before fixation, an unbiased view of culture health and maturity can be correlated with a more detailed wide-field IMS analysis pipeline. As such the aims of this section are as follows:

- Design an image analysis pipeline for 3D phase contrast imaging.
- Assess variability in IncuCyte pipeline measures

4.2 Developing an image analysis pipeline for IncuCyte megakaryocyte assay

Segmenting the image with various auto-thresholds (Li, Triangle, Default, and IJ - IsoData) created a mask of our IncuCyte images which allowed the identification of smaller, but not larger megakaryocytes (data not shown). Larger megakaryocytes tended to contain sporadic regions of high contrast, but also many regions with a value similar to the background of the image. Therefore, thresholds either split larger megakaryocytes into multiple individual ROIs, or failed to identify them altogether. Comparatively, smaller cells tended to have an even and high pixel value, giving them a high contrast in comparison to background.

To overcome this, two independent filters were applied to a phase contrast image, one with a high degree of smoothing to identify larger megakaryocytes and one with a low degree of smoothing to identify smaller megakaryocytes (figure 4.1). After smoothing images were processed into a binary mask through the IJ-IsoData auto-threshold. The masks generated were processed with a fill-holes function and a subsequent watershed function (figure 4.2), before filtered by size and circularity to remove unwanted artefacts and objects (figure 4.3). The final masks produced by the two workflows were merged together to produce a single binary mask to identify all megakaryocytes in the image (figures 4.4).

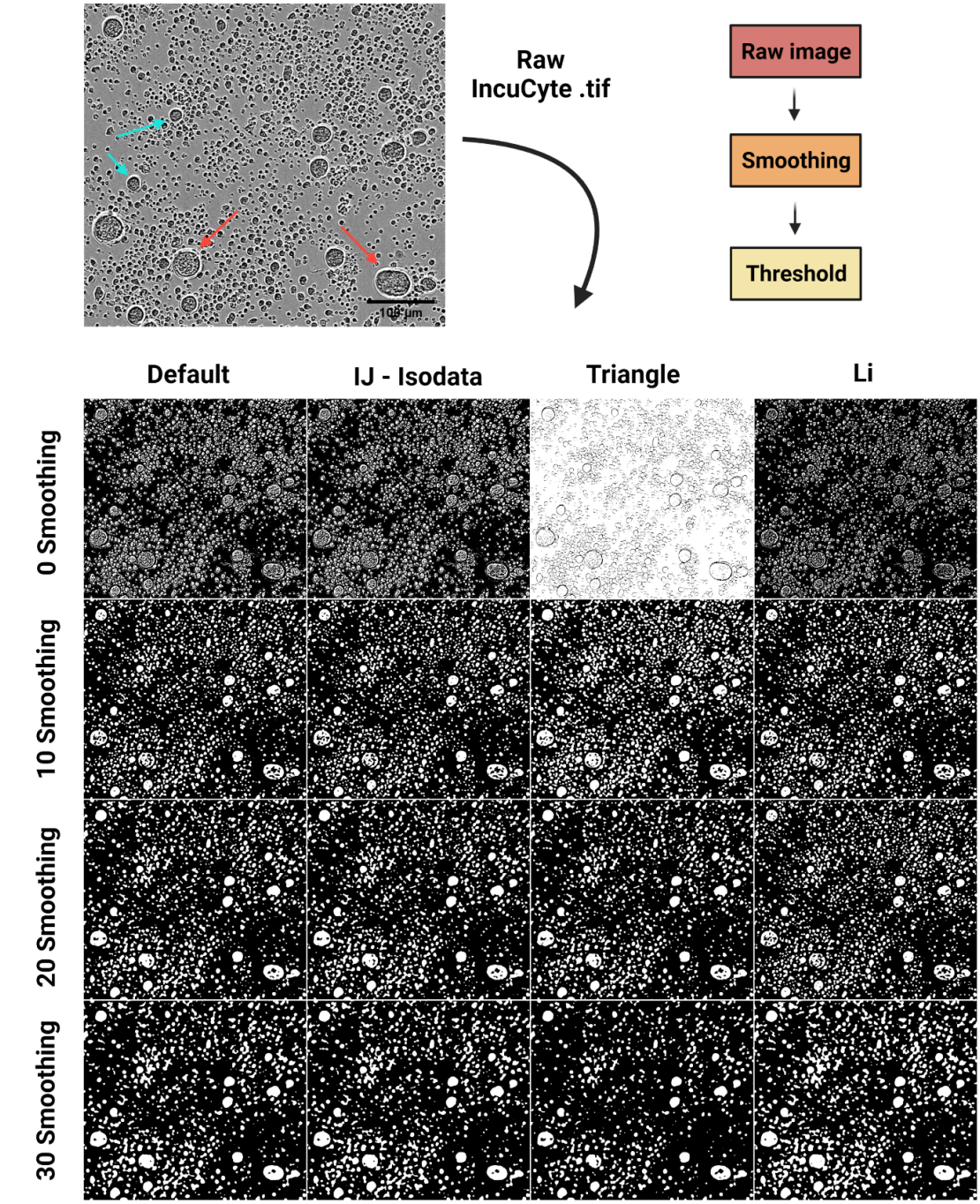


Figure 4.1. **Thresholding and smoothing of IncuCyte images**. Megakaryocytes were cultured for three days of differentiation, and imaged with an IncuCyte incubated microscope with a phase contrast filter. To segment megakaryocytes structures, threshold functions available through Fiji were applied to images: Default, IJ-IsoData, Triangle, Li. Smoothing was applied at 0x, 10x, 20x, and 30x iterations to remove speckling from the image. Within the raw image both large (**red arrow**), and small (**cyan arrow**) megakaryocytes can be identified. With the addition of smoothing, megakaryocytes intensity becomes more uniform and is easy to segment. At high smoothing, small megakaryocytes begin to fuse with background hematopoietic stem cells, whilst at a low smoothing large megakaryocyte are still fairly non-uniform and contain gaps. Representative of four murine megakaryocyte cultures.

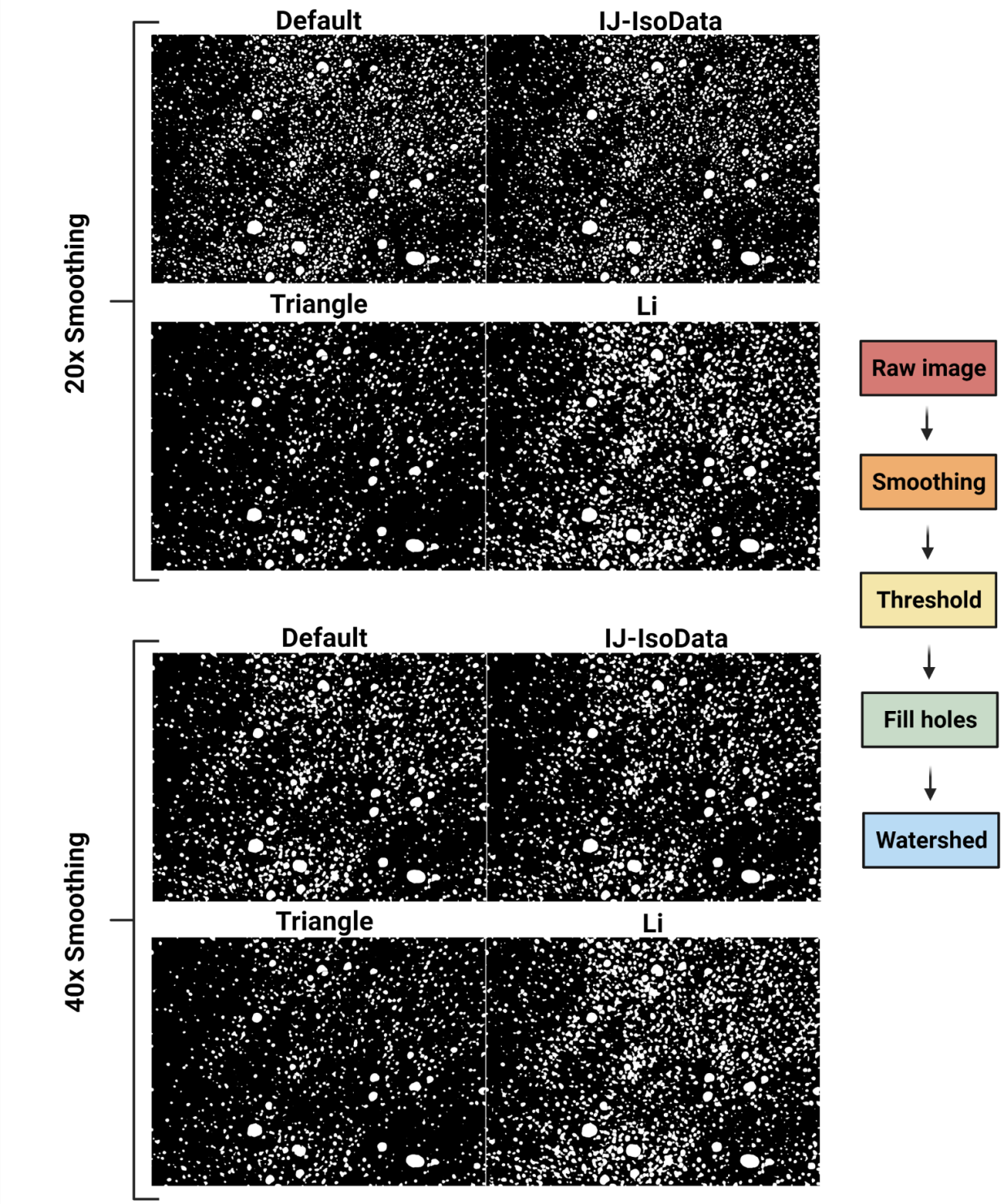


Figure 4.2. **Thresholding and smoothing w. fill holes and watershed of IncuCyte images**. Megakaryocytes were cultured for three days of differentiation, and imaged with an IncuCyte incubated microscope with a phase contrast filter. Post threshold and smoothing, a fill holes and watershed function was applied to aid segmentation. Large megakaryocytes were better defined at high smoothing, however smaller megakaryocytes are better defined at a lower smoothing. Here, IJ-IsoData appears to give the best assumption of morphology for large and small megakaryocytes. Images are representative of four murine megakaryocyte cultures.

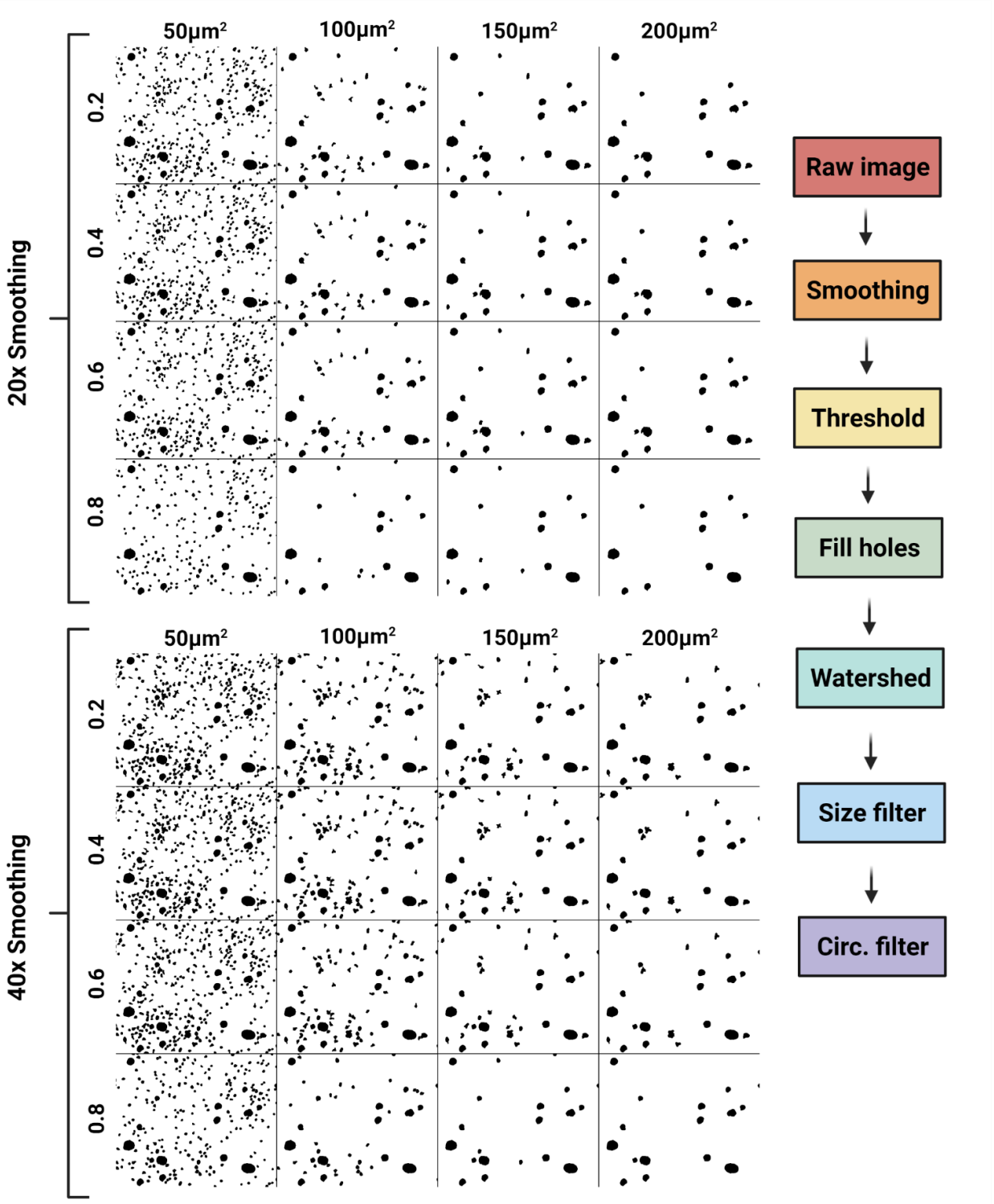


Figure 4.3. **Thresholding and smoothing w. circularity and size filters of IncuCyte images**. Megakaryocytes were cultured for three days of differentiation, and imaged with an IncuCyte incubated microscope with a phase contrast filter. Post segmentation (figure 4.1 & 4.2) particles were filtered based on size (50 - 200 µm^2) and circularity (0.2 - 0.8). A high size filter removed objects that are too small to be megakaryocytes, whilst a high circularity filter removes objects that are not circular. The 20x workflow used a circularity filter: 0.6 to 1, and a size filter of 200 to infinity, whilst the 40x workflow used a circularity filter of 0.7 to 1, and a size filter of 250 to infinity. Representative of four murine megakaryocyte cultures.

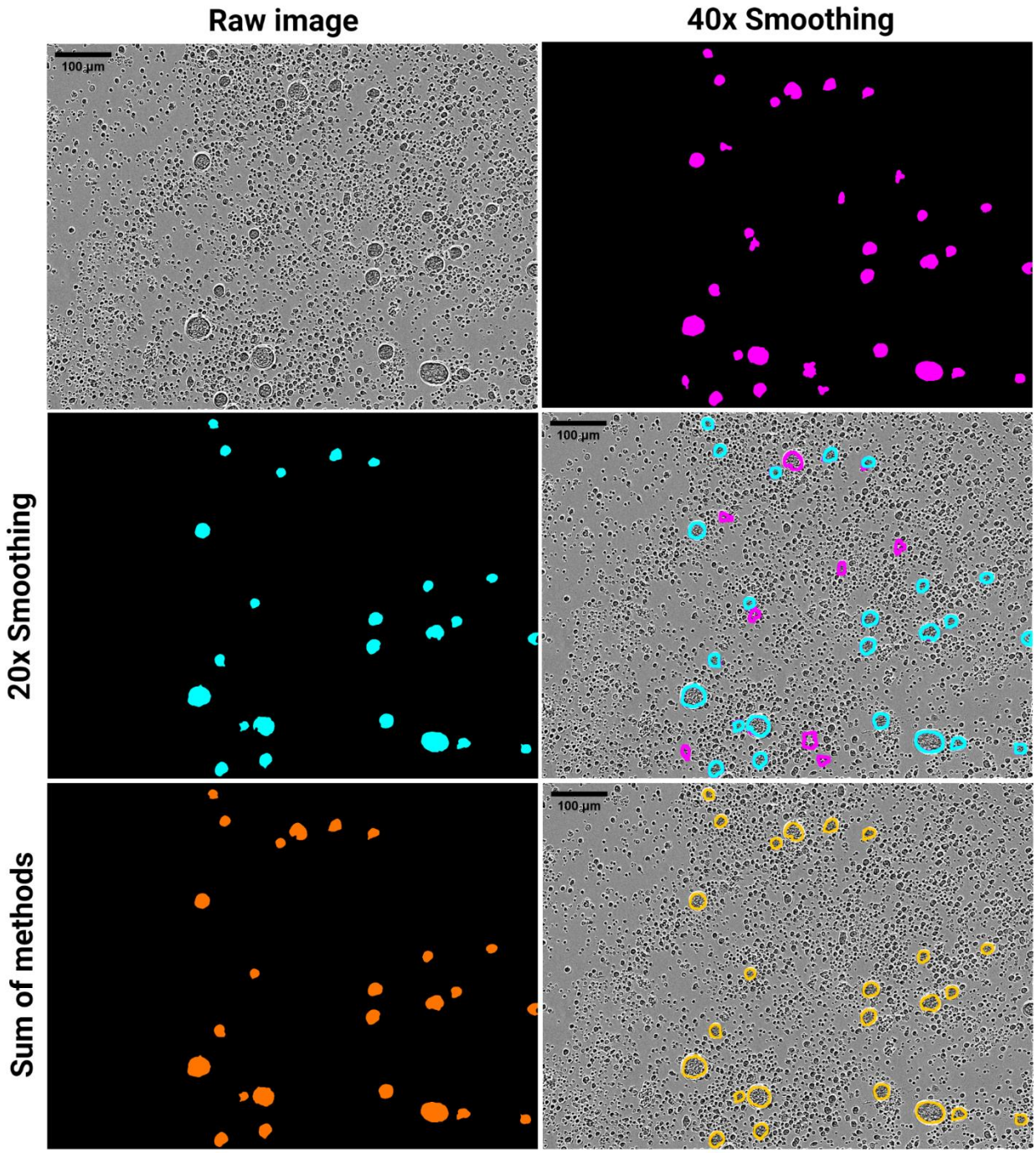


Figure 4.4. **Concatenation and summation of both 20x and 40x smoothing workflows**. Megakaryocytes were cultured for three days of differentiation, and imaged with an IncuCyte incubated microscope with a phase contrast filter. Images were segmented using the auto-threshold IJ-IsoData, and smoothing at 20x (**Cyan**) or 40x (**Magenta**) (figure 4.2 & 4.3). High smoothing identifies more artefacts, but also all large megakaryocytes. By filtering smaller objects including small megakaryocytes, the 40x workflow can be overlaid on the 20x to identify both large and small megakaryocytes. These two images were concatenated, and the maximum intensity of both images was used to produce the final mask (**Orange**). Images representative of four murine megakaryocytes cultures.

4.3 IncuCyte IMS analysis pipeline shows no significant difference between cultures derived from separate mice

Variability in parameter measurements derived from the IncuCyte IMS analysis pipeline was assessed similarly to the wide-field IMS analysis pipeline in chapter 3. Hematopoietic stem cells isolated from individual mice were divided into three separate cultures, with this process repeated four times and resulting in a total of twelve megakaryocyte cultures.

Overall, both cultures derived from individual mice, and from multiple mice display a similar variance (~ > 3 to 5 NSDoM, and ~ > 5 to 7 NSDoNSD), and histogram similarity (69 to 81 %). However, a non-parametric Kruskal Wallis test again shows false negative comparisons of the cultures, indicating that cultures are too variable. As with wide-field fluorescent analysis, conducting a one-way ANOVA on the means of populations showed no significant different between any of the cultures (table 4.1 & 4.2, & figure 4.5).

Table 4.1. **Variance within IncuCyte cultures derived from individual mice**. Murine megakaryocyte cultures were imaged at day three of differentiation by an incubated microscope with a phase contrast filter, and processed with the IncuCyte analysis pipeline. Statistical values were measured to evaluate variance between morphological parameters for each dye within individual mice. The table shows the average histogram similarity (Histogram ~), normalised standard deviation of mean (NSDoM), normalised standard deviation of normalised standard deviation (NSDoNSD), and number of groups with a p-value < 0.05 as defined by a pairwise Kruskal-Wallis test. Ranges of values across cultures derived from a single mouse are highlighted in blue. Values have been colour coded for convenience and refer to figure 3.10. Data was gathered from four murine megakaryocyte cultures.

	IncuCyte (Individual)			
	Histogram	**NSDoM**	**NSDoNSD**	**KW>0.05**
Area	69.9 ± 3.6	5.5 ± 21.8	6.0 ± 61.7	4/12
Perimeter	73.9 ± 2.4	2.9 ± 21.6	6.7 ± 45.8	4/12
Circularity	81.5 ± 5.1	0.7 ± 37.1	7.0 ± 37.1	6/12
Feret's min	70.1 ± 5.9	2.4 ± 25.7	6.4 ± 44.2	3/12
Feret's max	71.1 ± 3.5	2.6 ± 19.1	5.9 ± 60.3	3/12

Table 4.2. **Variance within IncuCyte cultures derived from multiple mice**. Murine megakaryocyte cultures were imaged at day three of differentiation by an incubated microscope with a phase contrast filter, and processed with the IncuCyte analysis pipeline. Statistical values were measured to evaluate variance between morphological parameters for each dye between multiple mice. The table shows the average histogram similarity (Histogram ~), normalised standard deviation of mean (NSDoM), normalised standard deviation of normalised standard deviation (NSDoNSD), and number of groups with a p-value < 0.05 as defined by a pairwise Kruskal-Wallis test. Ranges of values across cultures derived from individual mouse are highlighted in blue. Values have been colour coded for convenience and refer to figure 3.10. Data was gathered from four murine megakaryocyte cultures.

	IncuCyte (Multiple)			
	Histogram ~	**NSDoM**	**NSDoNSD**	**KW>0.05**
Area	70.9 ± 5.0	5.9 ± 29.0	6.9 ± 21.9	2/9
Perimeter	73.4 ± 2.3	2.8 ± 30.3	5.5 ± 41.9	2/9
Circularity	78.1 ± 3.2	0.8 ± 35.3	7.4 ± 14.4	1/9
Feret's min	70.6 ± 5.1	3.0 ± 29.6	6.4 ± 46.9	2/9
Feret's max	72.0 ± 5.4	2.5 ± 34.7	5.9 ± 30.3	2/9

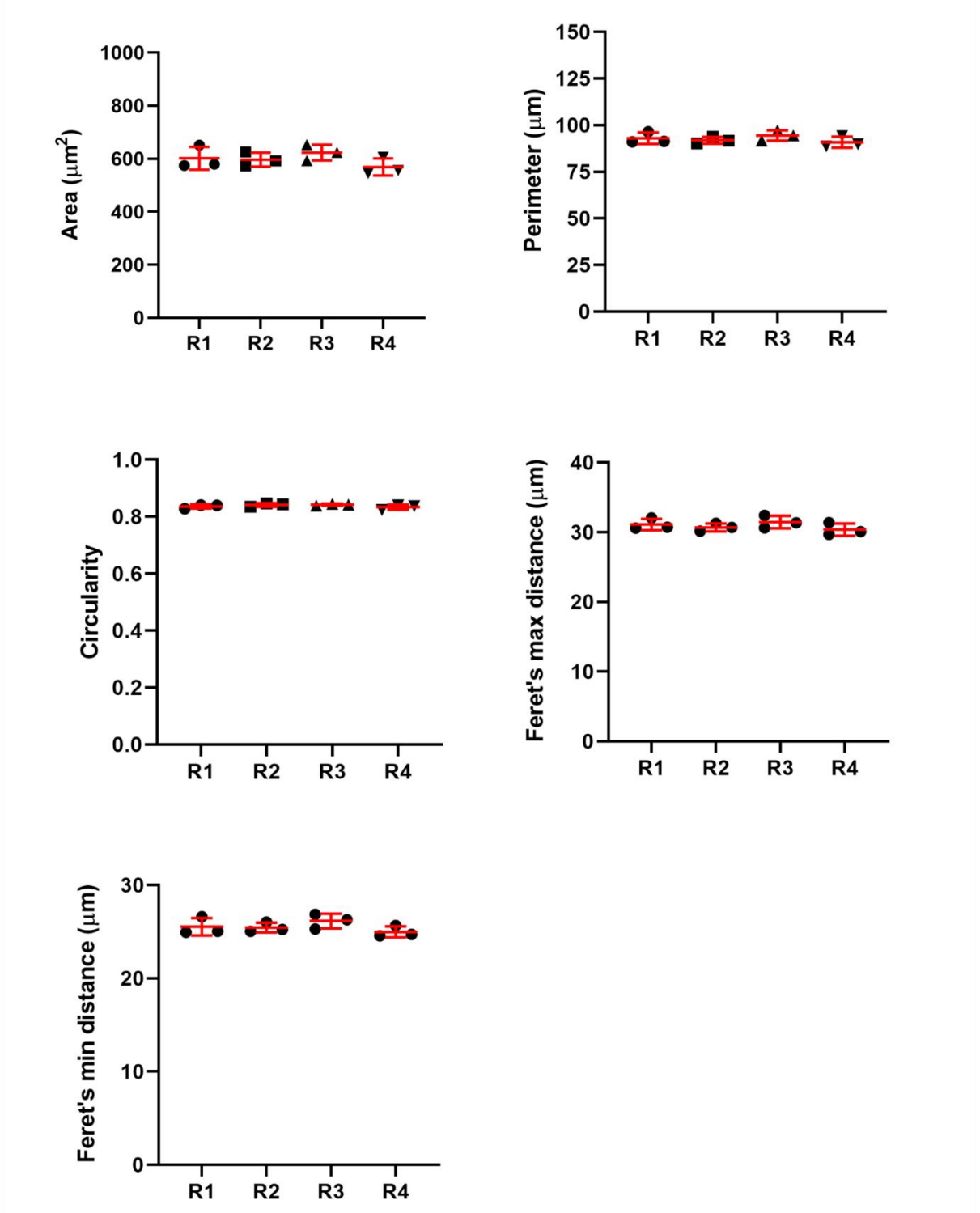


Figure 4.5. **Variance in IncuCyte ROI populations means**. Morphological parameters were measured in cultures at day three of differentiation via the wide-field analysis pipeline. Three cultures were derived from individual mice (R1 to R4) to compare variability in the assay. The mean of each population was taken and compared. Parameters mean values lie within a small range, indicating consistency in cultures. A one-way ANOVA showed no significant difference between populations. Data was gathered from four murine megakaryocyte cultures.

4.4 Summary of Chapter 4

At the start of this chapter aims were outlined. For the ease of reading, these aims will be directly linked to the corresponding findings and solutions for a later more in-depth discussion.

- Design an image analysis pipeline for 2D phase contrast imaging

  A pipeline was successfully designed to pre-process, segment, and measure 2D megakaryocyte morphology in phase contrast images.

- Assess variance in IncuCyte pipeline measures

  Similarly to wide-field analysis, the IncuCyte analysis pipeline measurements show no significant difference in population means between cultures derived from separate mice, however non-parametric analysis of comparisons between whole populations show significant differences.

5 A TEMPORAL ANALYSIS OF IMS DEVELOPMENT *IN VITRO*

5.1 Aims

Previous studies have identified several characteristic stages of IMS development; however it is essential to understand when, and how abundantly these stages of IMS development occur within the lifetime of the *in vitro* culture. By doing so, productive stages within *in vitro* culture development can be isolated for iSPIM imaging. As such the aims of this chapter are as follows:

- Characterise IMS morphological development throughout *in vitro* culture lifetime.
- Identify substrates to aid megakaryocyte immobilisation
- Measure the cytotoxicity of reagents used for live-cell SPIM imaging

5.2 Introduction

Previous work by our lab and others has identified several characteristic stages of IMS development that lead up to proplatelet formation including (Antkowiak et al., 2016; Bender et al., 2015; Dütting et al., 2017; Eckly et al., 2014).:

- Accumulation

  An accumulation of IMS at the cell cortex

- Compression

  Small internal nodes or accumulations of IMS

- Expansion

  A large expanse of continuous IMS

- Polarisation

A large, polarised mass of IMS

- Proplatelet formation

  Extension of proplatelets

In vitro, proplatelet formation, the terminal stage of IMS development, begins within a period of three to five days after addition of TPO. However, due to technicalities and limitations of both the SPIM system and data handling, it is not possible to image developing megakaryocytes for the length of five days. Therefore, to efficiently capture high resolution, three-dimensional, time-lapse images of IMS development, it is essential to understand when, and how abundantly these stages of IMS development occur within the lifetime of the culture.

Megakaryocytes are also non-adhesive on standard tissue culture plastic and glass slides. High resolution, live cell imaging of non-adhesive, free moving cells requires modification of the culture environment to restrict movement over the long period of image capture. To this end, a combination of substrates and hydrogels are frequently used in live-cell imaging to coat coverslips or embed cells during imaging. These include poly-L-lysine (Fischer et al., 2008; Mazia et al., 1975), vitronectin (Jensen et al., 2009), agarose (Au - Schumacher & Au - Søgaard-Andersen, 2018), and methylcellulose (Aguilar et al., 2018; Aguilar et al., 2016; Au - Boscher et al., 2021). Whilst substrates and hydrogels can aid image acquisition, they can also affect megakaryocyte structure and maturation. Studies have shown that extracellular matrix composition and stiffness is found to regulate megakaryocyte and IMS development (Aguilar et al., 2016; Leiva et al., 2018), with megakaryocytes also actively shaping the extracellular bone marrow environment by excreting extracellular matrix proteins (Malara et al., 2014). To restrict megakaryocyte movement during image acquisition

without heavily perturbing healthy megakaryocyte development, we test these various reagents, measuring megakaryocyte mobility and IMS viability.

To briefly reiterate, this chapter aims to monitor the temporal dynamics of IMS development in our cultures to highlight when IMS morphological stages are most abundant, and to measure megakaryocyte mobility and IMS viability in the presence of different culture environments.

5.3 Mature megakaryocytes are most abundant between D2-3 of *in vitro* cultures

Megakaryocytes are non-adherent cells when grown on standard tissue culture plastic. To allow for initial assessment of their differentiation, cells harvested at each day of culture were immobilised onto fibrinogen coated coverslips and stained for GP1b-α and DAPI to monitor megakaryocyte maturation and endomitosis respectively. Whilst spreading on fibrinogen helps retain megakaryocytes on the slides and allows for the levels of GP1B-α expression to be assessed, IMS morphology is lost during spreading. In tandem, the size and number of individual maturing megakaryocytes was also measured over a five-day period using an IncuCyte.

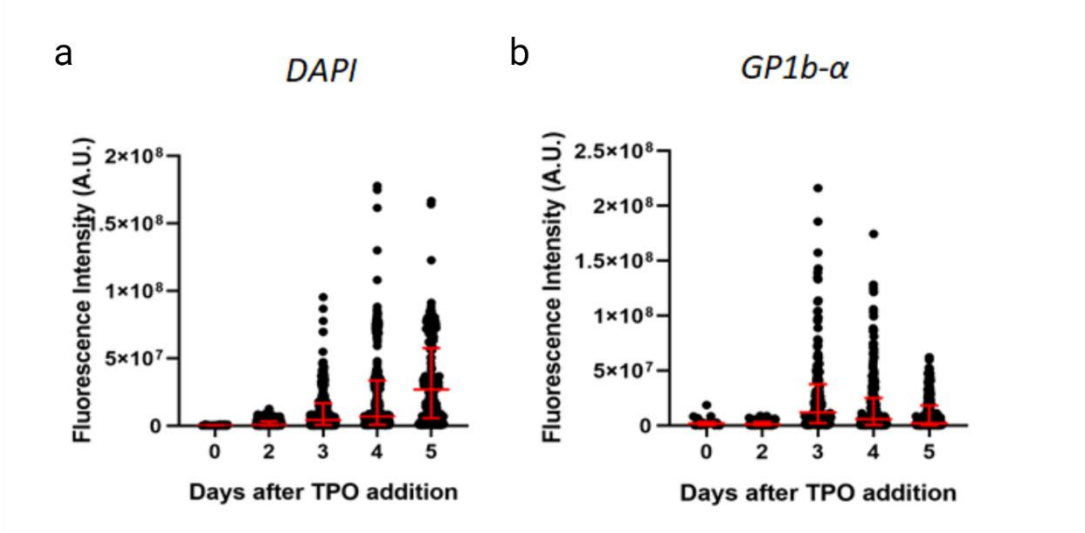


Figure 5.1 **Change in nucleus size and GP1b-α expression in maturing megakaryocytes.** The fluorescence intensity of **a)** DAPI and **b)** GP1b-α in megakaryocytes from day 0 (prior to TPO addition) until day 5 was image by wide-field fluorescence microscopy and measured. The fluorescence intensity of both DAPI and GP1b-α increases drastically between days 2-3 of culture. The DAPI signal remains high whilst there is a gradual decrease of GP1b-α between days 3-5. Each data point represents a single cell and cells from 3 replicates are pooled. Bars indicate mean and standard deviation.

As expected, during the five-day culture the number of megakaryocytes observed increased. Furthermore, an increase in DNA content and GP1b-α expression of the cells (figure 5.1a and b), both markers of megakaryocyte maturation, was observed over time. In addition, the average cell size in the culture increased (figure 5.2a), which upon further analysis showed an increase in cells greater than 130 μm^2, indicative of mature megakaryocytes (figure 5.2b). The biggest change was observed between days 3 to 4. Interestingly, whilst the ploidy level peaked around day 4 and remained high until day 5, the Gp1b-α content, and size peaked at day 4 and then steadily declined until day 5. This suggests that from day 2 onwards the megakaryocytes cytoplasm is rapidly maturing, and the cells are becoming polyploidy and developing IMS. These mature megakaryocytes are then subsequently undergoing proplatelet

formation (or dying) causing their size and GP1b-α levels to decline. In contrast, the nucleus of the cells is left behind giving rise to the high DAPI staining seen in day 5 cultures.

Subdividing the megakaryocyte population in four partitions of area, it is apparent that whilst smaller megakaryocytes (135 to 500 μm^2) peak in abundance at day 2 to 3, larger megakaryocytes (501 to 2000 μm^2) appear most abundantly at day 4 to 5, suggesting that whilst the majority of development occurs between day 3 to 4 (figure 5.2b and c), early megakaryopoiesis events start between day 2 to 3 (figure 5.2b). Furthermore, it is also clear that whilst megakaryocyte number increases until day 3 there is a gradual decrease in total number of megakaryocytes from the culture thereafter. This suggests that megakaryocytes as small as 135 to 500 μm^2 undergo cell death, are capable of producing proplatelets, or fail to mature into larger megakaryocytes. This pattern is repeated throughout the increasing brackets of megakaryocyte size. Taken together this data indicates that the major development and expansion of IMS is likely occurring between days 2 and 4 of culture.

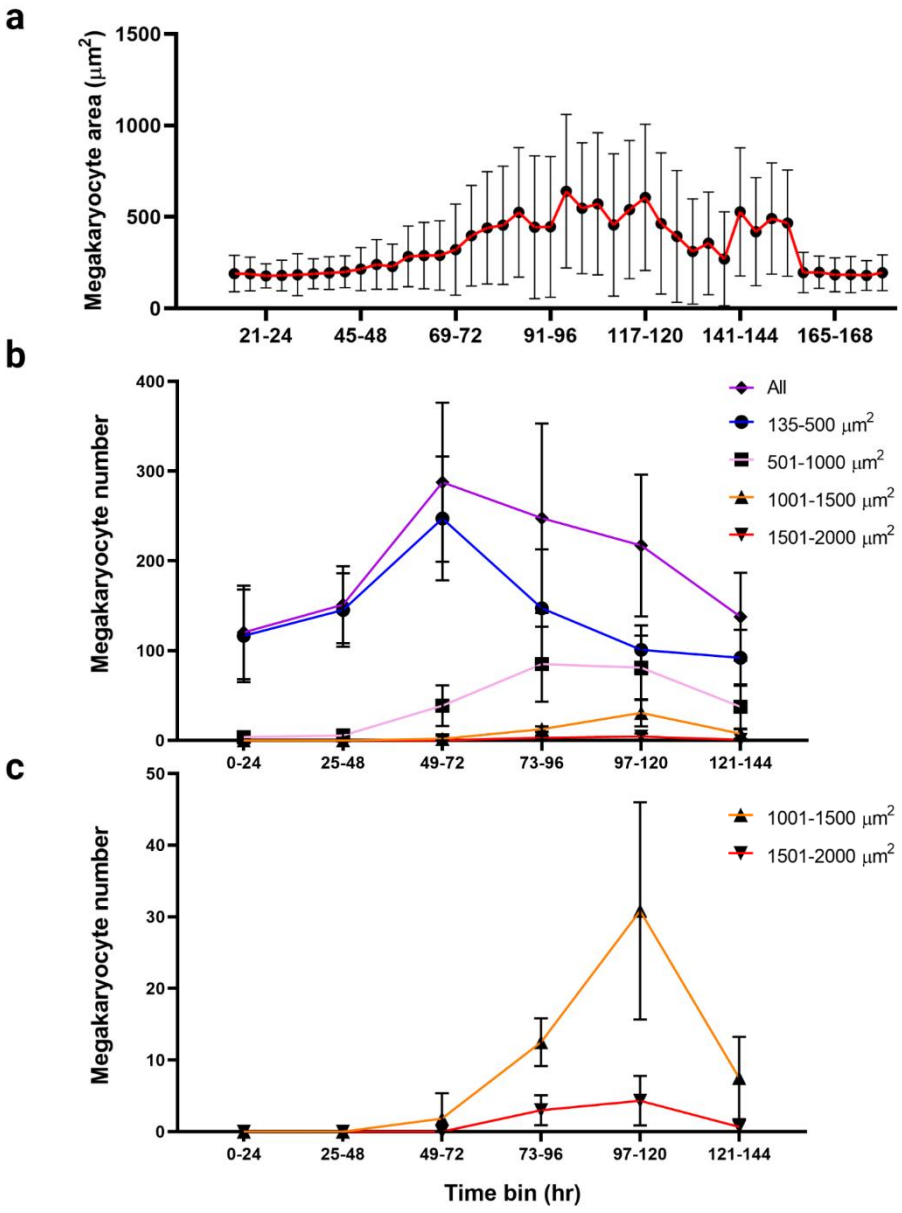


Figure 5.2 **Megakaryocyte size and abundance over time**. Murine megakaryocytes were differentiated across five days and imaged using an incubated IncuCyte microscope with a phase contrast filter. Images were segmented and processed using the IncuCyte analysis pipeline to measure megakaryocyte size change over time. **a)** Mean megakaryocyte area increases rapidly between 72 and 96 hrs, where it plateaus before a gradual decrease between 96 and 120 hrs. **b)** Total megakaryocyte number increases until 72 hrs where after it decreases. **c)** Smaller megakaryocytes peak between days 48 to 72 hrs, whereas larger megakaryocytes are highly abundant between 72 and 120 hrs. Each data point represents a population of cells, and cells from 3 replicates are pooled. Bars indicate mean and standard deviation.

5.4 Megakaryocytes are immobilised by poly-L-lysine without perturbing IMS development

To assess how far megakaryocytes moved over the duration of the imaging window, cells grown on plastic (control), poly-L-lysine or vitronectin, or embedded in methylcellulose or agarose were imaged over time, and a tracking pipeline was implemented to measure cell speed and velocity. Raw images were converted to binary masks using a Huang auto-threshold. Noise was then removed with a despeckle function before particles were filtered for circularity (0.5 - 1) and size (135 – 1250 μm^2). These image masks were then processed by the TrackMate plugin (Tinevez et al., 2017). Tracks created were parsed and organised with MATLAB, where the speed, velocity, number of tracks, and length of tracks was calculated (figure 5.3a).

To calculate object speed, equation 2.1 was used where distance was equal to track length (in μm) and time was equal to the number of frames multiplied by the time interval (in min).

$$\text{speed} = \frac{\text{distance}}{time} \tag{2.1}$$

To calculate object velocity, equation 2.2 was used where displacement was equal to the distance between starting point and finish point, or the distance from the origin (in μm). This was calculated using equation 2.3 to find the hypotenuse of a right-angled triangle between the start and finish points.

$$\text{velocity} = \frac{\text{displacement}}{time} \tag{2.2}$$

$$c^2 = x^2 + y^2 \tag{2.3}$$

The number of tracks recorded (figure 5.3b) is indicative of how many cells are moving during the imaging window. Cells in methylcellulose have the lowest number of tracks measured, indicating that this semisolid hydrogel is able to restrain cells better than cells in media, in agarose or on vitronectin. However, upon closer inspection cells are found to deposit within bubbles in the gel. Interestingly, although poly-L-lysine has a large number of tracks, the average speed and velocity are low, second only to 0.4 % methylcellulose. Surprisingly, for cells in agarose there is a highly variable effect with some cells moving long distances and others hardly at all, however, the reasons for this are unclear**.** Measuring track length as an estimate of cell viability, all conditions appear to have an average track length of between 300 to 400 minutes, suggesting that megakaryocytes are healthy throughout the experiment in comparison to the control. Taken together, this data suggests that poly-L-lysine is the most appropriate method for immobilising megakaryocytes for live-cell studies as it balances restraint of megakaryocytes with ease of use. Poly-L-lysine also provided useful in immune staining of fixed megakaryocytes, where more cells remained after the protocol than with other immobilisation methods.

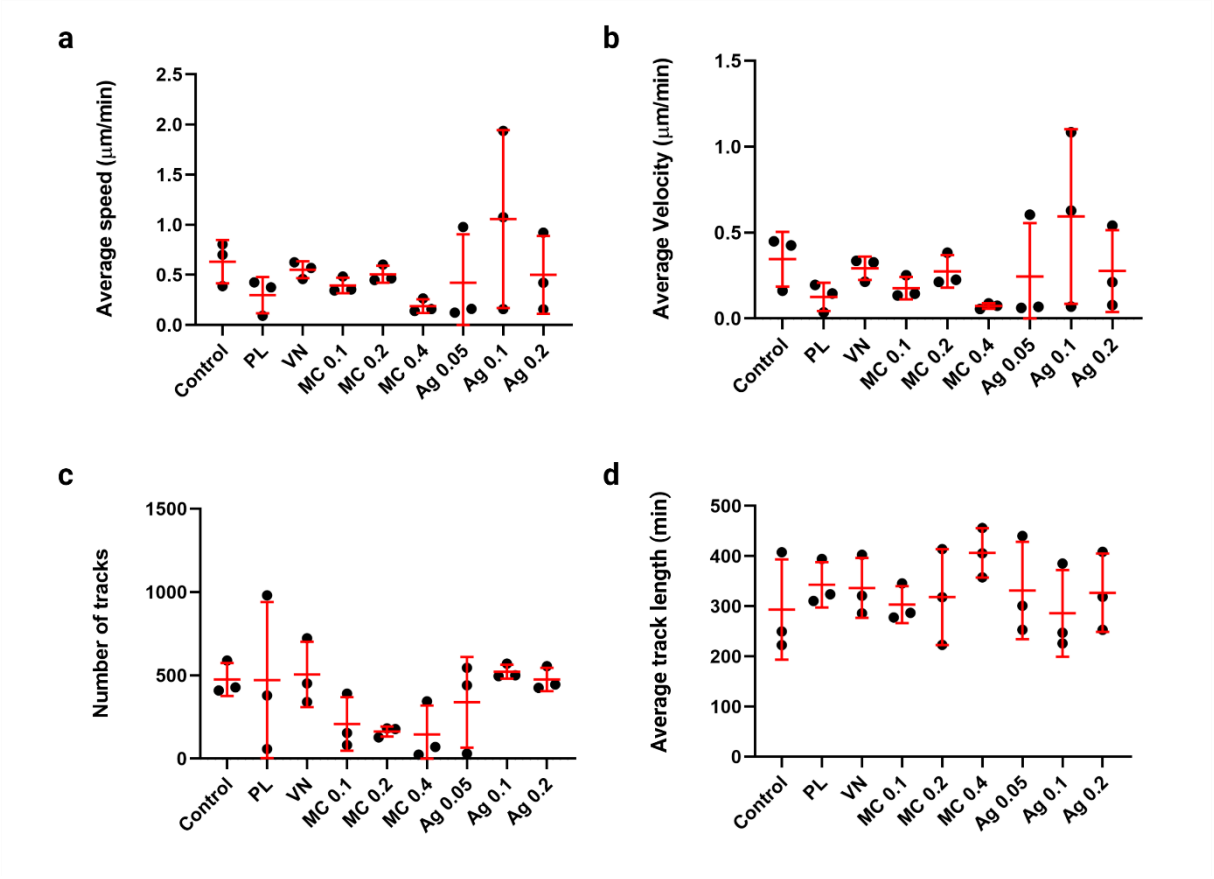


Figure 5.3 **Tracking of megakaryocytes.** Murine megakaryocytes expressing LifeAct-GPF were isolated at day three of differentiation and seeded onto/into different substrates and hydrogels. Megakaryocytes were imaged for 12 hours using a fluorescence wide-field in an incubated and CO_2 controlled chamber. A tracking script was created using Fiji and MATLAB to segment, track, and measure the **a**) **average speed**, **b**) **average velocity**, **c**) **number of tracks**, and **d**) **length of tracks** of megakaryocytes. Whilst methylcellulose at high concentrations reduces the number of tracks, bubbles within the gel trap megakaryocytes. However, whilst poly-L-lysine allows for a large number of tracks, it acts to reduce cell speed and velocity without effecting megakaryocyte distribution. Surprisingly, agarose imbedded cells show a lack of reliability in results. Each data point represents the mean value from a population of cells, and cells from 3 replicates are shown. Bars indicate mean and standard deviation.

5.5 Time course of IMS morphological stage within *in vitro* cultures

To determine the time scale of IMS development, and carry out a morphological examination of the stages. Megakaryocytes were fixed at each day of differentiation (1 to 5), and labelled with GP1b-α and phalloidin to allow an assessment of the IMS. IMS development within the cells was manually categorised into different stages based on observable phalloidin and GP1b-α morphology and structures described previously,

thereby creating a predictive model of the relative abundance of each stage at each day of culture (figure 5.4).

The vast majority of megakaryocytes across all days were categorised as M2 or M3, (71% average across all days), with M2 comprising the major division of megakaryocytes between days 1 to 2, (Day 1 to 5: 68%, 63%, 26%, 13%, 1% respectively), and M3 becoming more prevalent than M2 from day 3 onwards (Day 1 to 5**:** 20%, 20%, 50%, 53%, 43%). M1, M4, M5, and M6 were all very low in abundance across all days (1.5% average across all days) indicating that either they are very transient, that they are difficult to identify, or that they do not exist in our cultures. Also worth noting is that vacant and unhealthy megakaryocytes started to increase in abundance after day 3, accounting for 55% of all megakaryocytes by day 5.

Analysis of phalloidin and GP1b-α ROI populations show that there is a marked increase in GP1b-α IMS mean grey value, IMS area, and IMS integrated density before day 3 (figure 5.5 and 5.6). However, whilst GP1b-α ROIs parameter populations increase from day 1 to 4, phalloidin ROI populations only increase from day 2 to 4. This data confirms the expansion of the IMS as the cells mature, and that imaging of GP1b-α and phalloidin in these cells allows us to visualise the developing IMS. It also indicates the sensitivity of our analysis. Undifferentiated cells do not express GP1b-α and so we can detect its expression as an early marker of megakaryocyte differentiation. Furthermore, phalloidin and GP1b-α ROI populations of IMS area and IMS integrated density drops between day 4 to 5, which correlates with the timing of proplatelet formation and megakaryocyte ‘death’ described earlier (figures 5.1 & 5.2).

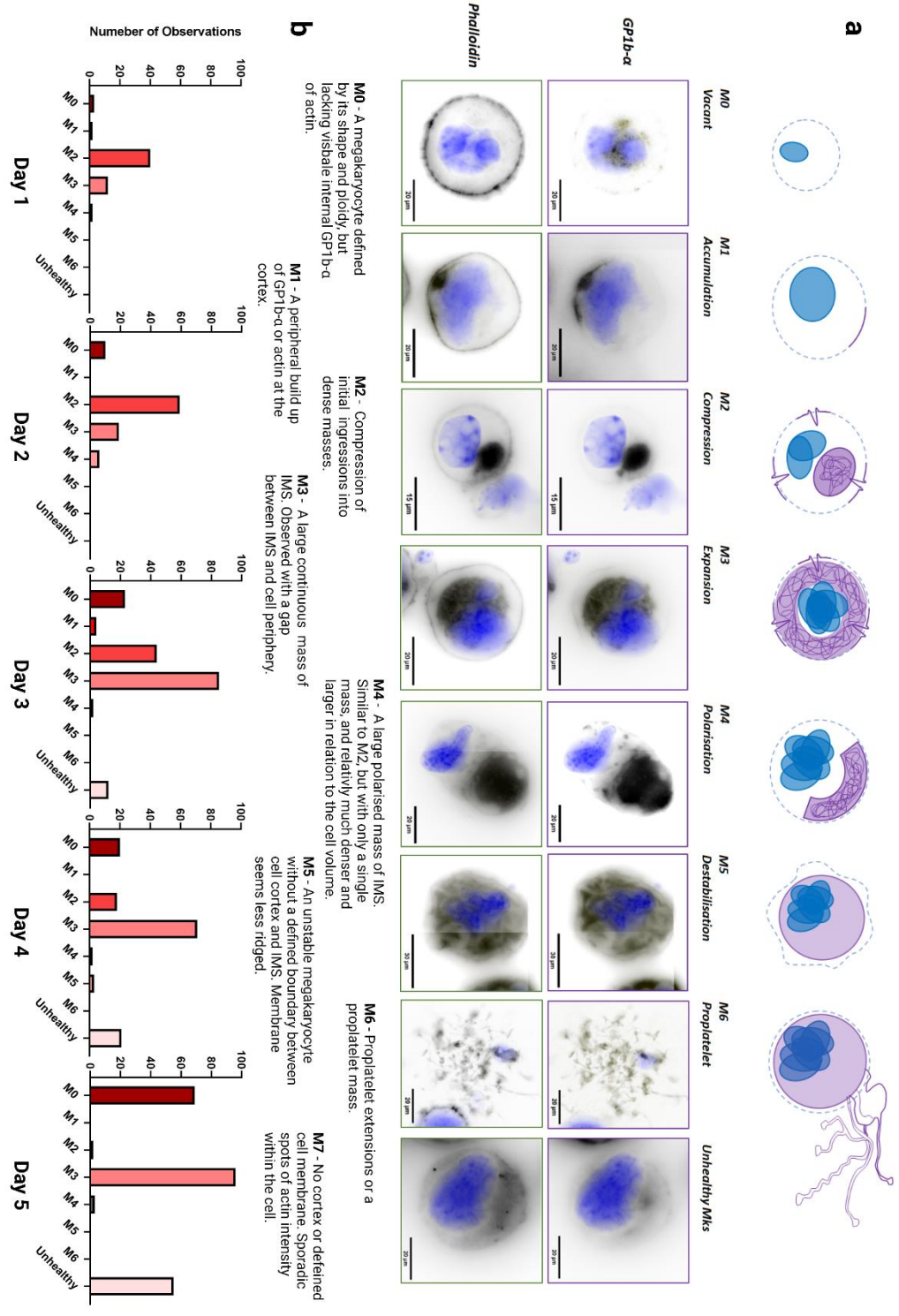


Figure 5.4 **Temporal dynamics of IMS stages during megakaryopoiesis.** Murine megakaryocytes were fixed at each day of differentiation, and stained with GP1b-α, phalloidin, and DAPI to label nuclei. Megakaryocytes were manual categorised into groups. **a)** Schematic of the different stages of IMS formation lined up with representative images of each stage. Cells were stained **b)** Quantitation of the number of cells at each stage of IMS differentiation over the 5 days of culture. Megakaryocytes largely differentiate to M2 from day 1 to 2, then progress to differentiate from M2 to M3 between days 2 to 5. Notably, unhealthy, and vacant megakaryocytes increase in population drastically between days 4 to 5. Each bar represents a population of cells, and cells from 4 replicates are pooled.

Comparing population histograms over culture maturation, phalloidin ROI populations increase in IMS mean grey value over time, with a large jump between days 2 to 3 (figure 5.7). Comparatively, GP1b-α ROI populations also increase in IMS mean grey value over time, but with a larger increase between days 1 to 2. Again, this suggests that GP1b-α increases before phalloidin. In both GP1b-α and phalloidin ROI populations, across most parameters there is a shift between days 2 to 4 towards a subpopulation. These included IMS area, IMS perimeter, IMS Feret's maximum diameter, IMS Feret's minimum diameter, and IMS circularity. Most prominently, in ROI populations of IMS mean grey value, IMS perimeter, and IMS circularity there is a shift between days 2 to 3.

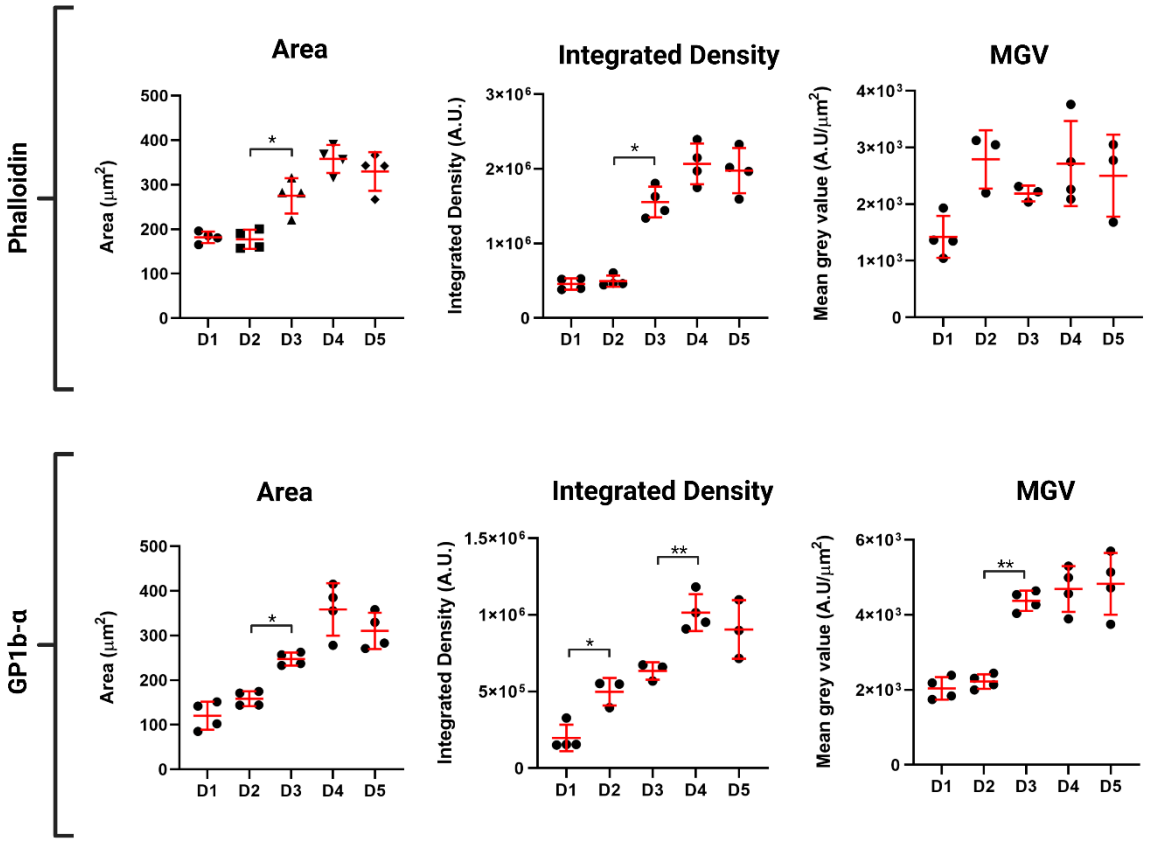


Figure 5.5. **Population means for basic IMS parameters over day 1-5**. Murine megakaryocytes were fixed at each day of differentiation, and stained with GP1b-α and phalloidin, and imaged with a fluorescence wide-field microscope. Images were analysed with the wide-field analysis pipeline to measure morphological parameters: area, integrated density, and mean grey value. Area and integrated density of IMS increases in both GP1b-α and phalloidin channels, however phalloidin values only increase after day 2, whereas GP1b- α values increase after day 1. All parameters begin to decrease after day 4, suggesting a decrease in mature megakaryocyte pool either by cell death, or proplatelet formation. Each data point represents the mean value of a population of cells. Data was gathered from four murine megakaryocyte cultures. Bars indicate mean and standard deviation.

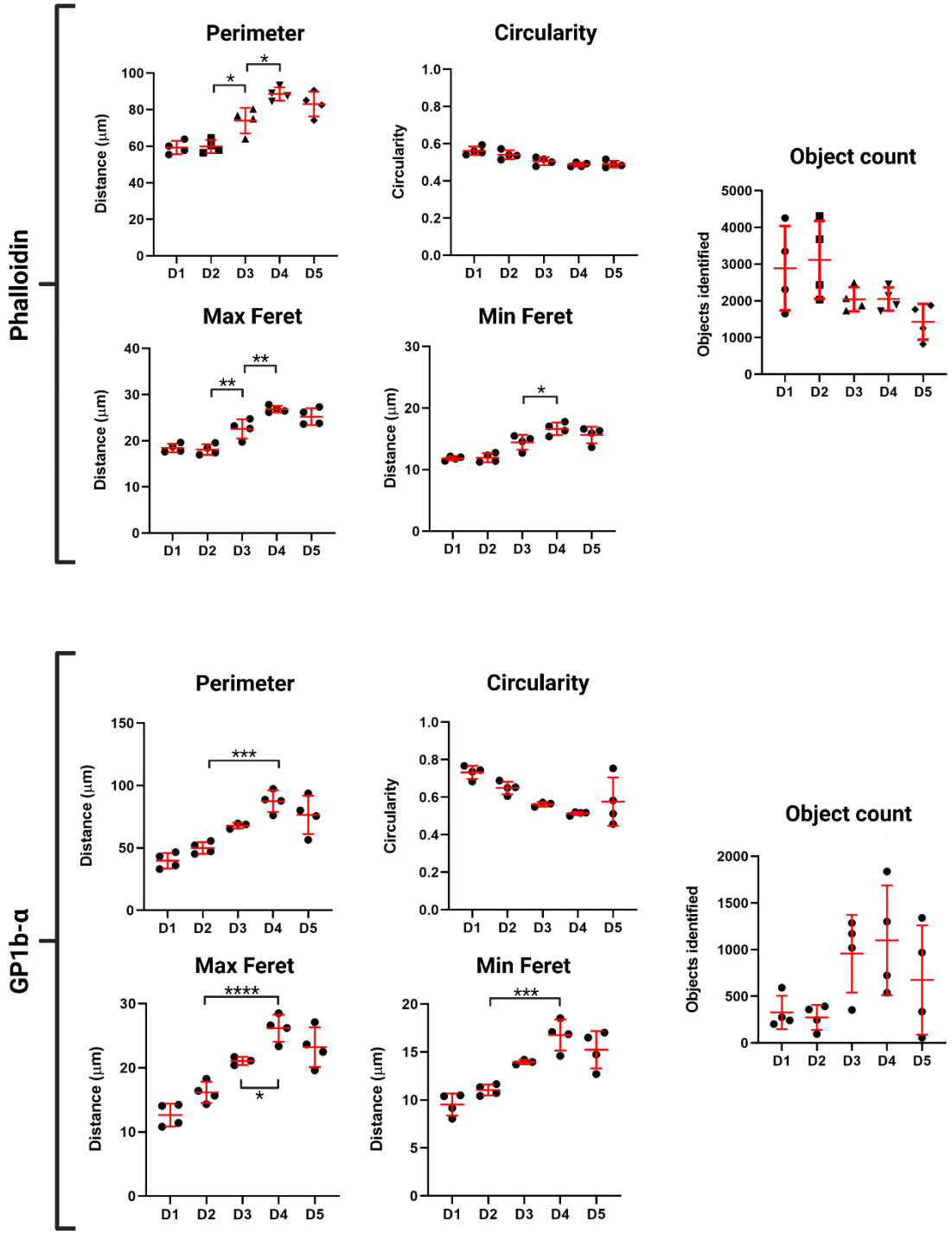


Figure 5.6. **Population means for IMS alternative parameters over day 1-5**. Murine megakaryocytes were fixed at each day of differentiation, and stained with GP1b-α and phalloidin, and imaged with a fluorescence wide-field microscope. Images were analysed with the wide-field analysis pipeline to measure morphological parameters: IMS circularity, Perimeter, Max and Min Feret's Diameter, as well as object count. IMS circularity reduced throughout culture lifetime, whereas IMS perimeter, IMS Feret's min and max diameter increased. Similarly to IMS area also increased, suggesting a growth of total IMS volume which becomes less spherical. Total number of IMS ROIs increases from day 2 to 3. Each data point represents the mean value of a population of cells. Data was gathered from four murine megakaryocyte cultures. Bars indicate mean and standard deviation.

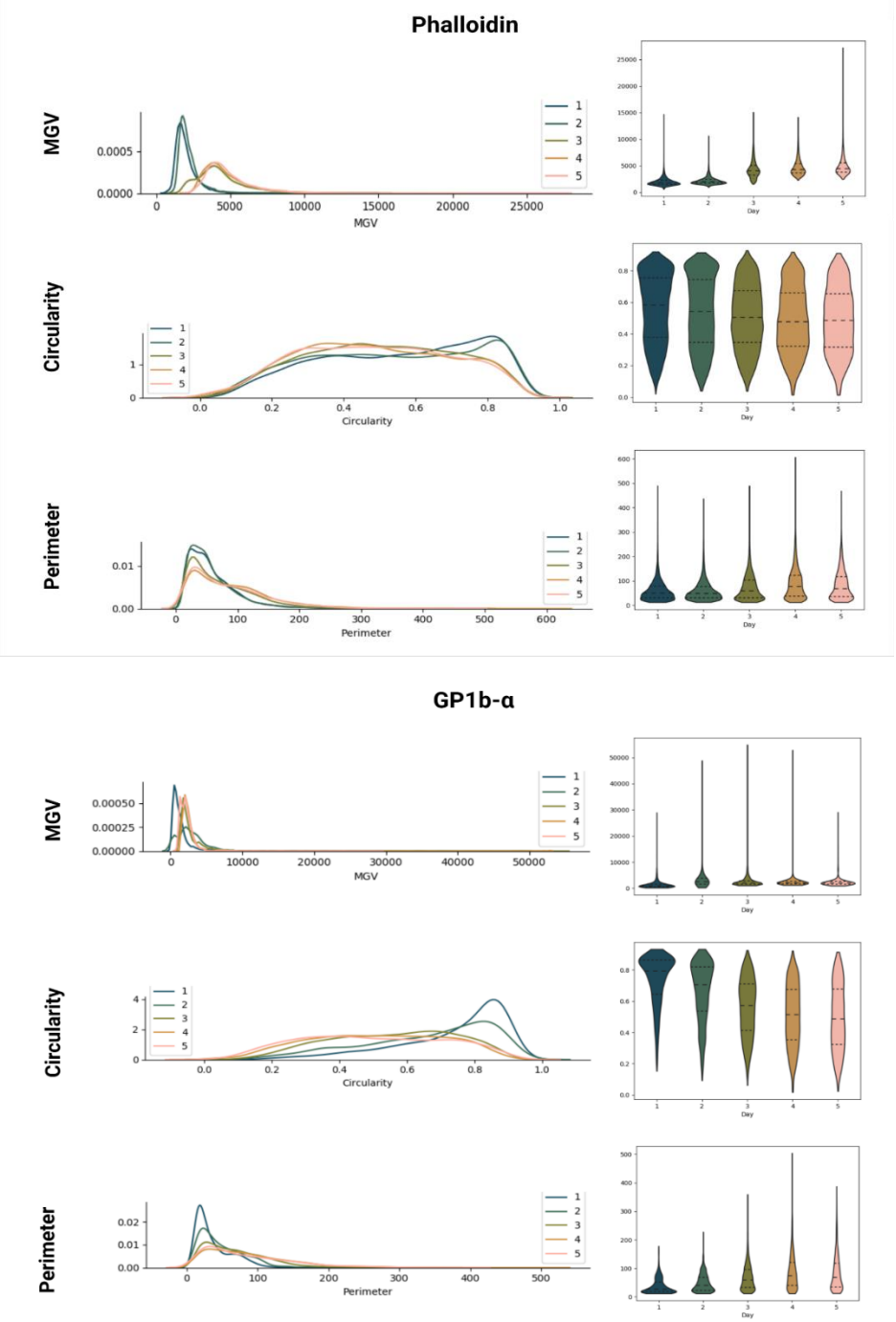


Figure 5.7. **KDE histograms of IMS population change over time.** Murine megakaryocytes were fixed at each day of differentiation, and stained with GP1b-α and phalloidin, and imaged with a fluorescence wide-field microscope. Images were analysed with the wide-field analysis pipeline to measure morphological parameters: Mean grey value, circularity, and Perimeter. Kernel density estimation (KDE) histograms depict population abundance over the relevant parameter. Days are represented by a different colour of histogram. After day 2, sub-populations of megakaryocytes begin to appear**.** Again, GP1b-α IMS mean grey value increases at day 2, whereas Phalloidin IMS mean grey value increases at day 3, suggesting that only base levels of phalloidin are required to drive initial stages of IMS development. Interestingly, at day 1 and 2 IMS objects appear into segregate clearly into two populations of perimeter. Data was gathered from four murine megakaryocyte cultures. Bars indicate mean and standard deviation.

5.6 Megakaryocytes develop normally in the presence of poly-L-lysine and CellMask

Whilst developing a methodology for SPIM analysis, several reagents were identified which may be present in the imaging media whilst megakaryocytes mature. These include poly-L-lysine, CellMask, and DMEM. However, it is unknown how the presence of these reagents will affect or perturb IMS morphology throughout maturation. Furthermore, heparin has been suggested to increase proplatelet formation within cultures (Strassel et al., 2012), and fluorescent beads are necessary for accurate 3D duel inverted SPIM reconstruction (Kumar et al., 2014). Here, the effect of seeding density of hematopoietic stem cells upon TPO addition, heparin, poly-L-lysine, CellMask, DMEM, and fluorescent beads is quantitatively measured.

With regards to hematopoietic seeding density, it is clear that with an increase in seeding density there is a decrease in IMS content across parameters, suggesting that there is competition for growth materials (figure 5.8).

In comparison to a $1x10^6$ seeding density, poly-L-lysine appears to cause a marginal reduction in IMS area and integrated density within both phalloidin and GP1b-α channels. Heparin, DMEM, CellMask and fluorescent beads also all cause change to IMS content across parameters. However, despite altering IMS content, cultures incubated in the presence of reagents still produce mature megakaryocytes exhibiting various IMS stages, with only fluorescent beads appearing to drastically alter IMS or megakaryocyte development.

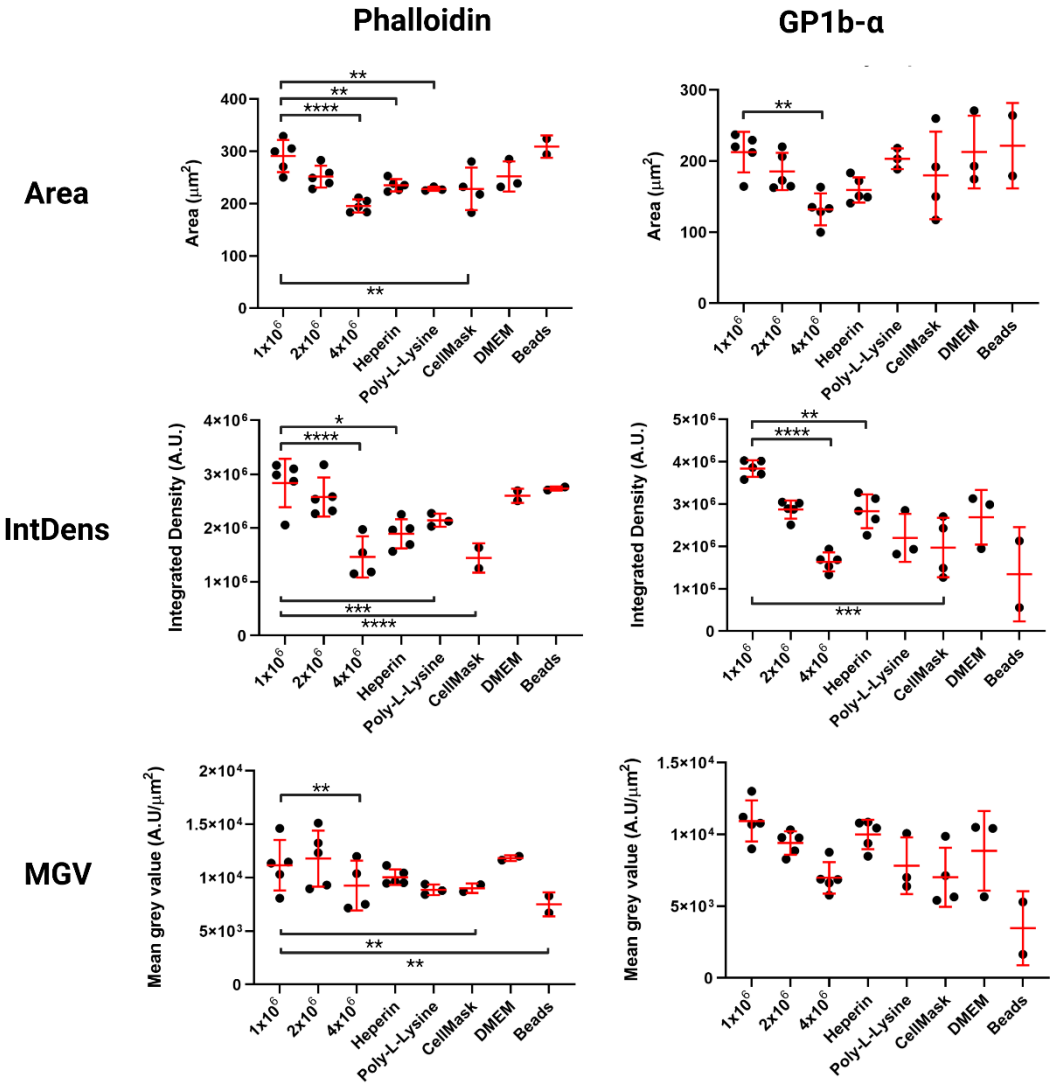


Figure 5.8. **Effect of SPIM reagents on IMS development.** Murine megakaryocytes were cultured the presence of SPIM imaging reagents: heparin, poly-L-lysine, CellMask, DMEM, and fluorescent beads. Cultures were also grown at various densities to evaluate the optimum imaging density. Megakaryocytes were fixed at day three of differentiation, and stained with GP1b-α and phalloidin, and imaged with a fluorescence wide-field microscope. Images were analysed with the wide-field analysis pipeline to measure morphological parameters: area, integrated density, and mean grey value. An increase in hematopoietic stem cell seeding density decreases the area and integrated density of both phalloidin and GP1b-α. Whilst all other reagents act to reduce the area and integrated density of IMS, none appear to drastically alter IMS or megakaryocyte development. Data was gathered from four murine megakaryocyte cultures. Bars indicate mean and standard deviation.

5.7 Summary of Chapter 5

At the start of this chapter aims were outlined. For the ease of reading, these aims will be directly linked to the corresponding findings and solutions for a later more in-depth discussion.

- Characterise IMS morphological development throughout *in vitro* culture lifetime.

Early-stage megakaryocytes appear abundantly at between days 2 to 3, whereas later stage megakaryocytes appear abundantly between days 3 to 4. Therefore, future imaging should be conducted within these windows.

- Identify substrates to aid megakaryocyte immobilisation

Poly-L-lysine acted to inhibit megakaryocyte mobility, thereby slowing megakaryocyte movement during imaging. With Poly-L-lysine megakaryocytes will remain inside the imaging window for a longer period of time.

- Measure the cytotoxicity of reagents used for live-cell SPIM imaging

IMS within megakaryocytes grows larger in less dense cultures. For future cultures, cells will be seeded at $1x10^6$. Furthermore, all reagents marginally inhibited IMS growth. To limit this, only CellMask and poly-L-lysine will be used for the iSPIM since they remain essential for quality imaging.

6 LIVE, SINGLE CELL ANALYSIS OF IMS MATURATION WITH SINGLE PLANE ILLUMINATION MICROSCOPY.

6.1 Aims

Transitioning IMS has never before been imaged in live megakaryocytes, providing a unique understanding of the precise IMS morphological pathways developing megakaryocytes undergo. As such the aims of this section are as follows:

- Design a labelling method for live cell imaging of megakaryocytes.
- Identify suitable morphological measurements of IMS.
- Design an image analysis pipeline for 4D SPIM imaging.
- Define IMS morphological stages through manual observation.
- Define IMS morphological stages through cluster analysis.
- Elucidate the transitions of IMS morphological stage.

6.2 Introduction

The next logical step in understanding the dynamics of IMS morphology is to observe individual, live-cell megakaryocyte transition through the IMS morphological stages. During the previous chapters a method for evaluating entire megakaryocyte populations based on various morphological measures of IMS content using wide-field was produced, assessed, and implemented. This method worked well to visualise a coarse change in IMS maturation, however iSPIM presents a method which can provide a higher resolution description of 3D morphology. Additionally, the low photo-toxicity of iSPIM makes it the optimum tool for live-cell, volumetric imaging.

The previously developed pipeline aimed to aid manual interpretation of IMS morphological stage by defining cultures based on their quantitative morphological parameters. Taking that concept forward, with single cell analysis each megakaryocyte will have a multivariate dataset of associated descriptive IMS morphological parameters, thereby allowing megakaryocyte maturation stage to be quantifiably defined. Whilst manually labelling these quantifications will give a proof and grounding to our quantification, machine learning techniques can also be employed to mine the dataset and determine unbiased categories of IMS morphology.

6.3 LifeAct and CellMask describe IMS in live-cell megakaryocytes

Previously, for fixed megakaryocyte imaging a GP1b-α antibody was used alongside phalloidin to visualise IMS and F-actin. For live cell imaging, hematopoietic stem cells were isolated from mice endogenously expressing LifeAct-GFP for megakaryocyte culturing. To visualise the localisation of live LifeAct-GFP within megakaryocytes, LifeAct-GFP megakaryocytes were fixed and stained with Alexa Fluor-647 GP1b-α antibody. This confirmed that LifeAct-GFP labels F-actin surrounding the IMS with a high contrast (figure 6.1a). Next, different fluorescent dyes were tested to see how well they delineated the IMS. Previously studies have shown that membrane dyes in solution are able to penetrate into the invagination pores on the surface of the plasma membrane and stain the IMS. Various dyes (FM-4-64, FM-1-43, FITC-dextran, HPTS, and CellMask) were added to solution to take advantage of this mechanism and highlight IMS continuous with the plasma membrane.

Within rat megakaryocytes FM dyes were taken up into the IMS, however within murine megakaryocytes there was little signal to noise ratio (Osman et al., 2016). Similarly, FITC-dextran (MW 40,000), failed to penetrate into the IMS with significant signal to

noise ratio, however HPTS and CellMask both highlighted membrane continuous with the plasma membrane of the megakaryocyte (figure 6.1b and 6.1c). To further show the relationship between GP1b-α, F-actin, and IMS continuous with the plasma membrane, CellMask was added to LifeAct expressing megakaryocytes, and both HPTS and CellMask were added to wild-type megakaryocytes. All dyes highlight similar structures within the megakaryocyte, illustrating that the IMS can be defined by either LifeAct or lipid dyes in live-cell experiments. CellMask proved the optimal choice for a lipid dye as it only labelled membrane once bound, whilst HPTS fluoresced in solution.

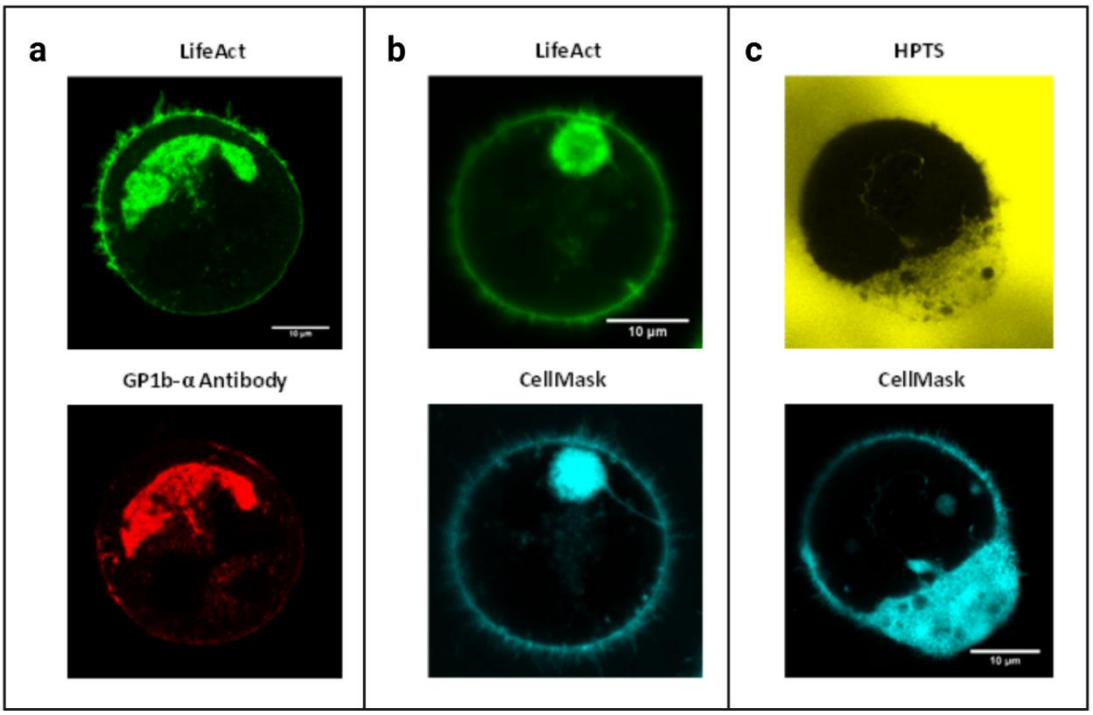


Figure 6.1 - **Live cell dyes for measuring IMS morphology. a)** Fixed megakaryocytes expressing LifeAct and stained with GP1b-α antibody. The LifeAct structure is highly similar to the IMS biomarker GP1b-α, suggesting that F-actin and GP1b-α highlight IMS areas. **b)** Live, LifeAct expressing megakaryocytes stained in solution with CellMask, a membrane impermeable lipid dye. The correlation between the structures suggests that CellMask also labels IMS structures corresponding to both f-actin and GP1b-α, and that these internal IMS membrane structures are continuous with the outer membrane. **c)** Live, wild-type megakaryocytes stained in solution with CellMask and HPTS, another membrane impermeable with pH indicating properties. Both CellMask and HPTS are taken up into different IMS structures. Scale bars are representative of 10 µm.

6.4 Developing an image analysis pipeline for 4D SPIM imaging

SPIM imaging produced vast datasets in excess of 60GB per experimental repeat. Each of these experiments contained two channels (LifeAct and CellMask), 15 to 30 time points, 400 to 1000+ z-slices at 0.3 µm spacing, and a camera size of 3794 x 1006. For processing, initially the dataset was deskewed, after which megakaryocytes needed to be segmented, identified, and labelled within each single SPIM image. To achieve this the LifeAct channel was binarized based on an intensity threshold, with the aim of identifying the actin heavy cell cortex. Different auto-thresholds were applied after a rolling ball background subtraction (radius: 50) to evaluate which best identified whole megakaryocytes. The Huang, Li, Mean and Triangle auto-thresholds worked well to highlight the majority of megakaryocyte structure, and any holes left within megakaryocytes were filled with the 'fill holes' operation before a 'watershed' function was applied to segment individual megakaryocytes. Again, here the heterogeneous intensity of different megakaryocytes served to produce some error. Some megakaryocytes were not entirely identified, leaving broken circles where whole cells should have been found.

Several different automatic solutions to this problem were implemented, but a manual approach seemed to be more efficient. As a result, megakaryocyte masks were manually corrected and labelled in 3D. Following this, centroids of 3D objects were identified, and their coordinates exported into a CSV file and tracked using the ARIVIS software.

Once megakaryocytes had been successfully identified, labelled in 3D, and tracked in 4D, they could be cropped from the raw image to create a library of smaller images containing each individual megakaryocyte. A second round of segmentation was

applied to each megakaryocyte to identify IMS objects. Segmenting individual megakaryocytes within independent images abrogated the effect of homogenous cultures in identifying IMS objects, as each segmentation was relative to the individual megakaryocyte. Once identified, IMS objects were linked in 3D before both the IMS objects and whole megakaryocyte objects were measured (figure 6.2).

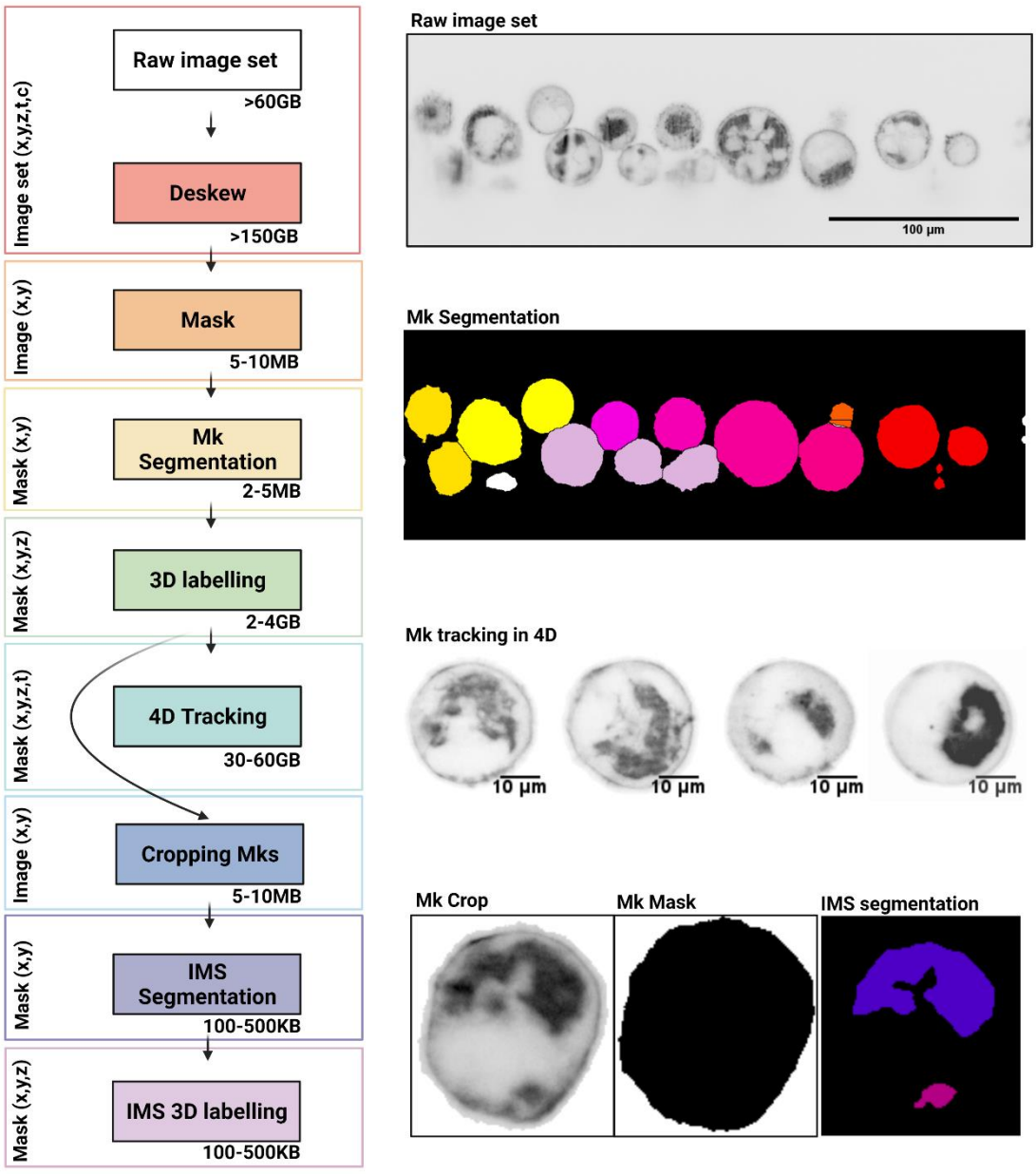


Figure 6.2. **Overview of image analysis pipeline for SPIM imaging.** Murine megakaryocytes were cultured for 2 days then isolated, and imaged for 12 hours from day 2 via iSPIM imaging. Images were deskewed, binarized into a mask with the Triangle auto-threshold, and segmented via morphological operations (colours represent individually segmented megakaryocytes) and a watershed function. Megakaryocyte objects were identified and labelled by measuring object connectivity in 3D before tracking was applied to identify object centroids. Megakaryocyte objects were cropped from the raw image set and individually binarized and segmented to identify heterogeneous IMS independently of other megakaryocytes in culture. Once labelled, 3D IMS objects were measured.

6.5 Defining parameters to describe 3D IMS maturation

As with widefield analysis, the next step was to identify parameters which would define megakaryocyte stage. Since single megakaryocytes had already been isolated and identified, it was possible to measure the megakaryocyte morphology as well as that off the IMS within it. Therefore, to assess megakaryocyte maturation the megakaryocyte volume, megakaryocyte surface area, IMS volume, IMS surface area, IMS integrated density, IMS mean grey value, IMS surface area to volume ratio, and the number of IMS objects within a megakaryocyte were used to define maturation.

Importantly, many megakaryocytes would contain more than a single object. To define a single megakaryocyte the values of the multiple IMS objects within it were either summated (IMS volume, IMS surface area, or IMS integrated density), or where relevant a weighted average of these objects was calculated (IMS surface area to volume ratio, IMS mean grey value).

After defining parameters, bivariate relationships and univariate histograms were plotted (figure 6.3a), and the coefficient of variance was measured to evaluate the variation in the population (figure 6.3b). If megakaryocyte maturation is occurring in the population, then parameters defining IMS are more likely to also have a broad distribution. Equally, to eliminate redundant information in our model, the correlation between parameters was also evaluated (figure 6.4). Parameters which were either a derivative of a second parameter, or showed a high level of correlation were considered for exclusion when using dimensionality reduction and data mining tools for analysis.

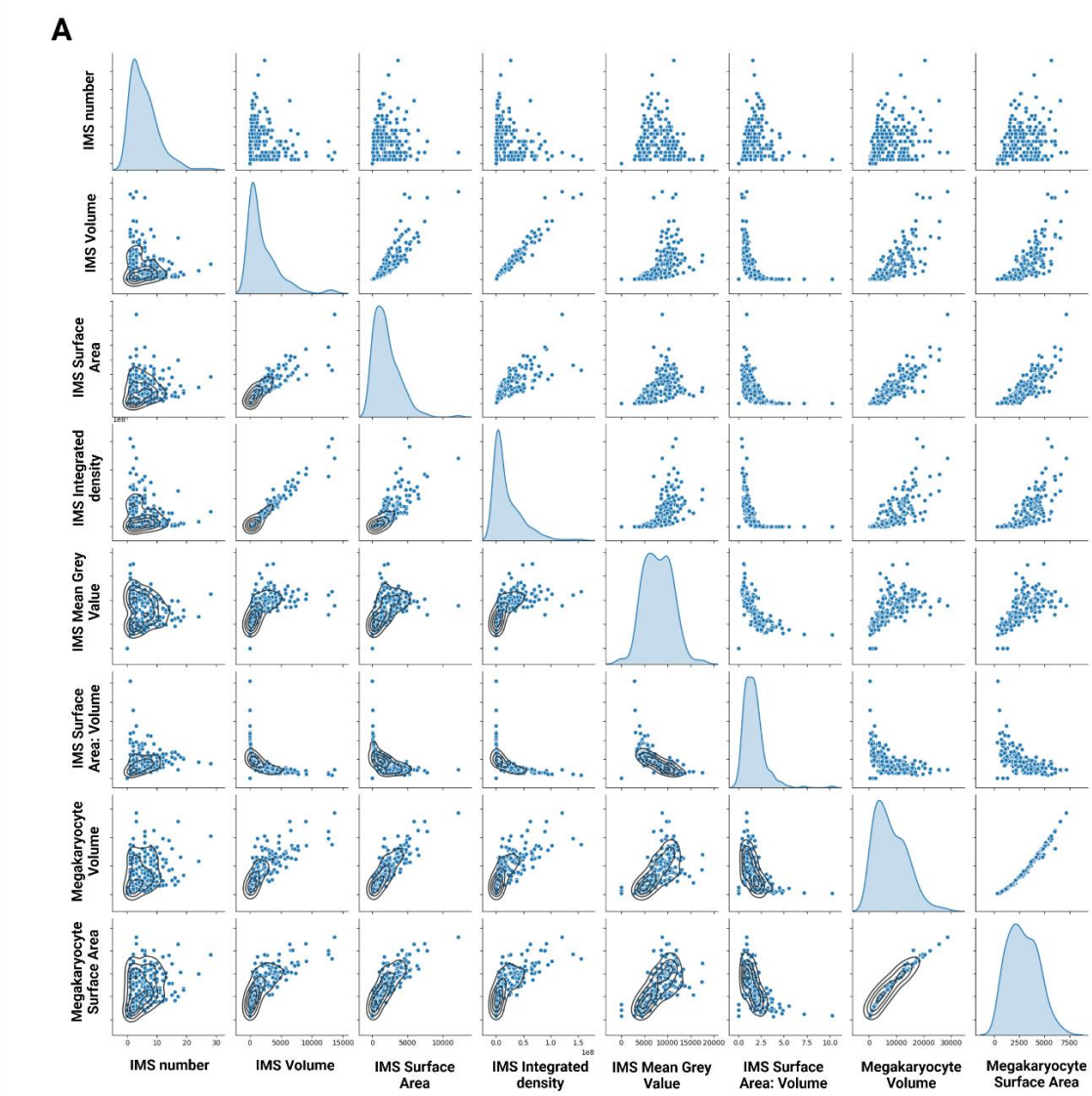


Figure 6.3. **Pair plot and coefficient of variance for parameters.** Murine megakaryocytes were cultured for 2 days then isolated, and imaged for 12 hours from day 2 via iSPIM imaging. Images were segmented and analysed (figure 6.2), before morphology of IMS and megakaryocytes was measured to yield a multivariate dataset. **a)** Pair plot of all parameters to show the bivariate relationships. Importantly, IMS object number increases with IMS mean grey value, then decreases again as IMS becomes heavily dense, and IMS mean grey value peaks and plateaus as megakaryocytes increase in size and integrated density of IMS with a small group of outliers at the peak mean grey value and medium integrated density of volume. **b)** Coefficient of variance of each parameter, showing the distribution of points from the mean. Megakaryocyte volume, megakaryocyte surface area, and IMS volume have the largest variance, with IMS surface area: volume ratio, IMS surface area, and IMS integrated density having the lowest variance. This can also be visualised in the histogram plots shown along the diagonal of the pair plot. Data was taken from one murine megakaryocyte culture, representative of 248 megakaryocytes. Contours represent population density.

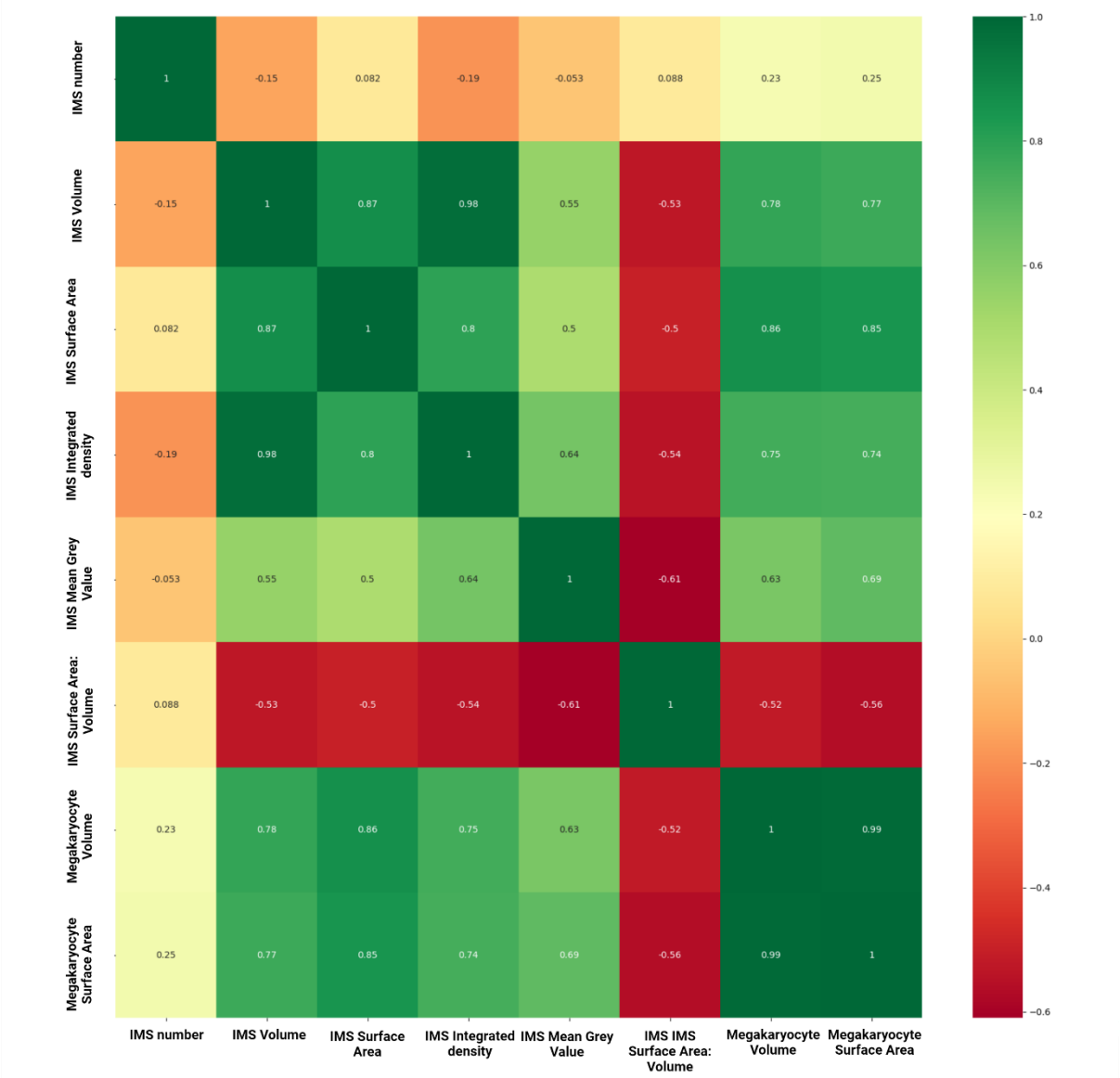


Figure 6.4 **Correlation heat map of iSPIM data.** Murine megakaryocytes were cultured for 2 days then isolated, and imaged for 12 hours from day 2 via iSPIM imaging. Images were segmented and analysed (figure 6.2), before morphology of IMS and megakaryocytes was measured to yield a multivariate dataset. Correlation is indicated by red (negative correlation), and green (positive correlation). Morphological parameters with correlation, may show similar information, and therefore be redundant on our model. Megakaryocyte volume and surface area share a large degree of correlation, as does IMS integrated density and volume. IMS object number appears to share very little correlation with other parameters. Data was taken from one murine megakaryocyte culture, representative of 248 megakaryocytes. Contours represent population density.

6.6 Describing IMS parameter relationships throughout megakaryocyte maturation

Next, the first time point of the dataset was described to understand the relationships between morphological parameters. Data points were colour coded by their manually defined stage to highlight if stages were present within the culture, and if they cluster in different regions of plots (figure 6.5 and 6.8).

Briefly looking at the morphological contents of the culture, it is clear that all stages of megakaryocyte are present, however the culture contains a large number of expanded megakaryocytes (M3), with only a very small fraction of compression megakaryocytes (M2). Furthermore, compression megakaryocytes (M2) observed in prior cultures seemed smaller, with a lower number of IMS objects, and a small IMS volume. Therefore, by manual observation it appears that more mature and developed compression megakaryocytes (M2) are lacking in this culture. Despite this, a large proportion of proplatelets formed, illustrating that the full breadth of stages required for successful megakaryopoiesis is occurring within this culture. Importantly, the different IMS stages group in separate regions of the graphs, despite some overlap. This reinforces that our method of analysis can be used to classify morphological stage.

Looking in more detail at the relationships between parameters defining LifeAct IMS structures, four key relationships can be identified:

1) Integrated density of IMS increases more rapidly over megakaryocyte volume, however, later stages of megakaryocyte (M4, M5, and M6) have a proportionally larger integrated density to megakaryocyte volume (figure 6.6a). This suggests that later

stage megakaryocytes all produce more IMS than megakaryocytes of the same size, indicating a mechanism to increase IMS production within these morphologies.

2) IMS mean grey value increases as megakaryocyte volume increases. However, later stages of megakaryocyte (M4 +) have a much higher mean grey value in comparison to other stages. Interestingly these later stages also occur close to the centre of megakaryocyte volume distribution, with larger megakaryocytes predominantly being expanded megakaryocytes (M3) with a lower IMS mean grey value (figure 6.6b). This shows that throughout megakaryocyte growth, cells can either form highly dense IMS structures, or continue expanding with an increase in IMS integrated density proportional to their volume increase. Furthermore, this also indicates that larger expanded megakaryocytes (M3) are incapable of forming later stages of IMS development (M4 +), and also that a higher IMS mean grey value is indicative of terminally differentiating megakaryocytes. The breadth of megakaryocyte volume that later stages of IMS development (M4 +) inhabit suggests that progress towards these later stages of IMS development and terminal proplatelet formation is rapid.

3) Early-stage megakaryocytes (M1, and M2) have a high IMS surface area to volume ratio, with later stages of megakaryocytes (M4, and M5) having a low IMS surface area to volume ratio. Whilst early-stage megakaryocytes (M1, and M2) have a small IMS volume, their high IMS surface area to volume ratio indicates a lack of IMS compactness (figure 6.6c). A low IMS surface area to volume ratio in later stage megakaryocytes (M4, and M5) suggests that these megakaryocytes have a very compact, or spherical IMS. This reinforces the idea that IMS is contracting and becoming more compact as the megakaryocyte develops.

4) Early (M1) and late-stage (M4, and M5) megakaryocytes have a low number of IMS objects within them, whilst expansion (M3) and compression (M2) megakaryocytes have a low to high number of IMS objects within them (figure 6.6d). This highlights that IMS can appear at multiple locations within a megakaryocyte, but contracts and accumulates at a single region during later stages of megakaryocyte development (M4, and M5), adding to the argument that megakaryocytes form a single polarised IMS region as they progress towards proplatelet formation.

Next, by creating a uniform manifold approximation and projection for dimension reduction (uMAP) plot, the proximity of morphologies based on all parameters in the dataset can be visualised in 2D (figure 6.7a). The uMAP shows a clear progression form early-stage megakaryocytes (M1, and M2) to later stage megakaryocytes (M3 +), reinforcing the current theory of development. However, later stage megakaryocytes (M4 +) are adjacent to expansion megakaryocytes (M3), which again suggests that megakaryocytes either develop into later stage megakaryocytes (M4 +), or continue to expand as expansion megakaryocytes (M3). Random megakaryocytes at each stage were also shown graphically, correlating megakaryocyte structure to the parameter values within a bivariate plot of megakaryocyte volume vs IMS mean grey value (6.7b).

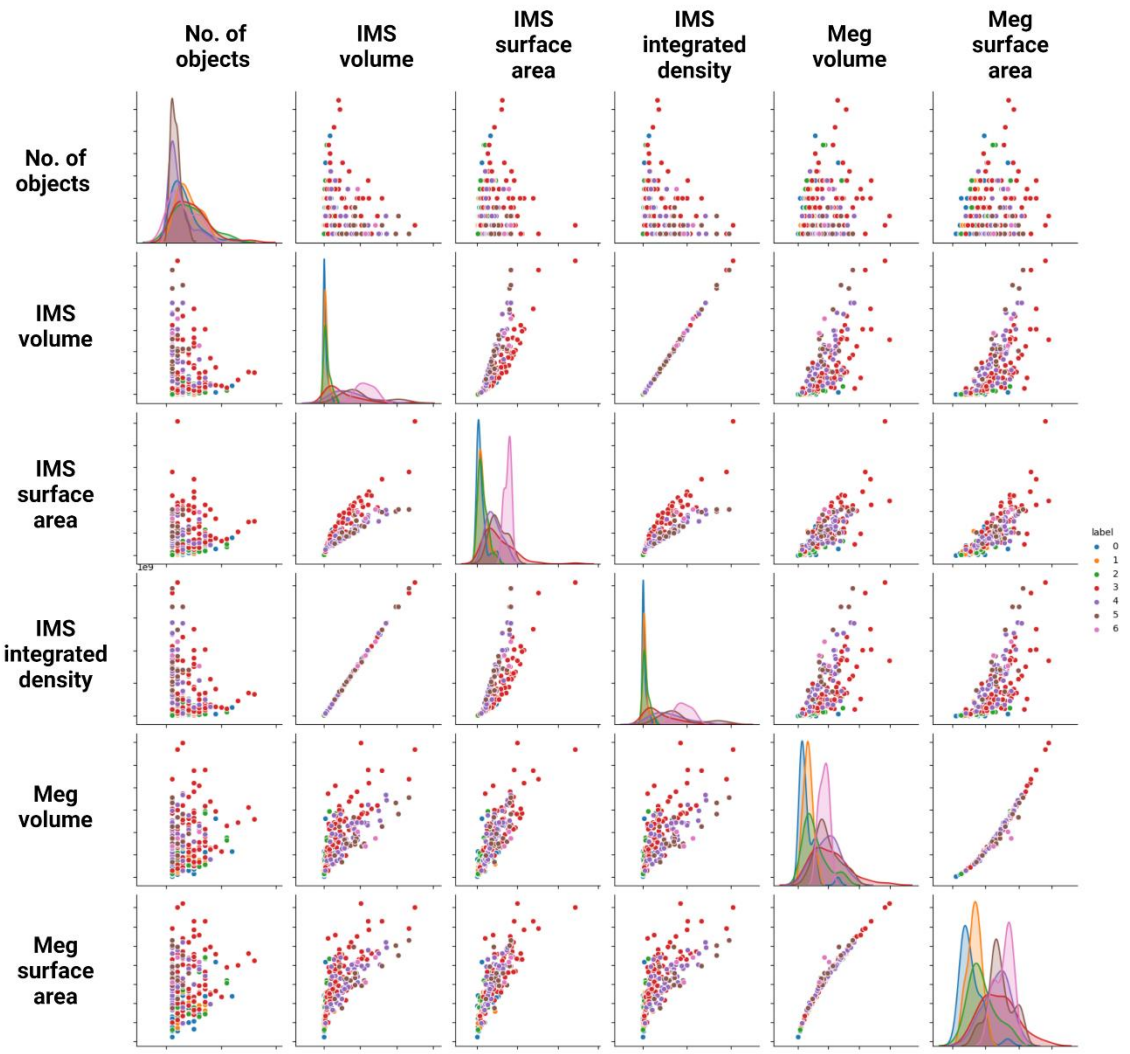


Figure 6.5 **Manual categorisation of LifeAct SPIM at 30 minutes, pair plot.** Murine megakaryocytes were cultured for 2 days then isolated, and imaged for 12 hours from day 2 via iSPIM imaging. Images were segmented and analysed (figure 6.2), before morphology of IMS and megakaryocytes was measured to yield a multivariate dataset. Manual labelling megakaryocyte stage highlights M0 (Blue), M1 (Orange), M2 (Green), M3 (Red), M4 (Purple), M5 (Brown), and M6 (Pink). Stages within the different plots overlap, but clearly congregate in different regions. This emphasises that each manually defined stage is morphologically distinct, and can be defined by the morphological parameters plotted here. Data was taken from one murine megakaryocyte culture, representative of 248 megakaryocytes. Contours represent population density.

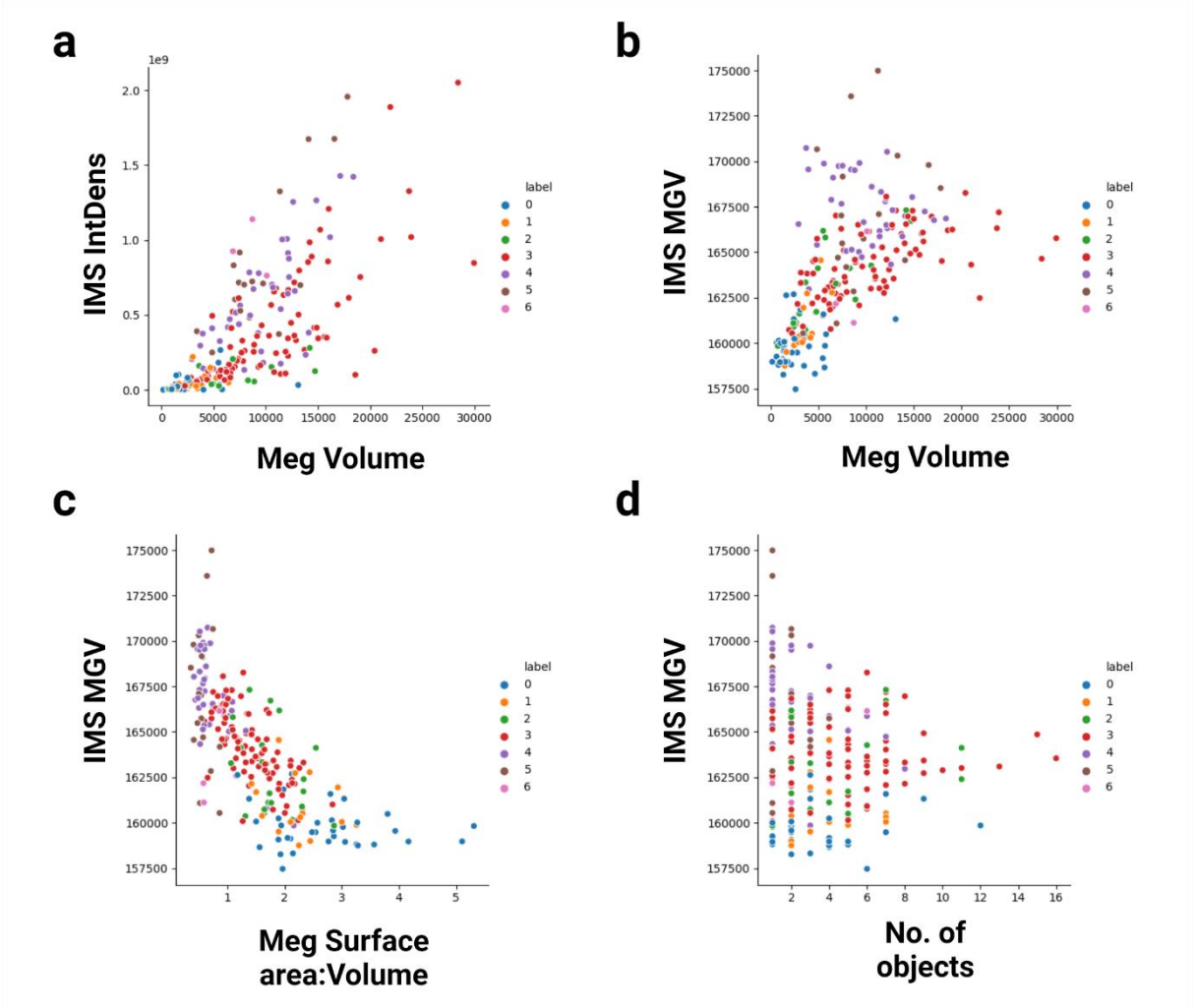


Figure 6.6 **Manual categorisation of LifeAct SPIM at 30 minutes, bivariate relationships.** Murine megakaryocytes were cultured for 2 days then isolated, and imaged for 12 hours from day 2 via iSPIM imaging. Images were segmented and analysed (figure 6.2), before morphology of IMS and megakaryocytes was measured to yield a multivariate dataset. **a)** Megakaryocyte volume vs IMS integrated density. Integrated density increased more rapidly as megakaryocyte volume increased. M4, M5 and M6 are defined by a higher integrated density relative to megakaryocyte volume. **b)** Megakaryocyte volume vs IMS mean grey value. Whilst integrated density increased over megakaryocyte volume, the density of the IMS either plateaus (M3) or increases drastically within a small breadth of megakaryocyte volume (M4, M5 and M6). **c)** IMS surface area to volume ratio vs IMS mean grey value. IMS surface area to volume ratio negatively correlates with IMS stage, with later stages (M4, and M5) having a low IMS surface area to volume ratio, and earlier stages (M1, and M2) having a high IMS surface area to volume ratio. **d)** Number of IMS objects vs IMS mean grey value. Whilst both late (M4, and M5) and early (M1) stages of IMS have a low number of IMS objects, early to middle stages (M2, and M3) can contain many IMS objects. Data was taken from one murine megakaryocyte culture, representative of 248 megakaryocytes.

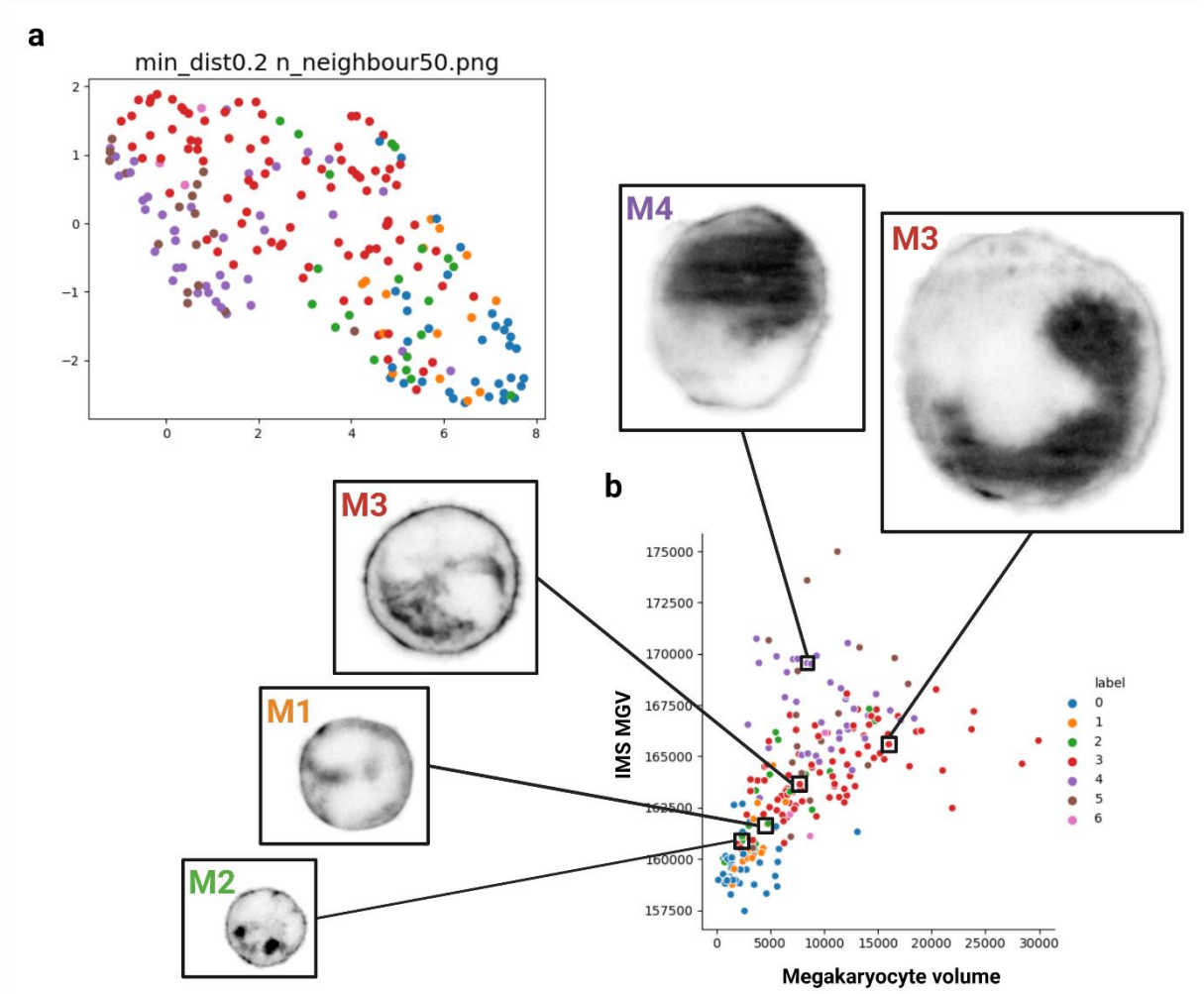


Figure 6.7 **Manual categorisation of LifeAct SPIM at 30 minutes, uMAP.** Murine megakaryocytes were cultured for 2 days then isolated, and imaged for 12 hours from day 2 via iSPIM imaging. Images were segmented and analysed (figure 6.2), before morphology of IMS and megakaryocytes was measured to yield a multivariate dataset. **a)** Uniform manifold approximation and projection for dimension reduction (uMAP) plot of the multivariate dataset, combining IMS volume, IMS surface area, number of IMS objects, IMS integrated density, megakaryocyte volume, and megakaryocyte surface area into a single 2D representation. Minimum distance (0.0, 0.1, 0.2, 0.5, 0.8, 0.99) and nearest neighbour (2, 5, 10, 15, 20, 50, 100, 200) were varied to find the best fitting uMAP. The uMAP supports the theory of IMS maturation, with morphological stages spatial positioned sequentially. Later stages of IMS development (M4 +) are positioned adjacent to expansion megakaryocytes (M3) reinforcing the theory that megakaryocytes either form M4 + stages, or continue to expand and grow as M3 stage cells. **b)** Images of actual megakaryocytes from the dataset correlated to their position in a bivariate plot of megakaryocytes volume vs IMS mean grey value. Early megakaryocytes (M1 and M2) contain sporadic accumulations of IMS, which expands and branches to fill the cell (M3). Megakaryocytes cultures branch to either form dense, polarised megakaryocytes (M4) or continue expanding to form large, expansion megakaryocytes (M3). Data was taken from one murine megakaryocyte culture, representative of 248 megakaryocytes.

When looking at the relationships between parameters defining CellMask IMS structures it is apparent that they behave similarly to LifeAct IMS parameters, demonstrating the close relationships between IMS and F-Actin (figure 6.9). Furthermore, the clear segregation of manual morphological stages also illustrates that structures can be morphologically classified based on both their LifeAct and CellMask defined IMS. The only exception to this rule was CellMask IMS mean grey value, which showed a much greater overlap between manual classifications when compared to LifeAct (figure 6.9b). Polarised (M4) stage megakaryocytes appeared to have a lower relative IMS mean grey value, whilst accumulation (M1) and compression (M2) megakaryocytes appeared to have greater relative IMS mean grey value. CellMask is added to the media and imaging solution, and is taken up through invagination pores on the megakaryocyte plasma membrane. The disparity in IMS mean grey value between CellMask and LifeAct channels may be due to the rate of uptake of CellMask into different morphological stages, and a lack of CellMask saturation after only 30 minutes of incubation and 30 minutes of imaging.

Overall, the various morphological properties of IMS discussed in this subchapter are outlined in figure 6.10.

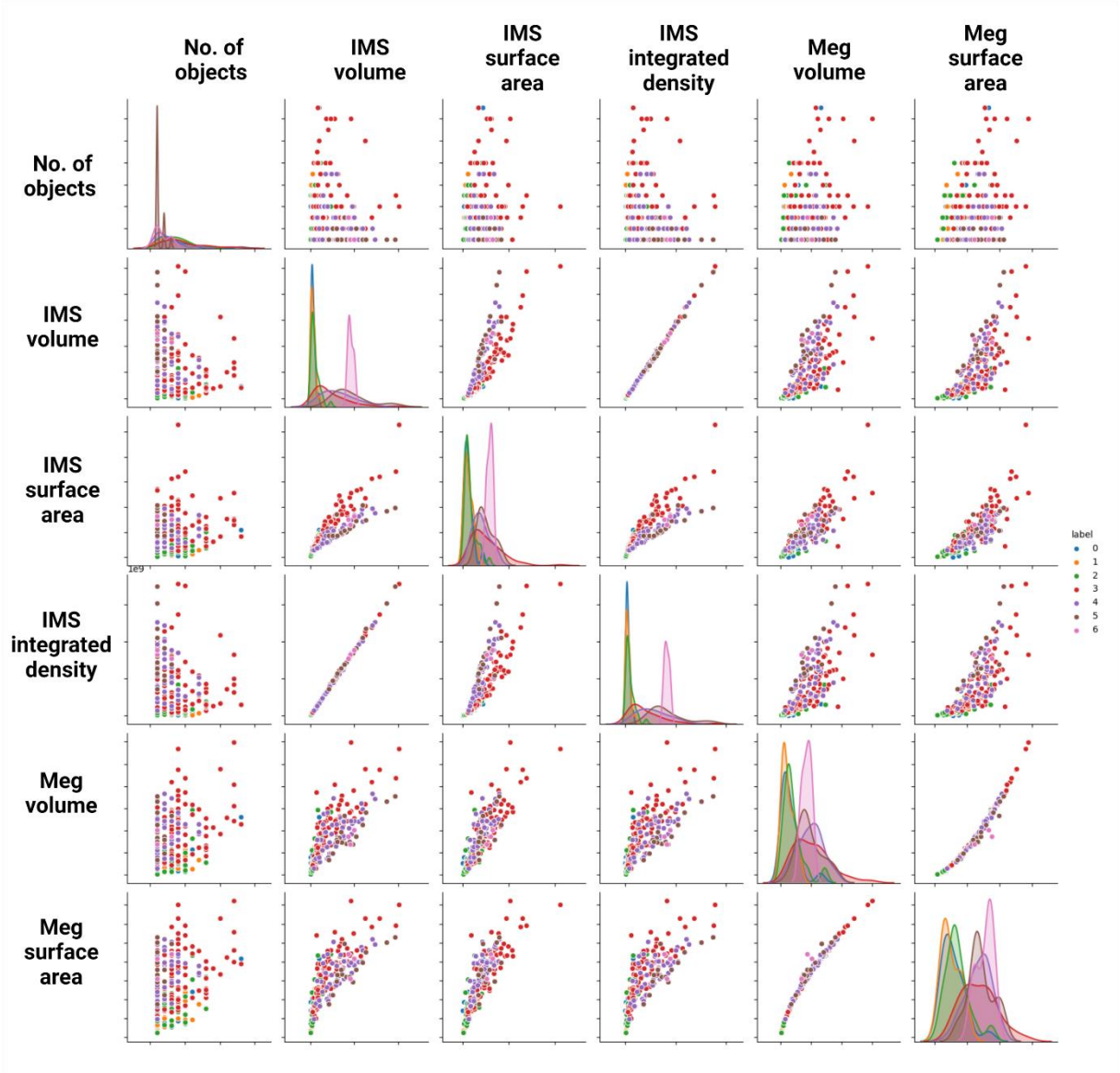


Figure 6.8 **Manual categorisation of CellMask SPIM at 30 minutes, pair plot.** Murine megakaryocytes were cultured for 2 days then isolated, and imaged for 12 hours from day 2 via iSPIM imaging. Images were segmented and analysed (figure 6.2), before morphology of IMS and megakaryocytes was measured to yield a multivariate dataset. Pair plot of number of IMS objects, IMS volume, IMS surface area, IMS integrated density, megakaryocyte volume, and megakaryocyte surface area. Manual labelling megakaryocyte stage highlights M0 (Blue), M1 (Orange), M2 (Green), M3 (Red), M4 (Purple), M5 (Brown), and M6 (Pink). As with LifeAct, IMS stages within the different plots overlap, but clearly congregate in different regions. This emphasises that each manually defined CellMask IMS stage is morphologically distinct, and can be defined by the morphological parameters plotted here. Data was taken from one murine megakaryocyte culture, representative of 248 megakaryocytes.

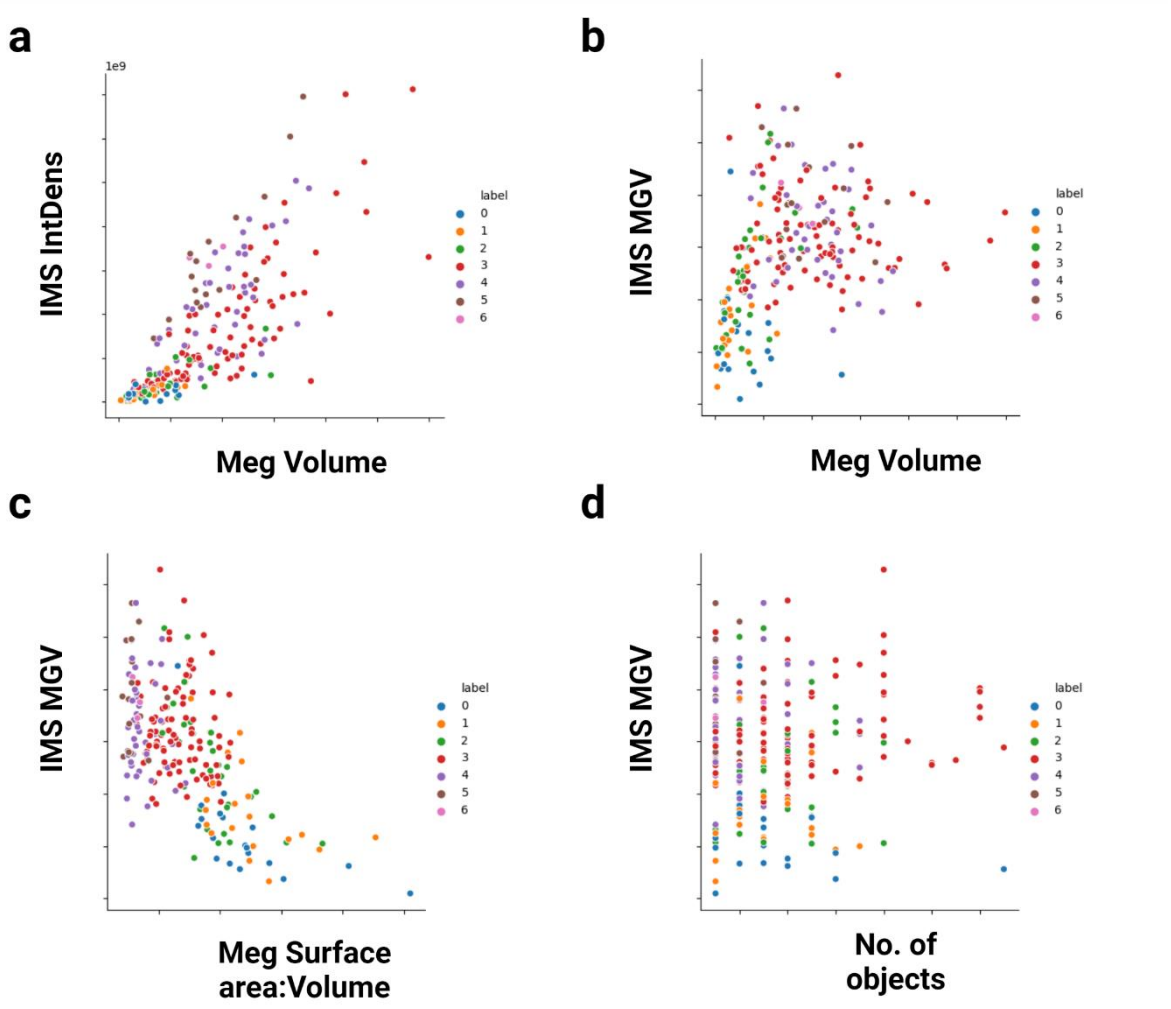


Figure 6.9 **Manual categorisation of CellMask SPIM at 30 minutes, bivariate relationships.** Murine megakaryocytes were cultured for 2 days then isolated, and imaged for 12 hours from day 2 via iSPIM imaging. Images were segmented and analysed (figure 6.2), before morphology of IMS and megakaryocytes was measured to yield a multivariate dataset. **a)** Megakaryocyte volume vs IMS integrated density, **b)** Megakaryocyte volume vs IMS mean grey value, **c)** IMS surface area to volume ratio vs IMS mean grey value, and **d)** Number of IMS objects vs IMS mean grey value. All parameters behave similarly to LifeAct, demonstrating the close relationship between IMS membranes and F-actin. The one exception to this rule was IMS mean grey value, which showed less definition, and more overlap between different manually defined groups. CellMask is added to the media and is taken up my megakaryocytes over time. This disparity in IMS mean grey value may be due to the rate of uptake of CellMask into the different morphological stages, and a lack of CellMask saturation after an hour of incubation. Data was taken from one murine megakaryocyte culture, representative of 248 megakaryocytes.

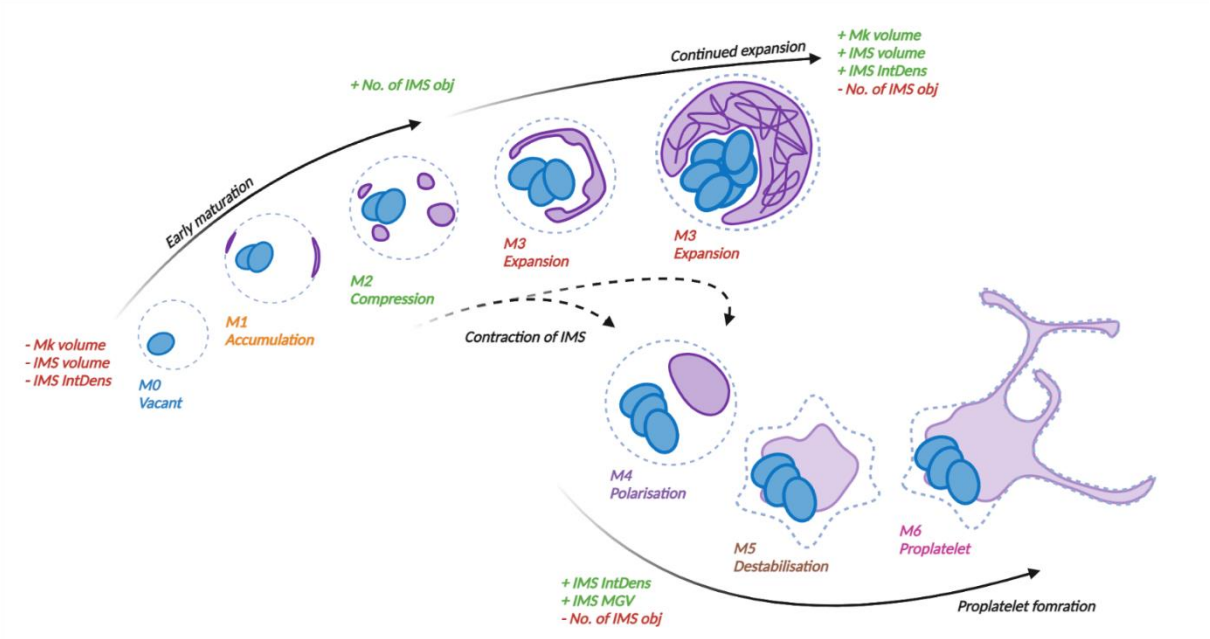


Figure 6.10 **Invaginated membrane system differentiation.** The IMS is initially observed nucleating within the megakaryocyte of small cells, often at more than one location, before expanding into a network of inter-connecting nodes. These megakaryocytes continue to expand in both megakaryocyte and IMS volume. Mature megakaryocytes ($5x10^3$ to $15x10^3$ μm^3) appear to either commit to a proplatelet formation pathway by contracting IMS to a highly dense mass, or continue to expand into even larger and more densely packed megakaryocytes of increasingly higher ploidy. Megakaryocytes appear to differentiate through early maturation towards a continual expansion of the IMS. Within a sub-population of megakaryocytes, IMS appears to contract and polarise preluding proplatelet formation. The lack of larger, polarised megakaryocytes suggests that these two pathways are distinct, and overly expanded megakaryocytes cannot polarise.

6.7 Unsupervised K-means cluster analysis accurately segments developing megakaryocytes into four categories

Groups within multi-variate datasets can be identified in an unbiased manner by using machine learning approaches such as K-means. Initially, an appropriate number of clusters needs to be defined to input into the k-means algorithm. With too many clusters data points of similar values will be incorporated into different clusters,

however with too little clusters data points with different values will be incorporated into the same cluster. The fitting of clusters to a plot can be measured by inertia: the mean distance between each data point and its assigned centroid. An elbow plot displays inertia against the number of clusters and can be used to find the optimum number of clusters for a dataset. This can be found by identifying were the relationship transitions from an exponential decrease in inertia to an even decrease, or the ‘elbow’ of the plot. An elbow plot for actin IMS shows that four clusters is optimal for an unsupervised k-means classification (figure 6.11a).

Looking at how the LifeAct IMS dataset is classified by k-means, clusters have the least overlap when plotting IMS integrated density against megakaryocyte volume, suggesting these two parameters contribute largely to cluster association (figures 6.11 to 6.12).

Furthermore, there was a great deal of overlap observed in manual morphologies within each cluster, especially between cluster 1 and cluster 4. Whilst cluster 1 contained a larger quantity of polarised (M4) megakaryocytes, proportionally cluster 4 contains a similar percentage. Both clusters 1 and 4 also contain a high percentage of proplatelet formation, however this is most likely due to the high variability in proplatelet forming megakaryocytes morphological properties. Overlap between clusters is expected since maturation is a continual process without distinct clusters, and there are a larger number of morphological groups then clusters. However, generally the clusters agree with the manual definitions of our megakaryocytes, partitioning our dataset into early megakaryocytes (cluster 0: M0 ~ 33%, M1 ~ 16%, and M2 ~ 16%), maturing megakaryocytes (cluster 2: M2 ~ 16%, M3 ~ 71%), late megakaryocytes (cluster 3: M3 ~ 60%, M4 ~ 20%, M5 ~ 20%, and M6 ~ 4%), and dense megakaryocytes

(cluster 1: M3 ~ 51%, M4 ~ 45%, and M6 ~ 4%), (figure 6.13b). Furthermore, clustering identifies two distinct populations within our manually defined expansion (M3) megakaryocytes, categorising them into early stage M3 and late stage M3 megakaryocytes (figure 6.13a). This reinforces the idea that megakaryocytes maturate by expanding either receiving a signal for polarisation and forming proplatelet, or continually expanding to expanding without forming proplatelet.

Looking at CellMask IMS, k-means cluster analysis segments the dataset similarly to LifeAct IMS. The slight difference between the clustering of the two channels can be attributed to the variance in integrated density induced by a lack of CellMask saturation (data not shown).

Whilst our manually assigned labels more intimately show segmentation of megakaryocyte morphological stage with more distinct categorise (proven by simply observing the distinct positioning of each manually categorised megakaryocytes in the data set) cluster analysis segmentation provides an accurate description of megakaryocyte maturation and can be used for quick, coarse measurements without the need for labour intensive manual observations (figures 6.13).

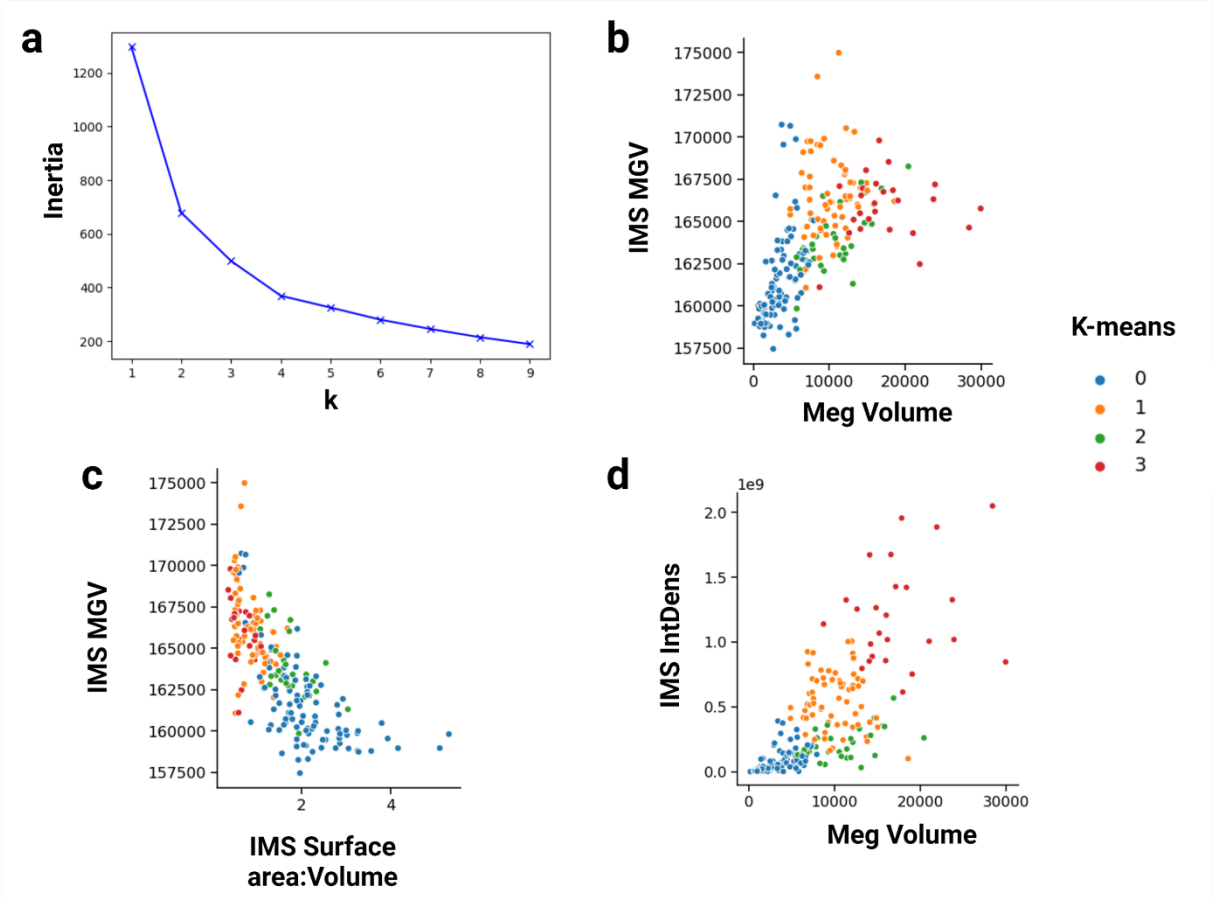


Figure 6.11 **K-means categorisation of LifeAct SPIM at 30 minutes, bivariate relationships.** Murine megakaryocytes were cultured for 2 days then isolated, and imaged for 12 hours from day 2 via iSPIM imaging. Images were segmented and analysed (figure 6.2), before morphology of IMS and megakaryocytes was measured to yield a multivariate dataset. K-means cluster analysis was then used to categorise data points into four clusters. **a)** Number of clusters (k) vs inertia. **b)** Megakaryocyte volume vs IMS mean grey value. **c)** IMS surface area to volume ratio vs IMS mean grey value. **d)** Megakaryocyte volume vs IMS integrated density. Data was taken from one murine megakaryocyte culture, representative of 248 megakaryocytes.

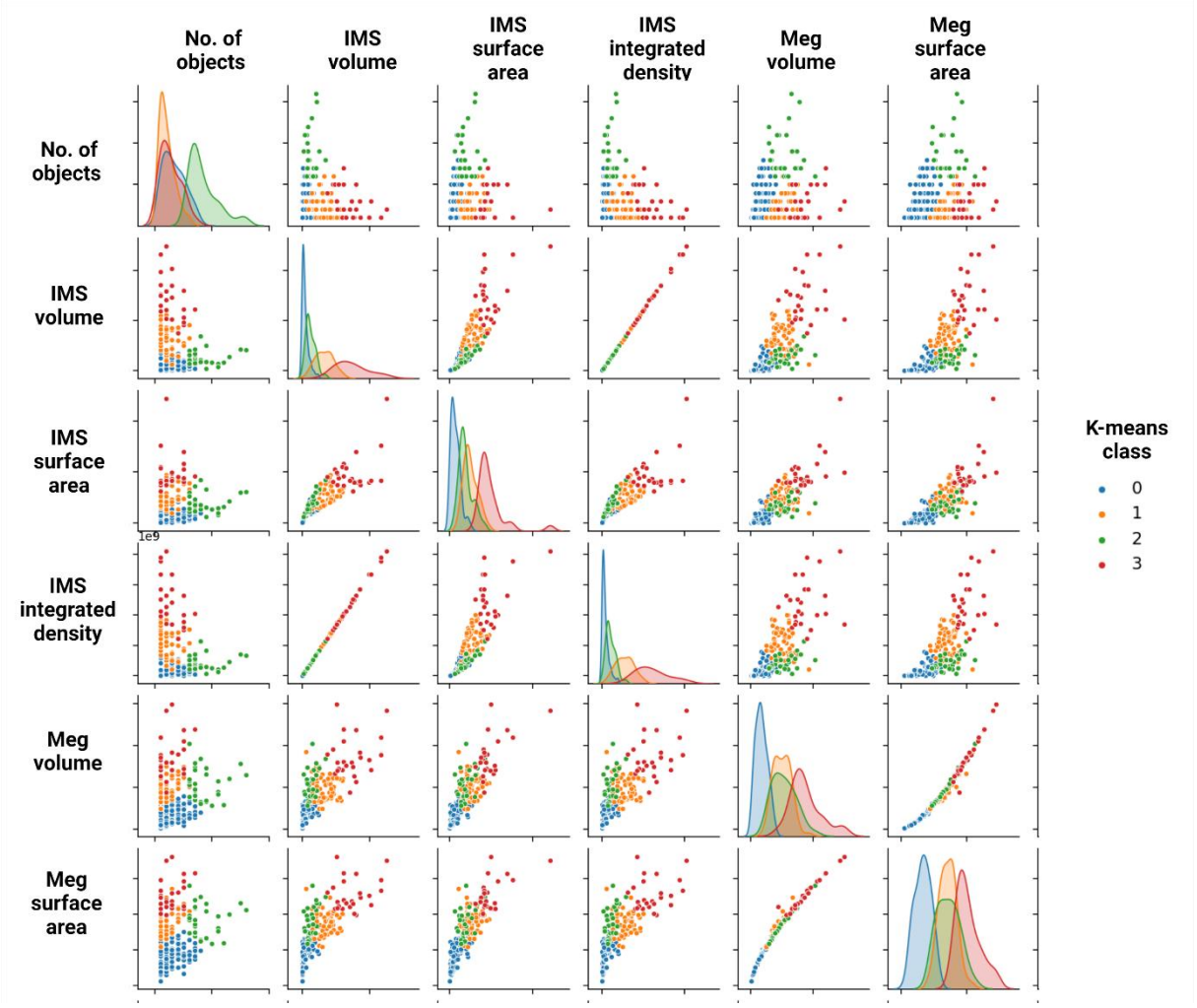


Figure 6.12 **K-means categorisation of LifeAct SPIM at 30 minutes, pair plot.** Murine megakaryocytes were cultured for 2 days then isolated, and imaged for 12 hours from day 2 via iSPIM imaging. Images were segmented and analysed (figure 6.2), before morphology of IMS and megakaryocytes was measured to yield a multivariate dataset. K-means cluster analysis was then used to categorise data points into four clusters. **a)** Number of IMS objects, IMS volume, IMS surface area, IMS integrated density, megakaryocyte volume, and megakaryocyte surface area. K-means was plotted assuming 4 clusters. Data was taken from one murine megakaryocyte culture, representative of 248 megakaryocytes.

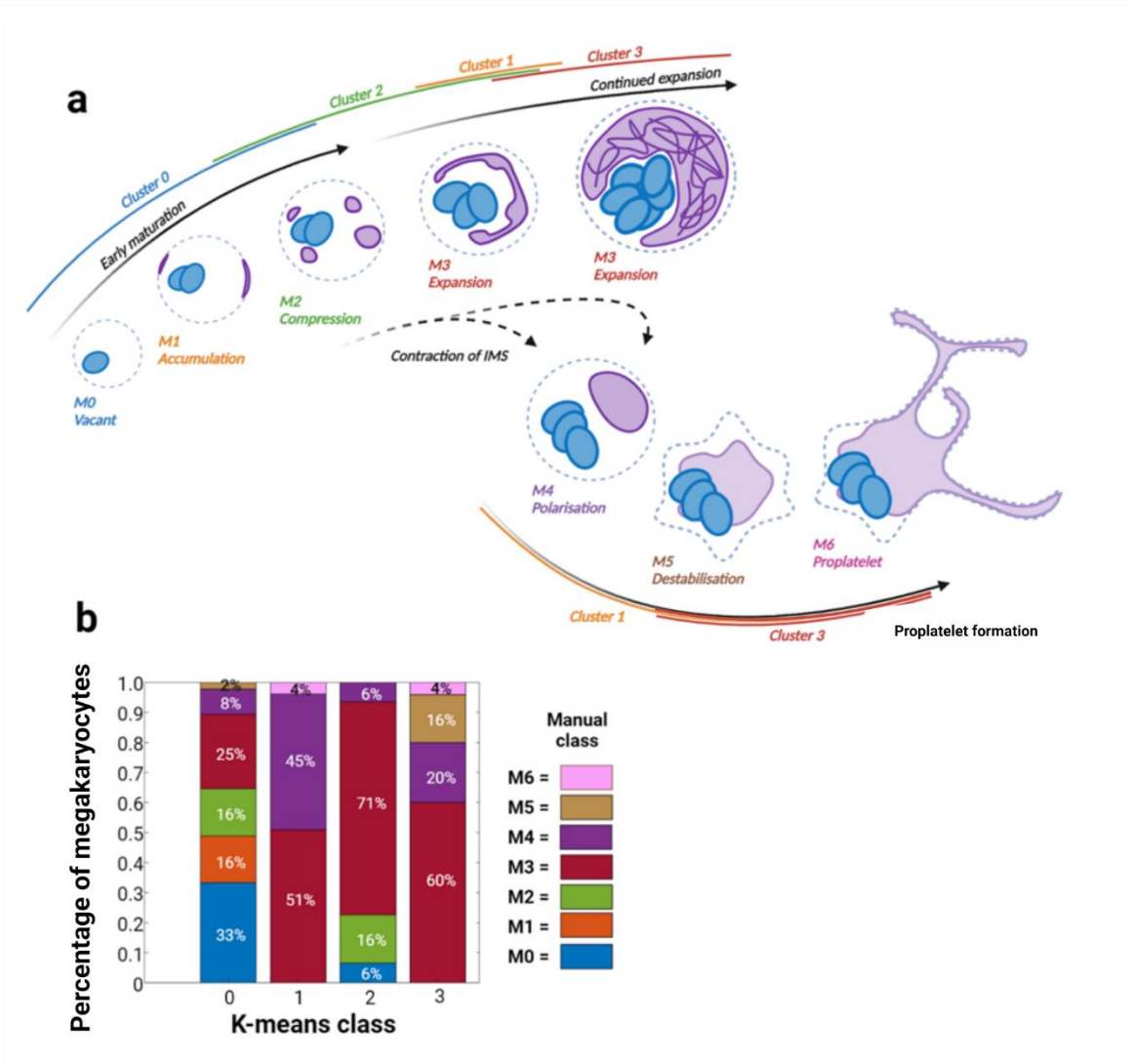


Figure 6.13 **IMS differentiation with k-means segmentation.** Murine megakaryocytes were cultured for 2 days then isolated, and imaged for 12 hours from day 2 via iSPIM imaging. Images were segmented and analysed (figure 6.2), before morphology of IMS and megakaryocytes was measured to yield a multivariate dataset. **a)** Clusters overlaid on megakaryocyte maturation. Clusters accurately segment megakaryocyte maturation in accordance with manual morphological labelling. **b)** Cluster content of manually labelled groups. Whilst there is a great deal of overlap between manually morphological groups within clusters, this is expected due to the continuous nature of megakaryopoiesis, and the smaller number of clusters than manually defined groups. Significantly, expansion (M3) broach all groups, with a higher percentage in cluster 2 and 3. Polarised megakaryocytes (M4) appear in both cluster 1 and 3, but at a higher percentage within cluster 1. Broadly, these clusters define early megakaryocytes (cluster 0), polarised/pre-proplatelet megakaryocytes (cluster 1), maturing megakaryocytes (cluster 2), and late megakaryocytes (cluster 3). Data was taken from one murine megakaryocyte culture, representative of 248 megakaryocytes.

6.8 Exploring the dynamics of IMS morphological transitions throughout megakaryocyte development

Next, individual time points of the SPIM acquisition were measured to find the change in manually defined and k-means derived labels over time. By measuring the quantity of each classification, and the changes in classification occurring between individual megakaryocytes per time point, the rates of change in morphologies could be predicted.

Looking at the change in quantity of LifeAct k-means defined clusters, similar conclusions can be drawn (figure 6.14a):

1) Early megakaryocytes (cluster 0) also decreases over time.
2) Maturing megakaryocytes (cluster 2) stay consistent in quantity whilst late megakaryocytes (cluster 3) increase in quantity. Suggesting whilst megakaryocytes mature from towards polarisation (cluster 1) and continued expansion (cluster 3), the pool of mature megakaryocytes (cluster 2) are replenished from early megakaryocytes (cluster 0).
3) Polarised megakaryocytes (cluster 1) decrease in quantity, suggesting that polarised megakaryocytes are progressing terminally towards proplatelet formation.

Looking at the change in quantity of manually defined LifeAct IMS morphologies over time, several relationships can be drawn (figure 6.14b):

1) Early megakaryocytes (M0, and M1) decrease in quantity whilst maturing megakaryocytes (M2, and M3) increase in quantity, indicating that there is a shift of early megakaryocytes to more mature and expanded megakaryocytes.

2) Likewise, whilst M6 increases in quantity over time, M5 and M4 decrease in quantity suggesting a movement of megakaryocytes from polarised morphologies either towards proplatelet forming megakaryocytes or back towards expansion megakaryocytes.

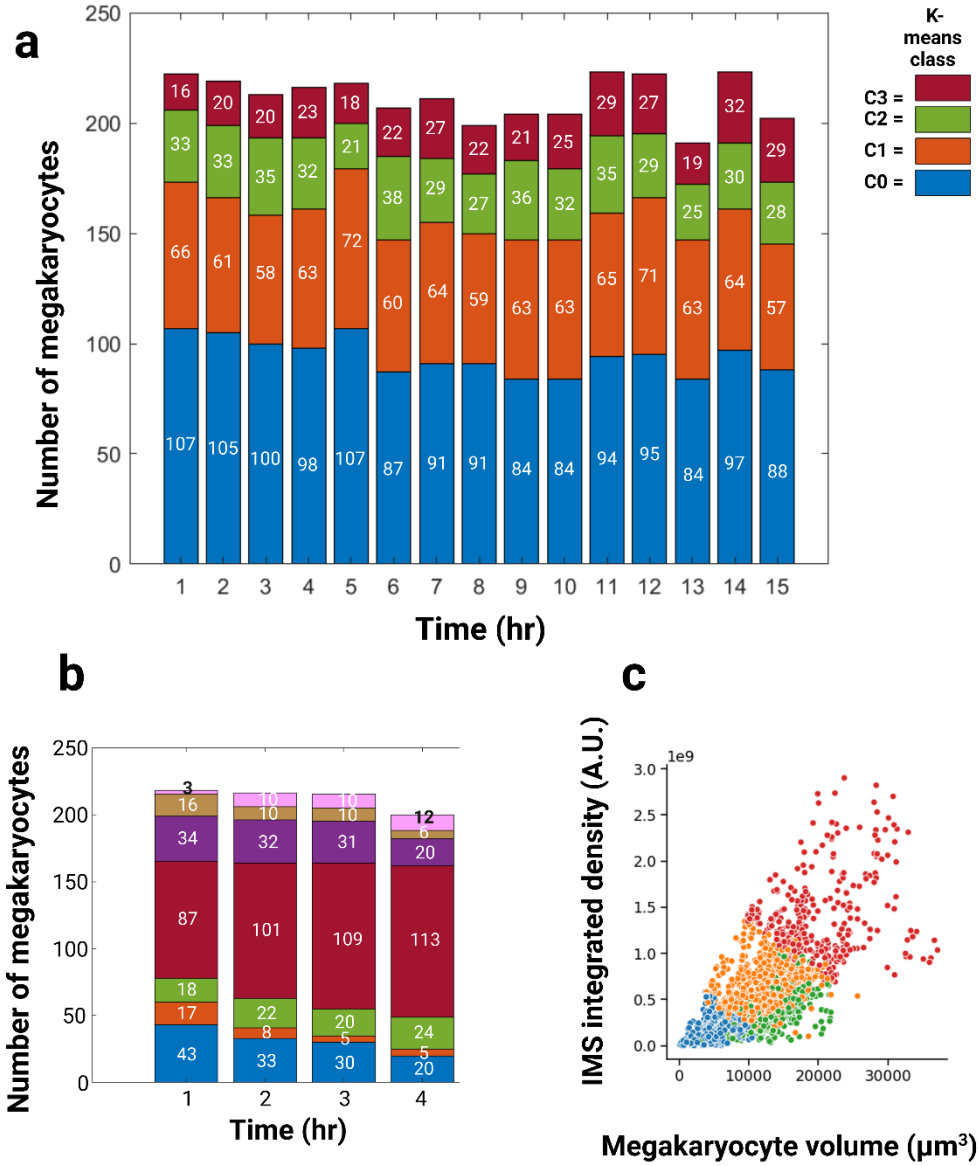


Figure 6.14 **Quantification of LifeAct IMS differentiation over time.** Murine megakaryocytes were cultured for 2 days then isolated, and imaged for 12 hours from day 2 via iSPIM imaging. Images were segmented and analysed (figure 6.2), before morphology of IMS and megakaryocytes was measured to yield a multivariate dataset. K-means cluster analysis was then used to categorise data points into four clusters. **a)** K-means defined clusters illustrates a similar result to the manually defined clusters, with early megakaryocytes (cluster 0) decreasing in number while late megakaryocytes (cluster 3) increase. Polarised megakaryocytes (cluster 1) also decrease in number, suggesting a progression towards proplatelet formation. Meanwhile, maturing megakaryocytes (cluster 2) stay proportionally the same, suggesting that whilst megakaryocytes are lost to polarisation and continued expansion, the pool is replenished by early megakaryocyte maturation. **b)** Quantification of manually defined stages of morphology. Vacant megakaryocytes (M0) and accumulation megakaryocytes (M1) decrease in number consistently, whilst maturing megakaryocytes (M2 and M3) accumulate. This reinforces the idea of a pool of expansion megakaryocytes (M3) which either polarise or terminally expand. Polarised megakaryocytes (M4) and destabilised megakaryocytes (M5) decrease in quantity as proplatelet forming megakaryocytes increase (M6), suggesting that these populations are progressing towards terminal proplatelet formation. **c)** IMS integrated density vs megakaryocyte volume for data points across all time points. Data was taken from one murine megakaryocyte culture, representative of 248 megakaryocytes.

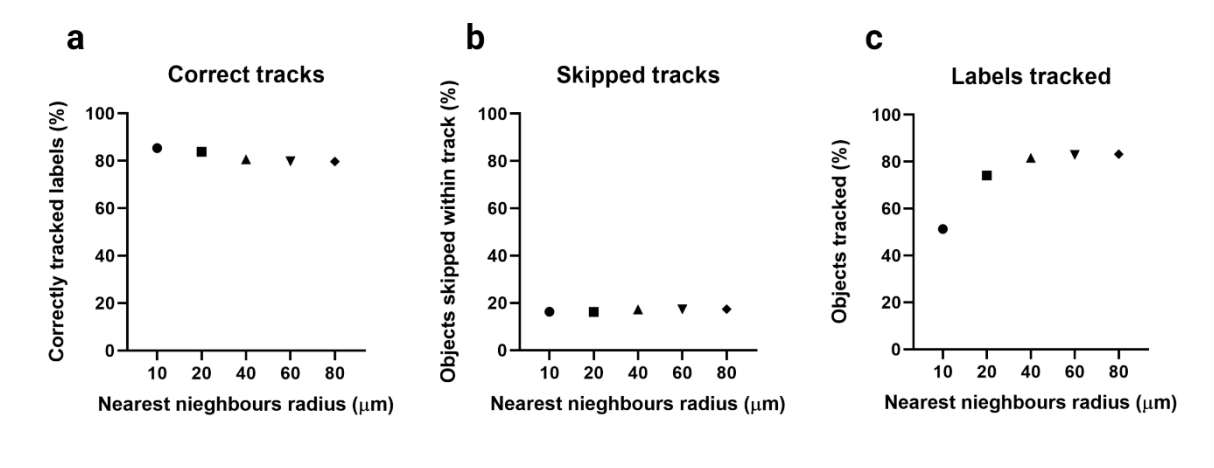


Figure 6.15 **ARIVIS tracking efficiency over time lapse images.** Murine megakaryocytes were cultured for 2 days then isolated, and imaged for 12 hours from day 2 via iSPIM imaging. Images were segmented and analysed (figure 6.2), before morphology of IMS and megakaryocytes was measured to yield a multivariate dataset. After segmentation, labelled objects were tracked throughout the time-lapse with ARIVIS. **a)** The percentage of correct tracks compared to manually tracked cells stays between 80% and 90% for each nearest neighbours distance, with 10 and 20 µm providing a marginally higher efficiency. **b)** The percentage of megakaryocytes skipped within a single track stayed around 15 to 20% for each nearest neighbours distance, with 10 and 20 µm containing the least number of skipped megakaryocytes. **c)** The number of megakaryocytes tracked within the cultures increased drastically from 50 to 80% between 10 and 40 µm nearest neighbours. Together these results suggest that a nearest neighbours of 60 µm provides the highest number of megakaryocytes tracked, with the highest compromise in tracking efficiency. Data was taken from one murine megakaryocyte culture, representative of 248 megakaryocytes.

For tracking, a nearest neighbour value between 10 and 80 µm was used in the tracking algorithm to test the efficiency for tracking megakaryocytes against a manually labelled test dataset (figure 6.15). Whilst a low nearest neighbour value gave a high percentage of correctly tracked megakaryocytes and a low percentage of skipped megakaryocytes within each track, the number of megakaryocytes tracked within the culture drastically increased from 50% to 80% between a nearest neighbour distance of 10 and 40 µm. Therefore, a value of 60 µm was chosen.

Once tracked, the transitions between IMS morphological stage within single megakaryocytes can be observed. In both manual, and k-means defined morphological stage, megakaryocytes appear to transition backwards and forwards.

Describing these backwards events in manually labelled LifeAct megakaryocytes (figure 6.16a):

1) Initially, vacant megakaryocytes (M0) are capable of transitioning towards accumulation, compression, and expansion megakaryocytes, with the majority travelling towards compression and expansion. Likewise, accumulation megakaryocytes (M1) and compression megakaryocytes (M2) transfer towards expansion megakaryocytes (M3), with a small minority of compression megakaryocytes (M2) going straight towards polarisation (M4). In general, megakaryocytes appear to be able to bypass these first few stages of IMS morphology, indicating that there are either several different mechanisms of IMS invagination, our system is unable to fully detect IMS invagination, or that IMS invagination is a very rapid process that occurs within the hour-long imaging intervals.
2) After megakaryocytes reach their compression (M2) and expansion phase (M3) transitions are limited, with the majority of transitions directed towards the morphological stage directly above it. This suggests that expansion (M3), polarisation (M4) and destabilization (M5) are all deliberate and necessary processes for forming proplatelets, and that megakaryocytes rarely form polarised megakaryocytes directly from compressed megakaryocytes. Therefore, rather than a biochemical pathway for directed polarisation occurring earlier in megakaryocyte differentiation, it appear that polarisation is triggered during the expansion phase.

Again, megakaryocytes also undergo transitions backwards in morphological stage, an event that seems unlikely to be productive *in situ*. This may be due the inherent

human error in manually labelling a megakaryocyte at each time point, or it may be due to the effects of *in vitro* culturing of megakaryocytes. Describing these backwards events in manually labelled megakaryocytes (6.16b):

1) Accumulated (M1), compressed (M2), expanded (M3), and polarised (M4) megakaryocytes can transition back to vacant cells, possibly highlighting cell death, or unhealthy megakaryocytes within the culture.
2) A smaller number of megakaryocytes transition back directly to the morphological stage bellow them, but the major backwards transition is between polarised megakaryocytes (M4), and expansion megakaryocytes (M3). This suggests that whilst megakaryocytes must polarise to form proplatelets, they are not committed to proplatelet formation until destabilisation (M5), and can revert to a pre-polarised state.

Transitions between K-means classified groups are much less definite, with a great deal more flux between all clusters (figure 6.16a and b):

1) Whilst there is a slight flow from early megakaryocytes (cluster 0) towards polarised (cluster 1), and late (cluster 3) megakaryocytes, maturing megakaryocytes (cluster 2) remain relatively unchanged throughout the time lapse, with equal flux from all other clusters. This shows that C2 megakaryocytes freely change between early, late, or polarised megakaryocytes. The small size of the cluster most likely contributes to this inaccuracy.
2) Interestingly, only a small minority of megakaryocytes transition towards late megakaryocytes (cluster 3), with the majority of early megakaryocyte (cluster

0), and maturing megakaryocytes (cluster 2) traversing towards polarisation (cluster 1).

Lastly, the rates of megakaryocyte parameter change was measured between all megakaryocytes of each k-means defined clusters. In general, as with the transition change between clusters, the rate change of megakaryocytes has a highly variable (figure 6.17a to f). However, when looking at mean rates of change, the values better reflect what is expected within the clusters (figure 6.17g). Importantly, the megakaryocyte volume and surface area reflects the maturity of the megakaryocyte, and can be used as a proof for the dataset, with larger, more ploidy megakaryocytes undergoing a more rapid increase in megakaryocyte volume and surface area. Looking at the change in IMS parameters however, more can be said about the mechanisms and rates at each k-means defined stage:

1) Early megakaryocytes (cluster 0) show the smallest increase in IMS volume (0.33 $\mu m^3 min^{-1}$) as well as IMS integrated density ($5.2x10^4$ A.U. min^{-1}), whilst late megakaryocytes (cluster 3) show a much larger increase in both IMS volume (1.65 $\mu m^3 min^{-1}$) and integrated density ($3.4x10^5$ A.U. min^{-1}).
2) Maturing megakaryocytes (cluster 2) show a drastic increase in IMS volume (3.92 $\mu m^3 min^{-1}$), IMS integrated density ($6.6x10^5$ A.U. min^{-1}), and even megakaryocyte volume (17.47 $\mu m^3 min^{-1}$) highlighting a drastic IMS increase in a cluster 2.
3) Polarised megakaryocytes (cluster 1) on the other hand actually showed a decrease in both IMS volume (-0.86 $\mu m^3 min^{-1}$) and IMS integrated density ($-1.2x10^5$ A.U. min^{-1}). The decrease in integrated density may be misleading. Integrated density is a summation of all grey values for the IMS volume, and

so a decrease in IMS volume will lead to a decrease in integrated density. However, the mean grey value of the remaining volume may still be increasing, reflecting the contraction of the IMS.

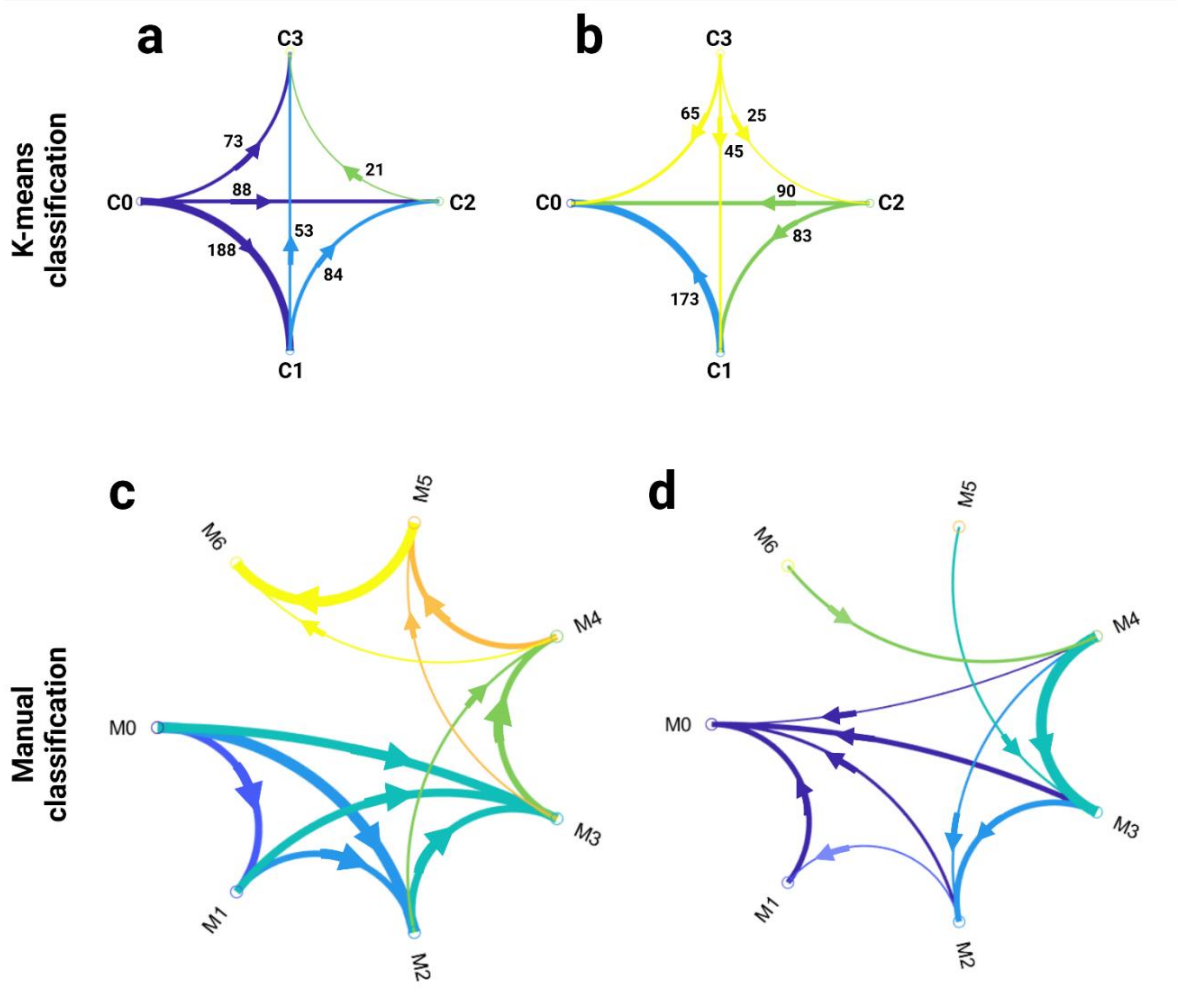
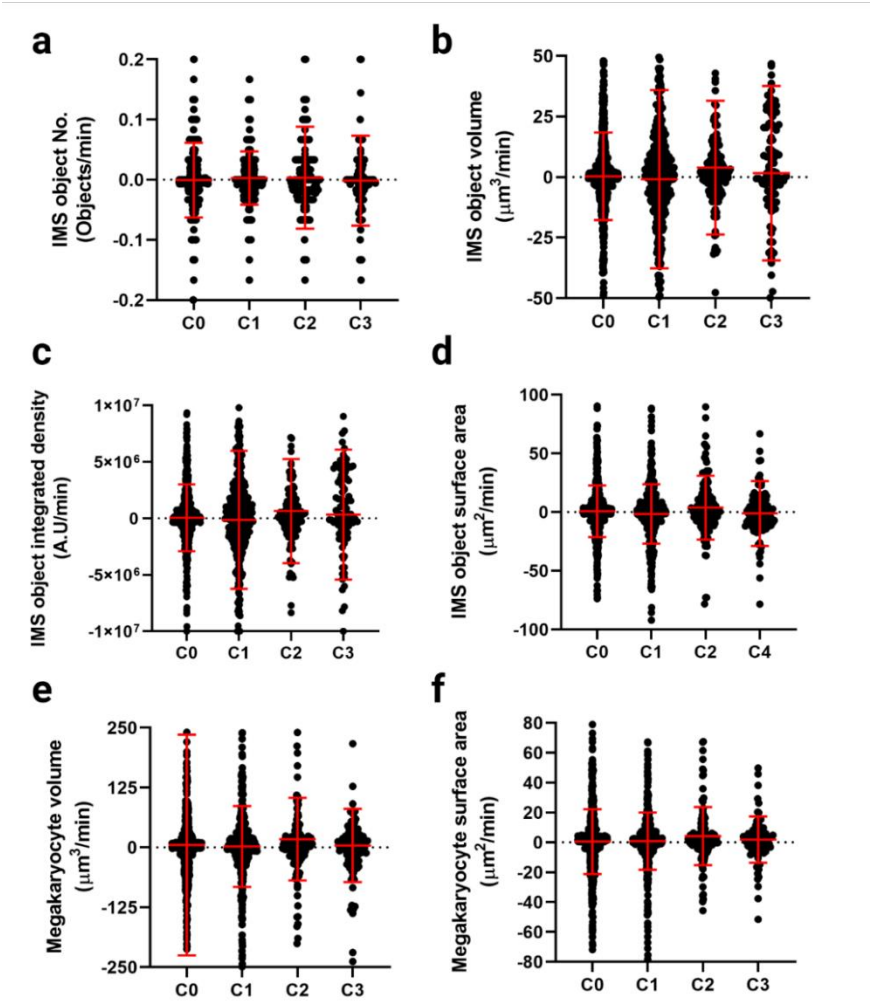


Figure 6.16 **Transitions of morphology over time.** Murine megakaryocytes were cultured for 2 days then isolated, and imaged for 12 hours from day 2 via iSPIM imaging. Images were segmented and analysed (figure 6.2), before morphology of IMS and megakaryocytes was measured to yield a multivariate dataset. K-means cluster analysis was then used to categorise data points into four clusters. **a)** Manual morphological stages progress forwards towards proplatelet formation (M6). Vacant (M0), accumulation (M1), and compression megakaryocytes (M2) progress towards expansion megakaryocytes (M3). Thereafter, megakaryocytes progress through polarisation (M4), and destabilisation (M5) towards proplatelet formation (M6). **b)** Manual morphological stages also progress backwards. Whilst many accumulation (M1), compression (M2), and expansion (M3) megakaryocytes transition backwards to vacant megakaryocytes, suggesting unhealthy cells in the culture, the majority of backwards transitioning is between polarised (M4) and expansion (M3) megakaryocytes. **c)** K-means shows a similar pattern to manual labelling for forward transitioning of morphological stage. Early megakaryocytes (cluster 0) transition towards polarised (cluster 1), maturing (cluster 2) and, late megakaryocytes (cluster 3), however the majority progress towards polarisation (cluster 1). A minority of megakaryocytes transition towards late megakaryocytes (cluster 3). **d)** K-means clusters transition backwards, almost as much as they do forwards. Data was taken from one murine megakaryocyte culture, representative of 248 megakaryocytes.



g

	Invaginated Membrane System				Megakaryocytes	
	No. objects	Volume	SA	IntDens	Volume	SA
0	$6x10^{-4}$	0.33	0.79	$5.2x10^{4}$	1.35	0.56
1	$6x10^{3}$	-0.86	-1.54	$-1.2x10^{5}$	2.15	0.88
2	$3x10^{3}$	3.92	3.84	$6.6x10^{5}$	17.47	4.23
3	$2x10^{-3}$	1.65	-1.16	$3.4x10^{5}$	4.13	1.86

Figure 6.17 **Rates of morphological parameter change within k-means defined clusters.** Murine megakaryocytes were cultured for 2 days then isolated, and imaged for 12 hours from day 2 via iSPIM imaging. Images were segmented and analysed (figure 6.2), before morphology of IMS and megakaryocytes was measured to yield a multivariate dataset. K-means cluster analysis was then used to categorise data points into four clusters. **a-f)** Populations of individual morphological parameters illustrate the variance in morphological change over time, with many megakaryocytes decreasing and increasing in value. **g)** By taking the mean value of each parameter population, a meaningful result is obtained. Megakaryocyte volume and surface area increase can be used as a proof for the dataset. Early (cluster 0) and late (cluster 3) megakaryocytes show expected values of IMS increase relative to the megakaryocyte size. Maturing megakaryocytes (cluster 2) exhibit a drastic increase in IMS volume, IMS integrated density, and megakaryocyte volume. Suggesting that this population undergoes a rapid maturation towards either polarisation or maturation. Data was taken from one murine megakaryocyte culture, representative of 248 megakaryocytes.

6.9 Investigating the ultrastructure of IMS morphological stages

Throughout development the IMS is interlaced with fine tubules, suggesting that the IMS is comprised of a network of tubules which congregate to form the macro structures seen with diffraction limited microscopy techniques. Interestingly, when looking at early stages of megakaryocyte development we observe that this tubule network intersects at many nodes or loci of varying size. As megakaryocytes increase in size, these loci appear to also grow in size and number, suggesting that compression stages are formed by a contraction of the IMS tubule network (figure 6.18 and 6.19).

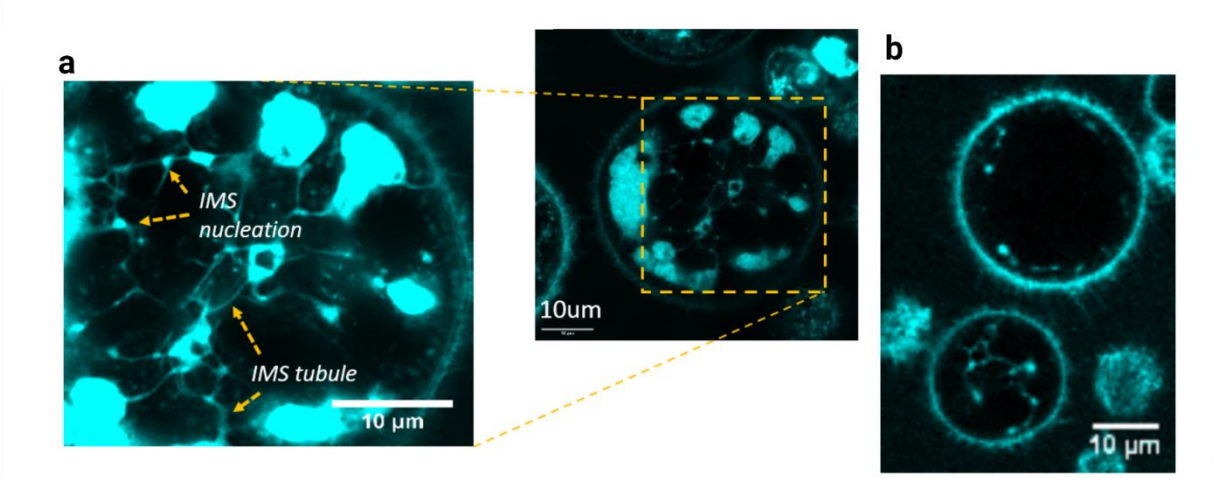


Figure 6.18 **IMS thread work and compression.** Murine megakaryocytes were cultured and isolated at either day 1 or 3 of culture. Live megakaryocytes were stained with CellMask to highlight IMS. **a)** IMS is interlinked by a network of tubules. At intersections or branches of these tubules, nodes appear. **b)** IMS network of tubules in early megakaryocytes highlights that IMS tubules and node appear before, or develop into compression events. Representative of three murine megakaryocyte cultures.

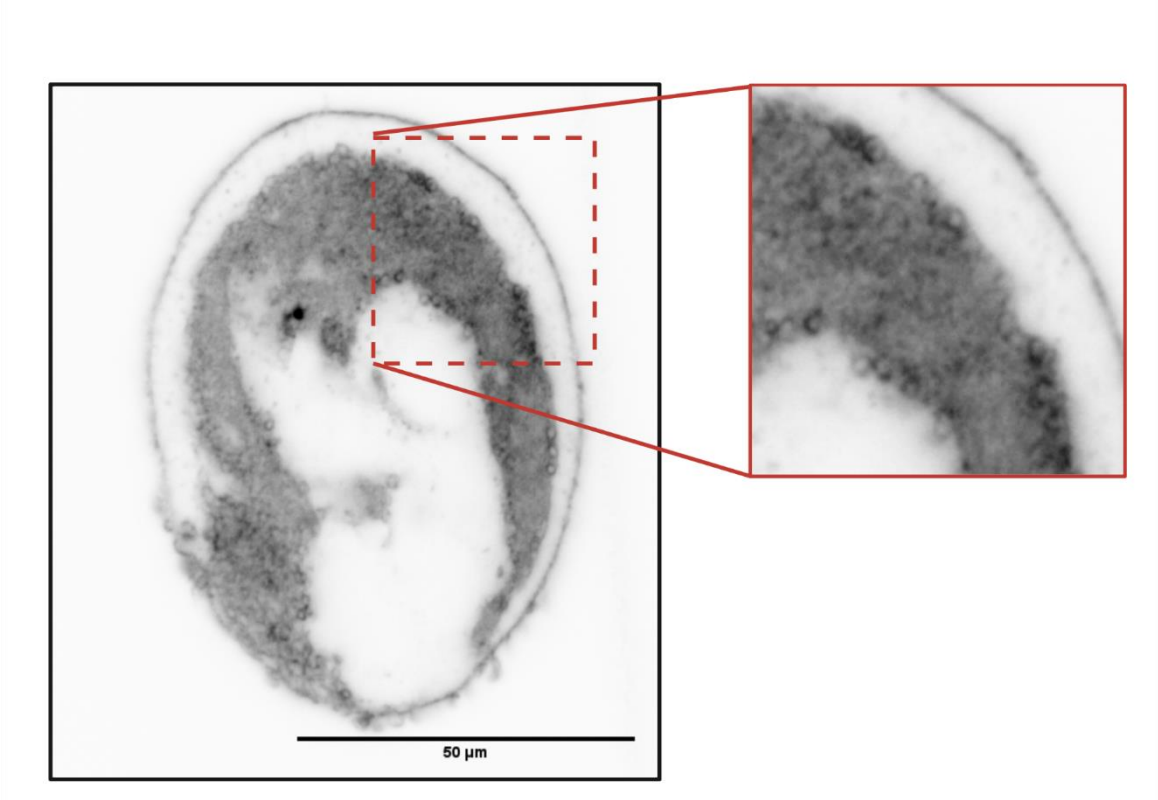


Figure 6.19 **Expansion microscopy of phalloidin at IMS during expansion**. Murine megakaryocytes were cultured and isolated at either day 3 of culture. Megakaryocyte were prepared for expansion microscopy with phalloidin staining, and imaged using iSPIM. Phalloidin ultrastructure shows loops and tubules of F-actin at the IMS. Expansion microscopy could be used to describe IMS ultrastructure more accurately at super resolution. Representative of one murine megakaryocyte culture.

6.10 Summary of Chapter 6

At the start of this chapter aims were outlined. For the ease of reading, these aims will be directly linked to the corresponding findings and solutions for a later more in-depth discussion.

- Design a labelling method for live cell imaging of megakaryocytes:

LifeAct expressing mouse megakaryocytes were stained with CellMask to label membrane continuous with the plasma membrane.

- Identify suitable morphological measurements of IMS:

The number of IMS objects, IMS volume, IMS integrated density, IMS mean grey value, IMS compactness (or surface area to volume ratio), megakaryocyte volume, megakaryocyte surface area were used to measure megakaryocyte maturation.

- Design an image analysis pipeline for 5D SPIM imaging:

A pipeline was successfully designed to pre-process, segment, label, and measure 3D IMS morphology. However, whilst manual aided segmentation is accurate, it is laborious. Further work will need to be conducted on automated segmentation tools.

- Define IMS morphological stages through manual observation:

IMS was shown to undergo theorised maturation (M0 to M6), however the megakaryocyte population divides at the expansion stage. Early megakaryocyte IMS rapidly becomes very dense. During the expansion (M3) phase, megakaryocytes can either plateau in IMS density, continuing to expand (M3), or continue to increase in IMS density and transition towards polarisation and proplatelet maturation (M4 to M6). Ultimately, megakaryocytes at each manually defined morphological stage could be segmented based on quantitative measures of IMS morphology.

- Define IMS morphological stages through cluster analysis:

Megakaryocytes were successfully segmented into four distinct clusters based on IMS morphology: Early megakaryocytes, maturing megakaryocytes, late megakaryocytes, and polarised megakaryocytes.

These clusters, whilst not as informative as more accurate manual labelling, provide descriptive data of megakaryocyte maturation.

- Elucidate the transitions of IMS morphological stage:

Both transitions within clusters and manually defined groups, and rates of change in IMS morphological parameters within clusters were successfully derived. Whilst early megakaryocyte maturation appears to be either redundant or rapid, later stages (M3 to M5) appear essential. Megakaryocytes may transition backward in morphology and do so predominantly between polarised (M4) and expansion (M3).

7 EXPLORING ACTIN DRIVEN BIOCHEMICAL MECHANISMS OF IMS DEVELOPMENT.

7.1 Aim

With a better understanding of the stages of IMS development, and the physical change in IMS morphology throughout those stages: invagination, contraction, movement, expansion, or expulsion, the mechanisms behind those forces can be probed in more detail. As such the aims of this section are as follows:

- Probe the role of F-actin in IMS development with Cytochalasin-D, and Jasplakinolide.
- Probe the role of the formins and ARP2/3 complex in driving F-actin nucleation during IMS development.
- Probe the role of phospholipase-C in IMS development with U73122, and U73343.

7.2 Introduction

The cytoskeleton of a cell produces the force required for shape change, intracellular trafficking, structural integrity and connectivity to the extracellular environment (Fletcher & Mullins, 2010), with actin filaments, microtubules, and intermediate filaments comprising the three major categories of cytoskeleton within the cell. Whilst proplatelet formation and extension is dependent on microtubule sliding via the dynein motor protein (Bender et al., 2015), aspects of IMS development such as invagination, polarisation and megakaryocyte migration towards the sinusoidal lumen, are shown to be regulated by the actin cytoskeleton (Antkowiak et al., 2016; Dütting et al., 2017). Actin dynamics, structure, composition, and location are regulated by hundreds of actin binding proteins, with two key actin nucleating proteins directly responsible for actin

structure. Formins promote straight filaments (Schönichen & Geyer, 2010; Zuidscherwoude et al., 2019), whilst the ARP2/3 complex promotes branching of filaments (Lane et al., 2014). Furthermore, propagation of force requires the direct anchorage of actin filaments to a membrane through either transmembrane proteins or direct interaction with lipids. Phosphoinositides are a group of phospholipids that bind directly to actin binding proteins such as formins, WASP/ WAVE proteins, and profilin, regulating actin polymerisation (Senju et al., 2017). Lipid uptake of megakaryocytes has been shown to be a vital component of IMS development (Valet et al., 2020), where phosphoinositides have been linked to IMS development (Schulze et al., 2006).

To elucidate the role of actin, formins, the ARP2/3 complex, and phosphoinositide on IMS phenotypes and classifications identified in the previous sections, megakaryocytes cultures were grown in the presence of several inhibitors:

- *Cytochalasin-D* is a cell permeable fungal toxin that binds to the barbed end of filamentous actin, blocking both addition and removal of actin monomers from the barbed end of the actin filament. Ultimately, this promotes destabilisation and depolymerisation of actin filaments. Whilst Cytochalasin-D acts to disassemble actin filaments, the individual actin monomers are released back into the global pool to be used elsewhere (Casella et al., 1981; Schliwa, 1982).

- *Jasplakinolide* is a cell permeable marine sponge toxin which acts to stabilise filamentous actin and promote polymerisation (Holzinger, 2010). Therefore, Jasplakinolide reduces the pool of actin monomers available for new filaments and reduces the dynamics of actin filaments.

- *Small molecule inhibitor of Formin Homology 2 domains (SMIFH2)* is a cell permeable formin inhibitor that targets the FH2 domain within formins to inhibit actin polymerisation (Rizvi et al., 2009). SMIFH2 has also been found to have off target and cytotoxic effects by reducing the expression of p53 (Isogai et al., 2015).

- *CK666* is a small molecule inhibitor of the ARP2/3 complex. CK666 acts as an allosteric effector, stabilising ARP2/3 in an inactive state and inhibiting therefore inhibiting actin nucleation. Since ARP2/3 acts to produce branched actin filaments, CK666 specifically inhibits branched actin structural formations. (Hetrick et al., 2013)

- *U73122* is an amino steroid that inhibits phospholipase C (PLC). U72133 acts to inhibit hydrolysis of phosphatidylinositol-4,5-bisphosphate ($PI4,5P_2$) to inositol triphosphate (IP_3), and acetyl glyceride. *U73343* is a biologically inert analogue of U73122, and is used as a control to measure the off-target effects of U73122 treatment (Macmillan & McCarron, 2010).

7.3 Probing F-actin involvement in IMS development through inhibition with Cytochalasin-D and Jasplakinolide

To assess the relationship between IMS development and the actin cytoskeleton, maturing megakaryocytes were treated with cytochalasin-D (0.05, 0.5, and 5 μM) and jasplakinolide (0.05, 0.5, and 5 μM) (Bubb et al., 2000; Stevenson & Begg, 1994).

Treatment with all concentrations of cytochalasin-D (0.05 to 5 μM) heavily disrupted IMS morphology, and promoted polarisation (M4) megakaryocytes whilst inhibiting expansion megakaryocytes (M3) (figure 7.1 and 7.3a). Characteristically, polarisations in the presence of cytochalasin-D were circular, and exhibit a dense GP1b-α IMS core surrounded by a ring of phalloidin (figure 7.3b). Quantification of phalloidin morphological parameters shows a drop in IMS area, but an increase in IMS mean grey value and integrated density at high cytochalasin-D concentrations (0.5 μM) (figure 7.4a). Interestingly, GP1b-α IMS morphological parameters illustrate a similar contraction, but with IMS mean grey value and IMS integrated density increasing at lower concentrations of cytochalasin-D (0.05 μM) (figure 7.4b), and almost all GP1b-α IMS structures disappearing at very high concentrations of cytochalasin-D (5 μM) (figure 7.1d). These findings suggest:

1) Decreased stability and dynamic turnover of actin filaments caused by cytochalasin-D promotes GP1b-α IMS accumulation, contraction, and polarisation.
2) Controversially, polarisation is upregulated heavily at low concentrations of cytochalasin-D (0.05 μM), when phalloidin decreases in area, integrated density, and mean grey value.
3) High densities of dynamically assembling F-actin inhibit GP1b-α IMS compression.

Megakaryocytes treated with jasplakinolide behaved subtly different to those treated with cytochalasin-D. Low concentrations of jasplakinolide (0.05 μM) perturbed expansion megakaryocyte (M3) development, and promoted both polarisation (M4),

and accumulation (M2) megakaryocytes (figure 7.2 and 7.3c). Typically, polarisations and accumulations were consistently circular (figure 7.3d), however polarisations were also observed either protruding or being expelled from the megakaryocyte (figure 7.3e). Interestingly, low concentrations of jasplakinolide (0.05 μM) caused in increase in both phalloidin and GP1b-α IMS volume, whilst only phalloidin integrated density, and mean grey value increased. High concentrations of jasplakinolide (0.5 μM) drastically abrogated IMS morphology and development. These findings suggest:

1) A reduction in dynamic F-actin promotes both F-actin and GP1b-α compression (M2) and polarisation (M4) megakaryocytes. Both these stages of development share a contraction of IMS.
2) A reduction in dynamic F-actin inhibits cortex stability, and promotes polarised IMS expulsion from the megakaryocyte.
3) An increase of GP1b-α IMS mean grey value and integrated density is not essential for formation of polarised megakaryocytes (M4).

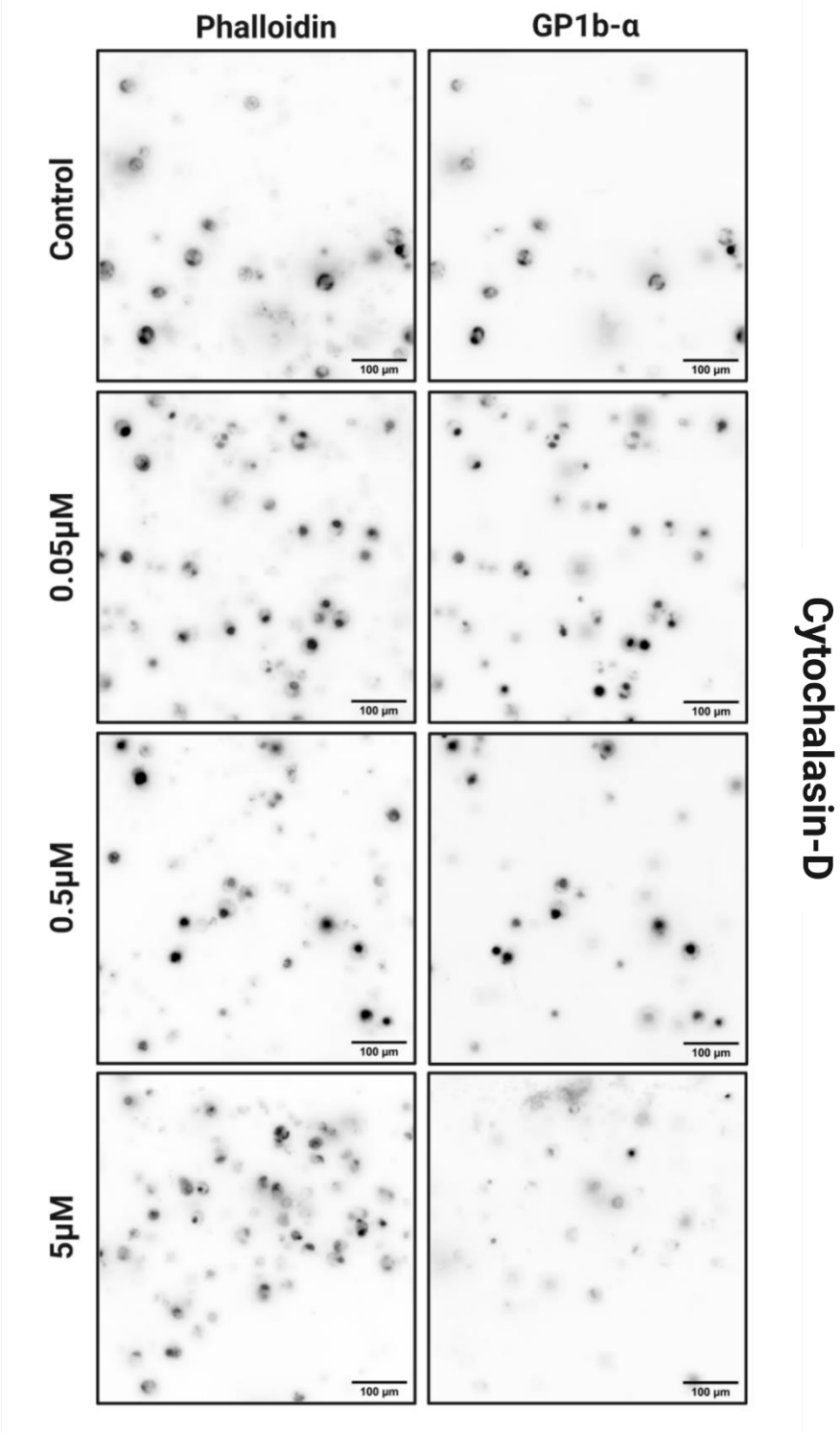


Figure 7.1 **Effect of cytochalasin-D on IMS development.** Megakaryocytes were cultured and differentiated for three days in the presence of cytochalasin-D at 0.05 μM, 0.5 μM, and 5 μM in DMOS. At day three, megakaryocytes were isolated, fixed, and stained with Phalloidin and GP1b-α antibody before being imaged with a fluorescence wide-field microscope. Cytochalasin-D induces a decrease in IMS volume, whilst promoting polarisation. A high concentration of cytochalasin-D (5 μM) induces almost a complete loss of GP1b-α IMS structures. Scale bar represents 100 μm. Representative images of three murine megakaryocyte cultures.

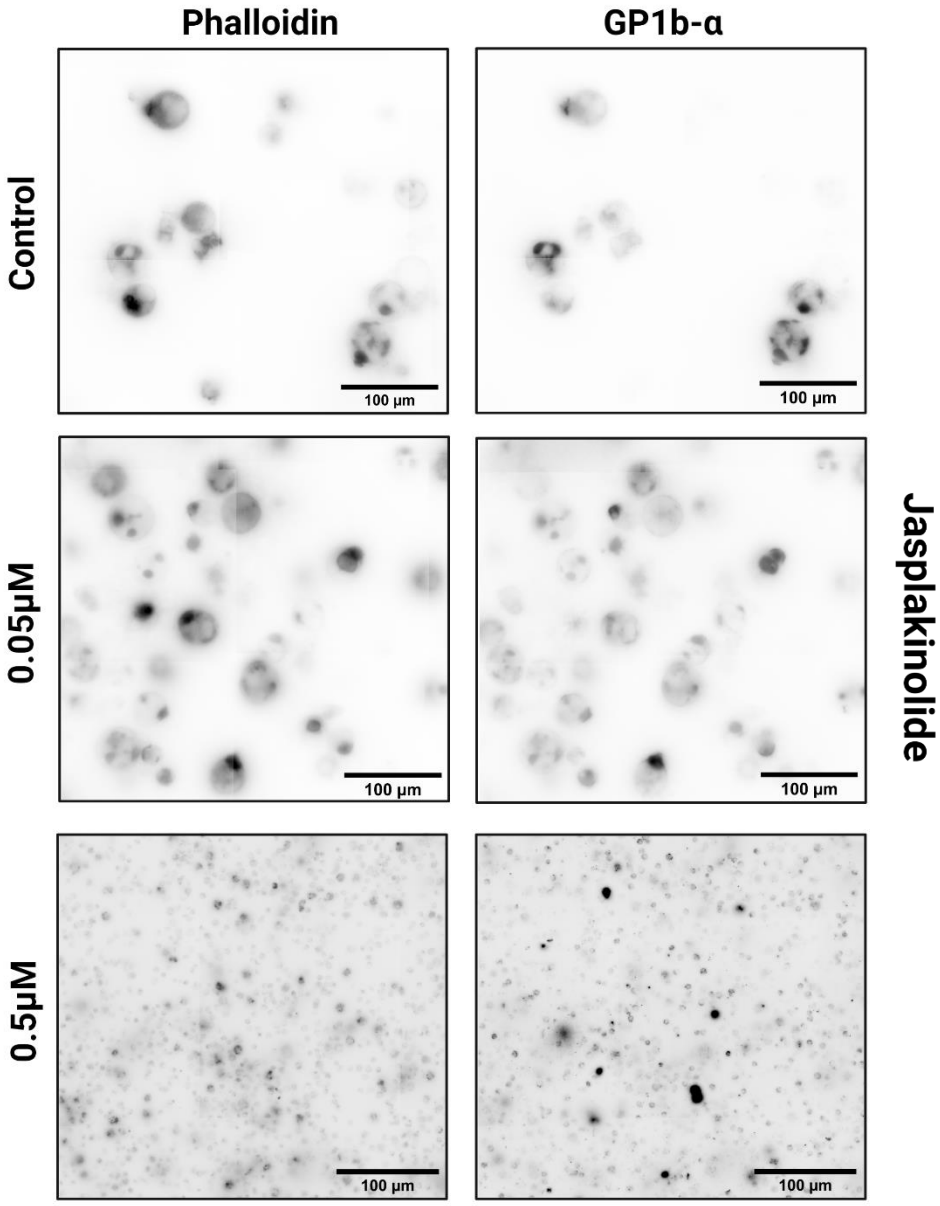


Figure 7.2 **Effect of jasplakinolide on IMS development.** Megakaryocytes were cultured and differentiated for three days in the presence of jasplakinolide at 0.05 µM, 0.5 µM, and 5 µM in DMOS. At day three, megakaryocytes were isolated, fixed, and stained with Phalloidin and GP1b-α antibody before being imaged with a fluorescence wide-field microscope. Jasplakinolide promotes accumulation (M3), and polarised (M4) structures at low concentrations (0.05 µM), with megakaryocyte exhibiting an increase in both phalloidin and GP1b-α IMS volume, integrated density, and mean grey value. Furthermore, unlike with cytochalasin-D inhibition, jasplakinolide induces polarised IMS to protrude and erupt from megakaryocytes. Scale bar represents 100 µm. Representative images of four murine megakaryocyte cultures.

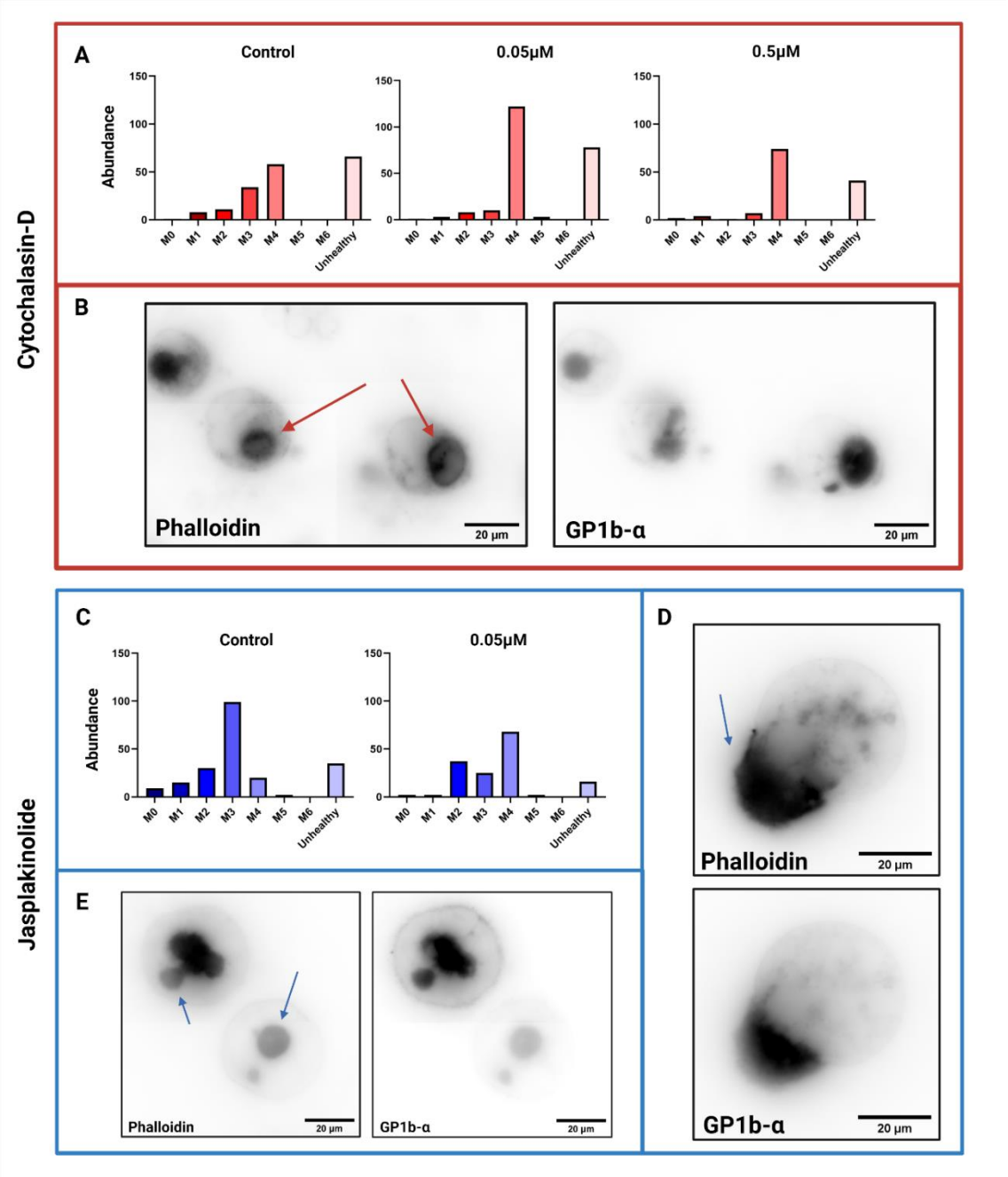


Figure 7.3 **Effect of cytochalasin-D and jasplakinolide on IMS morphological stage.** Megakaryocytes were cultured and differentiated for three days in the presence of cytochalasin-D or jasplakinolide at 0.05 µM, 0.5 µM, and 5 µM in DMOS. At day three, megakaryocytes were isolated, fixed, and stained with Phalloidin and GP1b-α antibody before being imaged with a fluorescence wide-field microscope. Images were manual analysed and classified by morphological stage. **a)** Cytochalasin-D promotes polarisation (M4), and down regulates expansion megakaryocytes (M3). **b)** Polarised regions in cytochalasin-D treated megakaryocytes typically exhibit circular, hollow polarisations of phalloidin, with a core of GP1b-α (Red arrows). **c)** Jasplakinolide induces polarisation (M4). **d)** However, these polarisations often protruded or erupted from megakaryocytes (Blue arrows). **e)** Furthermore, jasplakinolide also promoted accumulated megakaryocytes which also manifested circular IMS. Representative images of three murine megakaryocyte cultures.

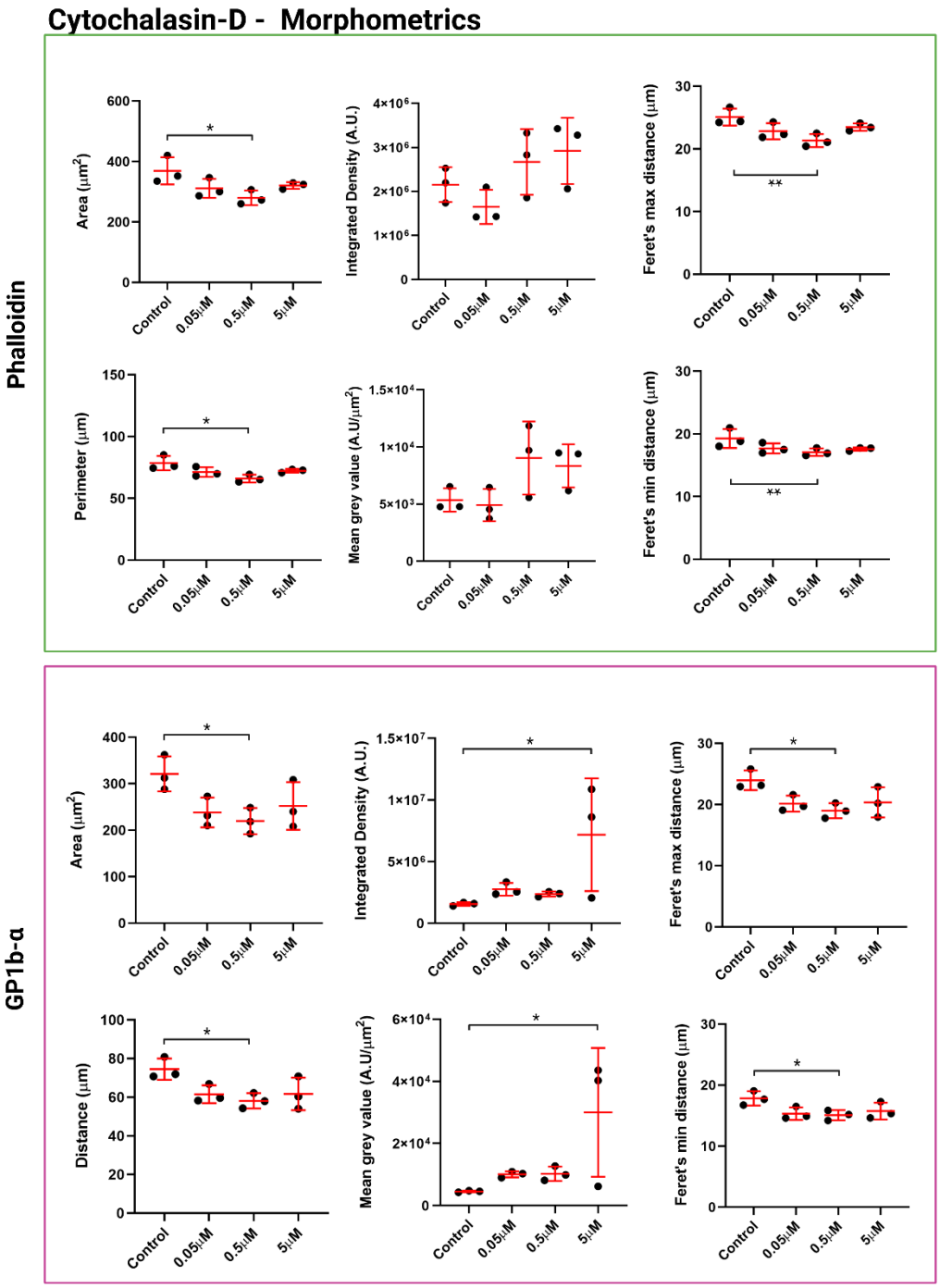


Figure 7.4 **Effect of cytochalasin-D on IMS morphometrics.** Megakaryocytes were cultured and differentiated for three days in the presence of cytochalasin-D at 0.05 μM, 0.5 μM, and 5 μM in DMOS. At day three, megakaryocytes were isolated, fixed, and stained with Phalloidin and GP1b-α antibody before being imaged with a fluorescence wide-field microscope. Images were then processed by the wide-field image analysis pipeline. **a)** Phalloidin area decreases, however phalloidin integrated density, and mean grey value increase at higher concentrations of cytochalasin-D (0.5 μM). **b)** Interestingly, at low concentrations of cytochalasin-D (0.05 μM) GP1b-α IMS area also decreases, whilst GP1b-α IMS integrated density and mean grey value increase despite the decrease in the same phalloidin parameters. Representative images of three murine megakaryocyte cultures.

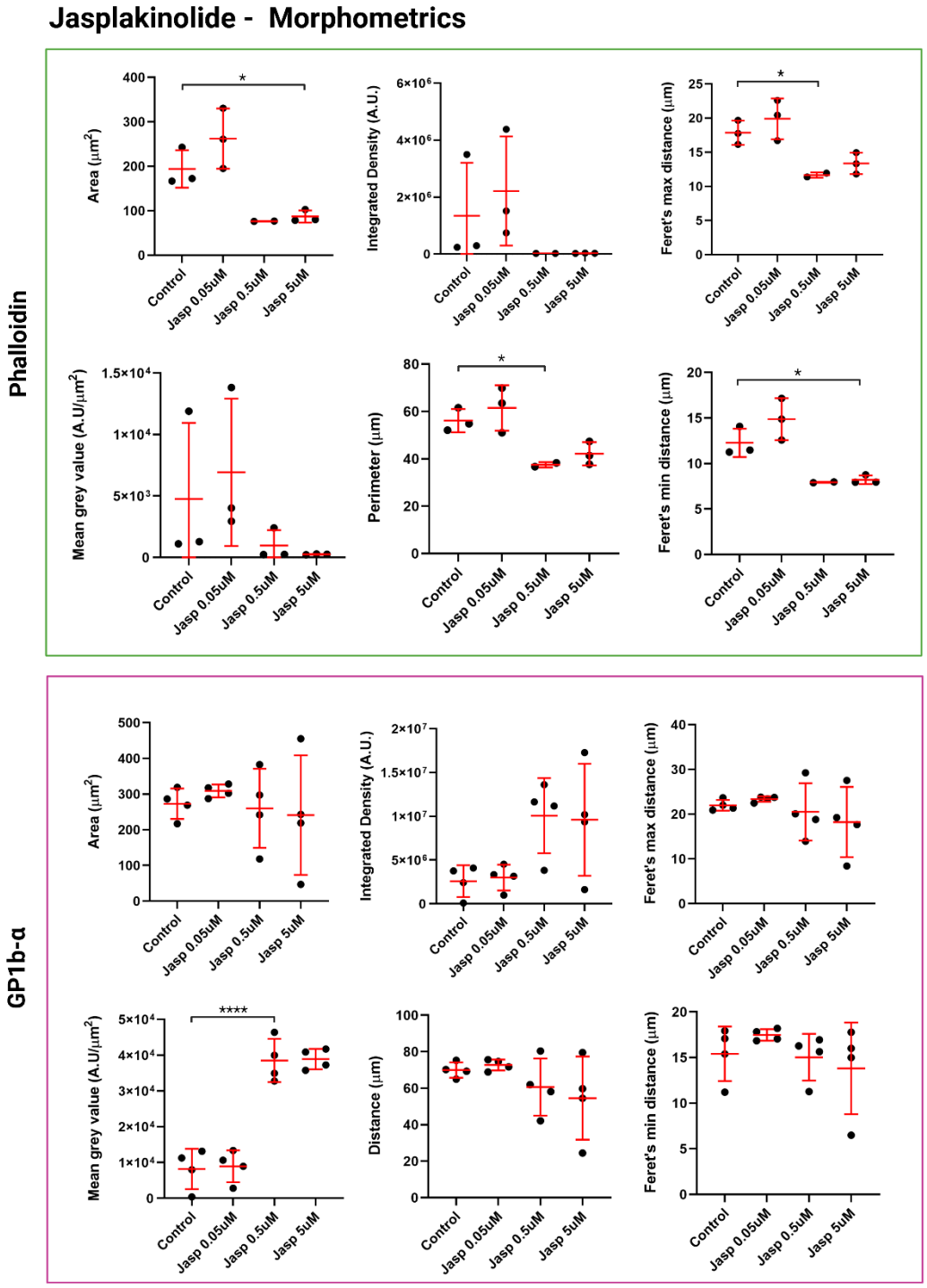


Figure 7.5 **Effect of jasplakinolide on IMS morphometrics.** Megakaryocytes were cultured and differentiated for three days in the presence of jasplakinolide at 0.05 μM, 0.5 μM, and 5 μM in DMOS. At day three, megakaryocytes were isolated, fixed, and stained with Phalloidin and GP1b-α antibody before being imaged with a fluorescence wide-field microscope. Images were then processed by the wide-field image analysis pipeline. **a)** Phalloidin area, integrated density, and mean grey value increase at lower concentrations of jasplakinolide (0.05 μM), but high concentrations (0.5 μM) abrogate phalloidin morphology. **b)** At low concentrations of jasplakinolide (0.05 μM) GP1b-α IMS area increases, whilst GP1b-α IMS integrated density and mean grey value remain constant. Representative images of four murine megakaryocyte cultures.

7.4 Probing the role of formins and ARP2/3 complex in IMS development through inhibition with CK666 and SMIFH2

Formins and Arp2/3 complex compete to assemble F-actin from the pool of G-actin within the cell. Whilst formins form parallel, straight F-actin structures, Arp2/3 complex forms branched F-actin structures. To assess mechanisms of F-actin assembly prevalent during IMS formation, megakaryocyte were treated with SMIFH2 (0.5, 5, and 50 µM) and CK666 (0.5, 5, and 50 µM) (Hetrick et al., 2013; Isogai et al., 2015).

Treatment with SMIFH2 induced an increase in expansion phase megakaryocytes (M3) within the culture, however these expansion megakaryocytes exhibited a thin IMS structure which was contained around the rim of the megakaryocyte (figure 7.6 and 7.8a). Notably, polarised megakaryocytes (M4) were not observed in control cultures, which clouds insight into the effect of SMIFH2 on later stages of IMS maturation. Interestingly, phalloidin area within SMIFH2 treated megakaryocytes remained consistent, whilst phalloidin integrated density and mean grey value decreased with an increasing concentration of SMIFH2. Conversely, GP1b-α IMS area decreased marginally with SMIFH2 treatment (5 µM), but GP1b-α IMS integrated density and mean grey value increase. Importantly, even at high concentrations of SMIFH2 (50 µM), megakaryocyte still matured to a reasonable size and developed IMS (figure 7.9). These finding suggest:

1) No comments can be made on the effect of SMIFH2 on polarisation.
2) Since mature megakaryocytes are present at high concentrations of SMIFH2 (50 µM), formin regulated F-actin nucleation does not appear to be essential for IMS development.
3) GP1b-α IMS condenses independently of formin activity.

Treatment with CK666 showed little effect on IMS developmental stage, however no polarisation was observed within the control sample (figure 7.7 and 7.8b). Despite this lack of morphological change, even a low concentration of CK666 (0.5 µM) causes a major reduction in phalloidin integrated density and mean grey value. However, both these parameters plateau in value at higher CK666 concentrations. Conversely, whilst GP1b-α IMS area decreases with low concentrations of CK666 (0.5 µM), GP1b-α IMS integrated density and mean grey value stay constant (figure 7.10). These findings suggest:

1) Inhibition of Arp2/3 dependent actin nucleation does not drastically affect GP1b-α IMS formation.
2) Whilst Arp2/3 dependent actin nucleation appears to account for a large portion of overall phalloidin IMS signal, Arp2/3 function seems to be redundant since IMS formation still occurs.

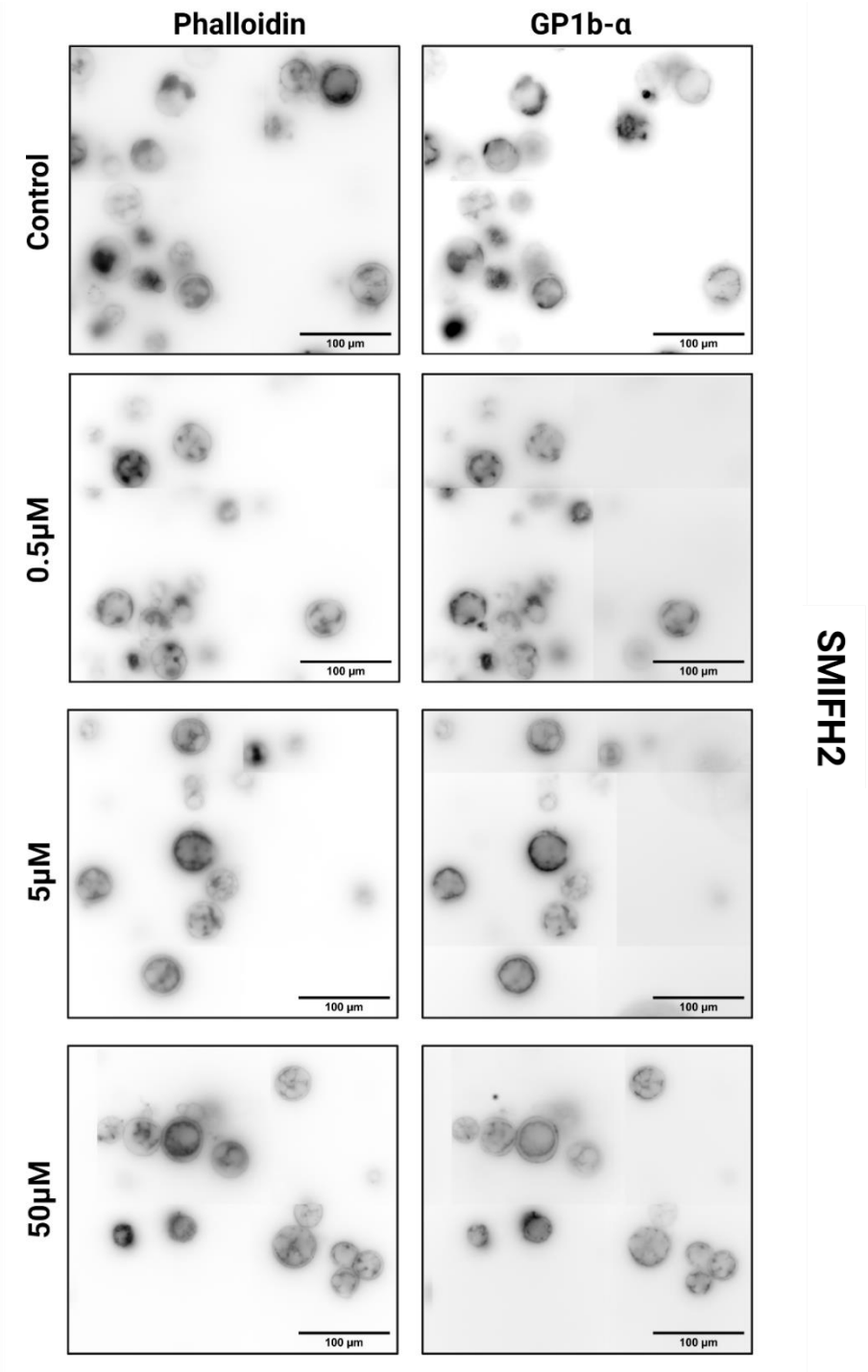


Figure 7.6 **Effect of SMIFH2 on IMS development.** Megakaryocytes were cultured and differentiated for three days in the presence of SMIFH2 at 0.5 µM, 5 µM, and 50 µM in DMOS. At day three, megakaryocytes were isolated, fixed, and stained with Phalloidin and GP1b-α antibody before being imaged with a fluorescence wide-field microscope. SMIFH2 treatment does not appear to significantly affect IMS morphology, however both phalloidin and GP1b-α IMS does appear to be thinner, and located more often to the rim of the megakaryocyte. Scale bar represents 100 µm. Representative images of three murine megakaryocyte cultures.

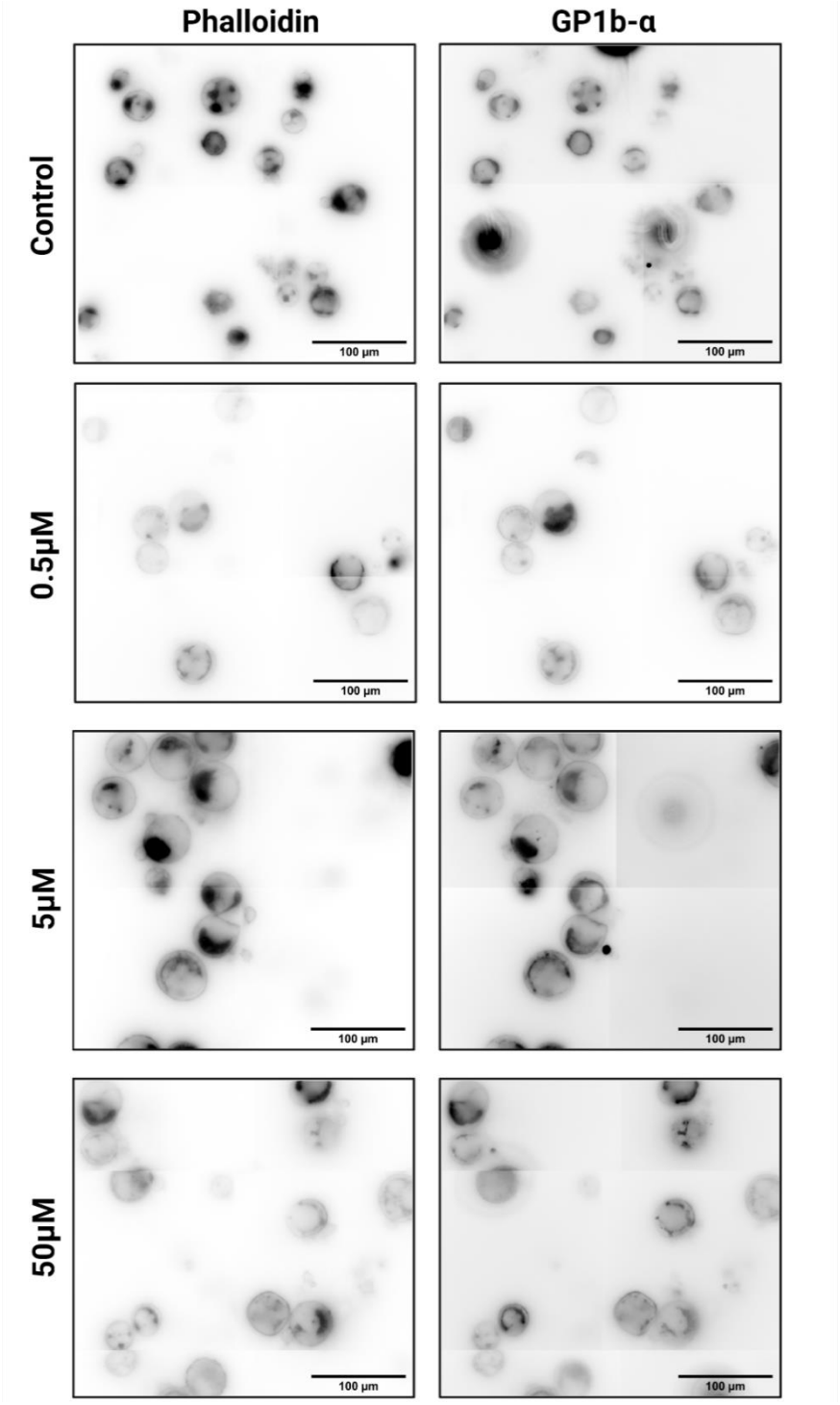


Figure 7.7 **Effect of CK666 on IMS development.** Megakaryocytes were cultured and differentiated for three days in the presence of CK666 at 0.5 µM, 5 µM, and 50 µM in DMOS. At day three, megakaryocytes were isolated, fixed, and stained with Phalloidin and GP1b-α antibody before being imaged with a fluorescence wide-field microscope. CK666 treatment does not appear to drastically effect IMS morphology. But again, both phalloidin and GP1b-α IMS does exhibits a thin structure sequestered to the rim of the megakaryocyte in higher concentrations of CK666. Scale bar represents 100 µm. Representative images of three murine megakaryocyte cultures.

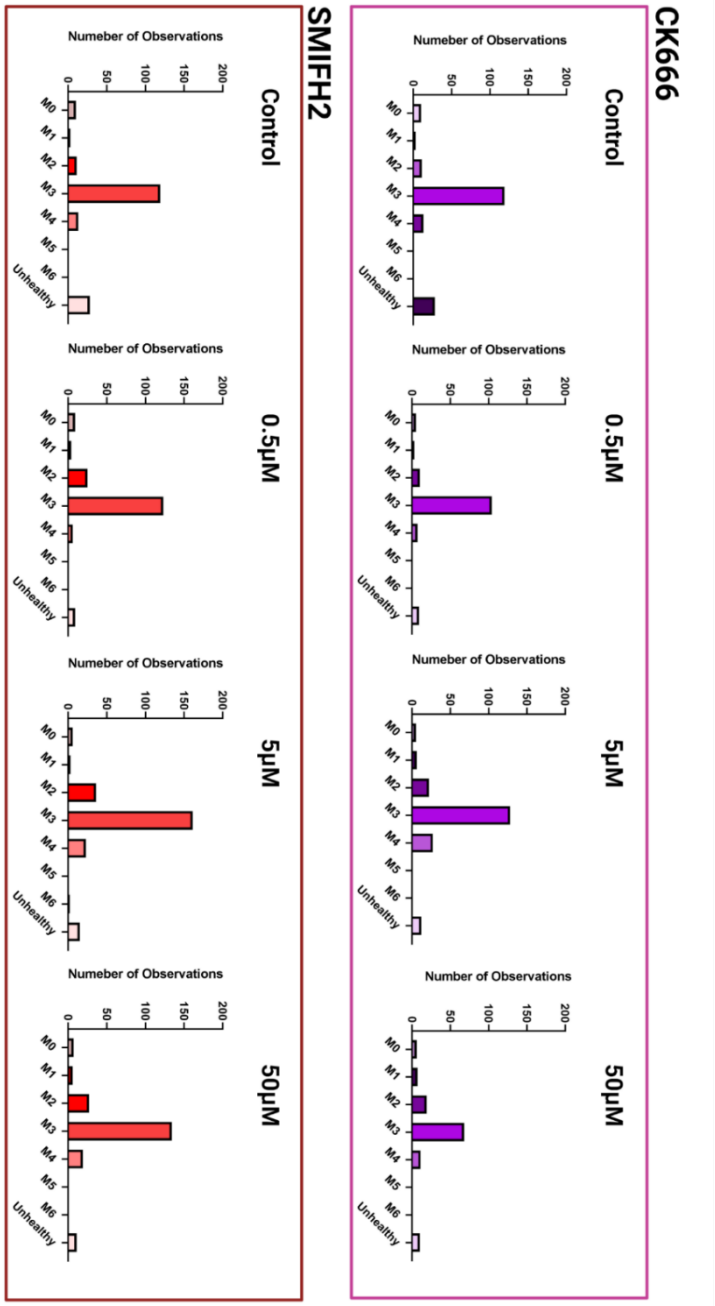


Figure 7.8 **Effect of SMIFH2 and CK666 on IMS morphological stage.** Megakaryocytes were cultured and differentiated for three days in the presence of CK666 or SMIFH2 at 0.5 µM, 5 µM, and 50 µM in DMOS. At day three, megakaryocytes were isolated, fixed, and stained with Phalloidin and GP1b-α antibody before being imaged with a fluorescence wide-field microscope. Images were then manually classified into morphological stages. **a)** High concentrations of SMIFH2 (0.5 µM) marginally promote expansion megakaryocytes (M3), but with little overall change in IMS morphology. Interestingly, at low concentrations of SMIFH2 (0.5 µM), the proportion of accumulation megakaryocytes (M2) increases. **b)** Similarly, CK666 treatment does little to change IMS morphology, however again, at higher concentrations of CK666 (5 µM) a larger proportion of accumulation megakaryocytes (M2) are observed. Polarised megakaryocytes (M4) within the control are lacking, suggesting that little can be concluded about the effect of SMIFH2 or CK666 on later IMS stages. Representative images of three murine megakaryocyte cultures.

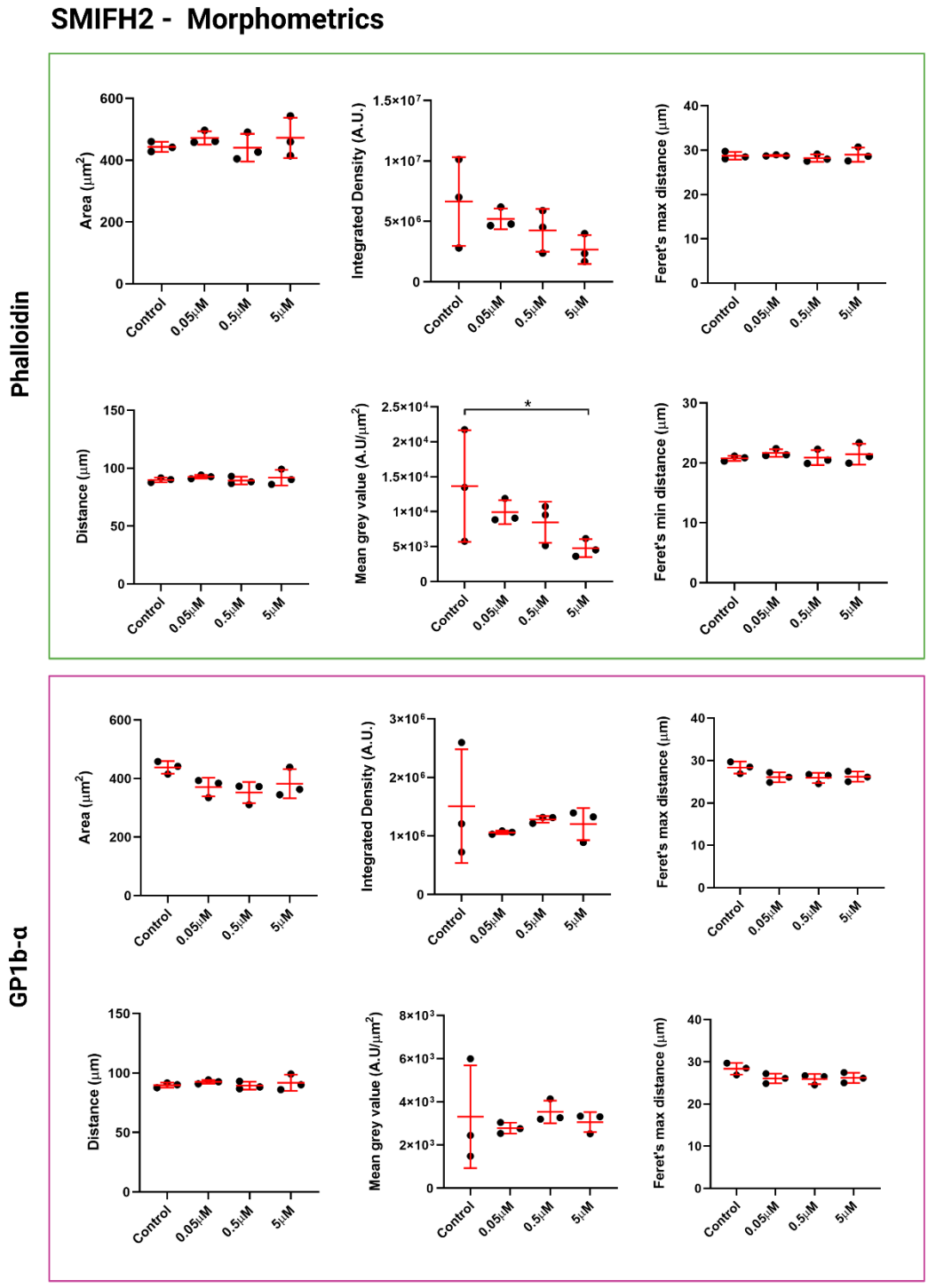


Figure 7.9 **Effect of SMIFH2 on IMS morphometrics.** Megakaryocytes were cultured and differentiated for three days in the presence of SMIFH2 at 0.5 μM, 5 μM, and 50 μM in DMOS. At day three, megakaryocytes were isolated, fixed, and stained with Phalloidin and GP1b-α antibody before being imaged with a fluorescence wide-field microscope. Images were then processed by the wide-field image analysis pipeline. **a)** Phalloidin area stays consistent, whereas phalloidin integrated density and mean grey value gradually decrease with an increase in SMIFH2 concentration. **b)** GP1b-α IMS integrated density and mean grey value appears to increase, whilst GP1b-α IMS area decreases. Representative images of three murine megakaryocyte cultures.

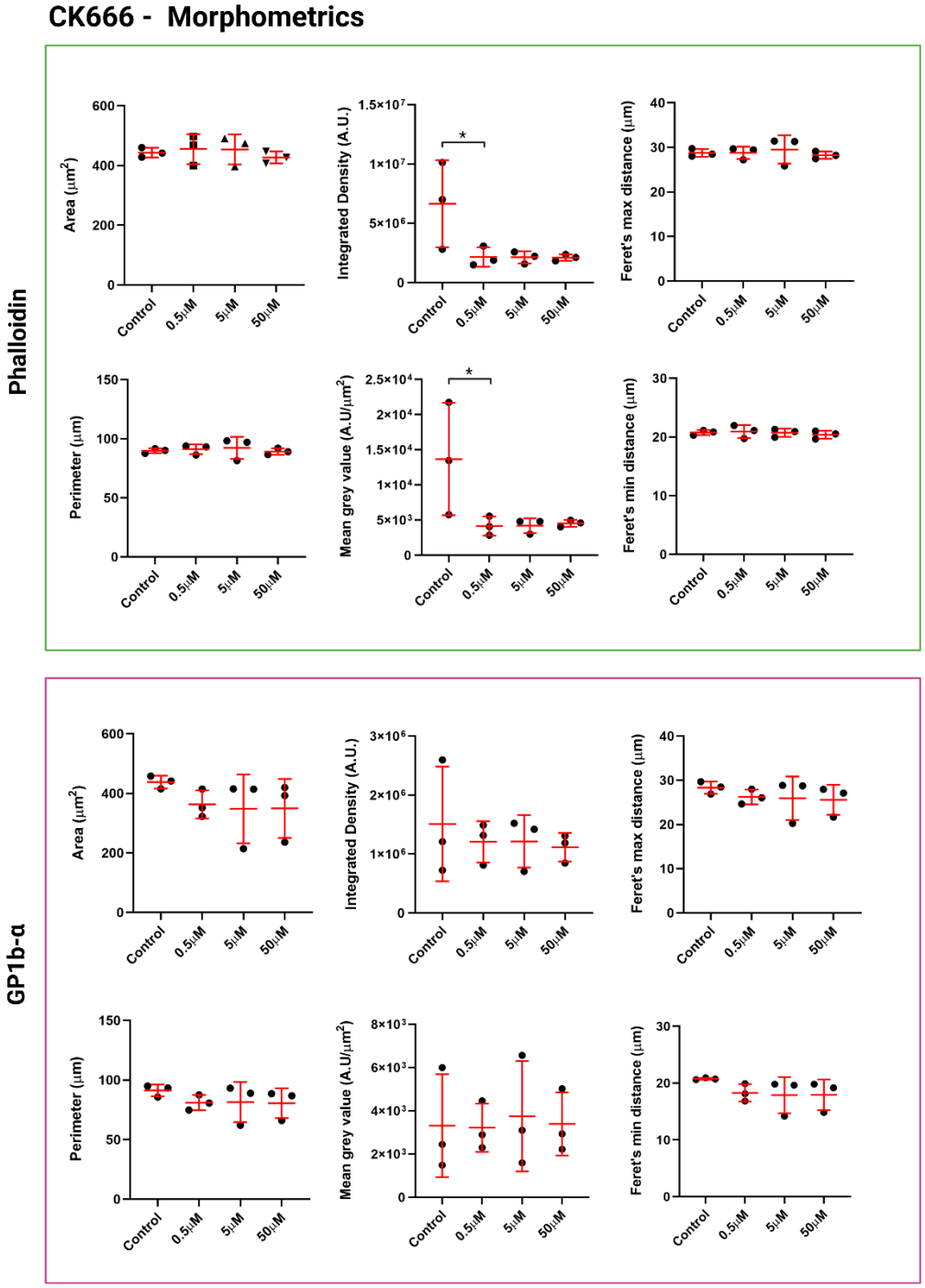


Figure 7.10 **Effect of CK666 on IMS morphometrics.** Megakaryocytes were cultured and differentiated for three days in the presence of CK666 at 0.5 µM, 5 µM, and 50 µM in DMOS. At day three, megakaryocytes were isolated, fixed, and stained with Phalloidin and GP1b-α antibody before being imaged with a fluorescence wide-field microscope. Images were then processed by the wide-field image analysis pipeline. **a)** Phalloidin area stays consistent, whereas phalloidin integrated density and mean grey value drastically decrease at low concentrations of CK666 (0.5 µm), before reaching a plateauing at higher concentrations of CK666. **b)** GP1b-α IMS integrated density and mean grey value appears to stay constant, whilst GP1b-α IMS area decreases. Representative images of three murine megakaryocyte cultures.

7.5 Probing the role of PLC in IMS development through inhibition with U73122

Phospholipase C (PLC) is a class of enzymes responsible for cleavage of phosphate groups from the carbon backbone of a phospholipid, making PLC an important regulator of phosphatidylinositol compounds (Nakamura & Fukami, 2017). PI-4,5-P_2 directly interacts with members of the actin cytoskeleton and regulates F-actin assembly, with an increase causing an upregulation of F-actin, and a decrease causing a reduction in F-actin polymerisation (Janmey et al., 2018; Shibasaki et al., 1997; Yamamoto et al., 2001). PLC inhibitor U73122 (0.1, 1, and 10 µM) and a biologically inert analogue U73343 (0.1, 1, and 10 µM) were used to probe the effect of PLC inhibition on IMS development.

Treatment with low concentrations of U73122 (0.1 µM) induced a drastic increase in accumulation (M2) and polarisation megakaryocytes (M4), with a corresponding decrease in expansion megakaryocytes (M3) (figure 7.12 and figure 7.13b). Furthermore, phalloidin area, integrated density, and mean grey value all decreased with U73122 concentration. Counter to this, GP1b-α IMS stayed consistent as U73122 concentration increased. Interestingly, whilst treatment with U73343 mimicked U73122, the effect on IMS morphological stage was not as drastic. However, morphometrics suggest U73122 results could be due to off-target effects (figure 7.14) (Macmillan & McCarron, 2010). These results suggest:

1) A PLC mediated mechanism governs accumulation (M2) and polarisation (M4).
2) A decrease in F-actin correlates with an increase in GP1b-α antibody binding.
3) A decrease in F-actin correlates to an increase in accumulated (M2), and polarised megakaryocytes (M4).

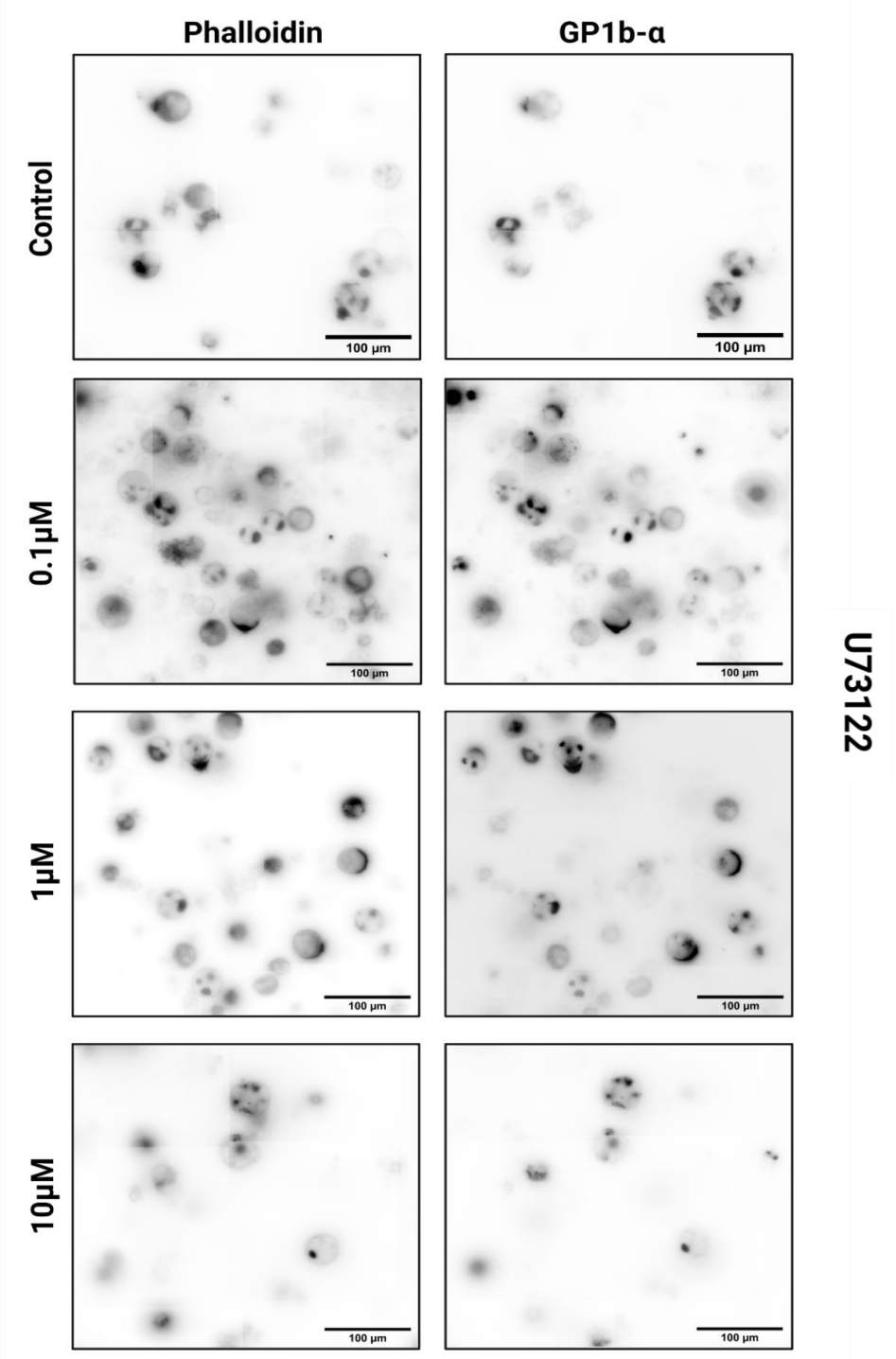


Figure 7.11 **Effect of U73122 on IMS development.** Megakaryocytes were cultured and differentiated for three days in the presence of U73122 at 0.1 µM, 1 µM, and 10 µM in DMOS. At day three, megakaryocytes were isolated, fixed, and stained with Phalloidin and GP1b-α antibody before being imaged with a fluorescence wide-field microscope. Images were then processed by the wide-field image analysis pipeline. Treatment with U73122 drastically alters IMS morphology. A low concentration of U73122 (0.1 µM) causes an increase in accumulation (M2) and polarisation megakaryocyte (M4), with a corresponding decrease in (M3). Higher concentrations of U73122 exaggerate this effect. Scale bar represents 100 µm. Representative images of three murine megakaryocyte cultures. Representative images of three murine megakaryocyte cultures.

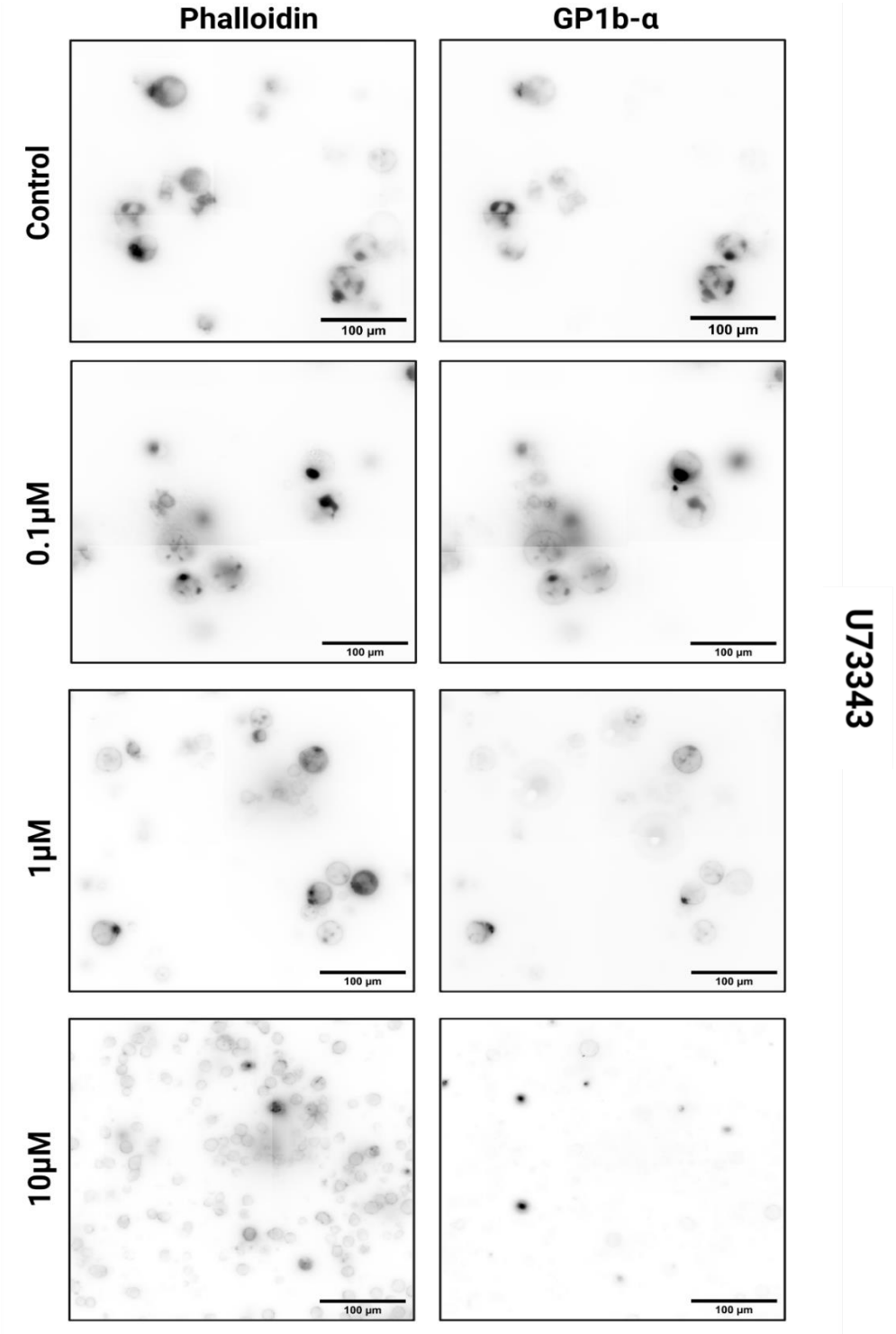


Figure 7.12 **Effect of U73343 on IMS development.** Megakaryocytes were cultured and differentiated for three days in the presence of U73343 at 0.1 μM, 1 μM, and 10 μM in DMOS. At day three, megakaryocytes were isolated, fixed, and stained with Phalloidin and GP1b-α antibody before being imaged with a fluorescence wide-field microscope. Images were then processed by the wide-field image analysis pipeline. U73343 does not affects IMS morphology, exhibiting an increase in accumulation (M2) and polarised megakaryocytes (M4). However, this change is not as drastic as with U73122 treatment. Scale bar represents 100 μm. Representative images of three murine megakaryocyte cultures.

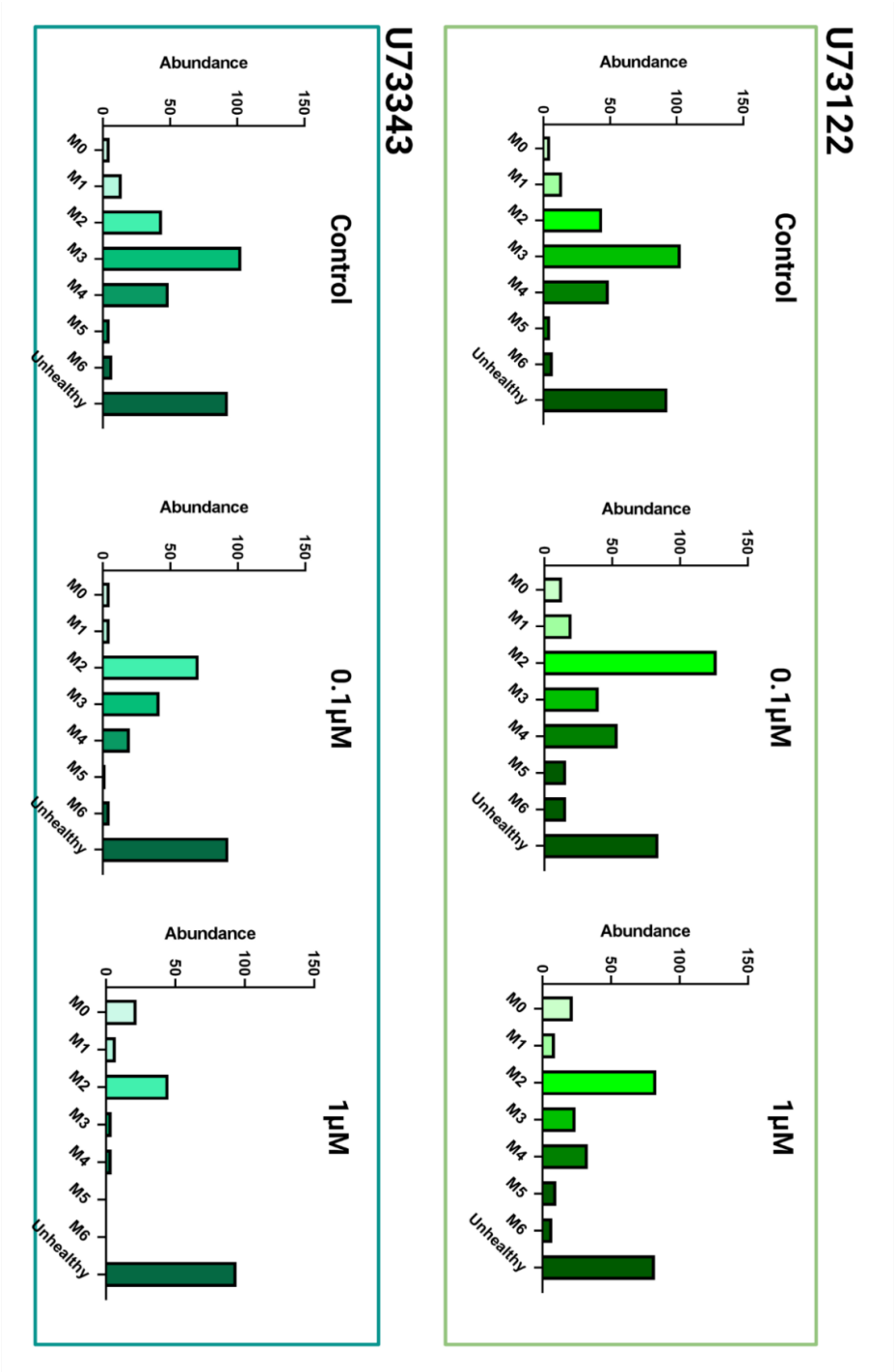


Figure 7.13 **Effect of U73122 and U73343 on IMS morphological stage.** Megakaryocytes were cultured and differentiated for three days in the presence of U73343 or U73122 at 0.1 µM, 1 µM, and 10 µM in DMOS. At day three, megakaryocytes were isolated, fixed, and stained with Phalloidin and GP1b-α antibody before being imaged with a fluorescence wide-field microscope. Images were manual quantified and classified by morphological stage. **a)** Treatment with U73343 at low concentrations (0.1 µM) promote accumulation (M2) polarisation megakaryocytes (M4), suggesting off-target effects. **b)** Similarly, treatment with low concentrations of U73122 also induces these changes in IMS morphological stage, but with an exaggerated effect. Representative images of three murine megakaryocyte cultures.

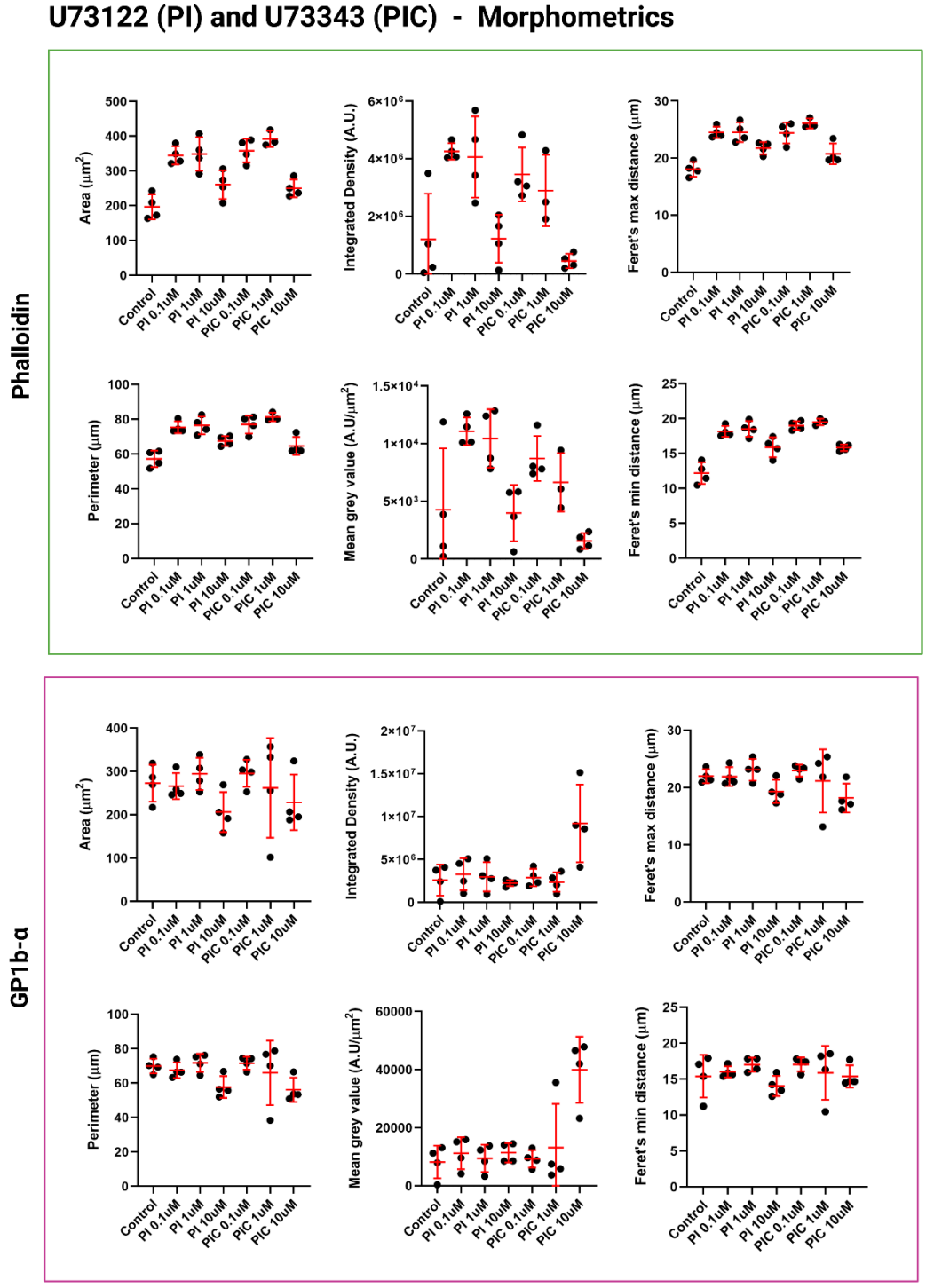


Figure 7.14 **Effect of U73122 and U73343 on IMS morphometrics.** Megakaryocytes were cultured and differentiated for three days in the presence of U73343 or U73122 at 0.1 μM, 1 μM, and 10 μM in DMOS. At day three, megakaryocytes were isolated, fixed, and stained with Phalloidin and GP1b-α antibody before being imaged with a fluorescence wide-field microscope. Images were manual quantified and classified by morphological stage. **a)** Phalloidin area, integrated density, and mean grey value decrease with an increase in U73122 concentration. **b)** Counter to this, GP1b-α IMS area, integrated density, and mean grey value stay consistent. However, U73343 also induces similar changes, suggesting results may be due to off target effects. Representative images of four murine megakaryocyte cultures.

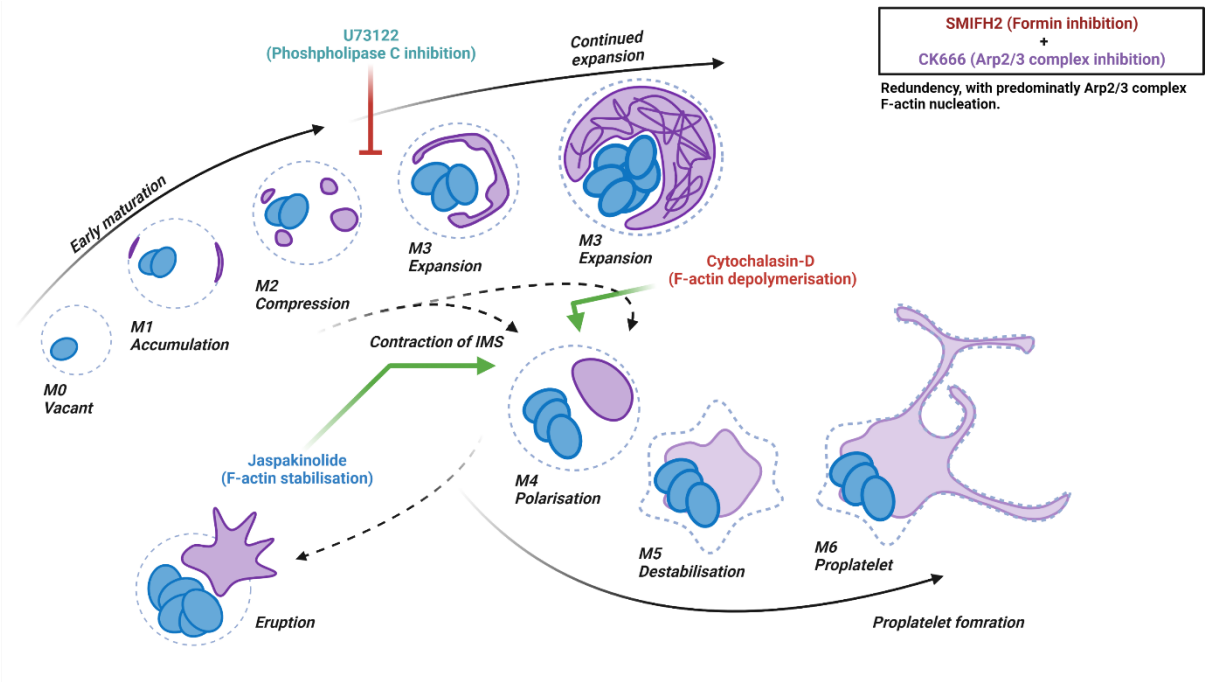


Figure 7.15 **Effect of inhibitors on IMS maturation.** U73122 appears to inhibit the progression of compression (M2) to expansion (M3) megakaryocytes, whilst cytochalasin-D and jasplakinolide promote polarisation (M4) of megakaryocytes. Furthermore, jasplakinolide promotes IMS eruption from the megakaryocyte. Lastly, CK666 inhibits F-actin integrated density, suggesting that F-actin structures at the IMS are nucleated by Arp2/3.

Overall, the effects on IMS morphology of the drugs discussed in this subchapter are outlined in figure 7.15.

7.6 Summary of Chapter 7

At the start of this chapter aims were outlined. For the ease of the reader, these aims will be directly linked to the corresponding findings and solutions for a later more in-depth discussion.

- Probe the role of F-actin in IMS development with cytochalasin-D, and jasplakinolide.

Cytochalasin-D inhibition promotes compression (M2) and polarisation (M4) megakaryocytes, and GP1b-α IMS recruitment, whilst reducing F-actin recruitment to the IMS.

Jasplakinolide inhibition promotes compression (M2) and polarization megakaryocytes (M4), and also decreases cortex stability leading to IMS eruption. Jasplakinolide inhibition also acts to increase F-actin recruitment to the IMS.

- Probe the role of the formins and ARP2/3 complex in driving F-actin nucleation during IMS development.

SMIFH2 inhibition does not drastically affect IMS morphology, suggesting that formins are not essential for IMS development.

CK666 inhibition causes a major reduction in F-actin recruitment to the IMS, but does not affect IMS morphology. This suggest that the ARP2/3 complex contributes to F-actin organisation and recruitment at the IMS, but is functionally redundant with other F-actin nucleating proteins.

- Probe the role of PLC in IMS development with U73122, and U73343.

PLC inhibition by U73122 promotes compression (M2) and polarisation megakaryocytes (M4), and reduces F-actin recruitment to the IMS. However, this may be due to off-target effects.

8 DISCUSSION

8.1 An updated model of IMS maturation

8.1.1 IMS formation

Previous work has shown the IMS to not only be continuous with the plasma membrane (Mahaut-Smith et al., 2003), but also established that a major driving force of IMS accumulation is an invagination of the plasma membrane preluded by an accumulation of GP1b-IX-V (Eckly et al., 2014). These studies have also suggested that the IMS originates from an invagination of the plasma membrane driven by the same mechanisms. Furthermore, electron microscopy has shown that sporadic pores are present on the plasma membrane of megakaryocytes which highlight IMS-like structures when megakaryocytes are incubated in soluble lipid dyes (Osman et al., 2016). Together these finding suggests that thin tubular membranes invaginate from the surface of the membrane, accumulate into interwoven networks at specific loci or ’macro’ IMS structures, and continue to ingress to expand the IMS.

Our data reinforces this theory, illustrating that megakaryocytes develop an intricate network or ‘thread work’ of interwoven IMS tubes which nucleate at loci throughout megakaryocytes at early stages of their development (figure 8.1a). Furthermore, both iSPIM and confocal data suggest that the number and size of these loci scale with megakaryocyte size, suggesting that as megakaryocyte age they form more and larger nucleation points. Interestingly, by staining fixed megakaryocytes with GP1b-α, these networks are often very difficult to visualise with iSPIM and wide-field fluorescence microscopy. Without looking in higher resolution at the thread work, it is not possible to comment on the structure. The tubules we do observe may be intertwined or thicker

tubules, with many smaller tubules unresolvable by diffraction limited techniques. From a mechanical standpoint, there are two forces at play in IMS formation (figure 8.1b):

- Invagination and continued invagination

  Binding force generating machinery (F-actin and myosin) to push against membrane whilst pulling membrane inwardly.

- Nucleation and compression

  Force to contract tubules at specific loci

Interestingly, evidence has also shown that the Golgi and endoplasmic reticulum (ER) are situated proximal to IMS accumulations (Eckly et al., 2014), which suggests that IMS lipid mass is also drawn from sources other than the plasma membrane. This presents a second option for the formation of tubules: an outward fusion of preformed tubules with the plasma membrane. Furthermore, within developing megakaryocytes we also observed large endocytic events in which CellMask was taken up to form compression (M2) and polarisation (M4) morphologies, presenting more potential mechanisms of invagination. iSPIM time-lapse data suggests that early stages of IMS formation are either very dynamic or very diverse, with a large flux between vacant (M0), accumulation (M1), compression (M2), and expansion (M3) megakaryocytes, which reinforces the theory that several mechanisms of invagination may exist (figure 8.1c).

Interestingly, it is unclear how multiple compressed loci (M2) transition into the large mass defining expansion megakaryocytes (M3). However, iSPIM data shows that as megakaryocytes increase in volume the number of individual IMS objects increases to a point, but then decreases. This suggests that IMS nuclei either expand, or they move

within the cell to merge together. Interestingly, images of accumulation (M1) and compression (M2) megakaryocytes show that despite the immaturity of the cell, there is already an interconnecting network of tubules linking each nucleation point. This suggests that this merging of accumulation nuclei happens with single tubules initially, either due to a fine thread work of IMS already within the megakaryocyte before nucleation, or as a direct result of nucleation with tubules forming from each loci.

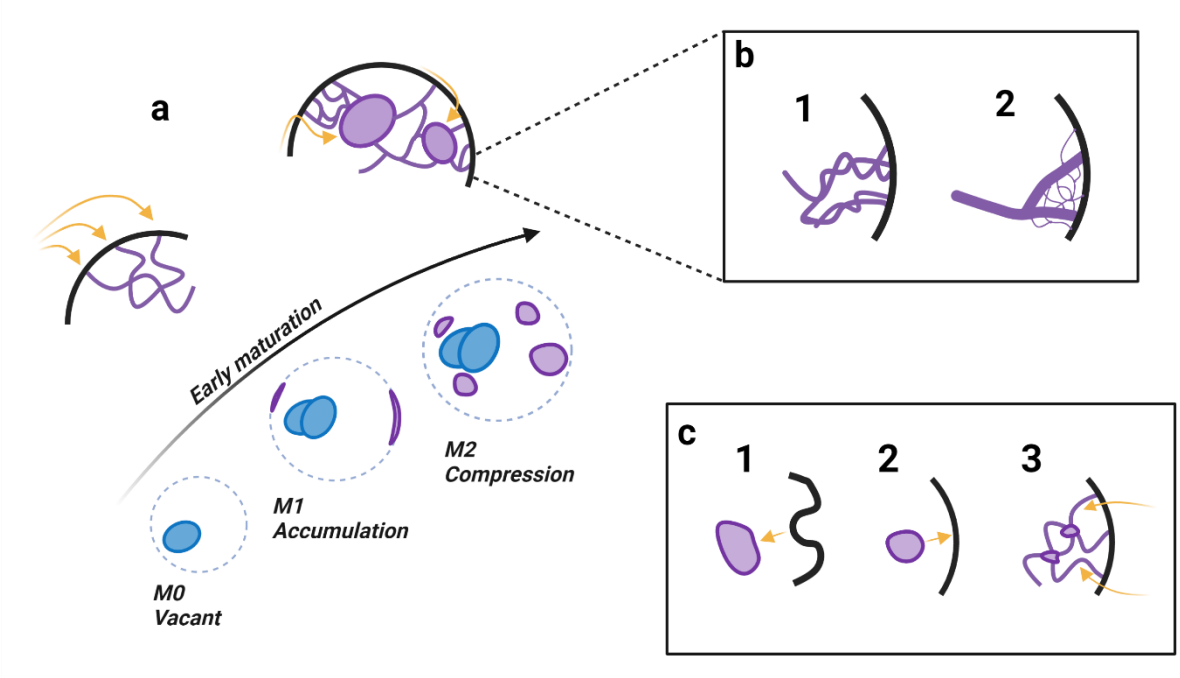


Figure 8.1 **Early maturation theory. a)** It is hypothesised that IMS initially invaginate from the plasma membrane (M1) before compressing at nodes throughout the megakaryocyte (M2). Golden arrows represent the invagination of the membrane. Our data backs this theory, highlighting a network of small tubules interlinking and preluding IMS macro-structures. **b)** Two potential structures of visible tubules 1) multiple tubules form coils, or 2) thick tubules. **c)** Theories of IMS formation 1) large endocytosis of plasma membrane, 2) exocytosis of internal membranes connect to plasma membrane, 3) slow invagination through multiple ingression pores.

8.1.2 IMS expansion and polarisation

As megakaryocytes develop the IMS expands to fill the cell, leaving only a small peripheral region near the plasma membrane empty (M3). The current theory of IMS

development suggests that this expansion process precedes IMS polarisation (M4) and later proplatelet formation (M6). Our data suggests that this is not the case. iSPIM data shows that polarised megakaryocytes have a large volume of IMS, a highly dense IMS, and a medium megakaryocyte and IMS volume. Megakaryocytes which have a larger megakaryocyte volume are all in the expansion stage, which highlights that once a megakaryocyte reaches a certain size it can no longer polarise. Therefore, whilst expansion megakaryocytes do prelude polarisation, megakaryocytes can either be triggered to polarise, or continue expanding terminally. These two populations are also identified with K-means cluster analysis, illustrating that expansion megakaryocytes (M3) can be classified into two categories:

- Partial expansion

Expansion megakaryocytes that may still polarise.

- Terminal expansion

Expansion megakaryocyte which may not polarise.

Furthermore, polarisation is a necessary intermediate step between expansion (M3) and proplatelet formation (M6), shown by measuring transitions of IMS morphological stage. Megakaryocytes rarely transitioned directly from expansion megakaryocytes (M3) to deformation (M5) or proplatelet forming megakaryocytes (M6). However, polarised megakaryocytes (M4) often transitioned backwards towards expansion megakaryocytes (M3), illustrating that polarisation megakaryocytes (M4) have not committed towards proplatelet formation. Backwards transitions seem counterproductive to cell development, however this is an *in vitro* culture where the signals present *in situ* are not fully replicated. *In situ,* evidence has been given to

suggest that polarisation is linked to megakaryocyte migration, with polarisation directed towards the sinusoidal lumen, however megakaryocytes polarised *in vitro* without these stimuli.

8.1.3 IMS destabilisation and proplatelet formation

Interestingly, proplatelets also formed within our cultures. Although, proplatelet forming cells were not easy to segment or describe morphologically, we did observe an intermediate stage of IMS formation between polarisation (M4) and proplatelet formation (M6). iSPIM data shows that the destabilised megakaryocyte (M5) is a necessary intermediate stage of IMS morphological development, with only a small number of megakaryocytes directly transitioning from polarised megakaryocytes (M4) to proplatelet forming megakaryocytes (M6). The destabilised megakaryocyte (M5) is marked by a fluid-like plasma membrane and IMS, with a hazy or blurred IMS in comparison to earlier stages. These observations indicate that membranes within the megakaryocyte destabilise before proplatelet formation, perhaps alluding to a mechanism of F-actin depolymerisation. This would make sense, since IMS membrane is already continuous with the membrane, it does not need to be trafficked to meet the demand in surface area caused by proplatelet protrusions. Similarly, the lack of a stable cortex would mean microtubule extensions need to provide less force to produce proplatelet extensions. Interestingly, the IMS in destabilised megakaryocytes is not polarised. This does not mean that a polarised destabilised megakaryocyte does not exist *in situ*, however it provides some evidence that polarised megakaryocytes are not polarising for directed proplatelet formation.

8.1.4 F-actin regulation in IMS maturation

Inhibitor studies using latrunculin-A and cytochalasin-D have shown that invaginations within the megakaryocyte are lost when F-actin dynamics is altered (Antkowiak et al., 2016; Eckly et al., 2014). This suggests that invagination of IMS tubules is driven by F-actin. Surprisingly, IMS persisted when we inhibited F-actin dynamics directly with jasplakinolide or cytochalasin-D, suggesting that:

- *Subtle changes to F-actin dynamics do not drastically effect IMS formation.*
- *IMS formation is an important and resilient structure in megakaryocyte development.*

Our data shows that F-actin content increases with low concentrations of jasplakinolide (0.05 µM), GP1b-α content remains constant. Jasplakinolide stabilises F-actin filaments and promotes longer, bundled filaments, suggesting invagination and compression occurs, but is not amplified by more stable actin filaments. However, at low concentration of cytochalasin-D (0.05 µM) GP1b-α content increased at IMS macro structures. Cytochalasin-D acts to prevent polymerisation, and promote rapid turnover of shorter filaments, suggesting that invagination and/or compression are promoted by dynamic filaments. Whilst compression is a localised event requiring high forces to contract tubules, invagination occurs across the entire plasma membrane. A dynamic F-actin may assemble more readily at multiple locations, providing more invagination furrows. Together, these results tie into prior evidence of the role of F-actin in IMS development:

- *F-actin organisation is essential for proper IMS development.*

- *Low concentrations of cytochalasin-D cause a noticeable increase in GP1b-α content.*
- *We suggest probing the role of a more dynamic actin in facilitating the invagination of IMS tubules.*

GP1b-IX-V plays an important role in IMS maturation, with a deficiency in GP1b-IX-V leading to macrothrombocytopenia and IMS structural aberration (Mekchay et al., 2019). Furthermore, GP1b-IX-V is a membrane bound protein, which directly interacts to F-actin via filamin-A (Kanaji et al., 2012), with FLNA deletion also leading to the early release of platelets and macrothrombocytopenia (Jurak Begonja et al., 2011; Nurden et al., 2011). Therefore, an inhibition of F-actin dynamics could simply lead to a compensatory mechanism of GP1b-IX-V recruitment.

Interestingly, multiple studies have shown the importance of F-actin in IMS contraction and movement, with MYH9 deletion leading to relaxing of the IMS membrane, illustrating that myosin mediated force generation acts during IMS formation. Furthermore, a RhoA/Cdc42 switch regulates polarisation (Dütting et al., 2017; Pleines et al., 2010), suggesting a separate composition of actin cytoskeleton between expanded and polarised megakaryocytes. Our results show that cytochalasin-D and jasplakinolide also both cause an increase in compression (M2), and polarised megakaryocytes (M4), with jasplakinolide also promoting an eruption of polarised masses. This suggests that a fine tuning of actin dynamics regulates both IMS contraction, IMS movement, and IMS expulsion in a myosin dependent manner.

8.1.5 F-actin nucleation proteins in IMS development

Studies have shown the importance of both Arp2/3 complex and formins in IMS maturation. Arp2/3 function is regulated by WASP mediated Cdc42 activity. A deficiency of WASP displays in thrombocytopenia (Jin et al., 2019), and an aberration of IMS structure. As previously discussed, Cdc42 is upregulated during IMS maturation and promotes polarisation. Similarly, formins: FHOD1, DAAM1, DIAPH are highly expressed throughout mature megakaryocyte development (Zuidscherwoude et al., 2019), and a deletion of FHOD1 and DIAPH leads to macrothrombocytopenia with defects in megakaryocyte development. These mechanisms of nucleation promote different F-actin structures. Arp2/3 complex nucleates branched F-actin structures, whilst formins promote bundled F-actin.

Our results show that inhibition with SMIFH2 or CK666 shows little effect on IMS morphological stage, however CK666 does have a large effect on phalloidin integrated density at low concentrations (0.5 μM). Interestingly, phalloidin integrated density stays constant at higher concentrations of CK666 (50 μM), indicating functional redundancy. Together, these results suggests that Arp2/3 plays and important role F-actin nucleation during IMS maturation, whereas the role of formins in F-actin nucleation during IMS maturation is redundant. Importantly, SMIFH2 inhibits the FH2 domain of formins, still allowing them to interact with other ABPs. Furthermore, we observed no polarisation within our cultures, potentially masking effects of SMIFH2 and CK666 in later stages of development. Therefore, this data along with literature findings indicate that:

- *IMS organisation and maturation is governed by Arp2/3 nucleated F-actin.*

- *Arp2/3 complex has functional redundancy with other F-actin nucleation proteins.*
- *F-actin during IMS maturation is branched, rather than bundled.*
- *Formins may still have a role in IMS development, through interaction with ABPs, the membrane, and microtubules.*

8.1.6 Lipids in IMS development

Lipid mass is a vital component of IMS development. This has been demonstrated by inhibiting lipid biogenesis (N. Barrachina et al., 2021), observing neutrophil phagocytosis (Cunin et al., 2019), and even differentiating megakaryocytes directly from adipose cells (Valet et al., 2020). The most likely argument for the role of lipid mass during IMS development and proplatelet formation is to facilitate the increase in surface area needed for invagination of the plasma membrane. Whilst proplatelet formation is a rapid process (Pluthero & Kahr, 2016), it demands a vast increase in megakaryocyte surface area, which can only be achieved by incorporating the accumulated IMS into the plasma membrane. IMS development is a slow process, and will require the constant synthesis, and trafficking of vesicles to the site of invagination. Lipids also have functional roles in structural rigidity, curvature (Casares et al., 2019), and protein signalling, leading to several studies have looked into lipid composition of megakaryocytes (Dautel et al., 2017; Pienimaeki-Roemer et al., 2015). Phosphatidylinositol compounds are often linked to F-actin regulation and have been shown to regulate IMS development (Bertović et al., 2020; Schulze et al., 2005; Wu et al., 2014).

Our data suggests that PLC inhibition with U73122 promotes expansion stage megakaryocytes. PLC catalyses the degradation of PI-4,5-P_2 to IP_3 and diacylglycerol,

therefore U73122 acts to promote PI-4,5-P_2 activity. This suggests that PI-4,5-P_2 plays a role in IMS expansion and uptake.

8.2 Providing a toolkit for measuring megakaryocyte maturation

Throughout this thesis one of the key aims has been to provide an imaging toolkit to examine IMS morphological development. Higher resolution microscopy techniques provide more structural detail at the sacrifice of FOV, practical difficulty, and statistical relevance in large populations of cells. This issue is solved, by imaging a greater number of megakaryocytes with low resolution techniques. Here the following microscopy techniques are used synergistically to probe IMS maturation at different levels of resolution and sample number (figure 8.2):

- Wide-field fluorescence and phase contrast microscopy

  Coarse, low-resolution overview of IMS maturation, with a high number of observations. Optimal for fixed cell imaging.

- iSPIM microscopy

  Large volumetric 3D imaging at a high spatial resolution, but still diffraction limited. Optimal for rapid, live-cell imaging.

- Expansion microscopy

  Super resolution imaging. Provides high structural detail, but of a small number of cells. Only for fixed cell imaging.

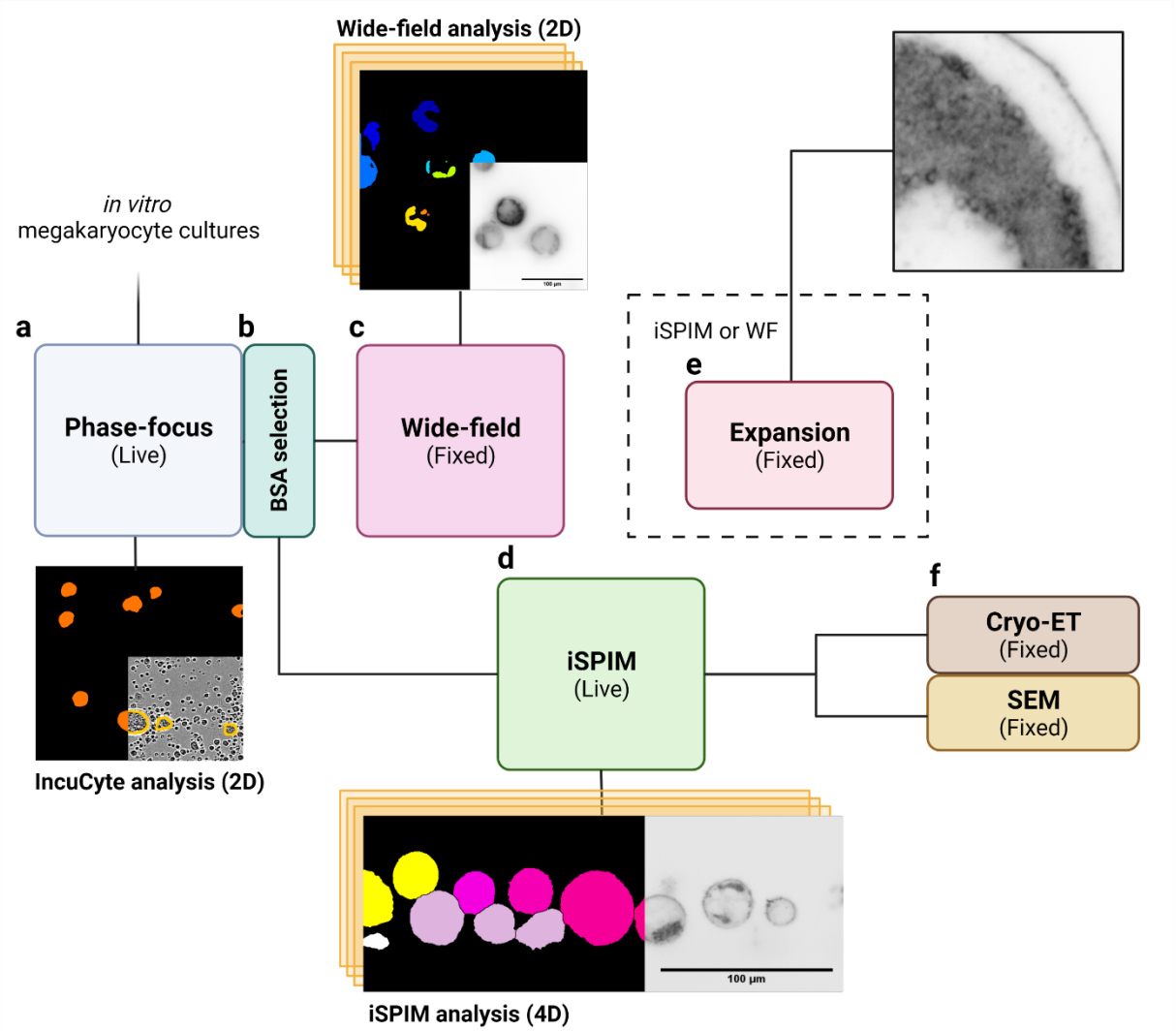


Figure 8.2 **IMS maturation tool kit analysis**. **a)** A phase contrast analysis pipeline can be used to check live-cell cultures before fixation, and provide a measure of culture health. **b)** A BSA gradient was used to isolate mature megakaryocytes. **c)** A wide-field analysis pipeline can be used to measure IMS morphology in a large population of megakaryocytes across multiple conditions. **d)** iSPIM analysis pipeline can be used to measure IMS in high spatial and temporal resolution in live cells. **e)** Expansion microscopy can be used to measure IMS ultra-structures at super resolution. **f)** Potentially, live megakaryocytes could be vitrified or fixed for electron microscopy methods. Electron microscopy would allow sub 10nm resolution of IMS structures.

8.2.1 Wide-field phase contrast microscopy

Phase contrast microscopy of *in vitro* cultures was a live-cell, non-invasive imaging technique, and was the first phase of imaging within the tool kit. This step could provide an immediate overview of culture health, and determine if a culture was proplatelet

forming. Furthermore, phase contrast images could be used as a reference to check against selection during fixation or BSA isolation protocols. Whilst this phase of imaging provided a useful and reliable measure of entire cultures without harming developing megakaryocytes, measures were limited to 2D cross-sections of megakaryocytes rather than more detailed 3D volumetric imaging. Quantitative phase imaging technology may prove a useful tool in providing the same function, but with a more detailed analysis of 3D structure (Park et al., 2018).

8.2.2 Wide-field fluorescent microscopy

Wide-field fluorescence microscopy was used to image a large number of fixed megakaryocytes at low resolution. This step provided a vital coarse overview of megakaryocyte development, and could be used with minimal preparation to measure multiple fixed cultures in parallel. Specifically, wide-field microscopy proved essential when screening the effects of various reagents and inhibitors on IMS maturation. The wide-field analysis pipeline provided quantification of a range of morphological parameters, however rather than describing 3D individual megakaryocytes this analysis described 2D IMS objects within each slice of volumetric tile scans. Segmentation of individual megakaryocytes presented the largest hurdle in single cell identification. Phalloidin labels F-actin within the cell cortex. Initially segmentation attempted to highlight the cell cortex, however the difference in intensity between the IMS and cortex, and the heterogeneity of megakaryocyte cultures caused auto-threshold functions to provide inaccurate masks. Several solutions to this were considered, including:

- Seeding segmentations based on DAPI labelling

High ploidy prevented single seeds within megakaryocytes, and phalloidin still failed to present a reliable mask of individual megakaryocytes.

- Multi-thresholding images into multiple layers

Successful identification of various intensities of IMS within the culture and could be coupled with a seeded watershed for coarse single cell identification.

- Identifying dyes which highlighted the entire megakaryocyte evenly

CD41 antibody provided an even, non-specific stain, leading to the identification of individual megakaryocytes of all stages of maturation. With optimum seeding density, and a standard watershed, megakaryocytes were labelled. Similarly to iSPIM analysis, these megakaryocytes could be cropped and individually measured.

Subsequently, it is recommended that for future measures with the wide-field analysis pipeline, CD41 Alexa-555 is coupled with GP1b-α Alexa-647, and phalloidin-488 at a seeding density of $1x10^6$ cells mL^{-1} for optimum segmentation.

Furthermore, to compare iSPIM and wide-field datasets, the IMS mean grey value was plotted against the IMS volume. Importantly, both iSPIM and wide-field analysis presented a similar relationship between these two measures, establishing that whilst wide-field analysis measures 2D IMS objects, it still presents a ground truth of IMS morphology similar to individually identified 3D megakaryocytes. Additionally, K-means cluster analysis of iSPIM data provided four distinct clusters which could be applied to datasets to predict IMS maturation. The similarity between iSPIM and wide-field data suggests that centroids derived from 3D measures, once scaled could be used to predict clusters on 2D wide-field datasets.

8.2.3 iSPIM microscopy

iSPIM was used to image a medium number of megakaryocytes, but at high temporal and spatial resolution. The major obstacles to iSPIM imaging included preparation time, acquisition time, data size, throughput, and segmentation. Similarly to wide-field analysis, segmentation proved the largest problem with acquiring data from iSPIM. Whilst huge datasets could be obtained overnight, limitations in accurate automated segmentation led to manual segmentation. Whilst this is a realistic option for 2D datasets, 5D datasets with 3D labelling requires a vast amount of manual labour. As with wide-field analysis, adding a non-specific megakaryocyte dye provided an accurate megakaryocyte mask. However, whilst iSPIM eliminated out of focus light, megakaryocytes tended to congregate in the centre of the sample holder leading to issues with accurate water shedding of masks. This issue was resolved by skeletonising masks, and measuring the angle of the object boundary. Assuming that objects were clusters of spherical megakaryocytes, by drawing orthogonal lines from the object boundary based on the boundary angle, the intersection of lines would illustrate the cell centres. For future work with iSPIM, automated segmentation would need to be tackled to make it a viable tool.

During iSPIM analysis K-means cluster analysis was used to data mine and segment the multi-variant dataset into different groups. However, many other multivariate analysis techniques act to segment dataset in different ways, offering alternative and potentially more accurate classification (Aguilar et al., 2013; Stoyanov et al., 2021): linear discriminant analysis, artificial neural networks, and classification trees to name a few. Furthermore, whilst individual IMS objects were

identified within each megakaryocyte, measurements were merged or averaged to provide a single value for each megakaryocyte. However, different biological mechanisms may act on different IMS ROIs within a single megakaryocyte, and individual IMS ROIs may more accurately portray IMS development. Similarly, only a handful of morphological measures was used to describe IMS development. Many more measures could be added to better define stages and aid machine learning driven categorisation and help dissect the morphological change occurring within populations (figure 8.3):

- Number of IMS merges

  The number of times individual IMS objects merge in a single megakaryocyte in a set time.

- Number of IMS divisions

  The number of times individual IMS objects divide in a single megakaryocyte in a set time.

- Number of IMS threads

  The number of IMS threads within a megakaryocyte.

- IMS movement

  The velocity travelled by an IMS object from its origin over a set time.

- IMS movement (away from the centroid)

  The velocity travelled by an IMS object from the megakaryocyte centroid over a set time.

- IMS movement (away from the nucleus)

The velocity travelled by an IMS object from the megakaryocyte centroid over a set time.

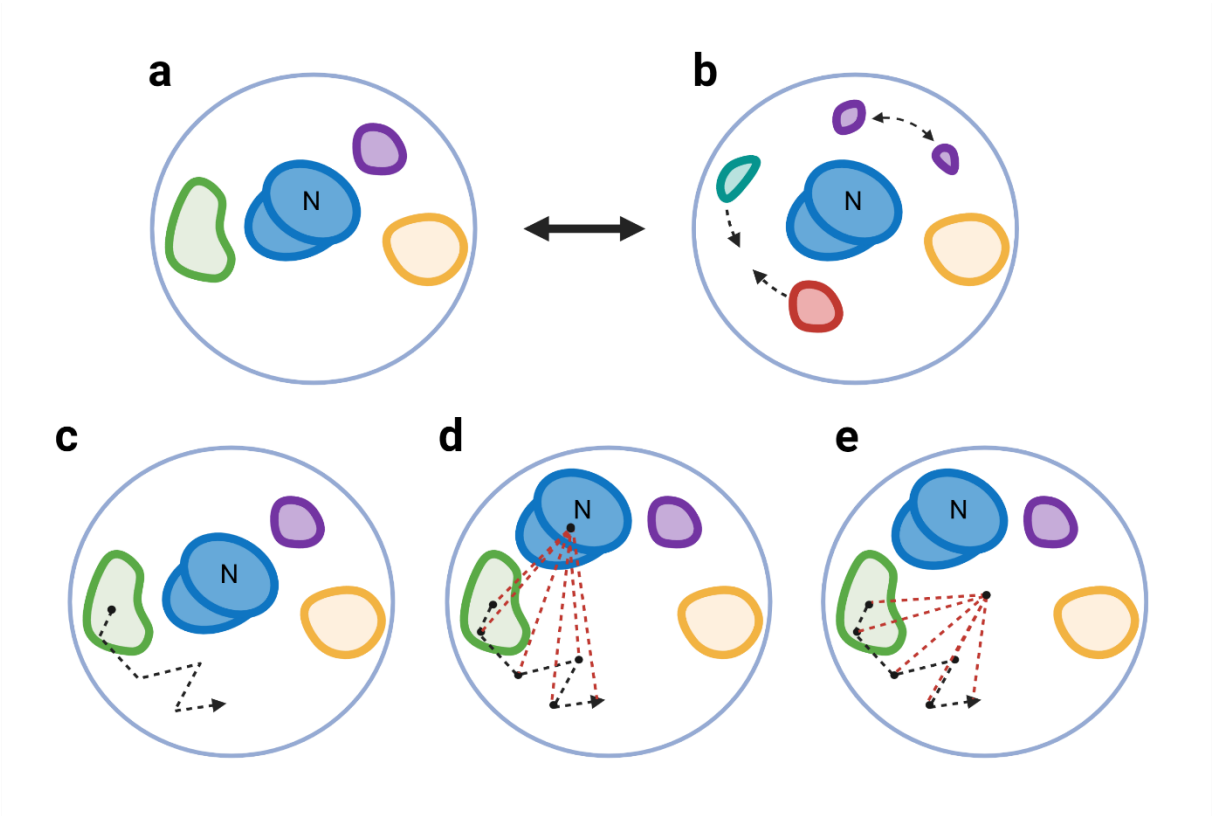


Figure 8.3 **Alternative phenotypic morphometrics**. **a-b)** Number of divisions and merges in IMS objects occurring within a single megakaryocyte, **c)** movement of IMS object, **d)** movement of IMS object relative to the nucleus, and **e)** movement of IMS object relative to megakaryocyte centroid.

8.2.4 Expansion microscopy

Expansion microscopy is a super resolution technique that requires the sample to be fixated, anchored, digested, and isotropically expanded (Chen et al., 2015; Gambarotto et al., 2019; Wassie et al., 2019). Once prepared, samples can be imaged both pre and post expansion, allowing the correlative imaging at both high resolution and low resolution of a single sample. Whilst expansion microscopy was only touched upon in this thesis, it presents a versatile tool for measuring detailed IMS structures. Expanded

samples can be imaged on both wide-field and iSPIM devices, and should be used as an extension of these techniques to probe each stage of IMS development individually. Practically, expansion microscopy is limited by the dyes compatible with anchoring. Whilst GP1b-α and phalloidin were used successfully for expanded samples, lipid dyes such as CellMask were incompatible. Furthermore, saline solutions are required to keep gels in a pre-expanded state. However, saline solutions also corrode metal, potentially damaging dipping objectives such as those used for iSPIM.

For super resolution imaging of IMS stages of maturation, specific IMS stages must first be identified or isolated. Typically, a lower magnification objective is coupled to super resolution devices to facilitate this need, however pre-expansion gels can be used to the same effect. Furthermore, a BSA gradient separates mature from immature megakaryocytes, whilst IMS mean grey value is a distinguishing factor in isolating IMS morphological stage. Therefore, tailoring a BSA gradient could provide a method of accurately dividing megakaryocyte *in vitro* cultures into different stages of megakaryocyte development for higher resolution imaging.

8.2.5 Further potential tools

Another interesting alternative to expansion microscopy is cryo-electron tomography (Baker et al., 2017; Plitzko et al., 2009). iSPIM or phase contrast samples could be taken at a specific point in development, vitrified, and imaged with cryo-correlative light and electron microscopy (CLEM) workflows (Jun et al., 2019; Zhang, 2013). However, since megakaryocytes grow up to 50 µm in diameter, vitrification throughout the cell would only occur under high pressure freezing techniques (Dobro et al., 2010; Manning & Richmond, 2015). High pressure freezing in most cases requires cryo-ultramicrotomy prior to cryo-electron microscopy of vitreous sections (CEMOVIS),

however the recent development of methods for high pressure freezing grids known as the waffle method may also produce quality vitrification (Kelley et al., 2020; Studer et al., 2014). Instead, samples could also be prepared for room temperature electron microscopy. These samples could either be sectioned via ultramicrotomy, or ablated by focused ion beam (FIB) milling prior to scanning electron microscopy (SEM) imaging (Hsieh et al., 2014). Furthermore, super resolution CLEM workflows also exist which would allow the IMS to be viewed in unprecedented detail (Kim et al., 2015).

9 Conclusion

This thesis presents an updated understanding of morphological IMS development, demonstrating that IMS develops through a specific sequence of morphological stages towards proplatelet production. Here we illustrated:

1) A network of IMS tubules preluding and interlinking larger IMS structures, highlighting tubule nodes at branched points.
2) A detailed morphological description and categorisation of megakaryocyte populations, illustrating that megakaryocytes either polarise or continually expand.
3) A definitive pathway for IMS development, highlighting that polarisation and destabilisation preludes proplatelet formation.
4) Rates of IMS development in megakaryocytes.

In probing F-actin dynamics during IMS development we also show evidence for:

1) Arp2/3 mediated F-actin assembly during IMS maturation
2) A mechanism in which F-actin dynamics intimately controls IMS polarisation and IMS expulsion.

Furthermore, we provide workflows and image analysis tools for in-depth analysis of IMS development in murine megakaryocytes. Our toolkit illustrates the use of a range of microscopy techniques which bridge the gap between high resolution, photo-toxicity, and sample size, allowing both detailed measurements of IMS ultrastructure, and IMS development in the wider context of large megakaryocyte populations. These tools, can also potentially be applied to human megakaryocytes. Throughout, we demonstrated the use of:

1) A wide-field analysis pipeline for screening many fixed-cell cultures of large megakaryocyte populations.
2) An IncuCyte analysis pipeline for screening many live-cell cultures of large megakaryocyte populations over time.
3) An iSPIM analysis pipeline for imaging developing IMS structure in high, but diffraction limited spatial and temporal resolution.
4) Expansion microscopy for imaging IMS ultrastructure.

10 ACKNOWLEDGEMENTS

I would like to thank Steve Thomas, my primary supervisor, for his continual support and mentorship throughout my PhD. Without his guidance and frequent pep-talks, I'm very sure I would have been driven mad by the image analysis and iSPIM long ago. I would also like to thank Martyn Mahaut-Smith, my second supervisor, for his assistance, advice on the project. Martyn's enthusiasm during meetings was contagious, and a source of drive throughout the PhD. I consider myself lucky to have had such understanding, patient, and caring advisors.

I'd also like to say a massive thank you to Evie Garlick and Emma Faulkner for being themselves. I felt more than a little lost and confused when I first started the PhD, but after Evie and Emma joined the lab, I would always have a friendly face to talk to, ask for advice, or just vent. Thank you both for your support and friendship. You turned the lab from a ball of anxiety into a welcoming home.

11 REFERENCES

Aguilar-Cuenca, R., Juanes-García, A., & Vicente-Manzanares, M. (2014). Myosin II in mechanotransduction: master and commander of cell migration, morphogenesis, and cancer. *Cellular and Molecular Life Sciences*, *71*(3), 479-492. https://doi.org/10.1007/s00018-013-1439-5

Aguilar, A., Boscher, J., Pertuy, F., Gachet, C., & Léon, C. (2018). Three-Dimensional Culture in a Methylcellulose-Based Hydrogel to Study the Impact of Stiffness on Megakaryocyte Differentiation. In J. M. Gibbins & M. Mahaut-Smith (Eds.), *Platelets and Megakaryocytes : Volume 4, Advanced Protocols and Perspectives* (pp. 139-153). Springer New York. https://doi.org/10.1007/978-1-4939-8585-2_9

Aguilar, A., Pertuy, F., Eckly, A., Strassel, C., Collin, D., Gachet, C., Lanza, F., & Léon, C. (2016). Importance of environmental stiffness for megakaryocyte differentiation and proplatelet formation. *Blood*, *128*(16), 2022-2032. https://doi.org/10.1182/blood-2016-02-699959

Aguilar, C., Westman, E., Muehlboeck, J. S., Mecocci, P., Vellas, B., Tsolaki, M., Kloszewska, I., Soininen, H., Lovestone, S., Spenger, C., Simmons, A., & Wahlund, L.-O. (2013). Different multivariate techniques for automated classification of MRI data in Alzheimer's disease and mild cognitive impairment. *Psychiatry Research: Neuroimaging*, *212*(2), 89-98. https://doi.org/https://doi.org/10.1016/j.pscychresns.2012.11.005

Alizadeh, E., Xu, W., Castle, J., Foss, J., & Prasad, A. (2018). A comprehensive suite of measures to quantify cell shape and actin organization. *bioRxiv*, 372755. https://doi.org/10.1101/372755

Antkowiak, A., Viaud, J., Severin, S., Zanoun, M., Ceccato, L., Chicanne, G., Strassel, C., Eckly, A., Leon, C., Gachet, C., Payrastre, B., & Gaits-Iacovoni, F. (2016). Cdc42-dependent F-actin dynamics drive structuration of the demarcation membrane system in megakaryocytes. *J Thromb Haemost*, *14*(6), 1268-1284. https://doi.org/10.1111/jth.13318

Au - Boscher, J., Au - Gachet, C., Au - Lanza, F., & Au - Léon, C. (2021). Megakaryocyte Culture in 3D Methylcellulose-Based Hydrogel to Improve Cell Maturation and Study the Impact of Stiffness and Confinement. *JoVE*(174), e62511. https://doi.org/doi:10.3791/62511

Au - Schumacher, D., & Au - Søgaard-Andersen, L. (2018). Fluorescence Live-cell Imaging of the Complete Vegetative Cell Cycle of the Slow-growing Social Bacterium Myxococcus xanthus. *JoVE*(136), e57860. https://doi.org/doi:10.3791/57860

Baker, L. A., Grange, M., & Grünewald, K. (2017). Electron cryo-tomography captures macromolecular complexes in native environments. *Current Opinion in Structural Biology*, *46*, 149-156. https://doi.org/https://doi.org/10.1016/j.sbi.2017.08.005

Bender, M., Thon, J. N., Ehrlicher, A. J., Wu, S., Mazutis, L., Deschmann, E., Sola-Visner, M., Italiano, J. E., & Hartwig, J. H. (2015). Microtubule sliding drives proplatelet elongation and is dependent on cytoplasmic dynein. *Blood*, *125*(5), 860-868. https://doi.org/10.1182/blood-2014-09-600858

Bernstein, B. W., & Bamburg, J. R. (2010). ADF/cofilin: a functional node in cell biology. *Trends in cell biology*, *20*(4), 187-195. https://doi.org/10.1016/j.tcb.2010.01.001

Bertović, I., Kurelić, R., Milošević, I., Bender, M., Krauss, M., Haucke, V., & Jurak Begonja, A. (2020). Vps34 derived phosphatidylinositol 3-monophosphate modulates megakaryocyte maturation and proplatelet production through late endosomes/lysosomes. *Journal of Thrombosis and Haemostasis*, *18*(7), 1756-1772. https://doi.org/https://doi.org/10.1111/jth.14764

Bezanilla, M., Gladfelter, A. S., Kovar, D. R., & Lee, W.-L. (2015). Cytoskeletal dynamics: a view from the membrane. *The Journal of cell biology*, *209*(3), 329-337. https://doi.org/10.1083/jcb.201502062

Binder, A., Bockmayr, M., Hägele, M., Wienert, S., Heim, D., Hellweg, K., Ishii, M., Stenzinger, A., Hocke, A., Denkert, C., Müller, K.-R., & Klauschen, F. (2021). Morphological and molecular

breast cancer profiling through explainable machine learning. *Nature Machine Intelligence*, *3*(4), 355-366. https://doi.org/10.1038/s42256-021-00303-4

Bluteau, D., Lordier, L., Di Stefano, A., Chang, Y., Raslova, H., Debili, N., & Vainchenker, W. (2009). Regulation of megakaryocyte maturation and platelet formation [https://doi.org/10.1111/j.1538-7836.2009.03398.x]. *Journal of Thrombosis and Haemostasis*, *7*(s1), 227-234. https://doi.org/https://doi.org/10.1111/j.1538-7836.2009.03398.x

Bock, H.-H. (2007). Clustering Methods: A History of k-Means Algorithms. In P. Brito, G. Cucumel, P. Bertrand, & F. de Carvalho (Eds.), *Selected Contributions in Data Analysis and Classification* (pp. 161-172). Springer Berlin Heidelberg. https://doi.org/10.1007/978-3-540-73560-1_15

Bubb, M. R., Spector, I., Beyer, B. B., & Fosen, K. M. (2000). Effects of Jasplakinolide on the Kinetics of Actin Polymerization: AN EXPLANATION FOR CERTAIN IN VIVO OBSERVATIONS*. *Journal of Biological Chemistry*, *275*(7), 5163-5170. https://doi.org/https://doi.org/10.1074/jbc.275.7.5163

Carlier, M.-F., & Shekhar, S. (2017). Global treadmilling coordinates actin turnover and controls the size of actin networks. *Nature Reviews Molecular Cell Biology*, *18*. https://doi.org/10.1038/nrm.2016.172

Carlsson, A. E. (2018). Membrane bending by actin polymerization. *Current opinion in cell biology*, *50*, 1-7. https://doi.org/10.1016/j.ceb.2017.11.007

Casares, D., Escribá, P. V., & Rosselló, C. A. (2019). Membrane Lipid Composition: Effect on Membrane and Organelle Structure, Function and Compartmentalization and Therapeutic Avenues. *International journal of molecular sciences*, *20*(9), 2167. https://doi.org/10.3390/ijms20092167

Casella, J. F., Flanagan, M. D., & Lin, S. (1981). Cytochalasin D inhibits actin polymerization and induces depolymerization of actin filaments formed during platelet shape change. *Nature*, *293*(5830), 302-305. https://doi.org/10.1038/293302a0

Catherine, S., Anita, E., Catherine, L., Claire, P., Monique, F., Jean-Pierre, C., Christian, G., & François, L. (2009). Intrinsic impaired proplatelet formation and microtubule coil assembly of megakaryocytes in a mouse model of Bernard-Soulier syndrome. *Haematologica*, *94*(6), 800-810. https://doi.org/10.3324/haematol.2008.001032

Chen, F., Tillberg, P. W., & Boyden, E. S. (2015). Expansion microscopy. *Science*, *347*(6221), 543-548. https://doi.org/doi:10.1126/science.1260088

Chetty, N., & Shukla, S. (2014). A Review ON K-means DATA Clustering APPROACH. *4*, 1847-1860.

Chudakov, D. M., Matz, M. V., Lukyanov, S., & Lukyanov, K. A. (2010). Fluorescent Proteins and Their Applications in Imaging Living Cells and Tissues. *Physiological Reviews*, *90*(3), 1103-1163. https://doi.org/10.1152/physrev.00038.2009

Combs, C. A. (2010). Fluorescence microscopy: a concise guide to current imaging methods. *Current protocols in neuroscience*, *Chapter 2*, Unit2.1-Unit2.1. https://doi.org/10.1002/0471142301.ns0201s50

Cunin, P., Bouslama, R., Machlus, K. R., Martínez-Bonet, M., Lee, P. Y., Wactor, A., Nelson-Maney, N., Morris, A., Guo, L., Weyrich, A., Sola-Visner, M., Boilard, E., Italiano, J. E., & Nigrovic, P. A. (2019). Megakaryocyte emperipolesis mediates membrane transfer from intracytoplasmic neutrophils to platelets. *eLife*, *8*, e44031. https://doi.org/10.7554/eLife.44031

Dautel, S. E., Kyle, J. E., Clair, G., Sontag, R. L., Weitz, K. K., Shukla, A. K., Nguyen, S. N., Kim, Y.-M., Zink, E. M., Luders, T., Frevert, C. W., Gharib, S. A., Laskin, J., Carson, J. P., Metz, T. O., Corley, R. A., & Ansong, C. (2017). Lipidomics reveals dramatic lipid compositional changes in the maturing postnatal lung. *Scientific Reports*, *7*(1), 40555. https://doi.org/10.1038/srep40555

Dobro, M. J., Melanson, L. A., Jensen, G. J., & McDowall, A. W. (2010). Chapter Three - Plunge Freezing for Electron Cryomicroscopy. In G. J. Jensen (Ed.), *Methods in Enzymology* (Vol. 481, pp. 63-82). Academic Press. https://doi.org/https://doi.org/10.1016/S0076-6879(10)81003-1

Drachman, J. G. (2004). Inherited thrombocytopenia: when a low platelet count does not mean ITP. *Blood*, *103*(2), 390-398. https://doi.org/10.1182/blood-2003-05-1742

Dunois-Lardé, C., Capron, C., Fichelson, S., Bauer, T., Cramer-Bordé, E., & Baruch, D. (2009). Exposure of human megakaryocytes to high shear rates accelerates platelet production. *Blood*, *114*(9), 1875-1883. https://doi.org/10.1182/blood-2009-03-209205

Dütting, S., Gaits-Iacovoni, F., Stegner, D., Popp, M., Antkowiak, A., van Eeuwijk, J. M. M., Nurden, P., Stritt, S., Heib, T., Aurbach, K., Angay, O., Cherpokova, D., Heinz, N., Baig, A. A., Gorelashvili, M. G., Gerner, F., Heinze, K. G., Ware, J., Krohne, G., . . . Nieswandt, B. (2017). A Cdc42/RhoA regulatory circuit downstream of glycoprotein Ib guides transendothelial platelet biogenesis. *Nature Communications*, *8*(1), 15838. https://doi.org/10.1038/ncomms15838

Duwé, S., & Dedecker, P. (2019). Optimizing the fluorescent protein toolbox and its use. *Current Opinion in Biotechnology*, *58*, 183-191. https://doi.org/https://doi.org/10.1016/j.copbio.2019.04.006

Eckly, A., Heijnen, H., Pertuy, F., Geerts, W., Proamer, F., Rinckel, J.-Y., Léon, C., Lanza, F., & Gachet, C. (2014). Biogenesis of the demarcation membrane system (DMS) in megakaryocytes. *Blood*, *123*(6), 921-930. https://doi.org/10.1182/blood-2013-03-492330

Fischer, A., Jacobson, K., Rose, J., & Zeller, R. (2008). Preparation of slides and coverslips for microscopy. *CSH protocols*, *2008*, pdb.prot4988.

Fletcher, D. A., & Mullins, R. D. (2010). Cell mechanics and the cytoskeleton. *Nature*, *463*(7280), 485-492. https://doi.org/10.1038/nature08908

Fujiwara, I., Vavylonis, D., & Pollard, T. D. (2007). Polymerization kinetics of ADP- and ADP-P_i-actin determined by fluorescence microscopy. *Proceedings of the National Academy of Sciences*, *104*(21), 8827-8832. https://doi.org/doi:10.1073/pnas.0702510104

Gambarotto, D., Zwettler, F. U., Le Guennec, M., Schmidt-Cernohorska, M., Fortun, D., Borgers, S., Heine, J., Schloetel, J.-G., Reuss, M., Unser, M., Boyden, E. S., Sauer, M., Hamel, V., & Guichard, P. (2019). Imaging cellular ultrastructures using expansion microscopy (U-ExM). *Nature Methods*, *16*(1), 71-74. https://doi.org/10.1038/s41592-018-0238-1

Gao, Y., Smith, E., Ker, E., Campbell, P., Cheng, E.-c., Zou, S., Lin, S., Wang, L., Halene, S., & Krause, D. S. (2012). Role of RhoA-specific guanine exchange factors in regulation of endomitosis in megakaryocytes. *Developmental cell*, *22*(3), 573-584. https://doi.org/10.1016/j.devcel.2011.12.019

Gobbi, G., Mirandola, P., Carubbi, C., Masselli, E., Sykes, S. M., Ferraro, F., Nouvenne, A., Thon, J. N., Italiano, J. E., & Vitale, M. (2013). Proplatelet generation in the mouse requires PKCε-dependent RhoA inhibition. *Blood*, *122*(7), 1305-1311. https://doi.org/https://doi.org/10.1182/blood-2013-04-490599

Goldschmidt-Clermont, P. J., Machesky, L. M., Baldassare, J. J., & Pollard, T. D. (1990). The Actin-Binding Protein Profilin Binds to PIP₂ and Inhibits Its Hydrolysis by Phospholipase C. *Science*, *247*(4950), 1575-1578. https://doi.org/doi:10.1126/science.2157283

Goode, B. L., & Eck, M. J. (2007). Mechanism and Function of Formins in the Control of Actin Assembly. *Annual Review of Biochemistry*, *76*(1), 593-627. https://doi.org/10.1146/annurev.biochem.75.103004.142647

Gritti, N., Kienle, S., Filina, O., & van Zon, J. S. (2016). Long-term time-lapse microscopy of C. elegans post-embryonic development. *Nature Communications*, *7*(1), 12500. https://doi.org/10.1038/ncomms12500

Hasin, Y., Seldin, M., & Lusis, A. (2017). Multi-omics approaches to disease. *Genome Biology*, *18*(1), 83. https://doi.org/10.1186/s13059-017-1215-1

Heissler, S. M., & Manstein, D. J. (2013). Nonmuscle myosin-2: mix and match. *Cellular and molecular life sciences : CMLS*, *70*(1), 1-21. https://doi.org/10.1007/s00018-012-1002-9

Hetrick, B., Han, M. S., Helgeson, L. A., & Nolen, B. J. (2013). Small molecules CK-666 and CK-869 inhibit actin-related protein 2/3 complex by blocking an activating conformational change. *Chemistry & biology*, *20*(5), 701-712. https://doi.org/10.1016/j.chembiol.2013.03.019

Hoebe, R. A., Van Oven, C. H., Gadella, T. W. J., Dhonukshe, P. B., Van Noorden, C. J. F., & Manders, E. M. M. (2007). Controlled light-exposure microscopy reduces photobleaching and phototoxicity in fluorescence live-cell imaging. *Nature Biotechnology*, *25*(2), 249-253. https://doi.org/10.1038/nbt1278

Holinstat, M. (2017). Normal platelet function. *Cancer metastasis reviews*, *36*(2), 195-198. https://doi.org/10.1007/s10555-017-9677-x

Holzinger, A. (2010). Jasplakinolide: An Actin-Specific Reagent that Promotes Actin Polymerization. In R. H. Gavin (Ed.), *Cytoskeleton Methods and Protocols* (pp. 71-87). Humana Press. https://doi.org/10.1007/978-1-60761-376-3_4

Hsieh, C., Schmelzer, T., Kishchenko, G., Wagenknecht, T., & Marko, M. (2014). Practical workflow for cryo focused-ion-beam milling of tissues and cells for cryo-TEM tomography. *Journal of Structural Biology*, *185*(1), 32-41. https://doi.org/https://doi.org/10.1016/j.jsb.2013.10.019

Icha, J., Weber, M., Waters, J. C., & Norden, C. (2017). Phototoxicity in live fluorescence microscopy, and how to avoid it. *BioEssays*, *39*(8), 1700003. https://doi.org/https://doi.org/10.1002/bies.201700003

Isogai, T., van der Kammen, R., & Innocenti, M. (2015). SMIFH2 has effects on Formins and p53 that perturb the cell cytoskeleton. *Scientific Reports*, *5*(1), 9802. https://doi.org/10.1038/srep09802

Janmey, P. A., Bucki, R., & Radhakrishnan, R. (2018). Regulation of actin assembly by PI(4,5)P2 and other inositol phospholipids: An update on possible mechanisms. *Biochemical and biophysical research communications*, *506*(2), 307-314. https://doi.org/10.1016/j.bbrc.2018.07.155

Jensen, L. J., Kuhn, M., Stark, M., Chaffron, S., Creevey, C., Muller, J., Doerks, T., Julien, P., Roth, A., Simonovic, M., Bork, P., & von Mering, C. (2009). STRING 8--a global view on proteins and their functional interactions in 630 organisms. *Nucleic acids research*, *37*(Database issue), D412-D416. https://doi.org/10.1093/nar/gkn760

Jin, Y.-Y., Wu, J., Chen, T.-X., & Chen, J. (2019). When WAS Gene Diagnosis Is Needed: Seeking Clues Through Comparison Between Patients With Wiskott-Aldrich Syndrome and Idiopathic Thrombocytopenic Purpura [Original Research]. *Frontiers in Immunology*, *10*. https://doi.org/10.3389/fimmu.2019.01549

Johnson, B., Fletcher, S. J., & Morgan, N. V. (2016). Inherited thrombocytopenia: novel insights into megakaryocyte maturation, proplatelet formation and platelet lifespan. *Platelets*, *27*(6), 519-525. https://doi.org/10.3109/09537104.2016.1148806

Jun, S., Ro, H.-J., Bharda, A., Kim, S. I., Jeoung, D., & Jung, H. S. (2019). Advances in Cryo-Correlative Light and Electron Microscopy: Applications for Studying Molecular and Cellular Events. *The Protein Journal*, *38*(6), 609-615. https://doi.org/10.1007/s10930-019-09856-1

Jurak Begonja, A., Hoffmeister, K. M., Hartwig, J. H., & Falet, H. (2011). FlnA-null megakaryocytes prematurely release large and fragile platelets that circulate poorly. *Blood*, *118*(8), 2285-2295. https://doi.org/10.1182/blood-2011-04-348482

Kanaji, T., Ware, J., Okamura, T., & Newman, P. J. (2012). GPIbα regulates platelet size by controlling the subcellular localization of filamin. *Blood*, *119*(12), 2906-2913. https://doi.org/10.1182/blood-2011-08-376566

Kelley, K., Jaroenlak, P., Raczkowski, A. M., Eng, E. T., Bhabha, G., Potter, C. S., Carragher, B., & Noble, A. J. (2020). Waffle method: A general and flexible approach for FIB-milling small and anisotropically oriented samples. *bioRxiv*, 2020.2010.2028.359372. https://doi.org/10.1101/2020.10.28.359372

Kiepas, A., Voorand, E., Mubaid, F., Siegel, P. M., & Brown, C. M. (2020). Optimizing live-cell fluorescence imaging conditions to minimize phototoxicity. *Journal of Cell Science*, *133*(4). https://doi.org/10.1242/jcs.242834

Kim, D., Deerinck, T. J., Sigal, Y. M., Babcock, H. P., Ellisman, M. H., & Zhuang, X. (2015). Correlative Stochastic Optical Reconstruction Microscopy and Electron Microscopy. *PloS one*, *10*(4), e0124581. https://doi.org/10.1371/journal.pone.0124581

Kumar, A., Wu, Y., Christensen, R., Chandris, P., Gandler, W., McCreedy, E., Bokinsky, A., Colón-Ramos, D. A., Bao, Z., McAuliffe, M., Rondeau, G., & Shroff, H. (2014). Dual-view plane illumination microscopy for rapid and spatially isotropic imaging. *Nature Protocols*, *9*(11), 2555-2573. https://doi.org/10.1038/nprot.2014.172

Kuznetsova, O. B., Savchenko, E. A., Andryakov, A. A., Savchenko, E. Y., & Musakulova, Z. A. (2019). Image processing in total internal reflection fluorescence microscopy. *Journal of Physics: Conference Series*, *1236*(1), 012039. https://doi.org/10.1088/1742-6596/1236/1/012039

Laissue, P. P., Alghamdi, R. A., Tomancak, P., Reynaud, E. G., & Shroff, H. (2017). Assessing phototoxicity in live fluorescence imaging. *Nature Methods*, *14*(7), 657-661. https://doi.org/10.1038/nmeth.4344

Lane, J., Martin, T., Weeks, H. P., & Jiang, W. G. (2014). Structure and Role of WASP and WAVE in Rho GTPase Signalling in Cancer. *Cancer Genomics - Proteomics*, *11*(3), 155. http://cgp.iiarjournals.org/content/11/3/155.abstract

Lederer, A. R., & La Manno, G. (2020). The emergence and promise of single-cell temporal-omics approaches. *Current Opinion in Biotechnology*, *63*, 70-78. https://doi.org/https://doi.org/10.1016/j.copbio.2019.12.005

Leiva, O., Leon, C., Kah Ng, S., Mangin, P., Gachet, C., & Ravid, K. (2018). The role of extracellular matrix stiffness in megakaryocyte and platelet development and function. *American journal of hematology*, *93*(3), 430-441. https://doi.org/10.1002/ajh.25008

Letort, G., Ennomani, H., Gressin, L., Théry, M., & Blanchoin, L. (2015). Dynamic reorganization of the actin cytoskeleton. *F1000Research*, *4*, F1000 Faculty Rev-1940. https://doi.org/10.12688/f1000research.6374.1

Levy, U., Silberberg, Y., & Davidson, N. (2019). Mathematics of vectorial Gaussian beams. *Advances in Optics and Photonics*, *11*(4), 828-891. https://doi.org/10.1364/AOP.11.000828

Lobo, J., See, E. Y.-S., Biggs, M., & Pandit, A. (2016). An insight into morphometric descriptors of cell shape that pertain to regenerative medicine [https://doi.org/10.1002/term.1994]. *Journal of Tissue Engineering and Regenerative Medicine*, *10*(7), 539-553. https://doi.org/https://doi.org/10.1002/term.1994

Lordier, L., Bluteau, D., Jalil, A., Legrand, C., Pan, J., Rameau, P., Jouni, D., Bluteau, O., Mercher, T., Leon, C., Gachet, C., Debili, N., Vainchenker, W., Raslova, H., & Chang, Y. (2012). RUNX1-induced silencing of non-muscle myosin heavy chain IIB contributes to megakaryocyte polyploidization. *Nature Communications*, *3*(1), 717. https://doi.org/10.1038/ncomms1704

Lürig, M. D., Donoughe, S., Svensson, E. I., Porto, A., & Tsuboi, M. (2021). Computer Vision, Machine Learning, and the Promise of Phenomics in Ecology and Evolutionary Biology [Review]. *Frontiers in Ecology and Evolution*, *9*. https://doi.org/10.3389/fevo.2021.642774

Machlus, K. R., & Italiano, J. E., Jr. (2013). The incredible journey: From megakaryocyte development to platelet formation. *Journal of Cell Biology*, *201*(6), 785-796. https://doi.org/10.1083/jcb.201304054

Macmillan, D., & McCarron, J. G. (2010). The phospholipase C inhibitor U-73122 inhibits Ca(2+) release from the intracellular sarcoplasmic reticulum Ca(2+) store by inhibiting Ca(2+) pumps in smooth muscle. *British journal of pharmacology*, *160*(6), 1295-1301. https://doi.org/10.1111/j.1476-5381.2010.00771.x

Mahaut-Smith, M. P., Thomas, D., Higham, A. B., Usher-Smith, J. A., Hussain, J. F., Martinez-Pinna, J., Skepper, J. N., & Mason, M. J. (2003). Properties of the Demarcation Membrane System in

Living Rat Megakaryocytes. *Biophysical Journal*, *84*(4), 2646-2654. https://doi.org/https://doi.org/10.1016/S0006-3495(03)75070-X

Malara, A., Currao, M., Gruppi, C., Celesti, G., Viarengo, G., Buracchi, C., Laghi, L., Kaplan, D. L., & Balduini, A. (2014). Megakaryocytes Contribute to the Bone Marrow-Matrix Environment by Expressing Fibronectin, Type IV Collagen, and Laminin [https://doi.org/10.1002/stem.1626]. *STEM CELLS*, *32*(4), 926-937. https://doi.org/https://doi.org/10.1002/stem.1626

Málnási-Csizmadia, A., & Kovács, M. (2010). Emerging complex pathways of the actomyosin powerstroke. *Trends in biochemical sciences*, *35*(12), 684-690. https://doi.org/10.1016/j.tibs.2010.07.012

Manning, L., & Richmond, J. (2015). High-Pressure Freeze and Freeze Substitution Electron Microscopy in C. elegans. In D. Biron & G. Haspel (Eds.), *C. elegans: Methods and Applications* (pp. 121-140). Humana Press. https://doi.org/10.1007/978-1-4939-2842-2_10

Mattia, G., Vulcano, F., Milazzo, L., Barca, A., Macioce, G., Giampaolo, A., & Hassan, H. J. (2002). Different ploidy levels of megakaryocytes generated from peripheral or cord blood CD34+ cells are correlated with different levels of platelet release. *Blood*, *99*(3), 888-897. https://doi.org/10.1182/blood.V99.3.888

Mazia, D., Schatten, G., & Sale, W. (1975). Adhesion of cells to surfaces coated with polylysine. Applications to electron microscopy. *The Journal of cell biology*, *66*(1), 198-200. https://doi.org/10.1083/jcb.66.1.198

McMahon, H. T., & Boucrot, E. (2015). Membrane curvature at a glance. *Journal of Cell Science*, *128*(6), 1065-1070. https://doi.org/10.1242/jcs.114454

Mekchay, P., Ingrungruanglert, P., Suphapeetiporn, K., Sosothikul, D., Ji-au, W., Le Grand, S., Israsena, N., & Rojnuckarin, P. (2019). Study of Bernard–Soulier Syndrome Megakaryocytes and Platelets Using Patient-Derived Induced Pluripotent Stem Cells. *Thrombosis and Haemostasis*, *119*. https://doi.org/10.1055/s-0039-1693409

Mendes Pinto, I., Rubinstein, B., Kucharavy, A., Unruh, J. R., & Li, R. (2012). Actin depolymerization drives actomyosin ring contraction during budding yeast cytokinesis. *Developmental cell*, *22*(6), 1247-1260. https://doi.org/10.1016/j.devcel.2012.04.015

Miao, Z., Humphreys, B. D., McMahon, A. P., & Kim, J. (2021). Multi-omics integration in the age of million single-cell data. *Nature Reviews Nephrology*, *17*(11), 710-724. https://doi.org/10.1038/s41581-021-00463-x

N. Barrachina, M., Pernes, G., Becker, I. C., Groeneveld, D., Luyendyk, J. P., Meikle, P. J., Lancaster, G. I., Murphy, A. J., & Machlus, K. (2021). Manipulation of Fatty Acid Metabolism Impairs Megakaryocyte Differentiation and Platelet Production. *Blood*, *138*, 577. https://doi.org/https://doi.org/10.1182/blood-2021-151316

Nakamura, Y., & Fukami, K. (2017). Regulation and physiological functions of mammalian phospholipase C. *The Journal of Biochemistry*, *161*(4), 315-321. https://doi.org/10.1093/jb/mvw094

Nakao, K., & Angrist, A. A. (1968). Membrane Surface Specialization of Blood Platelet and Megakaryocyte. *Nature*, *217*(5132), 960-961. https://doi.org/10.1038/217960a0

Nejedla, M., Sadi, S., Sulimenko, V., de Almeida, F. N., Blom, H., Draber, P., Aspenström, P., & Karlsson, R. (2016). Profilin connects actin assembly with microtubule dynamics. *Molecular biology of the cell*, *27*(15), 2381-2393. https://doi.org/10.1091/mbc.E15-11-0799

Nurden, P., Debili, N., Coupry, I., Bryckaert, M., Youlyouz-Marfak, I., Solé, G., Pons, A.-C., Berrou, E., Adam, F., Kauskot, A., Lamazière, J.-M. D., Rameau, P., Fergelot, P., Rooryck, C., Cailley, D., Arveiler, B., Lacombe, D., Vainchenker, W., Nurden, A., & Goizet, C. (2011). Thrombocytopenia resulting from mutations in filamin A can be expressed as an isolated syndrome. *Blood*, *118*(22), 5928-5937. https://doi.org/10.1182/blood-2011-07-365601

Nürnberg, A., Kitzing, T., & Grosse, R. (2011). Nucleating actin for invasion. *Nature Reviews Cancer*, *11*(3), 177-187. https://doi.org/10.1038/nrc3003

Oda, T., Iwasa, M., Aihara, T., Maéda, Y., & Narita, A. (2009). The nature of the globular- to fibrous-actin transition. *Nature*, *457*(7228), 441-445. https://doi.org/10.1038/nature07685

Osman, S., Taylor, K. A., Allcock, N., Rainbow, R. D., & Mahaut-Smith, M. P. (2016). Detachment of surface membrane invagination systems by cationic amphiphilic drugs. *Scientific Reports*, *6*, 18536-18536. https://doi.org/10.1038/srep18536

Pampaloni, F., Ansari, N., Girard, P., & Stelzer, E. H. K. (2011, 2011/05/22). Light sheet-based fluorescence microscopy (LSFM) reduces phototoxic effects and provides new means for the modern life sciences.*Proceedings of SPIE-OSA Biomedical Optics* Advanced Microscopy Techniques II, Munich.

Pan, J., Lordier, L., Meyran, D., Rameau, P., Lecluse, Y., Kitchen-Goosen, S., Badirou, I., Mokrani, H., Narumiya, S., Alberts, A. S., Vainchenker, W., & Chang, Y. (2014). The formin DIAPH1 (mDia1) regulates megakaryocyte proplatelet formation by remodeling the actin and microtubule cytoskeletons. *Blood*, *124*(26), 3967-3977. https://doi.org/https://doi.org/10.1182/blood-2013-12-544924

Park, Y., Depeursinge, C., & Popescu, G. (2018). Quantitative phase imaging in biomedicine. *Nature Photonics*, *12*(10), 578-589. https://doi.org/10.1038/s41566-018-0253-x

Pienimaeki-Roemer, A., Kuhlmann, K., Böttcher, A., Konovalova, T., Black, A., Orsó, E., Liebisch, G., Ahrens, M., Eisenacher, M., Meyer, H. E., & Schmitz, G. (2015). Lipidomic and proteomic characterization of platelet extracellular vesicle subfractions from senescent platelets. *Transfusion*, *55*(3), 507-521. https://doi.org/https://doi.org/10.1111/trf.12874

Pizarro-Cerdá, J., Chorev, D. S., Geiger, B., & Cossart, P. (2017). The Diverse Family of Arp2/3 Complexes. *Trends in cell biology*, *27*(2), 93-100. https://doi.org/10.1016/j.tcb.2016.08.001

Pleines, I., Cherpokova, D., & Bender, M. (2019). Rho GTPases and their downstream effectors in megakaryocyte biology. *Platelets*, *30*(1), 9-16. https://doi.org/10.1080/09537104.2018.1478071

Pleines, I., Eckly, A., Elvers, M., Hagedorn, I., Eliautou, S., Bender, M., Wu, X., Lanza, F., Gachet, C., Brakebusch, C., & Nieswandt, B. (2010). Multiple alterations of platelet functions dominated by increased secretion in mice lacking Cdc42 in platelets. *Blood*, *115*(16), 3364-3373. https://doi.org/10.1182/blood-2009-09-242271

Plitzko, J. M., Rigort, A., & Leis, A. (2009). Correlative cryo-light microscopy and cryo-electron tomography: from cellular territories to molecular landscapes. *Current Opinion in Biotechnology*, *20*(1), 83-89. https://doi.org/https://doi.org/10.1016/j.copbio.2009.03.008

Pluthero, F. G., & Kahr, W. H. A. (2016). Platelet production: new players in the field. *Blood*, *127*(7), 797-799. https://doi.org/10.1182/blood-2016-01-687707

Pollard, T. D. (2007). Regulation of Actin Filament Assembly by Arp2/3 Complex and Formins. *Annual Review of Biophysics and Biomolecular Structure*, *36*(1), 451-477. https://doi.org/10.1146/annurev.biophys.35.040405.101936

Pollard, T. D., Blanchoin, L., & Mullins, R. D. (2000). Molecular Mechanisms Controlling Actin Filament Dynamics in Nonmuscle Cells. *Annual Review of Biophysics and Biomolecular Structure*, *29*(1), 545-576. https://doi.org/10.1146/annurev.biophys.29.1.545

Poujol, C., Ware, J., Nieswandt, B., Nurden, A. T., & Nurden, P. (2002). Absence of GPIbalpha is responsible for aberrant membrane development during megakaryocyte maturation: ultrastructural study using a transgenic model. *Experimental hematology*, *30 4*, 352-360.

Poukkula, M., Kremneva, E., Serlachius, M., & Lappalainen, P. (2011). Actin-depolymerizing factor homology domain: A conserved fold performing diverse roles in cytoskeletal dynamics. *Cytoskeleton*, *68*(9), 471-490. https://doi.org/https://doi.org/10.1002/cm.20530

Poulter, N. S., & Thomas, S. G. (2015). Cytoskeletal regulation of platelet formation: Coordination of F-actin and microtubules. *The International Journal of Biochemistry & Cell Biology*, *66*, 69-74. https://doi.org/https://doi.org/10.1016/j.biocel.2015.07.008

Recio-Tótoro, B., Guerrero, A., & Lanz-Mendoza, H. (2021). Description, measurement, and automatic classification of the Plasmodium berghei oocyst morphology during early differentiation in vitro. *Current Research in Cell Biology*, *2*, 100007. https://doi.org/https://doi.org/10.1016/j.crcbio.2021.100007

Richardson, J. L., Shivdasani, R. A., Boers, C., Hartwig, J. H., & Italiano, J. E., Jr. (2005). Mechanisms of organelle transport and capture along proplatelets during platelet production. *Blood*, *106*(13), 4066-4075. https://doi.org/10.1182/blood-2005-06-2206

Riedl, J., Flynn, K. C., Raducanu, A., Gärtner, F., Beck, G., Bösl, M., Bradke, F., Massberg, S., Aszodi, A., Sixt, M., & Wedlich-Söldner, R. (2010). Lifeact mice for studying F-actin dynamics. *Nature Methods*, *7*(3), 168-169. https://doi.org/10.1038/nmeth0310-168

Rizvi, S. A., Neidt, E. M., Cui, J., Feiger, Z., Skau, C. T., Gardel, M. L., Kozmin, S. A., & Kovar, D. R. (2009). Identification and characterization of a small molecule inhibitor of formin-mediated actin assembly. *Chemistry & biology*, *16*(11), 1158-1168. https://doi.org/10.1016/j.chembiol.2009.10.006

Roy, M., Chakraborty, S., Mali, K., Chatterjee, S., Banerjee, S., Mitra, S., Naskar, R., & Bhattacharjee, A. (2017, 19-21 Oct. 2017). Cellular image processing using morphological analysis. 2017 IEEE 8th Annual Ubiquitous Computing, Electronics and Mobile Communication Conference (UEMCON),

Saarikangas, J., Zhao, H., & Lappalainen, P. (2010). Regulation of the Actin Cytoskeleton-Plasma Membrane Interplay by Phosphoinositides. *Physiological Reviews*, *90*(1), 259-289. https://doi.org/10.1152/physrev.00036.2009

Sabri, S., Foudi, A., Boukour, S., Franc, B., Charrier, S., Jandrot-Perrus, M., Farndale, R. W., Jalil, A., Blundell, M. P., Cramer, E. M., Louache, F., Debili, N., Thrasher, A. J., & Vainchenker, W. (2006). Deficiency in the Wiskott-Aldrich protein induces premature proplatelet formation and platelet production in the bone marrow compartment. *Blood*, *108*(1), 134-140. https://doi.org/https://doi.org/10.1182/blood-2005-03-1219

Sánchez-Corrales, Y. E., Hartley, M., van Rooij, J., Marée, A. F. M., & Grieneisen, V. A. (2018). Morphometrics of complex cell shapes: lobe contribution elliptic Fourier analysis (LOCO-EFA). *Development*, *145*(6), dev156778. https://doi.org/10.1242/dev.156778

Sasaki, A. (2022). Recent advances in the standardization of fluorescence microscopy for quantitative image analysis. *Biophysical Reviews*, *14*(1), 33-39. https://doi.org/10.1007/s12551-021-00871-0

Schachtner, H., Calaminus, S. D. J., Sinclair, A., Monypenny, J., Blundell, M. P., Leon, C., Holyoake, T. L., Thrasher, A. J., Michie, A. M., Vukovic, M., Gachet, C., Jones, G. E., Thomas, S. G., Watson, S. P., & Machesky, L. M. (2013). Megakaryocytes assemble podosomes that degrade matrix and protrude through basement membrane. *Blood*, *121*(13), 2542-2552. https://doi.org/https://doi.org/10.1182/blood-2012-07-443457

Schliwa, M. (1982). Action of cytochalasin D on cytoskeletal networks. *The Journal of cell biology*, *92*(1), 79-91. https://doi.org/10.1083/jcb.92.1.79

Schönichen, A., & Geyer, M. (2010). Fifteen formins for an actin filament: A molecular view on the regulation of human formins. *Biochimica et Biophysica Acta (BBA) - Molecular Cell Research*, *1803*(2), 152-163. https://doi.org/https://doi.org/10.1016/j.bbamcr.2010.01.014

Schulze, H., Korpal, M., Hurov, J., Kim, S.-W., Zhang, J., Cantley, L. C., Graf, T., & Shivdasani, R. A. (2005). Phosphatidyl Inositol (4,5)P2 Marks Megakaryocyte Internal Membranes and Is Associated with Megakaryocyte Maturation and Platelet Release. *Blood*, *106*(11), 732-732. https://doi.org/10.1182/blood.V106.11.732.732

Schulze, H., Korpal, M., Hurov, J., Kim, S.-W., Zhang, J., Cantley, L. C., Graf, T., & Shivdasani, R. A. (2006). Characterization of the megakaryocyte demarcation membrane system and its role in thrombopoiesis. *Blood*, *107*(10), 3868-3875. https://doi.org/10.1182/blood-2005-07-2755

Senju, Y., Kalimeri, M., Koskela, E. V., Somerharju, P., Zhao, H., Vattulainen, I., & Lappalainen, P. (2017). Mechanistic principles underlying regulation of the actin cytoskeleton by phosphoinositides. *Proceedings of the National Academy of Sciences*, *114*(43), E8977. https://doi.org/10.1073/pnas.1705032114

Shibasaki, Y., Ishihara, H., Kizuki, N., Asano, T., Oka, Y., & Yazaki, Y. (1997). Massive actin polymerization induced by phosphatidylinositol-4-phosphate 5-kinase in vivo. *The Journal of biological chemistry*.

Sit, S.-T., & Manser, E. (2011). Rho GTPases and their role in organizing the actin cytoskeleton. *Journal of Cell Science*, *124*(5), 679-683. https://doi.org/10.1242/jcs.064964

Spence, H. J., Dhillon, A. S., James, M., & Winder, S. J. (2004). Dystroglycan, a scaffold for the ERK-MAP kinase cascade. *EMBO reports*, *5*(5), 484-489. https://doi.org/10.1038/sj.embor.7400140

Stahelin, R. V. (2009). Lipid binding domains: more than simple lipid effectors. *Journal of lipid research*, *50 Suppl*(Suppl), S299-S304. https://doi.org/10.1194/jlr.R800078-JLR200

Stegner, D., vanEeuwijk, J. M. M., Angay, O., Gorelashvili, M. G., Semeniak, D., Pinnecker, J., Schmithausen, P., Meyer, I., Friedrich, M., Dütting, S., Brede, C., Beilhack, A., Schulze, H., Nieswandt, B., & Heinze, K. G. (2017). Thrombopoiesis is spatially regulated by the bone marrow vasculature. *Nature Communications*, *8*(1), 127. https://doi.org/10.1038/s41467-017-00201-7

Stelzer, E. H. K. (2015). Light-sheet fluorescence microscopy for quantitative biology. *Nature Methods*, *12*(1), 23-26. https://doi.org/10.1038/nmeth.3219

Stevenson, B. R., & Begg, D. A. (1994). Concentration-dependent effects of cytochalasin D on tight junctions and actin filaments in MDCK epithelial cells. *Journal of Cell Science*, *107*(3), 367-375. https://doi.org/10.1242/jcs.107.3.367

Stoyanov, D., Kandilarova, S., Aryutova, K., Paunova, R., Todeva-Radneva, A., Latypova, A., & Kherif, F. (2021). Multivariate Analysis of Structural and Functional Neuroimaging Can Inform Psychiatric Differential Diagnosis. *Diagnostics*, *11*(1), 19. https://www.mdpi.com/2075-4418/11/1/19

Strassel, C., Eckly, A., Léon, C., Moog, S., Cazenave, J.-P., Gachet, C., & Lanza, F. (2012). Hirudin and heparin enable efficient megakaryocyte differentiation of mouse bone marrow progenitors. *Experimental Cell Research*, *318*(1), 25-32. https://doi.org/https://doi.org/10.1016/j.yexcr.2011.10.003

Strassel, C., Eckly, A., Léon, C., Petitjean, C., Freund, M., Cazenave, J. P., Gachet, C., & Lanza, F. (2009). Intrinsic impaired proplatelet formation and microtubule coil assembly of megakaryocytes in a mouse model of Bernard-Soulier syndrome. *Haematologica*, *94*(6), 800-810. https://doi.org/10.3324/haematol.2008.001032

Studer, D., Klein, A., Iacovache, I., Gnaegi, H., & Zuber, B. (2014). A new tool based on two micromanipulators facilitates the handling of ultrathin cryosection ribbons. *Journal of Structural Biology*, *185*(1), 125-128. https://doi.org/https://doi.org/10.1016/j.jsb.2013.11.005

Suarez, C., Carroll, R. T., Burke, T. A., Christensen, J. R., Bestul, A. J., Sees, J. A., James, M. L., Sirotkin, V., & Kovar, D. R. (2015). Profilin regulates F-actin network homeostasis by favoring formin over Arp2/3 complex. *Developmental cell*, *32*(1), 43-53. https://doi.org/10.1016/j.devcel.2014.10.027

Suetsugu, S., Kurisu, S., & Takenawa, T. (2014). Dynamic Shaping of Cellular Membranes by Phospholipids and Membrane-Deforming Proteins. *Physiological Reviews*, *94*(4), 1219-1248. https://doi.org/10.1152/physrev.00040.2013

Tarazona, S., Balzano-Nogueira, L., Gómez-Cabrero, D., Schmidt, A., Imhof, A., Hankemeier, T., Tegnér, J., Westerhuis, J. A., & Conesa, A. (2020). Harmonization of quality metrics and

power calculation in multi-omic studies. *Nature Communications*, *11*(1), 3092. https://doi.org/10.1038/s41467-020-16937-8

THOMAS, S. G., CALAMINUS, S. D. J., MACHESKY, L. M., ALBERTS, A. S., & WATSON, S. P. (2011). G-protein coupled and ITAM receptor regulation of the formin FHOD1 through Rho Kinase in platelets. *Journal of Thrombosis and Haemostasis*, *9*(8), 1648-1651. https://doi.org/https://doi.org/10.1111/j.1538-7836.2011.04357.x

Tillberg, P. W., Chen, F., Piatkevich, K. D., Zhao, Y., Yu, C.-C. J., English, B. P., Gao, L., Martorell, A., Suk, H.-J., Yoshida, F., DeGennaro, E. M., Roossien, D. H., Gong, G., Seneviratne, U., Tannenbaum, S. R., Desimone, R., Cai, D., & Boyden, E. S. (2016). Protein-retention expansion microscopy of cells and tissues labeled using standard fluorescent proteins and antibodies. *Nature Biotechnology*, *34*(9), 987-992. https://doi.org/10.1038/nbt.3625

Tinevez, J.-Y., Perry, N., Schindelin, J., Hoopes, G. M., Reynolds, G. D., Laplantine, E., Bednarek, S. Y., Shorte, S. L., & Eliceiri, K. W. (2017). TrackMate: An open and extensible platform for single-particle tracking. *Methods*, *115*, 80-90. https://doi.org/https://doi.org/10.1016/j.ymeth.2016.09.016

Valet, C., Batut, A., Vauclard, A., Dortignac, A., Bellio, M., Payrastre, B., Valet, P., & Severin, S. (2020). Adipocyte Fatty Acid Transfer Supports Megakaryocyte Maturation. *Cell Reports*, *32*(1), 107875. https://doi.org/https://doi.org/10.1016/j.celrep.2020.107875

Vargason, T., Howsmon, D., McGuinness, D., & Hahn, J. (2017). On the Use of Multivariate Methods for Analysis of Data from Biological Networks. *Processes*, *5*, 36. https://doi.org/10.3390/pr5030036

VerPlank, L., & Li, R. (2005). Cell Cycle-regulated Trafficking of Chs2 Controls Actomyosin Ring Stability during Cytokinesis. *Molecular biology of the cell*, *16*(5), 2529-2543. https://doi.org/10.1091/mbc.e04-12-1090

Vicente-Manzanares, M., Choi, C. K., & Horwitz, A. R. (2009). Integrins in cell migration--the actin connection. *Journal of Cell Science*, *122*(Pt 2), 199-206. https://doi.org/10.1242/jcs.018564

vicente-manzanares, M., Ma, X., Adelstein, R., & Horwitz, A. (2009). Non-muscle myosin II takes centre stage in cell adhesion and migration. *Nature reviews. Molecular cell biology*, *10*, 778-790. https://doi.org/10.1038/nrm2786

Voigt, S. P., Ravikumar, K., Basu, B., & Kalidindi, S. R. (2021). Automated Image Processing Workflow for Morphological Analysis of Fluorescence Microscopy Cell Images. *JOM*, *73*(8), 2356-2365. https://doi.org/10.1007/s11837-021-04707-w

Wandall, H. H., Rumjantseva, V., Sørensen, A. L. T., Patel-Hett, S., Josefsson, E. C., Bennett, E. P., Italiano, J. E., Jr., Clausen, H., Hartwig, J. H., & Hoffmeister, K. M. (2012). The origin and function of platelet glycosyltransferases. *Blood*, *120*(3), 626-635. https://doi.org/10.1182/blood-2012-02-409235

Wassie, A. T., Zhao, Y., & Boyden, E. S. (2019). Expansion microscopy: principles and uses in biological research. *Nature Methods*, *16*(1), 33-41. https://doi.org/10.1038/s41592-018-0219-4

Watanabe, N., Madaule, P., Reid, T., Ishizaki, T., Watanabe, G., Kakizuka, A., Saito, Y., Nakao, K., Jockusch, B. M., & Narumiya, S. (1997). p140mDia, a mammalian homolog of Drosophila diaphanous,is a target protein for Rho small GTPase and is a ligand for profilin. *The EMBO Journal*, *16*(11), 3044-3056. https://doi.org/https://doi.org/10.1093/emboj/16.11.3044

Wear, M. A., Schafer, D. A., & Cooper, J. A. (2000). Actin dynamics: Assembly and disassembly of actin networks. *Current Biology*, *10*(24), R891-R895. https://doi.org/https://doi.org/10.1016/S0960-9822(00)00845-9

Wilkinson, S., Paterson, H. F., & Marshall, C. J. (2005). Cdc42–MRCK and Rho–ROCK signalling cooperate in myosin phosphorylation and cell invasion. *Nature Cell Biology*, *7*(3), 255-261. https://doi.org/10.1038/ncb1230

Wu, C. Y., Lin, M. W., Wu, D. C., Huang, Y. B., Huang, H. T., & Chen, C. L. (2014). The role of phosphoinositide-regulated actin reorganization in chemotaxis and cell migration. *British journal of pharmacology*, *171*(24), 5541-5554. https://doi.org/10.1111/bph.12777

Wu, Y., Ghitani, A., Christensen, R., Santella, A., Du, Z., Rondeau, G., Bao, Z., Colón-Ramos, D., & Shroff, H. (2011). Inverted selective plane illumination microscopy (iSPIM) enables coupled cell identity lineaging and neurodevelopmental imaging in <em>Caenorhabditis elegans</em&gt. *Proceedings of the National Academy of Sciences*, *108*(43), 17708. https://doi.org/10.1073/pnas.1108494108

Xiao, Q., Hu, X., Wei, Z., & Tam, K. Y. (2016). Cytoskeleton Molecular Motors: Structures and Their Functions in Neuron. *International journal of biological sciences*, *12*(9), 1083-1092. https://doi.org/10.7150/ijbs.15633

Xue, B., & Robinson, R. (2013). Guardians of the actin monomer. *European journal of cell biology*, *92*. https://doi.org/10.1016/j.ejcb.2013.10.012

Yamamoto, M., Hilgemann, D. H., Feng, S., Bito, H., Ishihara, H., Shibasaki, Y., & Yin, H. L. (2001). Phosphatidylinositol 4,5-Bisphosphate Induces Actin Stress-Fiber Formation and Inhibits Membrane Ruffling in Cv1 Cells. *Journal of Cell Biology*, *152*(5), 867-876. https://doi.org/10.1083/jcb.152.5.867

Zeng, Z.-p., Xie, H., Chen, L., Zhanghao, K., Zhao, K., Yang, X.-s., & Xi, P. (2017). Computational methods in super-resolution microscopy. *Frontiers of Information Technology & Electronic Engineering*, *18*(9), 1222-1235. https://doi.org/10.1631/FITEE.1601628

Zhang, P. (2013). Correlative cryo-electron tomography and optical microscopy of cells. *Current Opinion in Structural Biology*, *23*(5), 763-770. https://doi.org/https://doi.org/10.1016/j.sbi.2013.07.017

Zimmermann, D., Homa, K. E., Hocky, G. M., Pollard, L. W., De La Cruz, E. M., Voth, G. A., Trybus, K. M., & Kovar, D. R. (2017). Mechanoregulated inhibition of formin facilitates contractile actomyosin ring assembly. *Nature Communications*, *8*(1), 703-703. https://doi.org/10.1038/s41467-017-00445-3

Zuidscherwoude, M., Green, H. L. H., & Thomas, S. G. (2019). Formin proteins in megakaryocytes and platelets: regulation of actin and microtubule dynamics. *Platelets*, *30*(1), 23-30. https://doi.org/10.1080/09537104.2018.1481937